Doctoral theses at NTNU, 2020:391

Sohrab Alex Mofid

Synthesis, Modeling and Characterization of Thermally Insulating and Optically Switchable Nanostructured Materials for Energy Efficiency Building Applications.

Doctoral thesis

Sohrab Alex Mofid

ISBN 978-82-326-5128-3 (printed ver.)
ISBN 978-82-326-5129-0 (electronic ver.)
ISSN 2703-8084 (online)
ISSN 1503-8181 (printed ver.)

NTNU
Norwegian University of
Science and Technology

NTNU
Norwegian University of Science and Technology
Thesis for the Degree of
Philosophiae Doctor
Faculty of Engineering
Department of Civil and Environmental
Engineering

Doctoral theses at NTNU, 2020:391

NTNU

Sohrab Alex Mofid

Synthesis, Modeling and Characterization of Thermally Insulating and Optically Switchable Nanostructured Materials for Energy Efficiency Building Applications.

Thesis for the Degree of Philosophiae Doctor

Trondheim, November 2020

Norwegian University of Science and Technology
Faculty of Engineering
Department of Civil and Environmental Engineering

NTNU
Norwegian University of
Science and Technology

NTNU
Norwegian University of Science and Technology

Thesis for the Degree of Philosophiae Doctor

Faculty of Engineering
Department of Civil and Environmental Engineering

ISBN 978-82-326-5128-3 (printed ver.)
ISBN 978-82-326-5129-0 (electronic ver.)
ISSN 2703-8084 (online)
ISSN 1503-8181 (printed ver.)

Doctoral theses at NTNU, 2020:391

Printed by NTNU Grafisk senter

Preface

The thesis presents the highlights of my research experience and achievements during my tenure as Ph.D. researcher from June 2015 to Jan 2020 at the Norwegian university of Science and Technology, Department of Civil and Environmental Engineering and the University of Boulder Colorado, Department of Mechanical Engineering, respectively. My research project " High-Performance Nano Insulation Materials (Hi-Per NIM)" was awarded by the Research Council of Norway within the Nano2021 program through NTNU and SINTEF, Project No. 250159. Furthermore, the Research Council of Norway is acknowledged for the support to the" Norwegian Micro- and Nano-Fabrication Facility" (NorFab, project no. 245963/F50).

I wish to express my sincere gratitude to my supervisor, Professor Bjørn Petter Jelle, for his inspired guidance, profound knowledge, insightful suggestions, prompt response and constant encouragement and support throughout the entire period of my research study. The enthusiasm, rigorous attitude and dedication to scientific research are strongly impressed on my memory. I would as well like to convey my gratitude to my co-supervisor, Tao Gao, for his insightful criticism, great patience and invaluable advices which greatly helped me improve the depth of my research. The provided level of expertise and knowledge with regards to research design and academic writing were instrumental in shaping my views and character as a research scientist. Furthermore, I would like to thank and acknowledge former Civil and Environmental Engineering Department head, Dr. Carl Christian Thodesen, for his significant effort, nurturing gestures and profound friendship and humility.

I would like to acknowledge and thank my supervisor in UC Boulder, Professor Ronggui Yang, for his invaluable knowledge, remarkable comments, distinguished creativity and immense encouragement during my research period in the U.S. I would as well like to acknowledge Associate Professor Xiabo Yin, for his generous and insightful scientific guidance, pronounced knowledge and noble lab skills. My immense gratitude to my research colleague and partner in UC Boulder, Xinpeng Zhao, for his remarkable effort, impressive skills and talented contribution to the research projects and his selfless attitude and friendship to me.

I would like express my heartfelt gratitude and respect to my Polish family, Marek, Maria and Justyna Bednarek, for their passionate guidance, infinite support and endless nurturing love and patience and humble encouragement. I wouldn't be where I am now without your love and support.

Last but not Least, I would like to extend a sincere heartfelt message of love and infinite gratitude to my family. I would like to acknowledge and say thank you to my dad, Homayoun Mofid, for being my role model and hero, best father a son could ever ask for, and a model of honesty, integrity, humility and most importantly, bright light to every party and community. I would like to thank my only sister, Sahar Mofid, for being the glue that firmly holds the family together, being the exemplary and unique character that always correct and nurture without no expectation in return. I'm proud to be your brother, I thank and salute you for your boundless love, immeasurable sacrifices, selfless and nurturing guidance, and most notably for being the best representation of our family. I would like to thank my dearest wife, Bridget Marie Mofid, for being more than a best friend and an irreplaceable company whom have been most present and worked side by side with me throughout my entire Ph.D research. Highlights and achievements were only made possible due to your constant motivation, encouragement and maintained level of support and love. I sincerely thank you for immeasurable patience, pure care & selflessness, inspiration and precious friendship that made me believe in science again.

I would like to dedicate this to my mother, Zhinous Kazemi and honor the memory of my late aunt, Venous Kazemi. My deepest love and utmost respect to the most influential individuals whom have granted me the gift of unconditional love. The absolute nurturing, resolute dedication, indefinite support and open-ended patience were only instrumental in forming my values and shaping my character. They both have shared a deep and enduring commitment in my pursuit of higher education and served as source of inspiration to me during my entire education. I can only hope to repay some of their kindness, adoration, devotion with dedicating this noble cause and achievement to them.

Contents

List of Articles

I. B.P. Jelle, B.G. Tilset, T. Gao, M. Grandcolas, O.M. Løvvik, R.A. Bohne, **S.A. Mofid**, S. Ng, E. Sagvolden, High-performance nano insulation materials for energy-efficient buildings, Proceedings of TechConnect World Innovation Conference 2017, TechConnect, 2017.

II. H.F. Gangåssæter, B.P. Jelle, **S.A. Mofid**, T. Gao, Air-filled nanopore based high-performance thermal insulation materials, Energy Procedia 132 (2017) 231-236.

III. H.F. Gangåssæter, B.P. Jelle, **S.A. Mofid**, Synthesis of silica-based nano insulation materials for potential application in low-energy or zero emission buildings, Energy Procedia 122 (2017) 949-954.

IV. S. Ng, B.P. Jelle, L.I. Sandberg, T. Gao, **S.A. Mofid**, Hollow silica nanospheres as thermal insulation materials for construction: Impact of their morphologies as a function of synthesis pathways and starting materials, Construction and Building Materials 166 (2018) 72-80.

V. **S.A. Mofid**, B.P. Jelle, T. Gao, Utilization of Hollow Silica Nanospheres for Thermal Insulation Purposes, Proceedings of TechConnect World Innovation Conference (2016) 259-262.

VI. B.P. Jelle, **S.A. Mofid**, M. Grandcolas, M. Sletnes, E. Sagvolden, Nano insulation materials exploiting the Knudsen effect, IOP Conference Series: Materials Science and Engineering, IOP Publishing, 2019, p. 012003

VII. **S.A. Mofid**, B.P. Jelle, X. Zhao, T. Gao, M. Grandcolas, B. Cunningham, S. Ng, R. Yang, Utilization of size-tunable hollow silica nanospheres for building thermal insulation applications, Journal of Building Engineering 31 (2020) 101336.

VIII. X. Zhao, **S.A. Mofid**, M.R. Al Hulayel, G.W. Saxe, B.P. Jelle, R. Yang, Reduced-scale hot box method for thermal characterization of window insulation materials, Applied Thermal Engineering 160 (2019) 114026.

IX. D. Hou, T. Li, X. Chen, S. He, J. Dai, **S.A. Mofid**, D. Hou, A. Iddya, D. Jassby, R. Yang, L.Hu, Z.J. Ren, Hydrophobic nanostructured wood membrane for thermally efficient distillation, Science Advances 5(8) (2019) eaaw3203.

X. X. Zhao, **S.A. Mofid**, B.P. Jelle, G. Tan, X. Li, X. Yin, R. Yang, Optically-switchable thermally-insulating VO_2-aerogel hybrid film for window retrofits, Applied Energy 278 (2020) 115663.

XI. X. Zhao*, **S.A. Mofid***, B.P. Jelle, T. Gao, X. Yin, R. Yang, Durability-enhanced vanadium dioxide thermochromic films for smart windows, Materials Today Physics 13 (2020) 100205.

XII. Y. Xie, X. Zhao, **S.A. Mofid**, J. Tan, B.P. Jelle, R. Yang, Influence of shell material on the optical performance of VO_2 core-shell nanoparticle-based thermochromic smart films, Materials Today Nano, (2020) 100102.

1. Introduction

1.1 General

Commercial and residential buildings account for ~ 40% of primary energy consumption in the U.S, E.U. and ~ 27.3% in China [1-3], and given the steady growth, the Energy Information Agency (EIA) predicted that the number is likely to reach > 45% by 2035 [4, 5]. Heating, cooling, ventilation and air-conditioning (HVAC) systems compromise more than ~ 50% of total building energy consumption. According to the European Commission and the derived data from the International Energy Agency (IEA), the heating energy, including space and water heating compromise the largest portion of the building energy use [6]. The space cooling on the other hand, occupy the smallest portion of the final energy demand. However, recent decade has seen a global climate change, which has significantly impacted the heating and cooling demands in different regions. Based on the current recorded statistics, a recent model predicted that residential heating demand will decrease by 34% and cooling demand will increase by 72% in the next century [7]. The total energy demand will primarily increase in cooling-dominant and less-developed regions. For this reason, the advanced design of building envelopes remains necessary to facilitate the heating and cooling issues. According to recent studies, the proper design of advanced building envelopes and building envelope energy retrofits can reduce the heating and cooling loads by over 50% [8, 9]. Moreover, The building energy efficiency measures can provide key solutions to address carbon emission and energy shortages. In general, there exists a strong consensus that the proper energy saving approaches can mitigate the global warming trends and reduce the Greenhouse gas (GHG). Therefore, in order to fulfil energy efficiency goals in 1) U.S.: reduction of energy use and GHG emissions of more than 50% by 2050 [10], 2) E.U: reduction of GHG emission by 50% and energy saving goal of more 20% by 2030 [11] and 3) China (world's largest

emitter of GHG gas): climate neutral, zero-emission and reduction of 27% energy demand by 2050 [12]; effective energy efficiency measures in building and construction sectors must be adopted and the heating and cooling demands must sharply reduce its energy consumption.

1.2 Objective of the current work

The main objective of the Ph.D dissertation was found on identifying and analyzing concepts necessary for design, synthesis, modelling, characterization and large-scale manufacturing of the nanostructured materials and nanocomposites that will directly benefit energy-efficiency issues in building envelopes and energy systems used in buildings. The potential application of these novel materials and technologies will result in significant reduction of CO_2 and efficient energy use.
The research design in this work has been mainly focused on:

I. Synthesis of nanostructured materials with unprecedented properties; explore technologies benefiting from material properties by design.

II. Investigation and modelling of thermal and optical transport properties of nanostructures for energy saving performance evaluation.

III. Characterization of thermal and optical properties of nanostructured materials; developing techniques and devices with unique functionalities enabled by the materials engineering.

IV. Developing scalable-manufacturing technique that enable large-scale deployment of these innovative nanostructures and nanomaterials for advanced applications in energy-efficient buildings and energy systems.

1.3 Scope of the current work

The research highlights and achievements in this work were in classified in four different sections, including, synthesis, characterization, modeling and manufacturing development and are reviewed as following:

1. Synthesis and fabrication of hybrid and thermal insulation materials used for applications in energy efficient buildings and energy systems:
   - *Synthesis and utilization of size-tunable (core/shell) PS@SiO_2 hollow silica nano spheres (HSNS) for thermal insulation applications in sustainable built environment.*
   - *Synthesis of dynamically switchable polymer solar films embedded with phase change nanomaterials for durability enhanced energy-efficient smart window applications.*
2. Design and development of accurate thermal property characterization method directly used for nanoinsulation materials for building applications:
   - *Reduced-scale hotbox method for thermally insulating and optically switchable nanomaterials at their early stage of development ranging from 0.06 to 0.2 m. (diameter or length) e.g, nanomebrane wood, porous insulation films.*
   - *Thermal property characterization of hydrophobic nanostructured wood membrane for thermally efficient distillation.*
3. Thermal and Optical modeling of window retrofit materials used for energy saving purposes in hot and cold climates.
   - *Optically-switchable thermally-insulating aerogel VO_2-PMMA (AVP) film for energy-efficiency window retrofits.*
   - *Optical performance of shell materials for core-shell (VO_2@Shell) based smart thermochromic window films.*
4. Scalable nanomanufacturing technique for large-scale employment of polymer films embedded with phase change nanoparticles for smart window applications:
   - *Roll-to-Roll scalable nanomanufacturing of biaxially-oriented polyethylene terephthalate (BoPET) sheet with a thin VO_2-PMMA polymer layer of ~ 4 μm for highly efficient thermochromic windows.*

1.4 Overview of the thesis

The thesis consist of background information, methodology, discussion and conclusion sections. Chapter 1 presents a general introduction, objectives and highlights of the research work. It also includes a short thesis overview as given in this section. Chapter 2 gives brief background information about the impact of various building components on energy consumption, evaluation and development of the thermal insulation materials including high-performance nano insulation materials and window insulation materials and retrofits, thermal characterization and thermal and optical modeling to evaluate the energy performance of the developed materials. Chapter 3 outlines the methods and experimental approach applied in this study, including synthesis approach and characterization techniques and methods while detailed output of the research work and achievements were presented in peer reviewed journal publications in Chapter 4. The conclusion, including short summary of the research work with the main finding is then given in Chapter 5. Finally, after the references follows the full scientific article publications.

2. Background

2.1 Energy Consumption of Building Envelopes

Reducing the energy demand for buildings remains an important objective as construction and building occupancy significantly contribute to the global carbon dioxide emissions (CO_2), accounting for approximately quarter of global CO_2 emission [13, 14]. CO_2 plays a strong contribution in the greenhouse gas effect which leads to rising global temperature [15]. To meet the demand, building insulation is considered the most effective strategy to reduce the energy consumption by preventing heat gain or loss through the building envelopes [15, 16]. Therefore, effective incorporation of thermal insulation in, i.e., walls, windows, roofs and floor and/or

improving the thermal efficiency of the existing buildings is the direct solution to conserve energy and consequently reduce the energy consumption of heating and cooling systems [17, 18]. Furthermore, utilizing the building insulation will promote fire protection, condensation control, thermal comfort and sound control. The heat gain and loss analysis are instrumental for discovering energy conservation targets. Thus, building components responsible for annual heat gain and loss in the hot and the cold climate, must be evaluated accordingly. In cold climates, the most prominent source of heat gain is the solar radiation [19, 20]. While windows, walls and infiltration are the main contributors to the heat loss in buildings in cold climates. Although, other factors, including door, roof and floor slabs also contribute to the heat loss but compared to windows and walls, their contributions remain insignificant. For example, The study by Kim *et al* [21] discussed the impact of insulation on building energy consumption and demonstrated the heat loss and the heat gain for various building components in cold climate (Michigan, Detroit) depicted in Figure 1. It is clearly seen that window insulation is a high priority strategy for residential energy conservation in cold climates. it can also be observed that energy efficient appliances is necessary to conserve the energy for homes in cold climates.

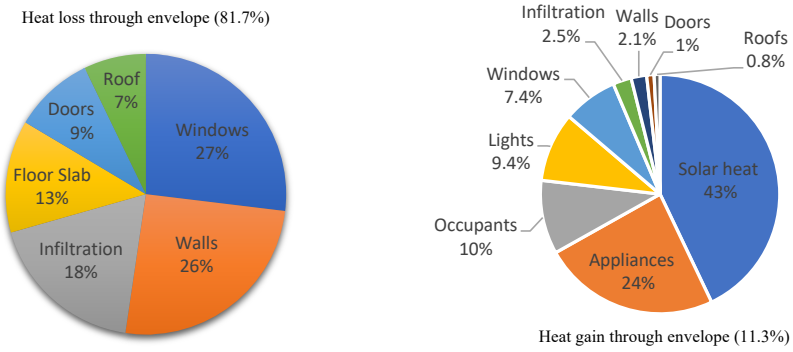

Figure 1. Heat loss and heat gain components (%) in Detroit, Michigan (**Cold climate**) respectively [21].

Similarly, in hot climates, solar radiation coupled with the heat conduction through windows possess the largest heat gain components in buildings [19, 22, 23]. However, compared with the same situation in cold climates, the case for Miami, Florida shows that percentages of conduction heat gain through building envelope and infiltration are higher. This is because of the greater exterior temperatures in a hot climate. From Figure 2 it is evident that since degree of the heat loss is insignificant in hot climates, residential energy conservation strategies should be primarily based on heat gain components.

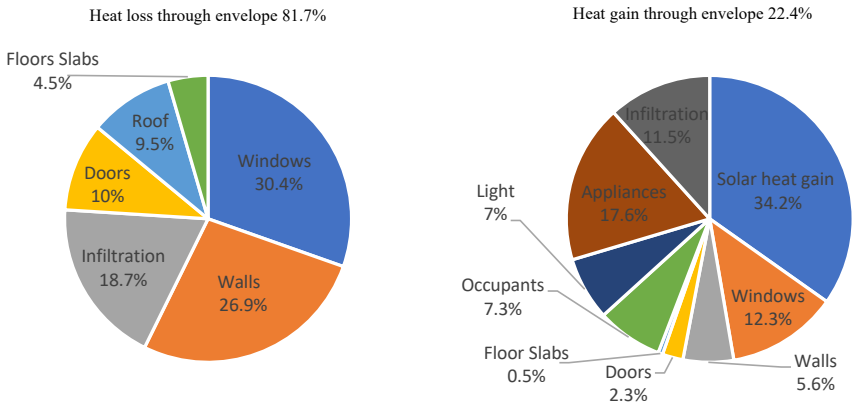

Figure 2. Heat loss and heat gain components (%) in Miami, Florida (**Hot climate**) respectively [21].

The analysis of heat gain and loss component in hot and cold climates reveal that: 1) solar heat gain constitutes single largest heat gain component which will be an asset for reducing the heating load during winter. 2) thermal insulation is primarily beneficial for reducing the heating load in cold climates but does hardly provide any tangibles in hot climates. In another words, while minimum insulation is desired and necessary, any extra insulation would necessarily not contribute to saving heating or cooling energy in hot climate. 3) infiltration can have a significant impact on the energy waste, which is directly dependent on the tightness of the building construction. 4) use

of energy efficient appliances not only decrease the electricity consumption but also reduce internal heat production, which, in turn help cooling loads in hot climates. In this work, thermal insulation and solar radiation were the primary concerns in design, modeling, synthesis of new generation of materials for building energy efficiency applications. In addition to thermal and optical enhancement, environmental stability, durability and mechanical robustness were discussed and improved in some cases.

2.2 Thermal Insulation

2.2.1 Thermal Transport Properties

The thermal insulation performance is directly characterized by the thermal conductivity (λ), which is mainly dependent on density, porosity, moisture content and mean temperature difference of the desired materials [24, 25]. ASTM standard defined the thermal conductivity (λ-value, W/mK) as the time rate of steady state heat flow through a unit area of homogenous material induced by a unit temperature gradient in a direction perpendicular to that unit area [26]. Typically thermal insulation materials exhibit heat flows by of combination of modes as following :

$$\lambda_{total} = \lambda_{convection} + \lambda_{conduction} + \lambda_{radiation} + \lambda_{leakage} \quad (1)$$

Where,

$$\lambda_{conduction} = \lambda_{solid} + \lambda_{gas} + \lambda_{coupling} \quad (2)$$

The convection thermal conductivity $\lambda_{convection}$ originates from thermal mass transport or movement of air and moisture. The solid thermal conductivity λ_{solid} is linked to thermal transport in between atoms by lattice vibrations, i.e. through chemical bonds between atoms. The gaseous thermal conductivity λ_{gas} arises from gas molecules colliding to one another and thus transferring

thermal energy from one molecule to another one. The thermal radiation λ_{rad} is associated with the emittance of electromagnetic radiation in the infrared (IR) wavelength region from a materials surface. Furthermore, the thermal leakage $\lambda_{leakage}$ signify moisture and air leakage driven by pressure difference and the thermal coupling normally account for second order effect between the various thermal conductivities in Eq.1, For example, solid and gaseous thermal conductivity interaction in low dimension porous insulation materials. In practice, the λ-value is evaluated at 24 °C according to relevant ASTM standards.

2.2.2 Traditional and State-of-art Insulation Materials

The following diagram presents the development of the insulation materials according to function, form and composition and classifies them into three different categories depicted in Figure 3.

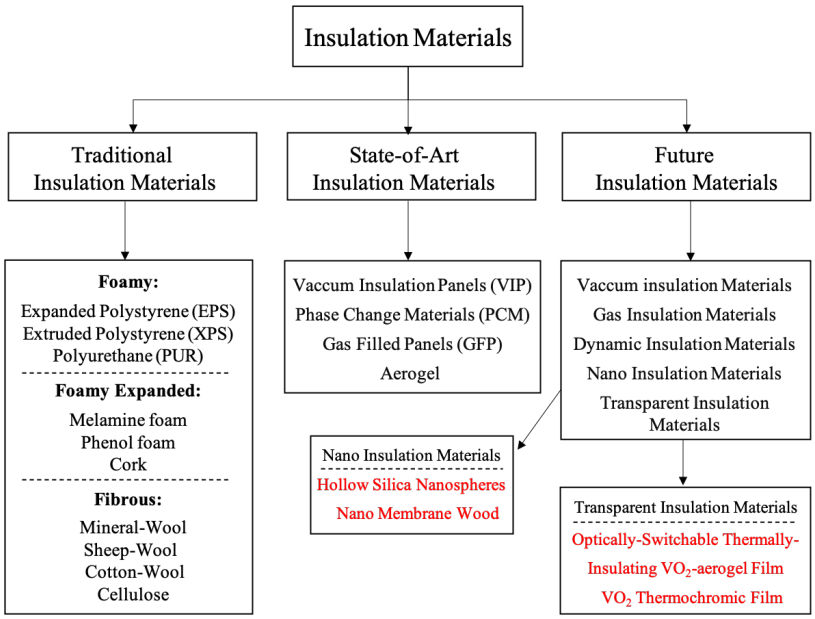

Figure 3. Classification of commonly used insulation materials, insulation materials developed in this work (red).

Traditional thermal insulation materials possess relatively high thermal conductivity values ranging from 30-50 mW/(mK) [27-30], with the lowest thermal conductivity value recorded for Polyurethane (PUR) at 20 mW/(mK) [31]. The thermal conductivity values also increases significantly with the surge in moisture content for traditional thermal building insulation materials [32]. In addition, health hazard issues, e.g., the toxic gas release from PUR during a fire, limit their ability as a viable option in passive and or energy efficient buildings. The two most promising state-of-art insulation materials today, including vacuum insulation panels and aerogels, have considerably lower thermal conductivities values than the traditional ones. Vacuum insulation panel (VIP) in pristine condition has 3 ~ 4 mW/(mK) [33]. However, air and vapor diffusion together with inevitable puncturing of the VIP envelope can increase the thermal conductivity to about 20 mW/ (mK) [34]. This represents a major drawback for all VIPs. Commercially available state-of-art aerogels represents the most promising insulation candidate material today with the reported thermal conductivity values between 13 to 14 mW/(mK) at ambient pressure (Aspen Aerogels 2008 ab) [35]. Aerogels are produced as transparent, translucent and opaque, thus enable broad range of potential building insulation applications [36, 37]. But the production cost of aerogel is still high and they possess fragile/deformable porous structure.

2.2.3. Possible Future Thermal Building Insulation

Proper design and choice of future insulation materials depend on the type of applications, desired materials physical, thermal and other properties. The essential properties and issues among others include thermal conductivity, environmental friendliness, climate aging durability, hydrophobicity, fire protection, robustness and production cost [38]. In general, as seen from Figure 1 and Figure 2, it is strategic to insulate buildings from main components, including walls and windows where the heat transfer predominately takes place. Therefore, due to distinctive

advantage of thermal insulation and solar collection [39], transparent window insulation materials have been considered as the main building insulation target. In addition, nano insulation materials with potential building applications in e.g. walls were also utilized in order to keep the contributions from each of the specific thermal conductivities in Eq.1. as low as possible.

2.2.4 Thermal Transport through Walls

In general, walls are responsible for approximately ~ 25% of heat loss in buildings. If walls are adiabatically insulated, so that net heat transfer through walls become negligible, it can save a maximum 25% of space heating energy which nearly account for 11% of annual building energy consumption [21, 40] . The measure of heat transmission through a building wall is assessed by the U-value. U-value, the heat transfer coefficient, determines the thermal quality of the building component. Therefore, the lower the U-value, the greater the wall's resistance to heat flow and the better it's insulation properties. Figure 4(a) illustrates the heat transfer across a typical masonry wall consisting of brick, insulation cavity and concrete. It is clearly seen that thermal transport between the wall and indoor and outdoor environment is through convection and radiation, and the heat transfer across the wall is directly through heat conduction. Figure 4(b) presents the corresponding thermal resistance network of masonry wall. The U-value (W/(m^{2}K)) of the wall can then be calculated as sum of the resistances as follows:

$$\frac{1}{U} = R_{total} = \frac{1}{1/R_{conv,o} + 1/R_{rad,o}} + \sum_{i}^{n} R_{wall} + \frac{1}{1/R_{conv,i} + 1/R_{rad,i}} \tag{3}$$

$$R_{wall} = R_{brick} + R_{Insulation} + R_{concrete} \tag{4}$$

where, $R_{conv,o} = 1/h_{conv,o}$ and $R_{rad,o} = 1/h_{rad,o}$ are the outdoor convective and radiative thermal resistances, respectively; $R_{conv,i} = 1/h_{conv,i}$ and $R_{rad,i} = 1/h_{rad,i}$ are the indoor

convective and radiative thermal resistances, respectively; h_{conv} and h_{rad} are the convective and radiative heat transfer coefficients, respectively; $R_{conc} = L_{conc}/k_{conc}$, $R_{ins} = L_{ins}/k_{ins}$, $R_{br} = L_{br}/k_{br}$, are the effective thermal conductance of brick, expanded polystyrene (EPS) insulation layer and concrete forming the wall, respectively; k and L are thermal conductivity and thickness of each layer, respectively. The residential wall thickness typically ranges from 0.25 to 0.35 m, while the insulation cavity occupies ~ 0.1 m (filled or partly filled with 0.025 mm airgap) [41, 42].

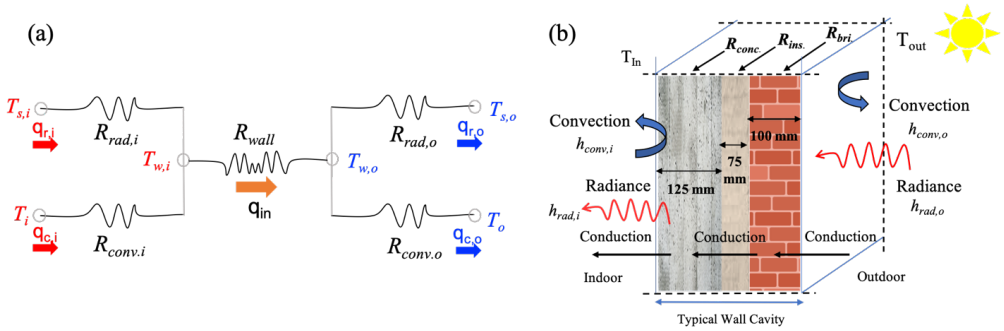

Figure 4.. (a) Thermal resistance network showing steady-state heat transfer through a multi-layer building wall. (b) Diagram of a typical multi-layer wall consisting of brick, insulation layer and concrete, where indoor and outdoor temperature are 20 °C and -10 °C, respectively and the wind speed is 4 m/s.

Table 1. presents the heat flow values from convection, conduction and the radiation contributions, where the thermal conductivity values of building brick, EPS and dense concrete with thicknesses L_1 = 100 mm, L_2 = 75 mm, L_3=125 mm are k_1 = 0.77 W/(mK), k_2 = 0.040 W/mK and k_3 = 1.6 W/mK, respectively [43-45]. The emissivity values of common building brick and concrete are 0.93 and 0.94, respectively . $T_{w,i}$ and $T_{w,o}$ are the inner and outer wall temperatures while $T_{s,i}$ and $T_{s,o}$ are surface temperatures of interior and exterior wall facing indoor and outdoor environment, respectively. Indoor temperature T_i and the outdoor temperature T_o are 20°C and -10°C, respectively. The wind speed is 4 m/s. The interior represents the combination of convection and

radiation thermal resistance from the inner wall while exterior presents the combination of convection and radiation thermal resistances from the exterior wall facing outdoor environment. The obtained heat flow values from Table 1 clearly shows that thermal insulation provides ~ 70 % of the total resistance (RSI). Assuming an extra 25 mm air space between the brick and EPS insulation layer, the contribution from the thermal insulation can be even higher.

Table 1. Calculated thermal resistance values from convection, radiation and the wall conduction.

Material Layer	**Conductivity (W/mK)**	**Thickness (mm)**	**Resistance (m^2K/W)**
Exterior*	N.A.	N.A.	0.30
Brick	0.77	100	0.13
Air Space**	N.A.	25	(0.17)
EPS Insulation	0.04	75	1.88
Concrete	1.6	125	0.078
Interior***	N.A.	N.A.	0.46
	Resistance (RSI) Total		2.85
	Overall Heat Transfer, U		0.35

* The exterior represents the combined values of convective and radiative thermal resistances of the brick wall facing the outdoor environment at -10 °C temperature. Given the windspeed 4m/s, the outer and inner surface of the brick was calculated at -9 °C and -7 °C, respectively.

** The flow of heat through an air gap is complicated by the convection (air flows) and radiation, so the calculated value in the table is variable but not important to accuracy in the calculation for most composite modern walls.

*** The interior represents the combined values of convective and radiative thermal resistances of the concrete wall facing indoor environment at 20 °C temperature. Based on the thermal conductivity of EPS insulation (0.04 W/mK) the outer and inner surface of the concrete wall was calculated at 17 °C and 18.5 °C, respectively.

The overall heat transfer through the wall can then be calculated as a function of U-value ($W/(m^2K)$) as follows:

$$Q_{loss} = U * A * (T_{in} - T_{out}) \quad (5)$$

Where, U is the overall heat transfer coefficient of the wall, A is the total surface area of the wall and T_{in} and T_{out} are the indoor and outdoor temperatures. From Table 1, it is clearly seen that resistance of the EPS insulation layer (1.88 m^2K/W) comprise ~ 70% of the total wall resistance.

Therefore, in order to reduce the heat loss through the wall, the objective of the current research and development should mainly focus on creation of highly efficient, sustainable insulating materials and systems which also provide a considerable insulating effect even when smaller cross-sections are used. Furthermore, the higher surface temperature due to enhanced thermal insulation will lead to improved thermal comfort and better condensation resistance.

2.2.4.1 Hollow Silica Nanospheres

New class of nano hybrids, hollow silica nanospheres (HSNS), has been proposed as a possible building block that may successfully bring about nano insulation materials with substantially reduced thermal conductivity [46, 47]. In general, HSNS shown in Figure 5 can be classified as an air cavity enclosed by an inorganic shell with tailored structural features, where the voids are usually correlated to the use of sacrificial templates during HSNS synthesis [48, 49].

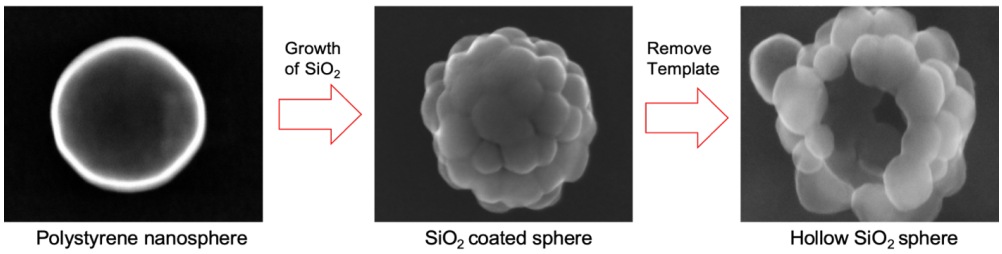

Figure 5. SEM images showing (left) PS nanosphere used as the template, (middle) PS template coated with silica nanoparticles, and (right) well-defined core-shell structure of a hollow silica nanosphere after template removal.

Distinctive advantage of HSNS for thermal insulation applications are amongst others, their controllability, thermal properties of HSNS being promptly modified by utilization of their structural characteristics, such as inner pore diameter and shell thickness. Furthermore, unique properties such as low density, high porosity, large surface to volume ratio and encapsulating

abilities make HSNS an ideal candidate material for potential thermal insulation applications [50]. The effective thermal conductivity of HSNS is the coupling result of λ_{solid} – thermal conductivity of solid backbone of HSNS, λ_{gas} – thermal conductivity of gas is governed by both the gas inside the HSNS nanoscale pores and the gas trapped within the particles constituting the shell. Structural parameters such as shell thickness, contact area between adjacent neighboring nano particles, hollow sphere size and the packing density could impact the heat conduction of the solid phase. The gaseous thermal conductivity is mainly determined by the size of the nanoscale pores. This can be interpreted by the Knudsen effect, which considers gaseous thermal transport in a space with small dimension [51, 52],

$$\lambda_{Kn} = \frac{\lambda_{gas,0}}{1 + 2\beta Kn} = \frac{\lambda_{gas,0}}{1 + \frac{\sqrt{2\beta \mathrm{K_B T}}}{\pi d^2 \mathrm{p}\delta}} \tag{6}$$

Where,

$$\mathrm{Kn} = \frac{\sigma_{mean}}{\delta} = \frac{\mathrm{K_B T}}{\sqrt{2}\pi d^2 \mathrm{p}\delta} \tag{7}$$

where $\lambda_{gas,0}$ is the gas thermal conductivity in the pores at STP (standard temperature and pressure) (W/(mK)), β is the coefficient characterizing the molecule-wall collision energy transfer (in)efficiency (between 1.5 - 2.0), K_B is the Boltzmann's constant ≈ $1.38 \cdot 10^{-23}$ J/K, T is the temperature (K), d is the gas molecule collision diameter (m), p is the gas pressure in pores (Pa), δ is the characteristic pore diameter (m), σ_{mean} is the mean free path of gas molecules (m) and Kn is the Knudsen number. It is evident that for pores with diameter of a few nanometers, the Knudsen effect becomes very large (small Knudsen number), which therefore results in a reduced gaseous thermal conductivity. Furthermore, the solid state thermal conductivity of the HSNS can be explained by Liang and Li [53]:

$$\frac{\lambda_N}{\lambda_B} = p\ exp\left(-\frac{l_0}{D}\right)\left[exp\left(\frac{1-\alpha}{D/D_0 - 1}\right)\right]^{3/2} \quad (8)$$

where λ_B is the thermal conductivity of the bulk material, l_0 is the phonon mean free path at room temperature, D is the featured size (e.g. diameter of nanoparticles), D_0 and α are material constants, p is a factor reflecting the surface roughness, $0 \leq p \leq 1$, where $p \rightarrow 1$ represents a smoother surface which results in higher probability of specular phonon scattering, whereas $p \rightarrow 0$ corresponds to a rougher surface with higher probability of diffusive phonon scattering [54, 55]. In relation to HSNS, given the same pore diameter, a thinner shell thickness, a smaller D, will lead to a lower solid-state thermal conductivity. In addition, the smaller contact area directly due to reduced particles sizes constituting the shell will lead to lower thermal conductivity. In this work, we have successfully synthesized low density HSNS with varying inner pore diameter, shell thickness and validated the size-dependent thermal conduction in the nanometer range [56].

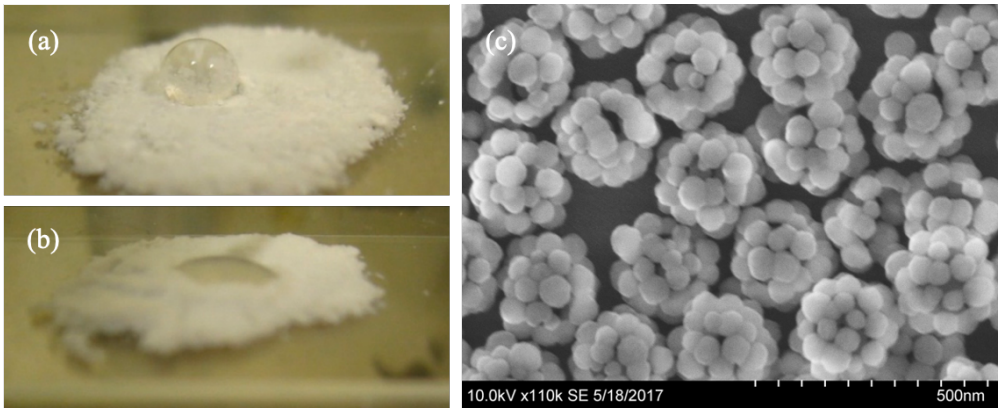

Figure 6. (a) Snapshot of hydrophobic HSNS powder , (b) Snapshot of hydrophilic HSNS powder, (c) SEM image of HSNS assemblies after 440 °C calcination [51].

The lowest thermal conductivity value, 14.3 mW/mK, was recorded for HSNS sample with density 0.1 g/cm^3, inner pore diameter, D ~ 85 nm and shell thickness, ST ~ 34 nm. The result indicates

that the gaseous thermal conductivity of the HSNS sample has been greatly suppressed due to a strong Knudsen effect inside the shell. In addition, given the same inner pore diameter, we found that decreasing the average nanoparticle size, constituting shell thickness, from ~ 104 nm to 34 nm, showed a reduced ~ 6 mW/(mK) difference in thermal conductivity suggesting that decreasing the spherical shell thickness or reducing the contact area can efficiently lower the contribution from the solid phase. Our study validated the size-dependent thermal conduction at the nanoscale and demonstrated that HSNS assemblies clearly yield thermal properties intermediate to those of gas and solid by tuning the structural parameters. In addition, essential issues concerning life cycle assessment [47], hydrophobic treatment [57] and environmental friendliness [46] have been incorporated to enable HSNS as the potential target for superinsulation materials used for thermal building insulation applications.

2.2.5 Thermal Transport through Window Panes

Due to high thermal conductivity ~1 W/mK and high infrared emissivity ~ 0.84 of the float the glass, windows remain the weakest thermal barrier between the indoor and outdoor environments, directly responsible for 40 ~ 60% of the total energy loss from buildings [58, 59]. According to the ASHRAE standard energy loss for single pane windows is in the range of 60 ~ 250 W/m^2 [60]. Based on a recent evaluation by the U.S. Department of Energy [61], energy-efficient window retrofits for the existing single-pane windows can potentially reduce 1.2 quads (1.266×10^{18}J) of domestic energy consumption in the United States. Figure 7(a) presents the thermal transport properties through the single pane windows, in which convection and radiation present the main components of the thermal transport between the glass pane and the indoor and outdoor environment while the heat transfer across the glass pane is through heat conduction. U-value

(W/(m^{2}K)) of the window, was calculated using Eq.(3), where $R_{conv,o} = 1/h_{conv,o}$ and $R_{rad,o} = 1/h_{rad,o}$ are the outdoor convective and radiative thermal resistances, respectively; $R_{conv,i} = 1/h_{conv,i}$ and $R_{rad,i} = 1/h_{rad,i}$ are the indoor convective and radiative thermal resistances, respectively; $R_{cond} = L_{gls}/k_{gls}$ is the effective thermal conductance of the glass pane, k_{gls} and L_{gls} are the thermal conductivity and thickness of the glass pane, respectively. Figure 7(c) compares the magnitudes of the heat transfer coefficients in the thermal resistance network shown in Figure 7(b), where the indoor and outdoor temperatures are 0 °C and 20 °C, respectively and the wind speed is 4 m/s [62]. The thermal conductivity, emissivity and thickness of the float glass is 0.96 W/mK, 0.84, and 3.0 mm [63].

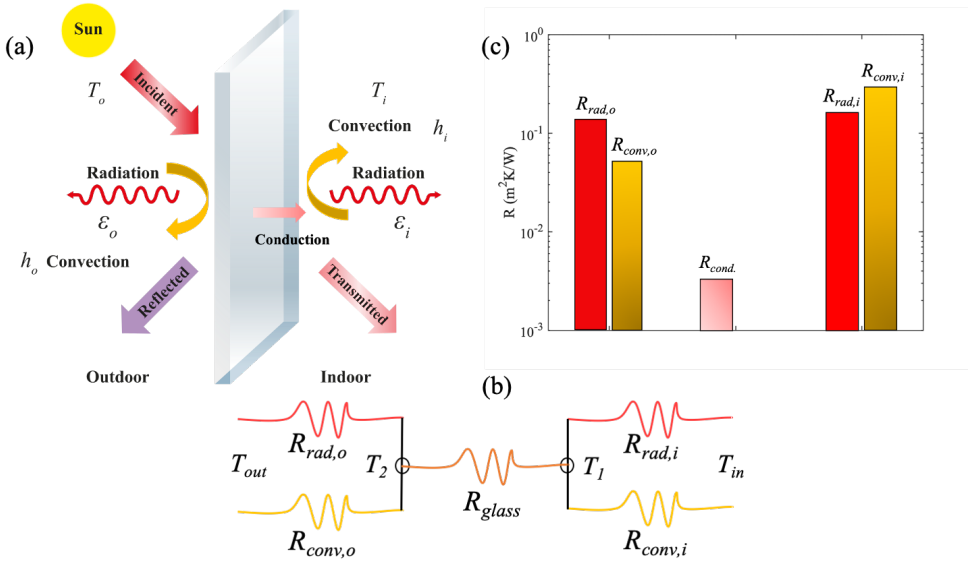

Figure 7. (a) Illustration of thermal transport properties, heat and solar radiation transfer across single pane window. (b) Thermal resistance network displaying heat transfer path across single pane windows. (c) Comparison of heat flow coefficients in thermal resistance network, where outdoor and indoor temperatures are 0 °C and 20 °C, and the wind speed is 4 m/s [62]; The thermal conductivity, emissivity and thickness of the glass are 0.96 W/mK, 0.84 and 3.0 mm, respectively [63].

Figure 7(c) clearly shows that thermal resistance of the float glass is much smaller than thermal resistances of radiation and convection. Furthermore, it is also seen that indoor radiative thermal resistance is smaller than the indoor convective thermal resistance, while the opposite case applies to the outdoor case. Normally, it is challenging to control convective heat transfer which is mainly determined by the ambient conditions such as temperature, pressure and wind speed. suggesting that increasing the indoor radiative thermal resistance is more efficient to help prevent the heat loss. Therefore, development of ideal retrofit candidates to reduce the energy loss through single pane windows should mainly focus on: (1) Enhancing the thermal resistance of the window panes to reduce the heat loss through conduction; (2) Decreasing the internal surface emissivity of window panes to reduce the heat loss due to infrared thermal radiation; (3) Utilizing the solar transmission adopting to ambient temperature to reduce heating demands in cold climates and cooling demands in hot climates. In addition to the energy performance, amongst others, adoptability, environmental sustainability, sound proof ability and most importantly visible transparency of may need to be utilized.

2.2.5.1 Thermochromic Solar Film

With a high solar transmittance > 90%, as much as ~ 800 W/m^2 solar irradiation reaches the indoor environment through windows during daytime [64, 65]. The transmitted solar energy significantly reduces the heating demands in cold climates. However, excessive solar irradiance also result in increased cooling demands in hot climates. Smart windows that could dynamically adjust the transmittance of solar irradiation have been subject of intense study of as one of the most promising strategy to reduce the energy consumption of buildings [66, 67]. In particular, Vanadium dioxide (VO_2) based thermochromic smart windows can regulate solar heat gain dynamically by adapting to the change of ambient temperature. This is due to the reversible metal-insulator transition (MIT)

of VO_2 at critical phase transition temperature T_c. When the temperature is lower than the critical phase transition temperature ($T < T_c$), VO_2 is in the semiconducting state and transparent to near-infrared (NIR) spectra of solar irradiation. When the temperature is higher than the critical phase transition temperature ($T > T_c$), VO_2 is in the metallic state and becomes translucent in NIR spectra [68, 69]. For pure crystalline VO_2, the critical phase transition temperature is ~ 68 °C but can be further modified to a lower temperature for a comfortable building environment using doping elements. i.e., tungsten and magnesium [70-74]. The performance of thermochromic smart windows is evaluated by two crucial optical performance parameters: 1) luminous (visible) transmittance (τ_{lum}, for wavelengths ranging between 380-780 nm), which represents the transmission of visible light useful for human vision under normal conditions, and 2) solar modulation ability ($\Delta\tau_{sol}$, the difference of solar radiation transmittance τ_{sol} before and after the phase transition for wavelengths ranging between 300-2500 nm), which represents the modulation of solar radiation energy passing through the window [75, 76]. Most of the currently available thermochromic films possess relatively low τ_{lum} and $\Delta\tau_{sol}$ [77-83]. In addition, the thermochromic performance of VO_2 decrease significantly when exposed to air for several months [84, 85], A humid environment would also greatly accelerate the oxidation process and turn thermodynamically unstable VO_2 into stable V_2O_5 with no solar modulation ability and thus deterring the practical deployment of VO_2 based smart windows. To improve the anti-oxidation ability and increase the lifetime of VO_2 nanoparticles, core-shell nanoparticles have been proposed, where environmentally stable oxides like SiO_2 [86], TiO_2 [87], and ZnO [88] have been used to increase the durability of VO_2 nanoparticles. However, in practical applications, when VO_2 nanoparticles transit periodically from monoclinic (M, $a_M = 5.75, b_M = 4.52$ Å, $c_M = 5.38$ Å, $\beta = 122.6°$) structure to tetragonal rutile (R, $a_R = b_R = 4.55$ Å, $c_R = 2.86$ Å) structure

[89], the interface stress between the VO_2 cores and oxide protection shells induced by the lattice structure transformation of VO_2 nanoparticles result in the formation of micro cracks at the interface. It is also important to note, although the introduction of a shell layer potentially enhances the durability of VO_2 nanoparticles and improves the solar luminous transmittance, it may lower the solar modulation ability of the film [87]. Here, simple method was proposed to enhance the life time of VO_2 nanoparticles, where the cross-linked and highly entangled poly (methyl methacrylate) (PMMA) chain with molecular weight (~ 950,000) was adopted to block gas diffusion and vapor penetration into the polymer matrix embedded with ~ 3% volume fraction of VO_2 nanoparticles (50 ~ 80 nm). The ~ 4 μm PMMA-VO_2 film was coated on ~ 50 μm thick transparent and chemically stable biaxially-oriented polyethylene terephthalate (BoPET) sheet using blade coating. The developed film shown in Figure 8(a) presents relative high luminous transmittance of ~ 50%, solar modulation ability of ~17.1%, and a low haze value of ~ 11% [90].

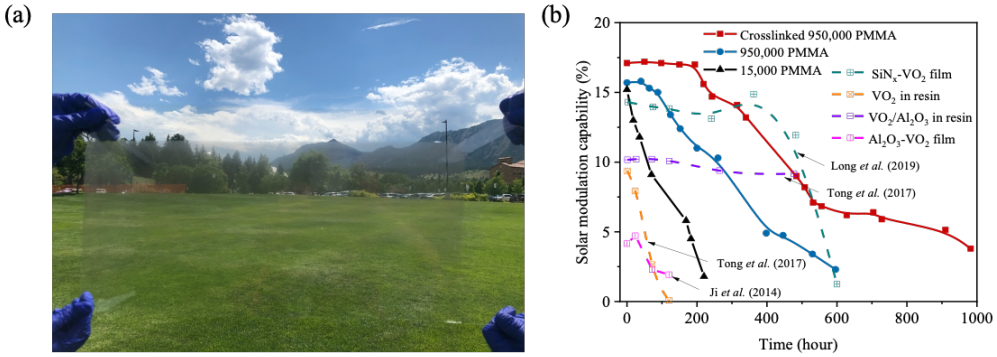

Figure 8. (a) Image of a PMMA-VO_2 film with a size of 600 mm × 300 mm (length × width), Spectral transmittance of the PMMA-VO_2 thin film in the solar spectrum, where the luminous transmittance is ~ 50% and the solar modulation ability is ~ 17.1% [90]. (b) Comparison of the solar modulation ability of the VO_2 nanoparticles embedded in non-cross-linked 150,000 PMMA, non-cross-linked 950K PMMA, cross-linked 950,000 PMMA matrixes and together with previous studies [91-93]. The aging tests are performed in the accelerated environmental chamber with 60 ºC temperature and ~ 95% relative humidity.

Accelerated environmental tests were performed to evaluate the durability of VO_2 nanoparticles [94, 95]. The tests were conducted at 60 ºC temperature , and the relative humidity > 95%, similar to the testing conditions reported in the literature [88, 93]. We have found out the lifetime of the VO_2 nanoparticles embedded in the cross-linked PMMA matrix with molecular weight ~ 950,000 developed in our work is ~ 900 hours, which is particularly better than the previously reported values for VO_2 nanoparticles coated by SiO_2 (~ 72 hours) [88], $Al(OH)_3$ (~ 120 hours) [88], and VO_2 thin film protected by Al_2O_3 (~ 100 hours) [92], and is comparable to the performances of VO_2 nanoparticles coated by Al_2O_3 (> 480 hours) [91] and VO_2 thin film protected by SiN_x (~ 600 hours) [93] shown in Figure 8(b). Our method provides an easy and yet effective strategy to improve the lifetime of VO_2 nanoparticles, suggesting a promising pathway toward environmentally stable and large-scale deployment of thermochromic films for energy-efficient smart windows. The detailed energy performance analysis in Article XI show that the developed PMMA-VO_2 film could greatly reduce the cooling demands in hot climates and improve the thermal comfort in cold climates.

2.2.5.2 Thermochromic Solar Film with Flexible Aerogel Insulation Layer

Naturally, although a thin film may substantially influence the radiative properties in the solar and infrared range (e.g. solar transmittance and emissivity), few of the existing VO_2 films can block heat loss caused by temperature difference due to low thermal resistance of the float glass. Besides heat loss, the temperature difference between the occupants and the innermost surface of windows also leads to “radiant temperature asymmetry” [96], causing human body lose thermal energy through infrared thermal radiation, which in turn affects the thermal comfort in buildings. Furthermore, moisture condensation occurs when the surface temperature of the window panes reach the dew point of the interior environment. Therefore, to prevent the energy loss and improve

thermal comfort and condensation resistance especially, in cold climates, thermal resistance of the single-pane windows must considerably improve. Currently, several kinds of transparent insulation materials have been explored to provide a high thermal resistance while retaining solar transmission. For example, silica aerogels with low thermal conductivity (~ 0.02 W/(mK)) and high optical transmittance (~ 0.9) [97, 98] have been widely presented as the potential candidate material for window insulation [35, 59, 99, 100], except silica aerogels usually possess poor mechanical flexibility and are very brittle. Recent studies by Shimizu *et al.* [101, 102] and Liu *et al.* [103] have reported significant enhancement in the mechanical performance of flexible and transparent aerogels using organic-inorganic cross-linked structures, showing great potential for window insulation applications. In addition, some other visibly-transparent thermally insulating materials, including cellulose nanofibers [104], polymer nanofoams [105] and hollow microcapsule embedded polymers [106, 107] have also been explored. However, most of the existing transparent insulation materials cannot dynamically respond to solar irradiation when the temperature changes. Hence, it remains difficult to achieve window retrofits that are simultaneously thermally insulating, visible-light transparent, and dynamically switchable in solar transmission. To address this issue, based on the recent progress of recently synthesized flexible and transparent aerogels [102] and promising solar transmission regulation ability of the enhanced durability VO_2-PMMA thermochromic film [108], an optically-switchable and thermally-insulating film as energy-efficient windows retrofit materials was proposed. The developed model consist of 3.0 mm aerogel insulation layer and 4μm VO_2-PMMA film coated on 50 μm biaxially-oriented polyethylene terephthalate (BoPET) sheet depicted in Figure 9(b). As shown in Figure 9(a), the temperature distribution across the window (AVP film and glass pane) is affected by

many factors such as room/ambient temperature, external wind speed, internal natural convection, surface emissivity and absorption of solar radiation by the window materials.

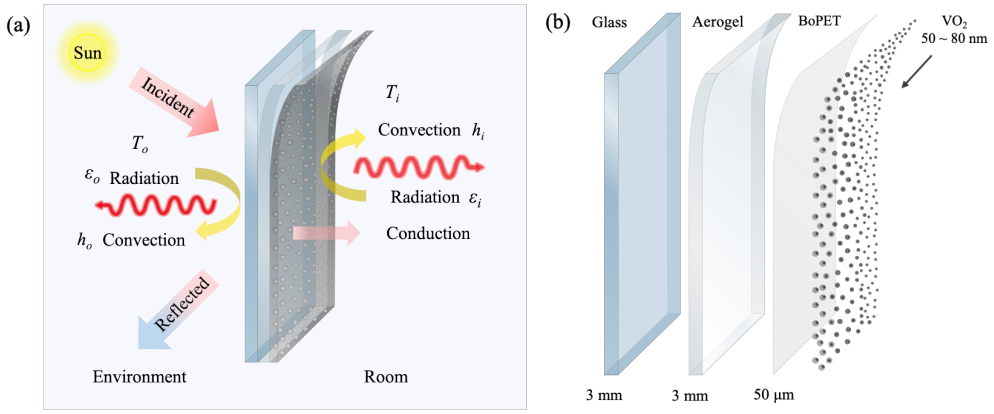

Figure 9. (a) Schematic illustration of heat transfer and solar radiation transfer across a south-facing single-pane window covered by an aerogel and VO_2 based thermochromic film. (b) illustration of float glass, the thermal conductivity, emissivity and thickness of the glass are 0.96 W/mK, 0.84 and 3.0 mm, respectively [63], aerogel layer, the thermal conductivity and thickness of the aerogel are 0.018 W/mK, 3.0 mm, respectively [102], 4 μm thick VO_2-PMMA film coated on 50 μm biaxially-oriented polyethylene terephthalate (BoPET) sheet. The size of the VO_2 nanoparticles are 50 ~ 80nm, the emissivity of VO_2-PMMA film is 0.9 [108].

The thickness of the aerogel film and the VO_2-PMMA thermochromic film influence the thermal performance of window. The thermal performance of the window is approximately evaluated by the overall heat transfer coefficient, U-value (W/(m^{2}K)) , which is defined as [63]:

$$\frac{1}{U} = \frac{1}{h_{o,all}} + \frac{1}{k_{gl}/L_{gl} + k_{argl}/L_{argl} + k_{vp}/L_{vp}} + \frac{1}{h_{i,all}} \tag{9}$$

where k_{argl} and L_{argl} are the thermal conductivity and thickness of aerogel, k_{gl} and L_{gl} are the thermal conductivity and thickness of glass, and k_{vp} and L_{vp} are the thermal conductivity and thickness of the VO_2-PMMA film, respectively. The $h_{o,all}$ and $h_{i,all}$ are the internal and external

overall heat transfer coefficients in which both the convective and radiative heat transfer are included. From Eq. (9), it is clear that increasing the thickness of the aerogel matrix (L_{argl}) can improve the thermal insulation performance of the AVP film. Figure 10(a) compares the U-values of a single-pane window (3.0 mm) covered by the AVP film, a single-pane window and an air-filled double-pane window [109] exposed to winter climates as a function of thickness, where the outdoor temperature is $T_o = -18$ ℃, the indoor temperature is $T_i = 21$ ℃, and the wind speed is 5.5 m/s (ASHRAE standard) [62], It clearly seen that an optimal 3.0 AVP reduced the thermal transmittance (U-value) of a single-pane window from 5.93 W/m^{2}K to 3.04 W/m^{2}K, which is close to the insulation performance of an air-filled double-pane window.

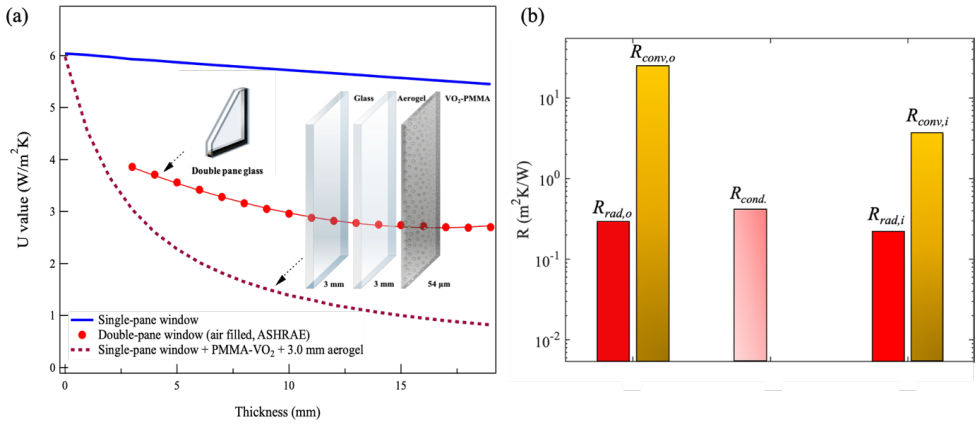

Figure 10. Influence of film thickness on the thermal of AVP film. (a) U-values of a AVP film as a function of the thickness of aerogel film. The corresponding heat transfer coefficients are evaluated according to Ref. [63]. (b) comparison of heat flow coefficients in thermal resistance network, where outdoor and indoor temperatures are -18 °C and 20 °C, and the wind speed is 5.5 m/s [62]; The thermal conductivity, emissivity and thickness of the glass are 0.96 W/mK, 0.84 and 3.0 mm, respectively [63], The thermal conductivity of the aerogel is 0.018 W/mK and the surface emissivity of the VO_2-PMMA is 0.9, respectively [102, 108].

However, as shown in Figure 10(b) it is also noted that the decline of U-value is nonlinear, and the decreasing rate becomes slower as the thickness of the aerogel matrix increases. This is because the U-values are dominated by the convective heat transfer along the window surface when the conductive thermal resistance of the window pane increases. This way, the proposed AVP film with a relatively low U-value, a relatively high luminous transmission, can both dynamically manipulate the solar transmission according to ambient temperature and minimize energy loss due to high thermal resistance of the aerogel without blocking out the useful energy and daylight from the sun. The energy analysis result in section 2.4 clearly showed that employing the aerogel-thermochromic film could not only reduce the heat loss but also greatly improve the performance of single-pane windows by improving thermal comfort and avoiding moisture condensation in cold climates and overheating and sun glare in hot climates.

2.3 Thermal Modelling

VO_2- PMMA Film

To evaluate the energy saving performance of a PMMA-VO_2 film in different climates and regions, a theoretical model considering both heat and solar radiation transfer was developed in this work. Figure 11(a) illustrates the heat and solar radiation transfer across a window pane, where the PMMA-VO_2 film with a thickness of ~ 4 μm is employed. Since the thickness of the window is much smaller than its width and length, the heat transfer in the *z*-direction can be treated as one-dimensional. Thus, the heat transfer in the z-direction can be described as follows:

$$k_{gla}\frac{d^2T(z)}{dz^2}-\frac{dI(z)}{dz}=0 \tag{10}$$

where k_{gla} is the thermal conductivity of the float glass, $T(z)$ is the temperature at position z, $dI(z)/dz$ is the solar radiation absorbed by glass per unit volume (W/m^3). $I(z)$ can be written as follows:

$$I(z) = \tau_{sol} I_o e^{-\beta_{gla} z} \tag{11}$$

where I_o is the incident solar energy, τ_{sol} is the solar transmittance of the PMMA-VO_2 film, and β_{gla} is the extinction coefficient of the float glass. Compared with the thickness of float glass (3 mm), the thickness of the PMMA-VO_2 (~ 4 μm) film can be ignored. Thus, the boundary conditions at $z = 0$ and $z = L_{gla}$ are as follows:

$$q_{z=0} = h_o(T_a - T_{z=0}) + \sigma\varepsilon_o(T_a^4 - T_{z=0}^4) + Q_{abs} \tag{12}$$

$$q_{z=L_{glass}} = h_i\left(T_{z=L_{gla}} - T_r\right) + \sigma\varepsilon_i\left(T_{z=L_{gla}}^4 - T_r^4\right) \tag{13}$$

where T_a and T_r are the external ambient temperature and the internal room temperature, respectively, h_e, h_i and $\varepsilon_e, \varepsilon_i$ are the external and internal convective heat transfer coefficients and average external and internal surface emissivities, $\sigma = 5.67 \times 10^{-8}\,\mathrm{Wm/K^4}$ is the Stefan-Boltzmann's constant, $Q_{abs} = \alpha_{sol} I_o$, is the absorbed solar irradiation by the PMMA-VO_2 film, and α_{sol} is the absorbance of the PMMA-VO_2 film, Eq. (10) was solved by the finite volume method [110]. The thermal conductivity and average surface emissivity of the float glass are assumed to be $k_{gla} = 0.96\,\mathrm{W/(mK)}$ and $\varepsilon_o \approx 0.84$ according to reference [63]. The surface emissivity of the PMMA-VO_2 film is $\varepsilon_o \approx 0.9$ From Figure 13(b), the solar transmittances (τ_{sol}) of the PMMA-VO_2 film in the insulating phase and metallic phase are 0.57 are 0.40, respectively. The reflectances (r_{sol}) of the PMMA-VO_2 in both the insulating and metallic phases were measured as 0.05. Thus, the absorbance can be calculated by $\alpha_{sol} = 1 - \tau_{sol} - r_{sol}$. The inside and external convective heat transfer coefficients can be evaluated by $h_i = 3.6\,\mathrm{W/(m^2K)}$

and $h_o = (10 + 4.1v)\ \mathrm{W/(m^2K)}$, where v (m/s) is the wind speed [63]. The weather conditions including ambient temperature (T_o), window speed (v) and solar irradiation density (I_o) are acquired from the NSRDB Data Viewer [111].

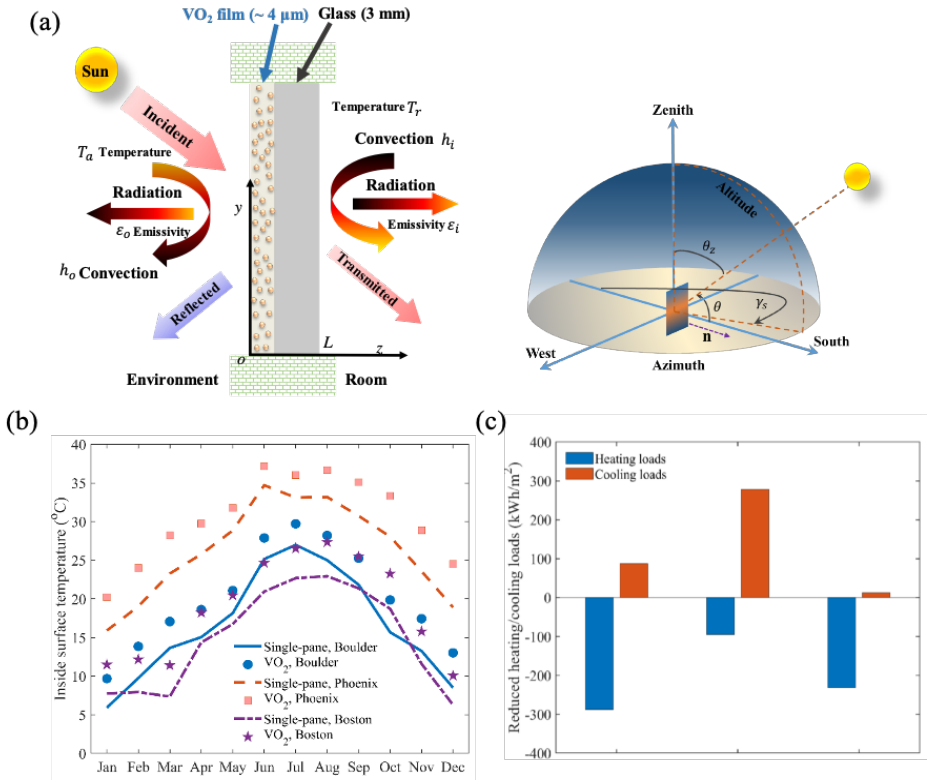

Figure 11. Thermal comfort and energy saving of the PMMA-VO_2 film in selected cities: Boulder (CO), Phoenix (AZ), and Boston (MA) [90]. (a) Schematic of heat and radiation energy transfer across a south-facing single-pane window covered by the PMAA-VO_2 film. (b) Influence of PMMA-VO_2 film on the inside surface temperature of a glass window. (b) Comparison of reduced annual heating/cooling loads of a south-facing window .

The inside surface temperatures of the single-pane window with and without VO_2 film are compared in Figure 11(b). After employing the PMMA-VO_2 film, the inside surface temperature of the single-pane window is ~ 5 °C higher than that of the single-pane window without a film,

indicating that the PMMA-VO_2 film can reduce the temperature difference between the occupants and the innermost surface of windows, which indeed improves the thermal comfort and condensation resistance of the single-pane window in cold climates significantly [96]. Since the solar transmittance of the PMMA-VO_2 film (0.57~0.4, Figure 13(b)) is smaller than the single-pane window (~ 90%), applying the PMMA-VO_2 film increase the heating loads in cold climates and reduce the cooling loads in hot climates. Figure 9(c) compares the reduced annual heating/cooling loads of a south-facing window in different regions. In this Figure, the positive/negative sign represents the reduced/increased energy. For simplicity, we have assumed that the transmitted solar energy decreases (increases) the heating (cooling) loads when the external ambient temperature is higher (lower) than the internal room temperature (21 ºC). Note that the transmitted solar energy includes both the directly transmitted solar irradiation and the absorbed solar energy by window pane and subsequently transferred towards the indoor room environment through heat conduction. Clearly, the cooling demands in the hot areas (e.g., Phoenix) are significantly reduced. However, in the cold areas (e.g., Boston), the increased heating loads in winter are much higher than the reduced cooling loads in summer, indicating that the PMMA-VO_2 film could increase the annual energy cost.

VO_2- PMMA with Aerogel

To evaluate the thermal comfort, condensation resistance and energy loss of single-pane windows employing 3.0 mm transparent flexible aerogel insulation layer with of ~ 4 μm thick VO_2-PMMA (AVP) film coated on ~50 μm chemically stable biaxially-oriented polyethylene terephthalate (BoPET) sheet, similar model (Eq.10 an Eq.11) considering both heat transfer and solar radiation transfer across the AVP film and glass pane was developed. Assuming the length and width of a window pane are much larger than its thickness and that the contact resistance between AVP film

and glass can be ignored, one-dimensional (1D) heat transfer equations across the AVP film and the glass pane is written as follows,

$$k_{arg}\frac{\partial^2 T(z)}{\partial z^2}-\frac{dI(z)}{dz}=0, \qquad z \le L_{arg} \tag{10b}$$

$$k_{gla}\frac{\partial^2 T(z)}{\partial z^2}-\frac{dI(z)}{dz}=0, \qquad L_{arg} < z \le L_{arg}+L_{gla} \tag{10c}$$

Where, k_{arg} and k_{gla} are the thermal conductivities of aerogel and glass, respectively, L_{aer} and L_{gla} are the thicknesses of aerogel and glass, respectively, $dI(z)/dz$ is the solar radiation absorbed in the aerogel and glass per unit volume, which can be roughly estimated by Eq. (11) and the boundary conditions are similar as Eq.(12) and Eq.(13). Because the boundary conditions shown in Eqs. (11-13) are determined by the temperature distribution in the window pane, an initial temperature distribution is given first. For clear and uncoated float glass, the thermal conductivity and average surface emissivity are assumed to be $k_g = 0.96\ \mathrm{W/(mK)}$ and $\varepsilon_i \approx 0.84$, respectively [63, 112]. According to the effective medium theory [113], the influence of VO_2 nanoparticles on the thermal resistance of the VO_2-PMMA film is negligible when their concentrations are very low. The thermal conductivity and average surface emissivity of the transparent aerogel film are assumed to be $k_{arg} = 0.018\ \mathrm{W/(mK)}$ and $\varepsilon_{arg} \approx 0.90$, respectively [103]. The internal heat transfer coefficient is assumed to be $h_i = 3.6\ \mathrm{W/(m^2K)}$ and external convective heat transfer coefficient can be evaluated by and $h_o = (10 + 4.1v)\ \mathrm{W/(m^2K)}$, where v (m/s) is the wind speed [63]. The spectral transmittances of aerogel and glass are taken from Ref.[35] and Ref. [63], respectively. Figure 10(a) shows the average heat/gain loss of a south-facing window with and without applied retrofit films on a winter day and a summer day, in which the positive/negative sign represents the conduction heat gain/loss. The selected dates are in particular the coldest (6th of January,2017)

and the hottest (24th of July, 2017) days in Boulder, CO, USA (40.0150° N, 105.2705° W, 1655 m altitude), respectively. The weather conditions are acquired from the NSRDB Data Viewer [111]. As seen in Figure 12(a) and earlier discussion, heat loss through single pane windows adopting VO_2-PMMA remains higher than single pane windows without the retrofit. This is because the solar transmittance of the PMMA-VO_2 film, in insulating phase (~0.57%), is smaller than single-pane window (~ 0.90%), which increases the heating loads in cold climates. Therefore, the adoption of the aerogel insulation layer proves necessary to reduce the heating demand during the winter. Figure 12(b) presents the combination of conduction and solar radiation heat transfer of a single pane window compared to window pane applying AVP, showing that employing AVP film can reduce ~ 50% heat loss caused by the temperature difference between external and internal environments at nighttime during winter. Figure 12(c) compares the internal surface temperature of single pane window in ambient when both VO_2-PMMA thermochromic film and AVP film are applied during winter. It is seen that during the daytime, at 12:00 am, single-pane window employing both VO_2-PMMA and AVP film almost present the same temperature (16 ~18 °C), however, due to the low surface temperature of both single pane windows and single pane applying VO_2-PMMA film, thermal discomfort and moisture condensation remain issues during nighttime. Figure 12(b) shows that compared to VO_2-PMMA film when the AVP film is applied, internal surface temperature of the window at 0:00 a.m. rises from ~ -3 °C to 10 °C. The rise in the internal surface temperature provides a greater thermal comfort for occupants and prevents moisture condensation, which not only prevents the clear view of windows, but also limit the humidity level inside the building critical for indoor air quality. Furthermore, Figure 12(b) compares the internal surface temperature of single pane window in ambient when both VO_2-PMMA thermochromic film and AVP film are applied during summer. It is seen that single pane

window employing VO_2-PMMA film possess the highest surface temperature (~ 40 °C) during daytime. This is because VO_2 nanoparticles reach their phase transition temperature due to high external ambient temperatures and absorbed solar irradiance.

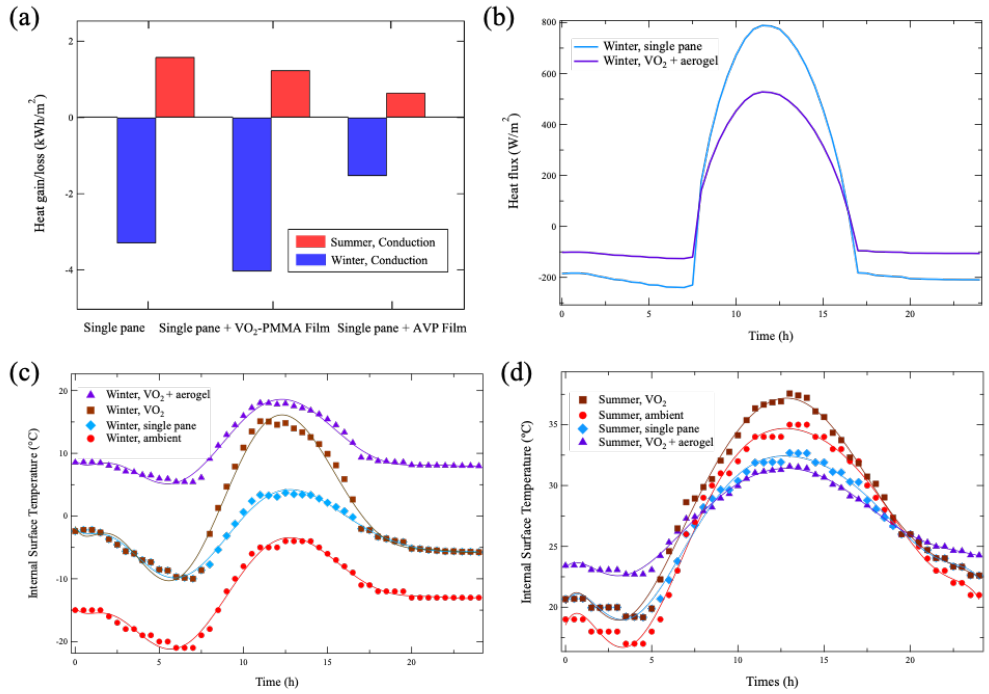

Figure 12. Thermal insulation performance of a south-facing window under practical weather conditions. (a) Average conduction heat loss/gain of a single-pane window employing both VO_2-PMMA and aeorogel+VO_2-PMMA film, respectively. Here the positive/negative value represents the heat gain/loss. (b) Combined conduction and solar radiation heat transfer of single-pane windows with/without aerogel+VO_2-PMMA film on a winter day. In winter days, the heat loss through window increases the heating demands, while the solar heating reduces the heating demands. In summer day, both the heat gain through heat conduction and solar irradiation increase cooling demands. (c) Internal surface temperature of single-pane windows in ambient compared to single pane window adopting VO_2-PMMA film and VO_2-PMMA film with aerogel insulation layer on a winter day. (d) Internal surface temperature of single-pane windows in ambient compared to single pane window adopting VO_2-PMMA film and VO_2-PMMA film with aerogel insulation layer on a summer day.

This way the solar irradiance transmitting through the window pane drops, which reduces the sun's glare and cooling demands caused by the extra solar heating. As the direct solar irradiance decreases and the solar incidence angle increases, the VO_2 changes from the metallic phase to the insulating phase at ~ 15:00 p.m.. In addition, because of the high thermal resistance of the aerogel, the conduction heat gain from the outdoor environment to the room decreases from ~ 1.2 kWh/m^2 to 0.6 kWh/m^2. The obtained results shows the employing the AVP film not only significantly reduce the heating and cooling loads of single-pane windows but also improve the thermal comfort and indoor humidity level.

2.4 Optical Modeling

The optical performance of the VO_2-PMMA thermochromic film is characterized by the luminous transmittance and solar modulation ability. The mean luminous (380-780 nm) transmittance τ_{lum} is defined as [89, 114]

$$\tau_{lum} = \frac{\int_{380\ nm}^{780\ nm} I_{lum,\lambda}\tau_\lambda d\lambda}{\int_{380\ nm}^{780\ nm} I_{lum,\lambda} d\lambda} \tag{11a}$$

where I_λ is the solar radiation intensity, and τ_λ is the transmittance of radiation at wavelength λ. The solar modulation ability $\Delta\tau_{sol}$ is defined by the difference of solar transmittance (280-2500 nm) before and after the phase transition,

$$\Delta\tau_{sol} = \tau_{sol}(T < T_c) - \tau_{sol}(T > T_c) \tag{11b}$$

where τ_{sol} is the mean solar (280-2500 nm) transmittance, which is defined by,

$$\tau_{sol} = \frac{\int_{280\ nm}^{2500\ nm} I_{sol,\lambda}\tau_\lambda d\lambda}{\int_{280\ nm}^{2500\ nm} I_{sol,\lambda} d\lambda} \tag{11c}$$

where $I_{sol,\lambda}$ is the solar spectrum of air mass 1.5 (AM1.5), which corresponds to the sun standing 37º above the horizon [115], In Eqs.1(a-c), the luminous transmittance τ_{lum} and solar modulation ability $\Delta\tau_{sol}$ of the VO_2-PMMA thermochromic film are determined by the size and volume fraction of the VO_2 nanoparticles. According to Li *et al.* [116], a 5.0 μm thick film with ~ 1% volume fraction of VO_2 nanoparticles has luminous transmission τ_{lum} of ~ 0.7. In order to achieve similar optical performances ($\tau_{lum} = 0.6 \sim 0.7$), the volume fraction of the VO_2 nanoparticles needs to remain very low ($\ll 1\%$). The low volumetric fraction guarantees that each VO_2 nanoparticle inside the VO_2-PMMA film can be considered as an individual scattering center. According to the Lorenz-Mie theory [117], the extinction coefficients can be evaluated as follows [88],

$$Q_{ext,\lambda} = \frac{2}{x^2}\sum_{n=1}^{\infty}(2n+1)\,\mathrm{Re}(a_n + b_n) \tag{12}$$

where a_n and b_n are the Mie scattering coefficients and functions of x and m_1, and Re (·) denotes the real part of a complex number, m_1 is the complex refractive index of VO_2 nanoparticle, and the size parameters $x = \pi a/\lambda$, a is the diameter, and λ is the wavelength of the incident wavelength. Since the VO_2 nanoparticles are randomly dispersed inside the PMMA matrix, assuming the total number of nanoparticles per volume is N, then the spectrum extinction coefficient $\beta_{V,\lambda}$(m^{-1}) can be expressed as the summation of the scattering cross-section of all the particles as follows [118],

$$\beta_{V,\lambda} = N\frac{1}{4}\pi b^2 Q_{ext} = \frac{3}{2}\frac{V_f Q_{ext}}{b} \tag{13}$$

where V_f is the volume fraction of the VO_2 nanoparticles. Because the volume fraction of the nanoparticles is very low, and the PMMA matrix is dielectric, the interaction between the

embedded nanoparticles and the PMMA matrix is ignored. Thus, the spectral extinction coefficient β_λ of the PMMA-VO_2 film is evaluated by [119],

$$\beta_\lambda \approx \beta_{V,\lambda} + \beta_{P,\lambda} \tag{14}$$

where $\beta_{P,\lambda}$ is the spectrum extinction coefficient of the PMMA matrix. The spectral transmittance τ_λ of the PMMA-VO_2 film with a thickness L is given by the Beer-Lambert law [117]

$$\tau_\lambda = e^{-\beta_\lambda L} \tag{15}$$

In our calculation, we select the volume fraction of VO_2 nanoparticles, according to Eqs. (10-15). When the size and volume fraction of the VO_2 nanoparticles are 80 nm and 0.4%, respectively, and the thickness of the matrix is 4 μm, the calculated solar transmittance is ~ τ_{sol} = 59% and solar modulation ability is $\Delta\tau_{sol}$ =19.2%. The solar transmittance and solar modulation ability of the fabricated PMMA-VO_2 film are 57% and 17.1%, respectively. Figure 13 compares the calculated and measured spectral transmittance of the PMMA-VO_2 film, confirming that theoretical model and the experimental result obtained from measuring the developed VO_2-PMMA film are in good agreement.

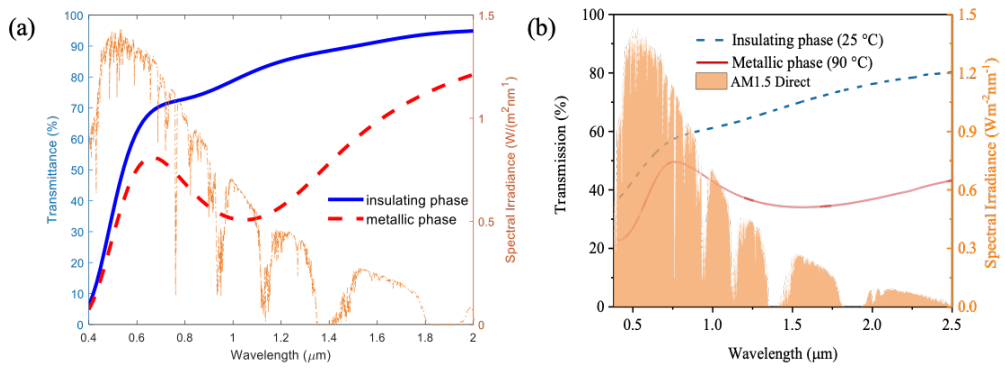

Figure 13. (a) Calculated spectral transmittance of the PMMA-VO_2 thin film according to Eqs. (10-15). (b) Measured spectral transmittance of the fabricated PMMA-VO_2 thin film [90].

To achieve higher solar transmittance and solar modulation ability performance, the volume fraction of the VO_2 nanoparticles should change according to the thickness of the film. The thin film with an area of 600 mm × 300 mm (length × width) and a thickness of ~ 4 μm is obtained as shown in Fig. 8(a), in which the PMMA-VO_2 film is coated on a 50 μm thick BoPET film. The uniformity of the coating is controlled by measuring the transmittance of the film at several different locations. The difference of the solar transmittances among different points was found to be smaller than 1%.

2.5 Thermal Characterization

Accurate characterization of thermal properties including thermal transmittance (U-value) and thermal conductivity (*k*-value*)* is key for design, evaluation, and adoption of new generation of materials, e.g, nano insulation materials, transparent porous insulation materials, used for energy efficiency applications in buildings. The U-value and the *k*-value are the two parameters used to select the type and thickness of insulation materials and evaluate economic performance in the building construction/renovation industry [120-122]. Therefore, developing a convenient tool that can be used to characterize the thermal transmittance and thermal conductivity of desired nanostructured materials with much smaller sizes (*e.g.* 0.2 m × 0.2 m) in real environment, especially during early stages of material development when large size samples are not yet available is highly required and desired. To achieve that objective, reduced-scale hot box system (RHS) that can accurately measure the U-value and the *k*-value of nanostructured materials, e.g., sizes ranging from 0.06 to 0.2 m (diameter or length) for both circular and square shapes under varying circumstances, considering humidity, wind was designed and developed [112]. Figure 14 displays the layout of the designed hotbox. The overall dimensions of the hot box are 0.5 m × 0.5 m × 0.6 m (*x*-*y*-*z* directions). The insulating walls are built using commercially

available extruded polystyrene foam (XPS, ~ 0.035 W/(mK)) with a wall thickness of 0.15 m. The inner chamber dimensions are 0.2 m × 0.2 m × 0.35 m (*x*-*y*-*z* directions) to provide easy access to the inner components such as sensors and the heating coils. The specimen is placed in the opening of the chamber, which separates the hot chamber from the cold room environment. Fourteen (14) T-type thermocouples (Omega, accuracy ± 0.5 °C or 0.4%) are used to monitor the surface temperatures of the specimen, insulating walls, air temperatures inside the hot chamber and the room environment. A heat flux meter (HFM) with dimensions 3.0 cm × 3.0 cm × 3.0 cm (greenTEG gSKIN®-XO, ± 3%) is used to measure the heat flow through the specimen,

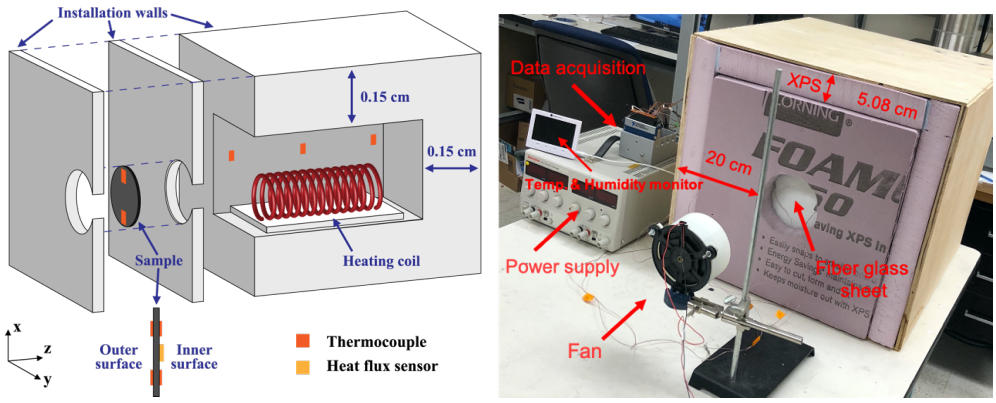

Figure 14. (left) Schematic illustration of the reduced-scale hot box system. The heating coil is used to control the temperature inside the chamber. (Right) snapshot of the assembled experimental setup [112].

The thermocouples and HFM are connected to a multiple channel data acquisition system (National Instruments, NI-9213). The measured temperatures and heat flux are recorded by LabVIEW software. The temperature inside the chamber can vary from room temperature to ~ 80.0 °C. The room temperature is set to be the cold chamber temperature. The humidity level inside the hot chamber can be controlled using a simple humidifier. Three sensors each placed within the chamber, outside the chamber and in the room environment, are used to monitor the temperature

and humidity. The wind speed is set using a fan perpendicular to the outer surface of the specimen shown in Figure 8. The specimen's surface emissivity is measured using infrared (IR) camera (T630sc from FLIR). The specimen is placed between the chamber and room environment and the air inside the chamber is heated using the heating coil. Then the U-value (W/(m^{2}K)) of the specimen is determined by the ratio between the heat flux Q (W/m^2) through the sample versus the temperature difference between the hot chamber and the cold room environment, i.e. shown in the following:

$$U = \frac{Q}{T_c - T_r} \tag{16}$$

where T_c is the chamber temperature and T_r is the room temperature. The RHS can also be used to measure the thermal conductivity of the specimen. If the inner surface temperature T_{sc} and the outer surface temperature T_{sr} of the specimen with a thickness of d are monitored, the thermal conductivity k (W/(mK)) of the material can be calculated according to Fourier's law of heat conduction as follows:

$$k = \frac{Qd}{T_{sc} - T_{sr}} \tag{17}$$

The measurement accuracy of heat flux plays an important role in determining both the thermal conductivity and the U-value of a material. Therefore, the specimens with known thermal properties are used to calibrate the accuracy of the heat flux measured by the heat flux transducer. The uncertainties of the measured U-value and $\boldsymbol{k}$-value depend on many factors, such as the accuracies of thermocouples and heat flux sensors, edge heat loss, geometry (e.g. shape, thickness) and thermal properties of specimens. According to the uncertainty propagation formula and Eq. (1), the uncertainty of the U-value can be determined by [123, 124]

$$\frac{\Delta U}{U} = \sqrt{\left(\frac{\Delta Q}{Q}\right)^2 + \left(\frac{\Delta T_c}{T_c - T_r}\right)^2 + \left(\frac{\Delta T_r}{T_c - T_r}\right)^2} \tag{18}$$

where ΔQ is the uncertainty of the heat flux going across the measured samples, and ΔT_h and ΔT_r are the uncertainties associated with the air temperature in the chamber and the room environment. For ΔQ, it consists of both the intrinsic uncertainty of the HFM and the edge heat loss which is closely related to the insulation conditions, geometry and thermal conductivities of the specimen. Here, the up limit (~ 0.75% of Q) is used to evaluate the uncertainty induced by the edge heat loss. For ΔT_h and ΔT_r, the thermal contact resistance between the thermocouple and sample surface and the heat loss through thermocouple leads are neglected. Thus, only the uncertainty measurement of the thermocouples are considered. In Eq. (3), it is shown that the uncertainty of the U-value decreases as the temperature difference increases. Therefore, to reduce the uncertainty, it is best to carry out the measurements under large temperature differences. Commercially available insulation materials with known thermal properties such as (fiberglass sheet (0.029 W/(mK) at 24℃) and black aerogel sheet (0.014W/(mK) at 24℃)) from McMaster-Carr, were used to calibrate the RHS. In addition, laser flash apparatus was also used to measure and validate the thermal properties of samples compared to the RHS. The measured thermal conductivities of both the fiberglass sheet and the black aerogel sheet were consistent with the results provided by the supplier and obtained from LFA, demonstrating that the measured heat fluxes by the RHS are accurate. Furthermore, measurement under varying conditions, humidity level (25%, 50%, 70% and 90%) and different wind speeds are made possible to determine their impact on the thermal transmittance and thermal conductivity of designed insulation materials, suggesting the developed RHS is a simple yet very effective technique to accurately measure thermal properties of nanostructured materials with small sample sizes. The established measurement method can

facilitate the development of next generation of insulation materials for energy-efficiency application. An example of such work can be seen from Article IX where hydrophobic nanostructured wood membrane for thermally efficient distillation application was designed and characterized using the developed RHS system.

3. Research Methodology

This chapter presents the methodology and the characterization techniques implemented to achieve the objectives of this research based on sustainable building principles while more detailed description of the experimental work including synthesis approach and procedures are given in each of the enclosed articles.

3.1 Materials

3.1.1 Hollow Silica nanospheres

Hollow Silica nanospheres were fabricated using sacrificial template method [125], where Polystyrene (PS) was used as template for providing the nucleation site for the growth of silica shell. PS was synthesized following a emulsion polymerization process [126], where polyvinylpyrrolidone/styrene ratio and potassium persulfate amount were varied to adjust the size of the obtained PS spheres [127, 128]. Thereafter Tetraethyl orthosilicate (TEOS) was used as the silica precursor to form the shell structure. In general, given the widespread knowledge that exists within silica-based materials, as well as possessing certain characteristics, e.g. abundance, low-cost, low thermal conductivity, non-flammable and environmentally friendliness, it is considered as one of the best possible candidate materials for achieving the hollow nanospheres for thermal insulation purposes. TEOS was then hydrolyzed and condensed on the PS sphere surface through

a modified Stöber approach under alkaline condition [129]. Besides TEOS other silica source materials such as water glass (Na_2SiO_3) may also be used for successful synthesis of HSNS [46]. To achieve complete coverage of the silica shell, TEOS concentration has to be higher than 0.2 M. This signified that a mono- to bilayer of nanosilica was formed around the PS template during the coating process. The coated PS-Silica sample was then subjected to 440 °C calcination remove the PS template. The hollow nansospheres were then formed demonstrating a raspberry-like morphology exhibiting highly porous structure. Detailed synthetic approach to gain insight into the mechanism and formations of HSNS, i.e, the influence of reaction parameters on the structural characteristics of HSNS, have been fully discussed in Article IV,VI,VII, respectively.

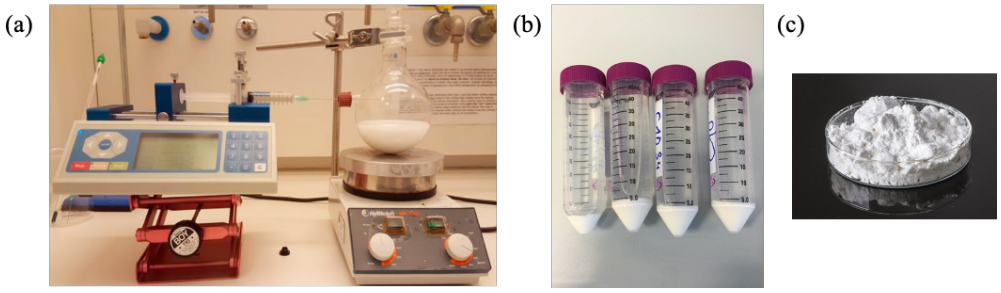

Figure 15. (a) TEOS solution added dropwise to Erlenmeyer round flask using a Nexus 3000 syringe pump with the precision rate 450 µl/min and a horizontal opening in the flask [130] (b) Coated PS@SiO2 spheres after centrifugation at 5000 rpm for 15 min. (c) Air dried silica powder after PS template removal at 440 °C calcination for 8 h (heating rate = 5°C/min).

3.1.2 PMMA-VO_2 Thermochromic Film

The PMMA-VO_2 thermochromic film was fabricated using blade coating method, where initially 50-80 nm VO_2 nanoparticles were ultrasonically dispersed into desired amount of PMMA 950K A4 shown in Figure 16(a). The monoclinic VO_2 (M) were synthesized using the hydrothermal method [88]. The VO_2@PMMA solution was then irradiated by the UV radiation (220 ~380 nm,

ADJ Products) for 10 hours in the room environment while being stirred at 300 rpm to generate crosslinks in the PMMA matrix shown in Figure 16(b). The crosslinking degree was controlled by both the dose and the duration of the UV radiation and was evaluated using the DSC measurement. Higher degree of crosslinking exhibited higher endothermic peak with higher decomposition rate. The radiation was chosen to be smaller than 2.0 J/cm^2 to prevent the brittleness of PMMA film after crosslinking [131]. Thereafter final mixture was maintained at a constant temperature of ~ 75 °C on a hotplate for 40 min. Afterwards the solution was loaded onto a ~ 50 µm thick transparent and chemically stable biaxially-oriented polyethylene terephthalate (BoPET) sheet laminated on a piece of float glass using blade coating method shown in Figure 16(c).

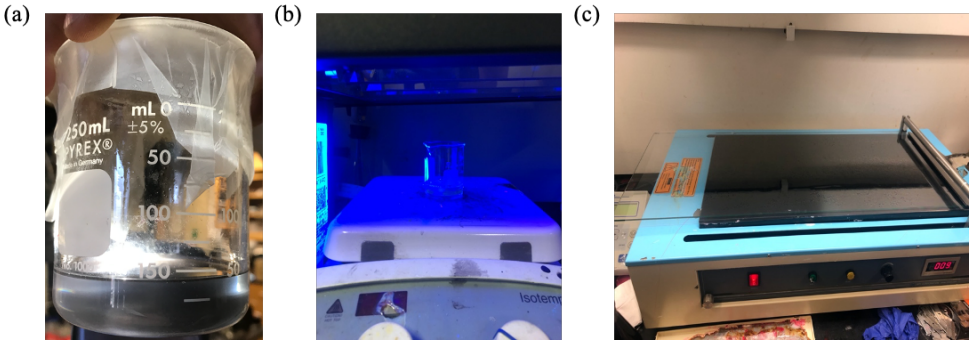

Figure 16. Uniform dispersion of the VO_2 nanoparticles (0.03 Vol%) in 20 ml PMMA 950K A4 using ultrasonic radiation and stirring to stabilize the solution, (b) Exposure of PMMA- VO_2 solution to UV radiation under constant 300 rpm stirring for 10 h. (c) Loading of the solution onto the BoPET sheet laminated on the float glass to form uniform wet film using the blading coating device.

The final thickness of the dried PMMA-VO_2 film was determined by the concentration of PMMA, the moving speed of the blade, and the gap between the blade tip and the substrate. Here the film was formed using blade coating at a speed of 15mm/s. After uniform coating of the wet film, it was dried in a fume hood for 2 hours. No obvious variation of the film brittleness was observed thereafter. Various synthesis methods of monoclinic VO_2 (M) can be found from the earlier studies

[86, 88, 132-134]. More details concerning fabrication of PMMA-VO_2 wet film can be found from Article XII.

3.2 Characterization Methods

3.2.1 Thermal Conductivity

Laser flash method, which employs noncontact and nondestructive temperature sensing [135], was used to determine the thermal diffusivities of nano insulation materials, e.g., hollow silica nanospheres, nanostructured wood membrane and aerogel. Special powder sample holder was employed to measure thermal properties of the HSNS assemblies shown in Figure 17(c). During the measurements, an instantaneous light is used as heat source to heat up the front side of the sample, and an infrared detector records the temperature response from the rear side of the sample. The two surfaces of the specimen are coated by graphite or black carbon spray shown in Figure 17 to absorb the laser light on the front side and enhance the emission intensity on the rear side [136-138].

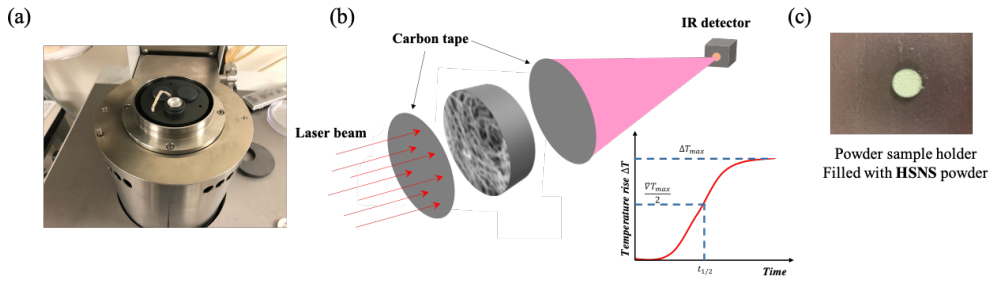

Figure 17. (a) Thermal diffusivity measurement, which displays sample holder place, coated with graphite spray at the top and bottom of sample holder. (b) The principle of the laser flash apparatus method [112]. (c) special sample holder filled with powder hollow silica nanospheres.

Under the assumption that the heat transfer is one-dimensional, the thermal diffusivity α (m^2/s) is calculated as,

$$\alpha = \frac{1.38d^2}{\pi^2 t_{1/2}}, \tag{19}$$

where d is the thickness of the sample (m) and $t_{1/2}$ is the measured time (s) that takes for the sample to heat to one half of the maximum temperature on the rear surface. The thermal conductivity k(W/(mK)) is then calculated by,

$$k = \alpha \rho c_p, \tag{20}$$

where ρ the mass density (kg/m^3) and c_p is the specific heat capacity (J/(kgK)). In our measurements, the commercial Netzsch laser flash apparatus (LFA 457) and Netzsch differential scanning calorimetry (DSC 204 F1 Phoenix) are used for the thermal diffusivity and the heat capacity measurements, respectively

3.2.2 Fatigue and Environmental Durability

Fatigue tests are used to determine the numbers of cycles (fatigue life) that a material or structure can withstand under cyclic loadings. The cracks or complete fractures may appear after a certain number of cycles due to the accumulative effect of the fluctuating stresses and strains at some points. Here, we have designed a fatigue test to ensure stability of the developed VO2-PMMA thermochromic film. The emergence of cracks in VO2-based films or complete fractures may occur due to the lattice transformation of VO2 during many cycles of phase transitions from the semiconducting to metallic state. The fatigue test design can be seen in Figure 16(a). The temperature control unit (LINKAM MDS600) with a programmable stage is used to control the temperature of the PMMA-VO2 film. The helium-neon (HeNe) laser (SIEMENS) (λ = 633 nm)

with microscope objective lens (NIKON, Plan Fluor ELWD 20x/0.45) was used as the light source. The bottom of the sample is coated with a ~ 100 nm thick silver layer. The intensity of the transmitted light through the sample was reflected by the silver coating and then recorded by the detectors. The difference between the metallic phase (25 ºC) and the insulator phase (90 ºC) vs. number of cycles, or in another word, change in solar modulation ability after certain number of cycles will precisely demonstrate the stability of the developed film.

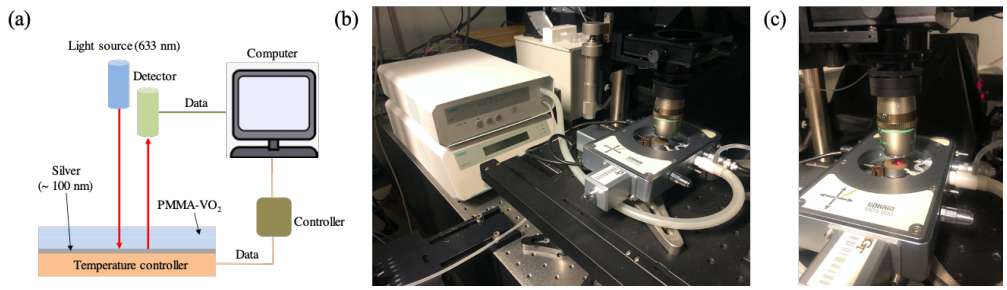

Figure 18. (a) Schematic illustrtation of the fatigue measurement setup [90], (b) programmable stage temperature controller (LINKAM TMS 94) together with a heating/freezing microscope (LINKAM MDS600), (c) A helium-neon (HeNe) laser with wavelength 633 nm focused through a microscope objective lens (NIKON, Plan Fluor ELWD 20x/0.45) on the VO_2-PMMA sample.

In addition to the fatigue test, environmental stability test was also performed to evaluate the durability of VO_2 nanoparticles in the polymer matrix. In practice, the natural oxidation of VO_2 is a long process, and the obvious variation of the thermochromic property in the ambient conditions may only be observed after a few months [84]. Therefore, accelerated environmental tests using A TPS (TENNEY) environmental chamber shown in Figure 19 was used to create a steady-state high temperature and high humidity (60 °C, relative humidity ~ 95%) for the durability testing of the PMMA-VO_2 films. Systematic measurements of spectral transmittance at both low temperature (25 ºC, insulating phase) and high temperature (90 °C, metallic phase) were recorded as a function

of time (h) to determine the variation of the thermochromic performance under the given circumstances. Each measurement was then repeated at least three times to ensure the testing reliability.

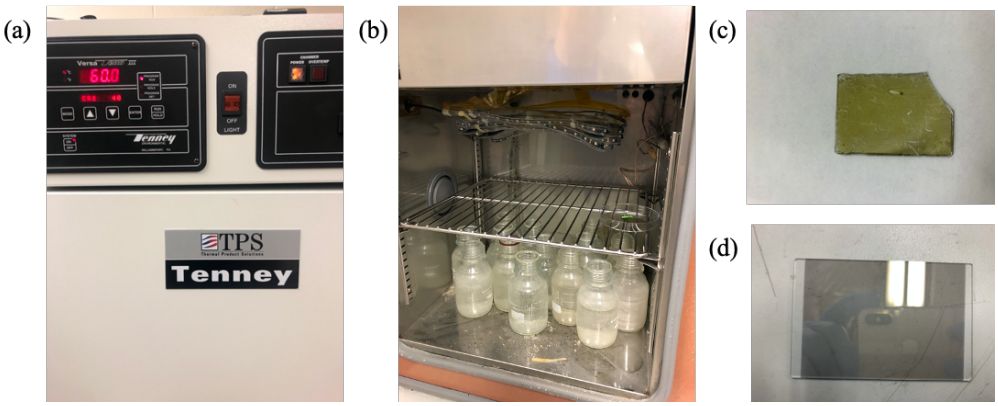

Figure 19. (a) A TPS (TENNEY) environmental chamber with steady state temperature of 60 ºC and the relative humidity ~ 95% (right). (b) Inside the chamber filled with tap water beakers. (c) The oxidized VO_2-PMMA film (yellow coating) exposed to steady temperature of 60 ºC and 95% relative humidity after ~ 980 hour in the environmental chamber. (c) Pristine VO_2-PMMA film coated on the microscope float glass with luminous transmittance of ~ 50%, solar modulation ability of ~ 17.1%.

3.2.3 Haze

Haze of the fabricated films, was measured using a UV-Vis-Near-IR spectrophotometer (Shimadzu UV-3101). Haze is used to characterize the percentage of the transmitted light whose propagation direction deviates a specific angle from the direction of the incident beam. According to the ASTM D1003-13 [139], haze is defined as,

$$H_\lambda = \frac{\tau_{dif,\lambda}}{\tau_{tot,\lambda}} = \frac{\tau_{dif,\lambda}}{\tau_{dif,\lambda} + \tau_{dir,\lambda}} \quad (21)$$

where $\tau_{dif,\lambda}$ refers to the light scattered more than 2.5° off from the incident light [139], and $\tau_{dir,\lambda}$ is the transmitted light within the angle of 2.5°. The diffuse transmittance can be measured by replacing the diffuse reflector at the outlet of the integrating sphere with a light trap to prevent the direct transmittance from influencing the measurement signal shown in Figure 18. Since the size of the synthesized VO_2 nanoparticles (50 to 80 nm) is much smaller than the wavelength of the visible light (0.4~ 0.8 μm), the scattering of the light passing through the PMMA-VO_2 films can be described as Rayleigh scattering [140], where the scattering density $I_{sca} \propto \frac{1}{\lambda^4}$ is inversely proportional to the wavelength of the visible light. Therefore, it is seen that the haze value decreases as the wavelength increase in Fig. 18(b). The averaged haze value in the visible range is calculated as,

$$H = \frac{\int_{380\ nm}^{780\ nm} H_\lambda I_\lambda d\lambda}{\int_{380\ nm}^{780\ nm} I_\lambda d\lambda} \tag{22}$$

where H_λ is the measured haze value at wavelength λ. According to Eq. (22), the averaged haze in the luminous range (380-780 nm) for the fabricated VO_2-PMMA thermochromic film in Article VIII is ~ 11%, as shown in Figure 20(b).

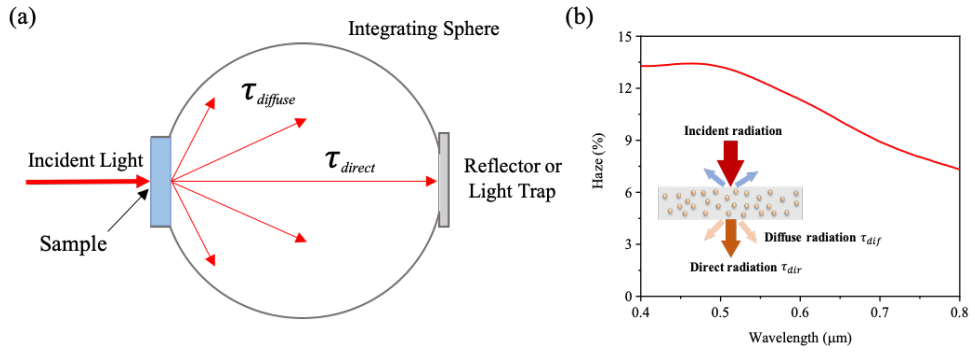

Figure 20. (a) Schematic illustration of solar transmittance and haze measurement method, (b) The spectral haze of the PMMA-VO_2 film [90] in the visible range with wavelengths of 0.4 ~ 0.8 μm, the averaged haze is ~ 11% [90].

3.2.4 FTIR

Optical performance, including spectral transmittance and solar modulation ability of the films, was measured using a commercial UV-Vis-Near-IR spectrophotometer (Cary 500, SCAN) together with our own built temperature control unit, which includes black anodized aluminum 6061 plate, and a variac (2 A, 120 V), thermocouple and thermometer shown in Figure 21. The total transmittance ($\tau_{\lambda,tot}$) were measured by placing the PMMA-VO_2 film and a diffuse reflector at the inlet and outlet of the integrating sphere, respectively (Figure 20(a)). The measured total spectral transmittances of the PMMA-VO_2 film at low temperature (~ 25 ºC) and high temperature (~ 90 °C) are shown in Figure 13(b).

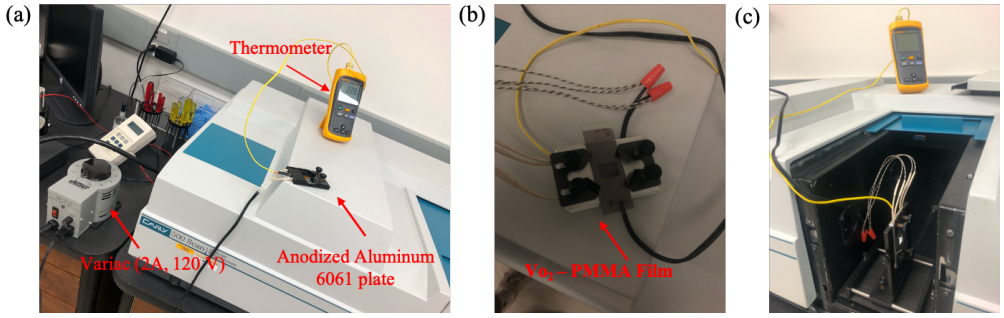

Figure 21. (a) UV-Vis-Near-IR spectrophotometer with the our own built temperature controlling unit setup, (b) VO_2-PMMA film placed on aluminum plate attached to the thermometer (c) Aluminum plate centered for direct passage of incident light through the sample ranging from (0.4~ 2.5 µm).

Since the metallic phase VO_2 blocks the near-infrared (NIR) solar radiation, it was found that the transmittance of the PMMA-VO_2 in the range of 0.8 ~ 2.5 µm was much smaller when the temperature of the PMMA-VO_2 film set at ~ 90 ºC.

3.2.4 DSC Measurement

The commercial Netzsch differential scanning calorimetry (DSC 204 F1 Phoenix) was used to determine the phase transition properties of the VO_2 powder over the temperature range from 0 to 110 °C, and the heat absorption properties of the PMMAs from 0 to 550 °C, respectively. The heating/cooling rate was set at 10 °C/min. Since the insulator-to-metal transformation of VO_2 is a first-order phase transition [141], the discontinuous variation of entropy results in the release or absorption of latent heat. As shown in Figure 22(a), when VO_2 transits from the monoclinic (M) insulator phase to the rutile (R) phase during the heating cycle, an endothermic (positive) peak with peak temperature ~ 71 °C is observed. when VO_2 transits from the monoclinic (M) insulator phase to the rutile (R) phase during the heating cycle, an endothermic (positive) peak with peak temperature ~ 71 °C is observed.

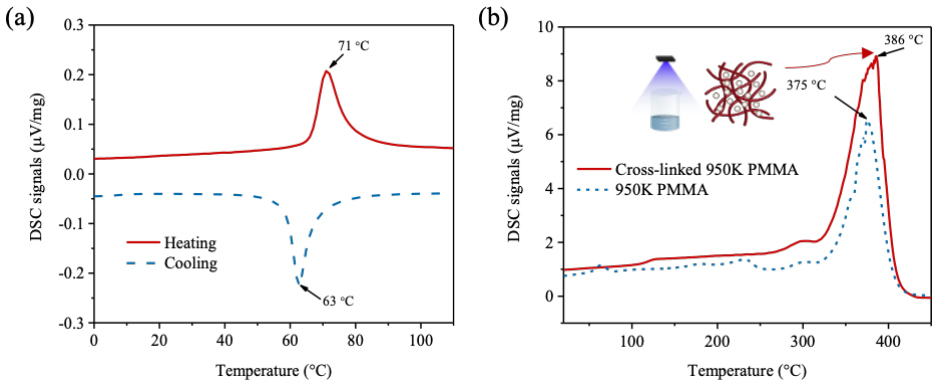

Figure 22. (a) Differential scanning calorimetry (DSC) of the VO_2 nanoparticles, where the positive peak represents an endothermic process, and the negative peak represents an exothermic process. (b) Comparison of the DSC thermograms of the cross-linked and non-cross-linked PMMA with molecular weight ~ 950,000 [90].

A corresponding exothermic (negative) peak, representing metal-to-insulator transition, occurs in the cooling cycle, where the peak temperature is ~ 63 ºC. Furthermore, since the crosslinking

process could generate new chemical bonding between neighboring chains, the cross-linked PMMA polymers are expected to have a higher endothermic peak and a larger maximum decomposition temperature [142]. Therefore, DSC measurement was also used to examine the cross-linked PMMA polymers under UV radiation (220 ~380 nm, ADJ Products) from the non-UV exposed 950,000 PMMA. Figure 22(b) clearly shows that the 950,000 PMMA under UV exposure has a higher endothermic peak (from ~ 6.0 μV/mg to ~ 9.5 μV/mg) and a larger maximum decomposition temperature (from 375 ºC to 386 ºC), indicating the crosslinking generation took place successfully.

4. Summary of Articles

The output of the research work is presented as scientific publications, both in the form of conference proceedings and peer-reviewed journal articles. The following gives short background information about each single article and how they are related. The articles order do not follow the sequential time line as to when each article was published but represents a story line based on the topic and correlation between each article on the particular subject.

Article I: High-Performance Nano Insulation Materials for Energy-Efficient Buildings.

Article I discusses the on-going quest for development of high-performance thermal insulation materials. hollow spheres, hollows fibers were represented as a stepping-stone towards achieving new insulation materials with thermal transport, initial experimental pathway and environmental impact being the main issues reviewed.

Article II: Air-filled Nanopore Based High-Performance Thermal Insulation Materials.

Article II presents new pathway towards possible development of high-performance thermal insulation material with regards to current drawbacks from state-of-art insulation solutions like vacuum insulation panels (VIP) and aerogel. Introduction of a new approach, including air-filled nanopore based materials through a controlled process were discussed to address and maybe remove the various disadvantages with respect to state-of-art insulation materials.

Article III: Synthesis of Silica-Based Nano Insulation Application in Low-Energy or Zero Emission Buildings Materials for Potential.

Article III presents preliminary synthesis route to formation of silica-based nano insulation material using sacrificial template method. Polystyrene (PS) were represented as the template material for coating of silica nano particles by using tetraethyl orthosilicate (TEOS) as the silica precursor. The study further investigates the influence of reaction parameters on the structural characteristics of silica-based nano insulation materials, and their possible integration as zero-emission thermal building insulation materials.

Article IV: Hollow silica nanospheres as thermal insulation materials for construction: Impact of their morphologies as a function of synthesis pathways and starting materials.

Article IV presents the robust and green synthesis methods to fabricate hollow silica nanospheres (HSNS) for thermal insulation applications. Two synthetic procedures with different reaction medium, using tetraethyl orthosilicate (TEOS) and water glass (Na_2SiO_3, WG) as silica precursors, in alkaline and acidic media were investigated. Thermal performance of HSNS using both methods were thoroughly discussed, in which formation of thermally insulating HSNS was favored using alkaline reaction. Meanwhile formation of HSNS using WG as silica precursor suggested a greener and more sustainable cost-effective method.

Article V: Utilization of Hollow Silica Nanospheres for Thermal Insulation purposes.

Using the same synthesis parameters in Article IV, Article V investigates the thermal performance of the fabricated hollow silica nanospheres based on the variation of structural parameters such as shell thickness and inner pore diameter. Hollow silica nanosphere assemblies with the same inner pore and different shell thickness sizes were synthesized and the effective thermal conductivity associated with each one were compared using the HotDisk method.

Article VI: Nano insulation materials exploiting the Knudsen effect.

Article VI discusses the thermal transport properties in the HSNS assemblies, where the heat transport by gas conductance and gas/solid state interactions in the nanoscale were predicted by the Knudsen effect. The gaseous, gas/solid thermal conductivity of HSNS is directly dependent on HSNS nanoscale pore size inside the shell and pore sizes within the shell. Therefore, HSNS with small inner pore diameters were synthesized to examine HSNS size-dependent thermal conduction

Article VII: Utilization of Size-Tunable Hollow Silica Nanospheres for Building Thermal Insulation Applications.

Based on the literature review accomplished in Article VI, thermal properties of HSNS as a function of the corresponding structural parameters such as inner pore diameter, porosity, packing density, shell thickness, and size of the silica nanoparticles constituting the shell of HSNS were investigated in Article VII. HSNS with inner pore size less than 100 nm was specifically synthesized to validate the size-dependent thermal conduction at the nanoscale. Consequently the lowest thermal conductivity value ~ 14 mW/(mK) was recorded for HSNS sample (0.1 g/cm^3) with inner pore diameter 85 nm and average particle size 34 nm using Laser Flash apparatus. due to versatility in modifying their thermal properties, HSNS represented the foundation for the development of superinsulation materials in building applications.

Article VIII: Reduced-scale hot box method for thermal characterization of window insulation materials.

Article VIII presents the development of accurate thermal property characterization technique, specifically designed for nanostructured materials ranging from 0.06 to 0.2 m (diameter or length),

e.g., window insulation materials, nano insulation materials during their early stage of development. The reduced-scale hot box system (RHS) measure both the thermal transmittance (U-value) and the thermal conductivity (*k*-value) of specimens in real environment considering humidity, temperature and the wind. The established measurement system was built to facilitate the design and development of next generation of novel materials for energy-efficiency applications, an example of which can be found in Article IX.

Article IX: Hydrophobic nanostructured wood membrane for thermally efficient distillation.

The developed reduced-scale hot box system in Article VIII was used to design and characterize the thermal conductivity of the newly synthesized hydrophobic nanostructured wood membrane from 40 °C to 60 °C under controlled humidity for thermally efficient distillation application. The results were validated using the Laser Flash Apparatus (LFA), where LFA 457 detector (NETZSCH, Burlington, MA) and differential scanning calorimetry method with a sapphire reference was used to determine thermal diffusivity measurement and the heat capacity of samples, respectively.

Article X: Optically-Switchable Thermally-Insulating VO_2-Aerogel Hybrid Film for Windows Retrofits.

Article X presents a developed theoretical model to investigate thermal and optical properties of thermally insulating, optically-switchable VO_2-Aerogel Hybrid (VAH) Film used for single-pane window retrofit. The proposed VAH film consist of 3.0 mm thick aerogel film embedded with a 0.01vol% core-shell structure VO_2/SiO_2 with inner diameter of 25 nm and outer diameter of 40 nm. The energy performance of the window employing the VAH film in hot and cold regions showed

that employing the VAH film could not only reduce the heat loss but also greatly improve the performance of single-pane windows by improving thermal comfort and avoiding moisture condensation in cold climates and overheating in hot climates.

Article XI: Durability-Enhanced Vanadium Dioxide Thermochromic Films for Smart Windows.

Article XI presents a new method for fabrication of Vanadium dioxide (VO_2) based thermochromic film for energy-saving smart windows. The developed thermochromic solar film include ~ 4 μm PMMA polymer matrix embedded with 0.03vol% of VO_2 (50 ~80 nm) coated on ~ 50 μm biaxially-oriented polyethylene terephthalate (BoPET) film. The influence of molecular entanglement and cross-linking of the PMMA martix on environmental durability of VO_2 nanoparticles in polymer matrix was studied. Furthermore, mechanical stability, large-scale production using blade coating method, and energy analysis in hot and cold regions were discussed.

Article XII: Influence of Shell Material on the Optical Performance of VO_2 Core-Shell Nanoparticle-based Thermochromic Films.

Article XII presents the theoretical model to investigate the influence of the optical constants of the shell materials and the shell thickness on the luminous transmittance and solar modulation ability of the VO_2 core-shell nanoparticle-based thermochromic and insulation films. The results reported in this work was directly used to guide the design of high-performance VAH film in Article X and the durability enhanced VO_2-PMMA film Article XII.

5. Conclusions

The work in this dissertation was mainly centered on new generation of materials and adopted strategies including theoretical and conceptual studies to improve the energy efficiency measures that ultimately reduce building energy consumption. The application and incorporation of the developed materials and components with tailor-made properties may result in making multi-functional building component and retrofits with significant environmental and economic benefits. Building insulation was discussed as a key component of energy conservation strategy as well as reducing negative environmental impact of the greenhouse gas effect. high-performance nano insulation materials and window insulation together were identified as the main energy conservation targets to consequently reduce the energy consumption of heating and cooling systems. To realize our objective, series of insulation materials including hollow silica nanospheres, aerogel-thermochromic film and solar thermochromic film with desired properties., e.g., low thermal conductivity, climate aging durability, environmental friendliness were proposed and developed. In addition, accurate characterization technique including reduced scale hotbox system was developed to facilitate thermal properties of nanostructured materials with small size, during their early stage development, for energy-efficiency building applications. Finally a theoretical model, coupled heat transfer and solar radiation heat transfer model was developed to evaluate the energy performance of the developed materials in different regions during hot and cold seasons.

The main findings and achievements in this thesis include :

- Introduction of hollow silica nanospheres as a possible building block for super insulation material with ultralow thermal conductivity. Highly porous hydrophobic hollow silica nanosphere assemblies (~ 0.1 g/cm^3) with varying sizes specifically less than 100 nm were successfully synthesized. The size-dependent thermal conduction at the nanoscale were validated, while the lowest thermal conductivity value for HSNS sample with 85 nm was recorded at 14 mW/mK.
- Fabrication of durability enhanced Vanadium dioxide (VO_2) based thermochromic film for energy-saving smart windows. The developed 4 μm VO_2-PMMA film achieved a high luminous transmittance of ~ 50%, 17% solar modulation ability, and a low haze of ~ 11%. The energy performance analysis showed that the developed PMMA-VO_2 film could greatly reduce the cooling demands in hot climates and improve the thermal comfort in cold climates.
- Investigation of optically-switchable, thermally insulating, visibly transparent Aerogel-thermochromic film as window retrofit material. The AVP film including 3.0 mm thick aerogel with 4 μm thick VO_2-PMMA film, demonstrated a thermal transmittance (U-value) of ~ 3.0 W/(m^{2}K), which is ~ 50% of the value of single-pane windows, a luminous transmittance of 0.6 (0.5) in cold (hot) climates, and a solar modulation ability of ~ 17%. It was shown that employing the AVP film will reduce ~ 50% heat loss through a single-pane window and greatly improve the thermal comfort and avoid moisture condensation in cold climate and overheating in hot climates.
- Development of reduced-scale hotbox system for thermal property characterization of nanostructured materials under early stage of development for energy-efficient building applications. The RHS system can accurately measure thermal transmittance and thermal conductivity measurement of materials in real environment, considering humidity, temperature,

wind. The developed method facilitated the design of high performance insulation materials for energy-efficient buildings.

References

[1] X. Cao, X. Dai, J. Liu, Building energy-consumption status worldwide and the state-of-the-art technologies for zero-energy buildings during the past decade, Energy and buildings 128 (2016) 198-213.
[2] D. Bosseboeuf, Energy Efficiency Trends and Policies in the Household and Tertiary Sectors An Analysis Based on the ODYSSEE and MURE Databases, (2015).
[3] EA, Energy Balances Of Non-oecd Countries, (2012).
[4] I. IEA, World energy outlook 2011, Int. Energy Agency 666 (2011).
[5] K. Amasyali, N.M. El-Gohary, A review of data-driven building energy consumption prediction studies, Renewable and Sustainable Energy Reviews 81 (2018) 1192-1205.
[6] U.S.E.I. Administration, Today in Energy, (2018).
[7] M. Isaac, D.P. Van Vuuren, Modeling global residential sector energy demand for heating and air conditioning in the context of climate change, Energy policy 37(2) (2009) 507-521.
[8] R. Cluett, J. Amann, Residential deep energy retrofits, American Council for an Energy Efficient Economy, 2014.
[9] I. El-Darwish, M. Gomaa, Retrofitting strategy for building envelopes to achieve energy efficiency, Alexandria Engineering Journal 56(4) (2017) 579-589.
[10] S. Nadel, L. Ungar, Halfway There: Energy Efficiency Can Cut Energy Use and Greenhouse Gas Emissions in Half by 2050, (2019).
[11] B. Knopf, P. Nahmmacher, E. Schmid, The European renewable energy target for 2030–An impact assessment of the electricity sector, Energy policy 85 (2015) 50-60.
[12] N. Zhou, China's energy and carbon emissions outlook to 2050, (2011).
[13] M. Zamovskis, R. Vanaga, A. Blumberga, Mathematical Modelling of Performance of New Type of Climate Adaptive Building Shell, Energy Procedia 113 (2017) 270-276.
[14] M. Miezis, K. Zvaigznitis, N. Stancioff, L. Soeftestad, Climate change and buildings energy efficiency–the key role of residents, Environmental and Climate Technologies 17(1) (2016) 30-43.
[15] L. Aditya, T. Mahlia, B. Rismanchi, H. Ng, M. Hasan, H. Metselaar, O. Muraza, H. Aditiya, A review on insulation materials for energy conservation in buildings, Renewable and sustainable energy reviews 73 (2017) 1352-1365.
[16] P.L. Simona, P. Spiru, I.V. Ion, Increasing the energy efficiency of buildings by thermal insulation, Energy Procedia 128 (2017) 393-399.
[17] X. Xu, Y. Zhang, K. Lin, H. Di, R. Yang, Modeling and simulation on the thermal performance of shape-stabilized phase change material floor used in passive solar buildings, Energy and Buildings 37(10) (2005) 1084-1091.
[18] S.B. Sadineni, S. Madala, R.F. Boehm, Passive building energy savings: A review of building envelope components, Renewable and sustainable energy reviews 15(8) (2011) 3617-3631.
[19] S. Grynning, A. Gustavsen, B. Time, B.P. Jelle, Windows in the buildings of tomorrow: Energy losers or energy gainers?, Energy and buildings 61 (2013) 185-192.

[20] S.A.M. X. Zhao, B.P. Jelle, G. Tan, X. Li, X. Yin, R. Yang, Optically-Switchable Thermally-Insulating VO2-Aerogel Hybrid Film for Windows Retrofits, Applied Energy (2020).
[21] J.-J. Kim, J.W. Moon, Impact of insulation on building energy consumption, Eleventh International IBPSA Conference, Building Simulation, Citeseer, 2009.
[22] S. Sekhar, K.L.C. Toon, On the study of energy performance and life cycle cost of smart window, Energy and Buildings 28(3) (1998) 307-316.
[23] A.S. Bahaj, P.A. James, M.F. Jentsch, Potential of emerging glazing technologies for highly glazed buildings in hot arid climates, Energy and Buildings 40(5) (2008) 720-731.
[24] A.A. Abdou, I.M. Budaiwi, Comparison of thermal conductivity measurements of building insulation materials under various operating temperatures, Journal of building physics 29(2) (2005) 171-184.
[25] M. Khoukhi, N. Fezzioui, B. Draoui, L. Salah, The impact of changes in thermal conductivity of polystyrene insulation material under different operating temperatures on the heat transfer through the building envelope, Applied Thermal Engineering 105 (2016) 669-674.
[26] A. C168-97, Standard Terminology Relating to Thermal Insulating Materials, ASTM International, (1997).
[27] L.-l. Jiao, J.-h. Sun, A thermal degradation study of insulation materials extruded polystyrene, Procedia Engineering 71(622) (2014).
[28] S. Doroudiani, H. Omidian, Environmental, health and safety concerns of decorative mouldings made of expanded polystyrene in buildings, Building and Environment 45(3) (2010) 647-654.
[29] A. Limam, A. Zerizer, D. Quenard, H. Sallee, A. Chenak, Experimental thermal characterization of bio-based materials (Aleppo Pine wood, cork and their composites) for building insulation, Energy and Buildings 116 (2016) 89-95.
[30] A.M. Papadopoulos, State of the art in thermal insulation materials and aims for future developments, Energy and buildings 37(1) (2005) 77-86.
[31] J.-W. Wu, W.-F. Sung, H.-S. Chu, Thermal conductivity of polyurethane foams, International Journal of Heat and Mass Transfer 42(12) (1999) 2211-2217.
[32] H. Zhang, W.-Z. Fang, Y.-M. Li, W.-Q. Tao, Experimental study of the thermal conductivity of polyurethane foams, Applied Thermal Engineering 115 (2017) 528-538.
[33] S.E. Kalnæs, B.P. Jelle, Vacuum insulation panel products: A state-of-the-art review and future research pathways, Applied Energy 116 (2014) 355-375.
[34] E. Wegger, B.P. Jelle, E. Sveipe, S. Grynning, A. Gustavsen, R. Baetens, J.V. Thue, Aging effects on thermal properties and service life of vacuum insulation panels, Journal of Building Physics 35(2) (2011) 128-167.
[35] R. Baetens, B.P. Jelle, A. Gustavsen, Aerogel insulation for building applications: a state-of-the-art review, Energy and Buildings 43(4) (2011) 761-769.
[36] D.M. Smith, A. Maskara, U. Boes, Aerogel-based thermal insulation, Journal of non-crystalline solids 225 (1998) 254-259.
[37] E. Cuce, P.M. Cuce, C.J. Wood, S.B. Riffat, Toward aerogel based thermal superinsulation in buildings: a comprehensive review, Renewable and Sustainable Energy Reviews 34 (2014) 273-299.
[38] M.S. Al-Homoud, Performance characteristics and practical applications of common building thermal insulation materials, Building and environment 40(3) (2005) 353-366.
[39] I.L. Wong, P. Eames, R. Perera, A review of transparent insulation systems and the evaluation of payback period for building applications, Solar Energy 81(9) (2007) 1058-1071.

[40] A. Galante, G. Pasetti, A methodology for evaluating the potential energy savings of retrofitting residential building stocks, Sustainable Cities and Society 4 (2012) 12-21.
[41] R.A. Aldrich, L. Arena, W. Zoeller, Practical residential wall systems: R-30 and beyond, Res. Rep. Prep. by Steven Winter Assoc. Inc Consort. Adv. Resid. Build (2010).
[42] F. Aldawi, F. Alam, A. Date, M. Alghamdi, F. Aldhawi, A new house wall system for residential buildings, Energy and Buildings 67 (2013) 403-418.
[43] I. Asadi, P. Shafigh, Z.F.B.A. Hassan, N.B. Mahyuddin, Thermal conductivity of concrete–A review, Journal of Building Engineering 20 (2018) 81-93.
[44] I. Gnip, S. Vėjelis, S. Vaitkus, Thermal conductivity of expanded polystyrene (EPS) at 10 C and its conversion to temperatures within interval from 0 to 50 C, Energy and Buildings 52 (2012) 107-111.
[45] M. Dondi, F. Mazzanti, P. Principi, M. Raimondo, G. Zanarini, Thermal conductivity of clay bricks, Journal of materials in civil engineering 16(1) (2004) 8-14.
[46] S. Ng, B.P. Jelle, L.I. Sandberg, T. Gao, S.A. Mofid, Hollow silica nanospheres as thermal insulation materials for construction: Impact of their morphologies as a function of synthesis pathways and starting materials, Construction and Building Materials 166 (2018) 72-80.
[47] T. Gao, B.P. Jelle, L.I.C. Sandberg, A. Gustavsen, Monodisperse hollow silica nanospheres for nano insulation materials: synthesis, characterization, and life cycle assessment, ACS applied materials & interfaces 5(3) (2013) 761-767.
[48] H.F. Gangåssæter, B.P. Jelle, S.A. Mofid, T. Gao, Air-filled nanopore based high-performance thermal insulation materials, Energy Procedia 132 (2017) 231-236.
[49] M. Fuji, C. Takai, H. Imabeppu, X. Xu, Synthesis and shell structure design of hollow silica nanoparticles using polyelectrolyte as template, Journal of Physics: Conference Series, IOP Publishing, 2015, p. 012007.
[50] X. Wang, J. Feng, Y. Bai, Q. Zhang, Y. Yin, Synthesis, properties, and applications of hollow micro-/nanostructures, Chemical reviews 116(18) (2016) 10983-11060.
[51] B.P. Jelle, S. Mofid, T. Gao, M. Grandcolas, M. Sletnes, E. Sagvolden, Nano insulation materials exploiting the Knudsen effect, IOP Conference Series: Materials Science and Engineering, IOP Publishing, 2019, p. 012003.
[52] B. Notario, J. Pinto, E. Solorzano, J.A. de Saja, M. Dumon, M.A. Rodríguez-Pérez, Experimental validation of the Knudsen effect in nanocellular polymeric foams, Polymer $V 56 (2015) 57-67.
[53] L. Liang, B. Li, Size-dependent thermal conductivity of nanoscale semiconducting systems, Physical Review B 73(15) (2006) 153303.
[54] L. Liu, X. Chen, Effect of surface roughness on thermal conductivity of silicon nanowires, Journal of Applied Physics 107(3) (2010) 033501.
[55] A.S. Teja, M.P. Beck, Y. Yuan, P. Warrier, The limiting behavior of the thermal conductivity of nanoparticles and nanofluids, Journal of Applied Physics 107(11) (2010) 114319.
[56] S.A. Mofid, B.P. Jelle, X. Zhao, T. Gao, M. Grandcolas, B. Cunningham, S. Ng, R. Yang, Utilization of size-tunable hollow silica nanospheres for building thermal insulation applications, Journal of Building Engineering (2020) 101336.
[57] M. Grandcolas, E. Jasinski, T. Gao, B.P. Jelle, Preparation of low density organosilica monoliths containing hollow silica nanospheres as thermal insulation materials, Materials Letters 250 (2019) 151-154.

[58] B.P. Jelle, A. Hynd, A. Gustavsen, D. Arasteh, H. Goudey, R. Hart, Fenestration of today and tomorrow: A state-of-the-art review and future research opportunities, Solar Energy Materials and Solar Cells 96 (2012) 1-28.
[59] T. Gao, B.P. Jelle, T. Ihara, A. Gustavsen, Insulating glazing units with silica aerogel granules: The impact of particle size, Applied Energy 128 (2014) 27-34.
[60] A.A.S. 55, Thermal Environmental Conditions for Human Occupancy., (2010).
[61] ARPA-E, Single-pan highly insulating efficient lucid designs (SHIELD) programoverview, (2014).
[62] R. American Society of Heating, A.-C. Engineers, ASHRAE Standard: Thermal Environmental Conditions for Human Occupancy, ASHRAE2010.
[63] B.P. Jelle, Solar radiation glazing factors for window panes, glass structures and electrochromic windows in buildings—Measurement and calculation, Solar Energy Materials and Solar Cells 116 (2013) 291-323.
[64] K. Ismail, J. Henríquez, Thermally effective windows with moving phase change material curtains, Applied Thermal Engineering 21(18) (2001) 1909-1923.
[65] R.C. Temps, K. Coulson, Solar radiation incident upon slopes of different orientations, Solar energy 19(2) (1977) 179-184.
[66] Y. Wang, E.L. Runnerstrom, D.J. Milliron, Switchable materials for smart windows, Annual review of chemical and biomolecular engineering 7 (2016) 283-304.
[67] H.N. Kim, S. Yang, Responsive Smart Windows from Nanoparticle–Polymer Composites, Advanced Functional Materials (2019) 1902597.
[68] Q. Hao, W. Li, H. Xu, J. Wang, Y. Yin, H. Wang, L. Ma, F. Ma, X. Jiang, O.G. Schmidt, VO_2/TiN Plasmonic Thermochromic Smart Coatings for Room-Temperature Applications, Advanced materials 30(10) (2018) 1705421.
[69] Y. Ke, X. Wen, D. Zhao, R. Che, Q. Xiong, Y. Long, Controllable fabrication of two-dimensional patterned VO_2 nanoparticle, nanodome, and nanonet arrays with tunable temperature-dependent localized surface plasmon resonance, ACS nano 11(7) (2017) 7542-7551.
[70] Y. Ke, Y. Yin, Q. Zhang, Y. Tan, P. Hu, S. Wang, Y. Tang, Y. Zhou, X. Wen, S. Wu, Adaptive thermochromic windows from active plasmonic elastomers, Joule 3(3) (2019) 858-871.
[71] Y. Ke, I. Balin, N. Wang, Q. Lu, A.I.Y. Tok, T.J. White, S. Magdassi, I. Abdulhalim, Y. Long, Two-dimensional SiO_2/VO_2 photonic crystals with statically visible and dynamically infrared modulated for smart window deployment, ACS applied materials & interfaces 8(48) (2016) 33112-33120.
[72] J. Zheng, S. Bao, P. Jin, TiO_2 (R)/VO_2 (M)/TiO_2 (A) multilayer film as smart window: Combination of energy-saving, antifogging and self-cleaning functions, Nano Energy 11 (2015) 136-145.
[73] M.K. Dietrich, F. Kuhl, A. Polity, P.J. Klar, Optimizing thermochromic VO_2 by co-doping with W and Sr for smart window applications, Applied Physics Letters 110(14) (2017) 141907.
[74] S. Chen, Z. Wang, H. Ren, Y. Chen, W. Yan, C. Wang, B. Li, J. Jiang, C. Zou, Gate-controlled VO_2 phase transition for high-performance smart windows, Science advances 5(3) (2019) eaav6815.
[75] Y. Cui, Y. Ke, C. Liu, Z. Chen, N. Wang, L. Zhang, Y. Zhou, S. Wang, Y. Gao, Y. Long, Thermochromic VO_2 for energy-efficient smart windows, Joule 2(9) (2018) 1707-1746.
[76] I. Balin, V. Garmider, Y. Long, I. Abdulhalim, Training artificial neural network for optimization of nanostructured VO_2-based smart window performance, Optics express 27(16) (2019) A1030-A1040.

[77] S.-Y. Li, G.A. Niklasson, C.-G. Granqvist, Thermochromic fenestration with VO_2-based materials: Three challenges and how they can be met, Thin Solid Films 520(10) (2012) 3823-3828.
[78] N.R. Mlyuka, G.A. Niklasson, C.G. Granqvist, Thermochromic VO_2- based multilayer films with enhanced luminous transmittance and solar modulation, physica status solidi (a) 206(9) (2009) 2155-2160.
[79] F. Xu, X. Cao, H. Luo, P. Jin, Recent advances in VO_2-based thermochromic composites for smart windows, Journal of Materials Chemistry C 6(8) (2018) 1903-1919.
[80] C.G. Granqvist, Oxide-based chromogenic coatings and devices for energy efficient fenestration: brief survey and update on thermochromics and electrochromics, Journal of Vacuum Science & Technology B, Nanotechnology and Microelectronics: Materials, Processing, Measurement, and Phenomena 32(6) (2014) 060801.
[81] D. Hou, T. Li, X. Chen, S. He, J. Dai, S.A. Mofid, D. Hou, A. Iddya, D. Jassby, R. Yang, Hydrophobic nanostructured wood membrane for thermally efficient distillation, Science advances 5(8) (2019) eaaw3203.
[82] Y. Gao, H. Luo, Z. Zhang, L. Kang, Z. Chen, J. Du, M. Kanehira, C. Cao, Nanoceramic VO_2 thermochromic smart glass: A review on progress in solution processing, Nano Energy 1(2) (2012) 221-246.
[83] A. Taylor, I. Parkin, N. Noor, C. Tummeltshammer, M.S. Brown, I. Papakonstantinou, A bioinspired solution for spectrally selective thermochromic VO_2 coated intelligent glazing, Optics express 21(105) (2013) A750-A764.
[84] L. Zhao, L. Miao, C. Liu, C. Li, T. Asaka, Y. Kang, Y. Iwamoto, S. Tanemura, H. Gu, H. Su, Solution-processed VO 2-SiO 2 composite films with simultaneously enhanced luminous transmittance, solar modulation ability and anti-oxidation property, Scientific reports 4 (2014) 7000.
[85] R. Lindström, V. Maurice, S. Zanna, L. Klein, H. Groult, L. Perrigaud, C. Cohen, P. Marcus, Thin films of vanadium oxide grown on vanadium metal: oxidation conditions to produce V2O5 films for Li-intercalation applications and characterisation by XPS, AFM, RBS/NRA, Surface and Interface Analysis: An International Journal devoted to the development and application of techniques for the analysis of surfaces, interfaces and thin films 38(1) (2006) 6-18.
[86] Y. Gao, S. Wang, H. Luo, L. Dai, C. Cao, Y. Liu, Z. Chen, M. Kanehira, Enhanced chemical stability of VO 2 nanoparticles by the formation of SiO 2/VO 2 core/shell structures and the application to transparent and flexible VO 2-based composite foils with excellent thermochromic properties for solar heat control, Energy & Environmental Science 5(3) (2012) 6104-6110.
[87] Y. Li, S. Ji, Y. Gao, H. Luo, M. Kanehira, Core-shell VO 2@ TiO 2 nanorods that combine thermochromic and photocatalytic properties for application as energy-saving smart coatings, Scientific reports 3 (2013) 1370.
[88] Y. Chen, X. Zeng, J. Zhu, R. Li, H. Yao, X. Cao, S. Ji, P. Jin, High performance and enhanced durability of thermochromic films using VO2@ ZnO core–shell nanoparticles, ACS applied materials & interfaces 9(33) (2017) 27784-27791.
[89] Y. Cui, Y. Ke, C. Liu, Z. Chen, N. Wang, L. Zhang, Y. Zhou, S. Wang, Y. Gao, Y. Long, Thermochromic VO2 for energy-efficient smart windows, Joule (2018).
[90] X. Zhao, S. Mofid, T. Gao, G. Tan, B. Jelle, X. Yin, R. Yang, Durability-enhanced vanadium dioxide thermochromic film for smart windows, Materials Today Physics 13 (2020) 100205.
[91] K. Tong, R. Li, J. Zhu, H. Yao, H. Zhou, X. Zeng, S. Ji, P. Jin, Preparation of VO2/Al-O core-shell structure with enhanced weathering resistance for smart window, Ceramics International 43(5) (2017) 4055-4061.

[92] Y.-X. Ji, S.-Y. Li, G.A. Niklasson, C.G. Granqvist, Durability of thermochromic VO2 thin films under heating and humidity: Effect of Al oxide top coatings, Thin Solid Films 562 (2014) 568-573.
[93] S. Long, X. Cao, N. Li, Y. Xin, G. Sun, T. Chang, S. Bao, P. Jin, Application-oriented VO2 thermochromic coatings with composite structures: Optimized optical performance and robust fatigue properties, Solar Energy Materials and Solar Cells 189 (2019) 138-148.
[94] B.P. Jelle, Accelerated climate ageing of building materials, components and structures in the laboratory, Journal of Materials Science 47(18) (2012) 6475-6496.
[95] B.P. Jelle, E. Sveipe, E. Wegger, A. Gustavsen, S. Grynning, J.V. Thue, B. Time, K.R. Lisø, Robustness classification of materials, assemblies and buildings, Journal of Building Physics 37(3) (2014) 213-245.
[96] P. Lyons, D. Arasteh, C. Huizenga, Window performance for human thermal comfort, Transactions-American Society of Heating Refrigerating and Air Conditioning Engineers 106(1) (2000) 594-604.
[97] A.S. Dorcheh, M. Abbasi, Silica aerogel; synthesis, properties and characterization, Journal of materials processing technology 199(1) (2008) 10-26.
[98] J.L. Gurav, I.-K. Jung, H.-H. Park, E.S. Kang, D.Y. Nadargi, Silica aerogel: synthesis and applications, Journal of Nanomaterials 2010 (2010) 23.
[99] C. Buratti, E. Moretti, Silica nanogel for energy-efficient windows, Nanotechnology in eco-efficient construction, Elsevier2013, pp. 207-235.
[100] M. Reim, W. Körner, J. Manara, S. Korder, M. Arduini-Schuster, H.-P. Ebert, J. Fricke, Silica aerogel granulate material for thermal insulation and daylighting, Solar Energy 79(2) (2005) 131-139.
[101] T. Shimizu, K. Kanamori, K. Nakanishi, Silicone-based organic–inorganic hybrid aerogels and xerogels, Chemistry–A European Journal 23(22) (2017) 5176-5187.
[102] G. Zu, T. Shimizu, K. Kanamori, Y. Zhu, A. Maeno, H. Kaji, J. Shen, K. Nakanishi, Transparent, superflexible doubly cross-linked polyvinylpolymethylsiloxane aerogel superinsulators via ambient pressure drying, Acs Nano 12(1) (2018) 521-532.
[103] Q. Liu, A.W. Frazier, X. Zhao, A. Joshua, A.J. Hess, R. Yang, I.I. Smalyukh, Flexible transparent aerogels as window retrofitting films and optical elements with tunable birefringence, Nano Energy 48 (2018) 266-274.
[104] Y. Kobayashi, T. Saito, A. Isogai, Aerogels with 3D Ordered Nanofiber Skeletons of Liquid-Crystalline Nanocellulose Derivatives as Tough and Transparent Insulators, Angewandte Chemie 126(39) (2014) 10562-10565.
[105] S. Liu, J. Duvigneau, G.J. Vancso, Nanocellular polymer foams as promising high performance thermal insulation materials, European polymer journal 65 (2015) 33-45.
[106] C.B. Kim, N.-H. You, M. Goh, Hollow polymer microcapsule embedded transparent and heat-insulating film, RSC Advances 8(17) (2018) 9480-9486.
[107] F. Hu, S. Wu, Y. Sun, Hollow-Structured Materials for Thermal Insulation, Advanced Materials (2018) 1801001.
[108] S.A.M. X.P. Zhao, T. Gao, G. Tan, B.P. Jelle, X.B. Yin, R.G. Yang, Durability-enhanced vanadium dioxide thermochromic film for smart windows, Materials Today Physics 13 (2020) 100205.
[109] A. Handbook, Fundamentals 2001, ASHRAE, Atlanta, USA (2001).
[110] R. Eymard, T. Gallouët, R. Herbin, Finite volume methods, Handbook of numerical analysis 7 (2000) 713-1018.

[111] https://maps.nrel.gov/nsrdb-viewer/.
[112] X. Zhao, S.A. Mofid, M.R. Al Hulayel, G.W. Saxe, B.P. Jelle, R. Yang, Reduced-scale hot box method for thermal characterization of window insulation materials, Applied Thermal Engineering 160 (2019) 114026.
[113] C.-W. Nan, R. Birringer, D.R. Clarke, H. Gleiter, Effective thermal conductivity of particulate composites with interfacial thermal resistance, Journal of Applied Physics 81(10) (1997) 6692-6699.
[114] X.-H. Li, C. Liu, S.-P. Feng, N.X. Fang, Broadband Light Management with Thermochromic Hydrogel Microparticles for Smart Windows, Joule (2018).
[115] C. Riordan, R. Hulstron, What is an air mass 1.5 spectrum?(Solar cell performance calculations), IEEE Conference on Photovoltaic Specialists, IEEE, 1990, pp. 1085-1088.
[116] S.-Y. Li, G.A. Niklasson, C.-G. Granqvist, Nanothermochromics: calculations for VO 2 nanoparticles in dielectric hosts show much improved luminous transmittance and solar energy transmittance modulation, Journal of Applied Physics 108(6) (2010) 063525.
[117] M.F. Modest, Radiative heat transfer, Academic press2013.
[118] C.-Y. Zhu, Z.-Y. Li, H.-Q. Pang, N. Pan, Design and optimization of core/shell structures as highly efficient opacifiers for silica aerogels as high-temperature thermal insulation, International Journal of Thermal Sciences 133 (2018) 206-215.
[119] X.-D. Wang, D. Sun, Y.-Y. Duan, Z.-J. Hu, Radiative characteristics of opacifier-loaded silica aerogel composites, Journal of non-crystalline solids 375 (2013) 31-39.
[120] R. Ricciu, L.A. Besalduch, A. Galatioto, G. Ciulla, Thermal characterization of insulating materials, Renewable and Sustainable Energy Reviews (2017).
[121] M. Ozel, Influence of glazing area on optimum thickness of insulation for different wall orientations, Applied Thermal Engineering 147 (2019) 770-780.
[122] A. Gounni, M.T. Mabrouk, M. El Wazna, A. Kheiri, M. El Alami, A. El Bouari, O. Cherkaoui, Thermal and economic evaluation of new insulation materials for building envelope based on textile waste, Applied Thermal Engineering 149 (2019) 475-483.
[123] F. Asdrubali, G. Baldinelli, Thermal transmittance measurements with the hot box method: Calibration, experimental procedures, and uncertainty analyses of three different approaches, Energy and buildings 43(7) (2011) 1618-1626.
[124] S. Yuan, G. Russell, W. Goss, Uncertainty analysis of a calibrated hot box, Insulation Materials: Testing and Applications: 4 th Volume, ASTM International2002.
[125] L.I.C. Sandberg, T. Gao, B.P. Jelle, A. Gustavsen, Synthesis of hollow silica nanospheres by sacrificial polystyrene templates for thermal insulation applications, Advances in Materials Science and Engineering 2013 (2013).
[126] F. Yohanala, R. Dewa, K. Quarta, W.S. Widiyastuti, Preparation of polystyrene spheres using surfactant-free emulsion polymerization, Modern Appl Sci 9 (2015) 121-126.
[127] B. Liu, Y. Wang, M. Zhang, H. Zhang, Initiator systems effect on particle coagulation and particle size distribution in one-step emulsion polymerization of styrene, Polymers 8(2) (2016) 55.
[128] D.-S. Yun, H.-S. Lee, H.-G. Jang, J.-W. Yoo, Controlling size and distribution for nano-sized polystyrene spheres, Bulletin of the Korean chemical society 31(5) (2010) 1345-1348.
[129] A.-T. Nguyen, C.W. Park, S.H. Kim, Synthesis of hollow silica by Stöber method with double polymers as templates, Bulletin of the Korean Chemical Society 35(1) (2014) 173-176.
[130] H.F. Gangåssæter, B.P. Jelle, S.A. Mofid, Synthesis of silica-based nano insulation materials for potential application in low-energy or zero emission buildings, Energy Procedia 122 (2017) 949-954.

[131] S. Eve, J. Mohr, Study of the surface modification of the PMMA by UV-radiation, Procedia Engineering 1(1) (2009) 237-240.
[132] M. Li, S. Magdassi, Y. Gao, Y. Long, Hydrothermal synthesis of VO2 polymorphs: advantages, challenges and prospects for the application of energy efficient smart windows, Small 13(36) (2017) 1701147.
[133] W. Li, S. Ji, Y. Li, A. Huang, H. Luo, P. Jin, Synthesis of VO 2 nanoparticles by a hydrothermal-assisted homogeneous precipitation approach for thermochromic applications, Rsc Advances 4(25) (2014) 13026-13033.
[134] R. Li, S. Ji, Y. Li, Y. Gao, H. Luo, P. Jin, Synthesis and characterization of plate-like VO2 (M)@ SiO2 nanoparticles and their application to smart window, Materials Letters 110 (2013) 241-244.
[135] D. Zhao, X. Qian, X. Gu, S.A. Jajja, R. Yang, Measurement techniques for thermal conductivity and interfacial thermal conductance of bulk and thin film materials, Journal of Electronic Packaging 138(4) (2016).
[136] I. Abdulagatov, Z. Abdulagatova, S. Kallaev, A. Bakmaev, P. Ranjith, Thermal-diffusivity and heat-capacity measurements of sandstone at high temperatures using laser flash and DSC methods, International Journal of Thermophysics 36(4) (2015) 658-691.
[137] T.-W. Lian, A. Kondo, M. Akoshima, H. Abe, T. Ohmura, W.-H. Tuan, M. Naito, Rapid thermal conductivity measurement of porous thermal insulation material by laser flash method, Advanced Powder Technology 27(3) (2016) 882-885.
[138] J. Zajas, P. Heiselberg, Determination of the local thermal conductivity of functionally graded materials by a laser flash method, International Journal of Heat and Mass Transfer 60 (2013) 542-548.
[139] A. International, ASTM D1003-13-Standard Test Method for Haze and Luminous Transmittance of Transparent Plastics, ASTM International West Conshohocken, 2013.
[140] C.F. Bohren, D.R. Huffman, Absorption and scattering of light by small particles, John Wiley & Sons2008.
[141] M.M. Qazilbash, M. Brehm, B.-G. Chae, P.-C. Ho, G.O. Andreev, B.-J. Kim, S.J. Yun, A. Balatsky, M. Maple, F. Keilmann, Mott transition in VO2 revealed by infrared spectroscopy and nano-imaging, Science 318(5857) (2007) 1750-1753.
[142] M.A. Hussein, R.M. El-Shishtawy, B.M. Abu-Zied, A.M. Asiri, The impact of cross-linking degree on the thermal and texture behavior of poly (methyl methacrylate), Journal of Thermal Analysis and Calorimetry 124(2) (2016) 709-717.

Article I

Bjørn Petter Jelle, Bente Gilbu Tilset, Tao Gao, Mathieu Grandcolas, Ole Martin Løvvik, Rolf Andre Bohne, Sohrab Alex Mofid, Serina Ng and Espen Sagvolden, **High-performance nano insulation materials for energy-efficient buildings**, Proceedings of TechConnect World Innovation Conference 2017, *TechConnect, 2017*.

High-Performance Nano Insulation Materials for Energy-Efficient Buildings

Bjørn Petter Jelle [ab]*, Bente Gilbu Tilset [c], Tao Gao [a], Mathieu Grandcolas [c], Ole Martin Løvvik [cd], Rolf André Bohne [a], Sohrab Alex Mofid [a], Serina Ng [b] and Espen Sagvolden [c]

[a] Norwegian University of Science and Technology (NTNU),
Department of Civil and Environmental Engineering, NO-7491 Trondheim, Norway.
[b] SINTEF Building and Infrastructure,
Department of Materials and Structures, NO-7465 Trondheim, Norway.
[c] SINTEF Materials and Chemistry,
Department of Materials and Nanotechnology, NO-0314 Oslo, Norway.
[d] University of Oslo (UiO),
Department of Physics, NO-0371 Oslo, Norway.
* Corresponding author: bjorn.petter.jelle@sintef.no (e-mail), +47-73593377 (phone).

ABSTRACT

High-performance nano insulation materials (Hi-Per NIM) may be developed by exploiting the Knudsen effect for reduced thermal conductivity and thus making air-filled nanoporous thermal insulation materials with a nanoporous air-filled structure. NIMs with very low thermal conductivity values will enable the use of normal or thin wall thicknesses in energy-efficient buildings. Especially for energy renovation of existing buildings, the reduced insulation thickness is of high interest. This study will present an exploration of attempting to achieve NIMs through experimental laboratory development of hollow silica nanospheres (HSNS), hollow silica nanofibres (HSNF) and hollow silica integrated nanospheres and nanofibres, alongside theoretical modelling and sustainability investigations.

Keywords: nano insulation material, NIM, hollow silica nanosphere, hollow silica nanofibre, thermal conductivity.

1 INTRODUCTION

Two state-of-the-art thermal insulation solutions and materials are vacuum insulation panels (VIP) and aerogel-based materials [1-3]. Fresh VIPs can have a thermal conductivity as low as 4 mW/(mK), while various aerogel products typically have thermal conductivity values between 12 - 18 mW/(mK) at ambient pressure. Both can be used for insulating e.g. buildings, pipelines and storage tanks, but both also have serious drawbacks.

The efficiency of a VIP will be dramatically reduced if the enclosing foil is broken, resulting in loss of vacuum. Hence, VIPs cannot be cut and fitted on the building site, and perforation with e.g. a nail would be detrimental. In addition, diffusion of air and moisture through the VIP foil into the VIP core will with time increase the thermal conductivity due to loss of vacuum (up to 20 mW/(mK) when punctured and full loss of vacuum). This drawback is partly solved for aerogels. They are highly porous nanomaterials where the gas thermal conductivity is reduced due to the small size of the internal pores. Aerogels may be more user-friendly than VIPs, but they exhibit substantially higher thermal conductivities, and dust formation can be a problem. Their areas of use are limited by high manufacturing costs and poor mechanical strength.

A *key challenge* is therefore to develop environmentally friendly high-performance insulation materials with superior mechanical properties, lower thermal conductivity and lower cost than the currently available aerogel products, which is the overall aim of the *High-Performance Nano Insulation Materials (Hi-Per NIM)* project presented herein. The current status of our attempts to develop nano insulation materials (NIM) by the sacrificial template method producing hollow silica nanospheres (HSNS) will be given. Moreover, challenges and opportunities related to possible development of hollow silica nanofibres (HSNF) and combinations of HSNS and HSNF will also be treated. Finally, some aspects regarding theoretical modelling and environmental impact of NIM will be illuminated.

2 THE KNUDSEN EFFECT

The thermal transport through a porous material when exposed to a temperature gradient may be quantified by the material's total thermal conductivity λ_{tot} (W/(mK)), which may be represented as a sum of conductivities associated with the following different thermal transfer mechanisms:

$$\lambda_{tot} = \lambda_{sol} + \lambda_{gas} + \lambda_{rad} + \lambda_{conv} + \lambda_{coup} \quad (1)$$

where λ_{sol} is the solid state thermal conductivity, λ_{gas} is the gas thermal conductivity, λ_{rad} is the radiation thermal conductivity, λ_{conv} is the convection thermal conductivity, and λ_{coup} is the thermal conductivity coupling term accounting for second order effects. To minimize the thermal conductivity, the sum of the above contributions

must be minimized. The coupling effect can be rather complex. Theoretical approaches to thermal performance of VIPs usually assume this coupling effect to be negligible, see e.g. the study by Heinemann [4]. Gas convection will be negligible for porous materials with very small pores.

For VIPs, the difference between 4 W/(mK) (non-aged, pristine condition) and 20 mW/(mK) (punctured) of 16 mW/(mK) is due entirely to gas thermal conductivity (omitting any changes to the solid core due to the loss of vacuum). That is, the combined solid state and radiation thermal conductivity of fumed silica is as low as 4 mW/(mK) or in principle somewhat lower as there is still a very small concentration of air inside a VIP causing gas conduction. Hence, as it is possible to make materials with such a very low solid state and radiation conductivity, there are rather good opportunities to make a high-performance thermal insulation material functioning at atmospheric pressure by lowering the gas thermal conductivity.

Thus, the stage is set for the opportunities to exploit the Knudsen effect, where the gas thermal conductivity $\lambda_{gas+gas/solid}$, also including the gas and solid state pore wall interaction, may be written in a simplified way as [1,2,5]:

$$\lambda_{gas+gas/solid} = \frac{\lambda_{gas,0}}{1+2\beta Kn} = \frac{\lambda_{gas,0}}{1+\frac{\sqrt{2}\beta k_B T}{\pi d^2 p \delta}} \quad (2)$$

where $\lambda_{gas,0}$ is the gas thermal conductivity in the pores at STP (standard temperature and pressure) (W/(mK)), β is a coefficient characterizing the molecule-wall collision energy transfer (in)efficiency (between 1.5 - 2.0), k_B is the Boltzmann's constant ($1.38 \cdot 10^{-23}$ J/K), T is the temperature (K), d is the gas molecule collision diameter (m), p is the gas pressure in pores (Pa), δ is the characteristic pore diameter (m), σ_{mean} is the mean free path of gas molecules (m), and $Kn = \sigma_{mean}/\delta$ is the Knudsen number.

Hence, by decreasing the pore size within a material below a certain level, i.e. a pore diameter of the order of 40 nm or below for air, $\lambda_{gas+gas/solid}$ may become very low even with air-filled pores, i.e. where the mean free path of the gas molecules is larger than the pore diameter. The solid state and gas interaction is taken care of by the β coefficient in Eq.2. Thus, the resulting $\lambda_{gas+gas/solid}$, also including the gas and pore wall interaction, versus pore diameter, may be calculated in this simplified model [1,2].

3 EXPERIMENTAL RESULTS AND POSSIBLE PATHWAYS

3.1 Spheres, Fibres and Combinations

A possible pathway is to make NIMs by assembling hollow nanostructures. These structures can be hollow nanospheres (HNS) (Fig.1) or hollow nanofibres (HNF) (Fig.1), where both material systems show great promise in lowering the bulk thermal conductivity. Further improvement is expected by combining the two systems to form a nanocomposite, as depicted in Fig.1.

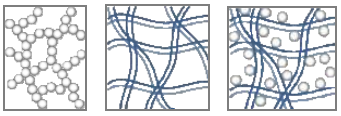

Figure 1. Schematic depiction of thermal insulation materials based on HNS (left), HNF (middle) and combined integrated HNS and HNF (right).

The material porosity must be optimized to reduce the solid contribution to thermal conductivity, i.e. shells must be thin, and still maintain strength to avoid sphere/fibre collapse. The distance between the hollow building blocks should be < 100 nm to minimize gas thermal conductivity.

Additional requirements for practical use include safe and easy handling and possibility for fitting on building site. Condensation of water within the pores must be avoided, thus the material should be hydrophobic.

3.2 Initial Experimental Pathways

Miscellaneous experimental pathways may be followed for manufacturing nanoporous thermal insulation materials by utilizing the Knudsen effect. Three of these are the membrane foaming, the internal gas release and the sacrificial template methods.

The membrane foaming method is using a membrane to prepare a foam with nanoscale bubbles, followed by hydrolysis and condensation of a precursor within bubble walls to make a solid structure. However, our initial membrane foaming attempts were not successful as the reaction was too slow and no suitable surfactant systems were found to stabilize alcohol-based foams. The internal gas release method uses a controlled decomposition or evaporation of a component to form nanobubbles in a liquid system, followed by formation of a solid shell along the bubble perimeter. Due to very demanding experimental conditions, work along this path has so far been terminated. The processes would require simultaneous formation of gas bubbles with a narrow size distribution throughout the reaction system, very homogeneous system temperature, rapid shell formation (before Ostwald ripening process), and extremely reactive chemicals requiring strict humidity control. Although experimental investigations along both the template foaming and internal gas release pathways have been abandoned so far, it should be noted that future experiments may prove different, though.

The sacrificial template method is based on the formation of a nanoscale liquid or solid structure, followed by reactions to form a solid shell along the template perimeter. The sacrificial template core is then chemically or thermally removed, thus resulting in a hollow sphere. In contrast to the two other methods, experimental work following the template method proved to be manageable and has provided interesting results.

3.3 Hollow Silica Nanospheres

The experimental work following the sacrificial template method has so far been concentrated on making hollow silica nanospheres (HSNS) by applying polyacrylic acid (PAA) and polystyrene (PS) as sacrificial templates, where the templates PAA and PS have been removed by a chemical washing and a heating process, respectively (the template materials diffusing and evaporating through the silica shell). Experimental procedures and details concerning various fabrications of HSNS are found in our earlier studies [6-8]. The principle behind the HSNS synthesis is illustrated in Fig.2 alongside scanning electron microscope (SEM) images of corresponding actual fabricated materials. Close resemblance between theoretical concepts and experimental practice is observed.

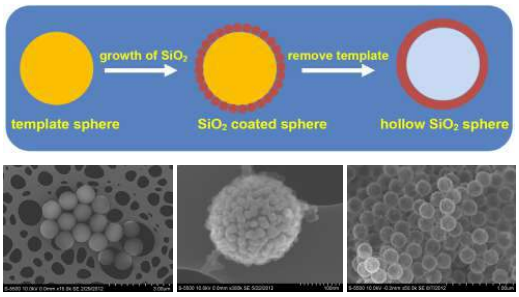

Figure 2. A principle drawing of the sacrificial template method for HSNS synthesis (top). SEM images (left to right) of PS templates, small silica particles coated around a spherical PS template, and HSNS after removal of PS.

The measured thermal conductivity for various powder samples of HSNS has typically been in the range 20 to 90 mW/(mK), though some uncertainties in the Hot Disk apparatus measurement method have to be clarified [9]. The specific powder packing of the HSNS in the bulk condition is also an issue to be addressed in this respect. Lowering the thermal conductivity is currently being attempted by a parameter variation and optimization of the hollow silica sphere inner diameter and wall (shell) thickness.

HNS materials must be hydrophobic in order to avoid water condensation, which is detrimental for thermal conductivity. Functionalization can be done during the production or structuring of HNS by adding hydrophobic silanes at appropriate steps in the reaction. It is also possible to apply a post-treatment, either by immersing the material in an impregnating bath or by gas phase transport of active components to external and internal surfaces.

3.4 Hollow Nanofibres

High-performance thermal insulation materials may also be achieved with hollow nanofibres (HNF). Structuring of HNF into a bulk material is expected to be less challenging than that for the HNS counterparts as long fibres tend to entangle together as depicted in Fig.1. This may also help to improve the corresponding mechanical strength compared to HNS based materials. Previous studies have revealed that the thermal conductivity of HNF is primarily dependent on their wall thickness [10], thus highlighting the importance of controlling the wall thickness of HNF through different experimental pathways. It is also reasonable that controlling other structural or compositional parameters, such as the wall materials and the packing manner/density of the HNF, would have an impact on the overall thermal conductivity of the resulting materials.

Several synthesis routes are available for HNF [11], such as self-assembly, electrospinning, and template-assisted approaches. Among these, the template-assisted method, which has also been used for the preparation of HNS, is considered to be specially promising, e.g. for control of the wall thickness. Various inorganic and organic nanofibres will be tested for use as template materials; in particular, the organic nanofibres may be produced via electrospinning, which is a continuous process well suited for up-scaling. It is important that for thermal insulation applications HNF materials must be hydrophobic to avoid water condensation. Surface functionalization methods similar to those used for HNS (in situ modification, liquid and gaseous post treatments) will be tested.

3.5 Sphere and Fibre Integration

Fibres are widely used to reinforce materials. Since the thermal conductivity of HNF is lower than that of their solid counterparts, HNF may be used as reinforcements for HNS-based NIMs as depicted in Fig.3, thus combining the advantages of HNS and HNF within one material.

Several methods are available for HNS-HNF composite synthesis. One possibility is to prepare dispersions of HNS and use them to impregnate HNF mats. Capillary forces during drying should be avoided by surface functionalization, proper solvent selection and well-controlled solvent removal to achieve evenly distribution of HNS throughout the HNF material.

Overall function and installation requirements will determine whether flexible foils are needed to support the HNS, HNF and/or composites (Fig.3). The foils could have several functions, e.g. provide mechanical support, prevent nanoparticulate dust during handling, control transport of water vapour and limit thermal radiation.

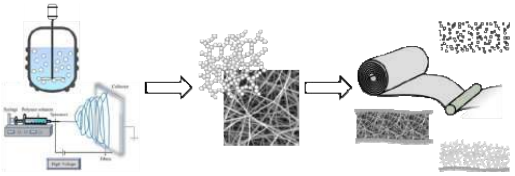

Figure 3. A possible schematic production route for low-density, hydrophobic, flexible NIM mats.

4 THEORETICAL MODELLING

Thermal properties of nanostructured materials are governed by processes at different scales. A decisive factor is the thermal conductivity of the solid phases, which is primarily limited by phonon scattering. Phonons are not only scattered by impurities and phonon-phonon interactions, but also when they reach the surfaces. Surface scattering may dominate at the nanometre scale. As a first estimate of these surface effects, we computed the thermal conductivity of a thin plate of α-quartz from first-principles quantum mechanics using the temperature dependent effective potential method [12-14]. The surface scattering was accounted for by using Minnich's approach [15]. A temperature range of 50 to 800 K was investigated. All underlying quantum mechanical computations were carried out using the PBE96 [16] density functional and the VASP program package [17]. The longer c-axis was assumed to lie in the plane, and thermal conductivity was studied along this axis. At 300 K the thermal conductivity is halved relative to bulk values when the film thickness is 4 nm. For more complex structures at more relevant size scales, Monte Carlo simulations may be used [18,19].

5 ENVIRONMENTAL IMPACT

Preliminary life cycle analysis (LCA) of NIM as HSNS has been carried out [6,7,20], and follow-up investigations are currently being conducted. Simplified health, safety and environmental (HSE) evaluations will be actively used to evaluate the sustainability and safety of possible production routes. Initial evaluations will be based on comparisons of chemical and environmental properties of alternative reactants, solvents, by-products and products associated with material production. Detailed HSE evaluation of the most promising materials and production routes will be carried out. The aim is to reduce risks associated with all stages of the materials' life cycle: Material production, use and end-of-life waste management and recycling, including safety measures for industrial production, which may differ from those for laboratory scale synthesis.

Full LCA will be performed as a part of selecting the most promising production routes. The assessment will include energy and material consumption, emissions of heat, emissions to air and water, and solid waste, in addition to the product. Then we will assess thermal conductivity and durability for the completion of the LCA, and compare the NIMs with conventional thermal insulation products.

6 CONCLUSIONS

In the on-going quest for high-performance nano insulation materials, hollow nano spheres and fibres and their possible integration represent promising stepping-stones towards developing new thermal insulation materials. Important issues being addressed are chemical synthesis and optimization, theoretical models for thermal transport, health, safety, environmental aspects and life cycle assessment.

ACKNOWLEDGEMENTS

This work has been supported by the Research Council of Norway within the Nano2021 program through the SINTEF and NTNU research project ”High-Performance Nano Insulation Materials” (Hi-Per NIM).

REFERENCES

[1] B.P. Jelle, A. Gustavsen and R. Baetens, *Journal of Building Physics*, **34**, 99-123, 2010.
[2] B.P. Jelle, *Energy and Buildings*, **43**, 2549-2563, 2011.
[3] S.E. Kalnæs and B.P. Jelle, *Applied Energy*, **116**, 355-375, 2014.
[4] U. Heinemann, *International Journal of Thermophysics*, **29**, 735-749, 2008.
[5] M.G. Kaganer, ”Thermal insulation in cryogenic engineering”, IPST Press, 1969 (Russian version 1966).
[6] T. Gao, B.P. Jelle, L.I.C. Sandberg and A. Gustavsen, *ACS Applied Materials and Interfaces*, **5**, 761-767, 2013.
[7] T. Gao, L.I.C. Sandberg and B.P. Jelle, *Procedia CIRP*, **15**, 490-495, 2014.
[8] L.I.C. Sandberg, T. Gao, B.P. Jelle and A. Gustavsen, *Advances in Materials Science and Engineering*, **2013**, 6 pages, Article ID 483651, 2013.
[9] B.P. Jelle, T. Gao, L.I.C. Sandberg, B.G. Tilset, M. Grandcolas and A. Gustavsen, *International Journal of Structural Analysis and Design*, **1**, 43-50, 2014.
[10] T. Gao and B.P. Jelle, *The Journal of Physical Chemistry C*, **117**, 1401-1408, 2013.
[11] T. Kijima, ”Inorganic and metallic nanotubular materials: Recent technologies and applications”, Springer, Heidelberg, 2010.
[12] O. Hellman, I.A. Abrikosov and S.I. Simak, *Physical Review B*, **84**, 180301(R) (4 pages), 2011.
[13] O. Hellman, P. Steneteg, I.A. Abrikosov and S.I. Simak, *Physical Review B*, **87**, 104111 (8 pages), 2013.
[14] O. Hellman and I.A. Abrikosov, *Physical Review B*, **88**, 144301 (5 pages), 2013.
[15] A.J. Minnich, *Applied Physics Letters*, **107** 183106 (4 pages), 2015.
[16] J.P. Perdew, K. Burke, and M. Ernzerhof, *Physical Review Letters*, **77**, 3865-3868, 1996.
[17] G. Kresse and J. Furthmüller, *Physical Review B*, **54** 11169-11186, 1996.
[18] J.-P.M. Péraud and N.G. Hadjiconstantinou, *Physical Review B*, **84**, 205331 (15 pages), 2011.
[19] N.G. Dou and A.J. Minnich, *Applied Physics Letters*, **108**, 011902 (4 pages), 2016.
[20] R.D. Schlanbusch, B.P. Jelle, L.I.C. Sandberg, S.M. Fufa and T. Gao, *Building and Environment*, **80**, 115-124, 2014.

Article II

Haakon Fossen Gangåssæter, Bjørn Petter Jelle, Sohrab Alex Mofid and Tao Gao, **Air-filled nanopore based high-performance thermal insulation materials**, *Energy Procedia* 132 (2017) pp 231-236.

Available online at www.sciencedirect.com

ScienceDirect

Energy Procedia 132 (2017) 231–236

Energy Procedia

www.elsevier.com/locate/procedia

11th Nordic Symposium on Building Physics, NSB2017, 11-14 June 2017, Trondheim, Norway

Air-Filled Nanopore Based High-Performance Thermal Insulation Materials

Haakon Fossen Gangåssæter[a*], Bjørn Petter Jelle[ab], Sohrab Alex Mofid[a], Tao Gao[a]

[a]*Norwegian University of Science and Technology (NTNU), Department of Civil and Environmental Engineering, NO-7491 Norway.*
[b]*SINTEF Building and Infrastructure, Department of Materials and Structures, NO-7465 Trondheim, Norway.*

Abstract

State-of-the-art thermal insulation solutions like vacuum insulation panels (VIP) and aerogels have low thermal conductivity, but their drawbacks may make them unable to be the thermal insulation solutions that will revolutionize the building industry regarding energy-efficient building envelopes. Nevertheless, learning from these materials may be crucial to make new and novel high-performance thermal insulation products. This study presents a review on the state-of-the-art air-filled thermal insulation materials for building purposes, with respect to both commercial and novel laboratory developments. VIP, even if today's solutions require a core with vacuum in the pores, are also treated briefly, as they bear the promise of developing high-performance thermal insulation materials without the need of vacuum. In addition, possible pathways for taking the step from today´s solutions to new ones for the future using existing knowledge and research are discussed. A special focus is made on the possible utilization of the Knudsen effect in air-filled nanopore thermal insulation materials.

Peer-review under responsibility of the organizing committee of the 11th Nordic Symposium on Building Physics.

Keywords: High-performance thermal insulation; Nano insulation material; NIM; Aerogel; Vacuum insulation panel; VIP.

1. Introduction

Immediate priorities and future goals will need to reflect the enhanced energy efficiency options combined with a decarbonized power sector that may reduce the CO_2 emission in the building sector. However, given constraints on

* Corresponding author. Tel.: +47 922 03 869.
E-mail address: haakonfg@stud.ntnu.no

1876-6102
Peer-review under responsibility of the organizing committee of the 11th Nordic Symposium on Building Physics
10.1016/j.egypro.2017.09.760

resources there is a call to focus more on efficient building envelopes to keep energy use down. The building envelope determines the amount of energy needed to heat and cool a building, and hence needs to be optimized to keep heating and cooling loads to a minimum. The importance of heating and cooling in total building energy use is very diverse with this share varying between 20% and 80%. Thus, thermal insulation with significantly lower thermal conductivity may contribute largely to an increased thermal resistance and hence an overall reduced energy consumption in buildings.

This study starts with giving an overview of the theoretical background of the process of heat conduction in thermal insulation materials applied in building envelopes, which helps developing an understanding of how such materials behave when used to achieve improved insulation properties. Furthermore, the study demonstrates the theoretical principle by utilizing the Knudsen effect for reduced thermal gas conductance in nanopores that has considerable impact on the overall thermal conductivity.

Secondly, this study presents the state-of-the-art solutions for building purposes, e.g. aerogels and vacuum insulation panels, discussing both benefits and drawbacks. The solutions are investigated with respect to both commercially available products and the global research front, and all property values are retrieved from sources late 2016. The final part will offer some recommendations and ideas on the direction in which the development could proceed, providing a pathway to further advance towards the goal of achieving the improved thermal insulation materials of tomorrow with a substantially lowered thermal conductivity value utilizing the Knudsen effect.

2. Heat transfer in materials

All materials have specific properties when it comes to conduction of heat, and this is irrespective to whether one are looking at solids, liquids or gases. Heat flows spontaneously from a higher temperature body to a lower temperature body, and this will happen as a result of solid state and gas conduction, radiation and convection [1]. The relation between the different contributions are often described as in the following [2]:

$$\lambda_{total} = \lambda_{solid} + \lambda_{gas} + \lambda_{rad} + \lambda_{conv} + \lambda_{coup} + \lambda_{leak} \quad (1)$$

where λ_{solid} is solid state conductivity, λ_{gas} is gas conductivity, λ_{rad} is radiation conductivity, λ_{conv} is convection conductivity, λ_{coup} is conductivity due to coupling effects between the other terms in Eq.1, and λ_{leak} is (air) leakage thermal conductivity.

In addition, it is important to identify which of the terms contribute most to the thermal transport. As we will see later for vacuum insulation panels (VIP), the gas conduction part is very large and the most dominant when the VIP is punctured.

3. The Knudsen effect

Conventional thermal insulation materials are produced so the effects of conduction, radiation and convection are minimized. Using low-radiative surfaces and porous structures reduces radiation, convection and solid conduction, but due to the size of the pores and the open-porous material, the gaseous thermal conduction is limited to the conductivity of air [3]. A solution to this is to utilize the Knudsen effect. This effect is explained by the equations in the following, and implies that a reduction of the pore size in the material to the nano range will effectively reduce the thermal conductivity [4]:

$$\lambda_{gas} = \frac{\lambda_{gas,0}}{1+2\beta Kn} \quad (2)$$

where

$$Kn = \frac{\sigma_{mean}}{\delta} = \frac{k_B T}{\sqrt{2}\pi d^2 p \delta} \quad (3)$$

where λ_{gas} is a combination of thermal conductivity of the gas inside the pores on nanoscale and the energy transfer when molecules collide with pore walls (the latter from the β factor), $\lambda_{gas,0}$ is the thermal conductivity for air at standard

temperature and pressure (STP), β is a unitless number between 1.5 and 2.0 which describes the (in)efficiency of energy transfer between molecules and pore walls when colliding [5], Kn is the Knudsen number, σ_{mean} is the mean free path of gas molecules, δ is the pore size of the material, d is the collision diameter of the gas molecules, p is the gas pressure inside the pores, k_B is the Boltzmann's constant, and T is the temperature [6]. It is clear from Eq.2 and 3 that for pores only a few nanometres in diameter the Knudsen number becomes large. This results in a low λ_{gas}. For example, a material with pore size of about 100 nm would achieve a λ_{gas} of somewhat below 8 mW/(mK). Note that the value for stagnant air at STP is 26 mW/(mK) [6].

The Knudsen effect is achieved when the pores have a dimension comparable or smaller than the mean free path of the gas molecules inside the pores. Knowing how to utilize and exploit the Knudsen effect will be very important in the development of high-performance thermal insulation materials based on air-filled pores for building applications.

4. Thermal insulation materials

Materials used as thermal insulation in buildings try to benefit from solutions that create products with low thermal conductivity. This can be achieved by reducing one or several of the contributions shown in Eq.1. In mineral wool, i.e. glass and rock wool products, such a reduction is achieved by bounding fibres together with the use of suitable resins, hence creating complex pore structures with limited/obstructed ways for heat transfer through the material [7]. Manufacturers have come a long way in creating porous materials with low thermal conductivities, e.g. mineral wool products with thermal conductivity values down to 32 mW/(mK).

The drawback with these materials appear together with the higher requirements to thermal insulation in buildings. For example, to achieve a U-value of e.g. 0.22 W/(m^2K) (minimum requirement for wall insulation in Norway per 26th of November 2016 [8]) with a standard mineral wool material, a thickness of approximately 150 mm is needed. For low-energy or zero emission buildings the requirements are even lower U-values. This may result in an insulation layer of more than 250 mm in thickness, which hence takes up valuable space and introduces challenges with convection between the wind and vapour barrier enclosing the insulation layer.

An increased research in the field of thermal building insulation materials have resulted in new materials with better performance in some areas. Aerogels and VIP are examples of materials that have noticeably lower thermal conductivity values [7].

4.1 Aerogels

Aerogels were discovered in 1931 by Samuel S. Kistler and are a silica gel where all the liquid components are replaced by air through a complex drying process. The remaining material creates a nanoporous structure with low thermal conductivity [9]. The solid thermal conductivity of silica is relatively high, but the silica aerogel has only a small fraction of solid silica. With a good purity and production method pore sizes of 5 to 70 nm are possible, where the air-filled pores will take up between 85 to 99.8% of the volume [4]. Pure aerogels have a low thermal conductivity typically between 12-20 mW/(mK).

Aerogels are constantly being developed, both regarding the production process and the final material product itself. Challenges with the material for building purposes have been inherent low density and thus high fragility, which complicates the handling process without fracturing the aerogel products. Therefore numerous different composites have been made in order to create a more robust material [10]. Mineral wool and aerogel have been mixed, with a resultant thermal conductivity of 19 mW/(mK) [7]. Hayase et al. report a development of another composite aerogel with a density of 20 kg/m^3 and a thermal conductivity of 15 mW/(mK) [11]. Also note that as aerogels may be produced as either opaque, translucent or transparent materials, these products may be used for several different building applications, e.g. in opaque walls, translucent solar walls or glazing systems and transparent windows or glazing systems. Table 1 gives an overview of the findings of several different variants of aerogels and their characteristics.

Table 1. Examples of aerogels, listed with important characteristics.

Aerogel	Density (kg/m^3)	Thermal conductivity (mW/(mK))

Stone wool and aerogel [7]	-	19
Polymethylsilsesquioxane-cellulose nanofibre bicomposite aerogels [11]	20	15
Aramid fibre reinforced silica aerogel [10]	150	22.7
Monolithic silica aerogels [12]	-	≈ 13

4.2 Vacuum insulation panels

Vacuum insulation panels (VIP) consist of a multilayer envelope that encloses an open-porous material, also known as the VIP core. To increase the thermal resistance of the panel, vacuum is formed inside the core [7]. The core material could consist of glass fibre, open-cell polyurethane foam, open-cell polystyrene foam, precipitated silica or aerogel. For achieving the lowest thermal conductivity, precipitated silica, fumed silica or aerogel should be used [13]. Numerous VIP are produced, and many of them can be purchased on the market from various suppliers [14].

VIP have several challenges that may make it difficult for them to become the thermal insulation material of the future. One of the main disadvantages is to keep the vacuum intact. This makes it hard to adapt panels at the building site, and the risk of punctures is always present. Thus, the VIP must be handled carefully [15]. Furthermore, the VIP envelope creates a thermal bridging effect [16]. A solution to reduce this problem is to put double, overlapping layers of panels, but this creates more work and higher material usage. Another problem with the envelope is that it is not absolutely air and vapour tight, thus air and water vapour will diffuse into the core as time passes, hence reducing the insulation performance substantially over time. Research is being carried out on how to create better envelopes with respect to the tightness. However, for most of these there will still be a diffusion process of air and water vapour through the VIP envelope and into the VIP core, which may be decreased but not fully stopped.

If the panel is perforated, the core material will still have a rather low thermal conductivity, i.e. VIP with an air-filled fumed silica core will have a thermal conductivity of around 20 mW/(mK). Note then that the difference between 4 mW/(mK) (pristine condition) and 20 mW/(mK) (punctured) of 16 mW/(mK) is due entirely to gas thermal conductivity (not considering any changes to the solid due to loss of vacuum). That is, the combined solid state and radiation thermal conductivity of fumed silica is as low as 4 mW/(mK) or in principle lower (as there is still a very small concentration of air inside a VIP, a small part of the 4 mW/(mK) value is due to gas conduction). Hence, as it is possible to make materials with such a very low solid state and radiation conductivity, lowering the gas thermal conductivity should be a good opportunity to make an air-filled nanopore based high-performance thermal insulation material at atmospheric pressure.

5. Thermal insulation materials of the future

Aerogel and VIP have very good characteristics as insulating materials for buildings. Low thermal conductivity results in both space and energy saving solutions. Much research has been carried out in recent years to improve structural properties of both materials, e.g. making aerogel more robust with the use of different fibres and try different core solutions for VIP. Both materials are commercially available for purchase from several suppliers, and represent some of the best alternatives for building insulators on the market today. However, as mentioned earlier, there remains several stumbling-blocks to a future widespread use of such materials as main insulators in buildings.

As seen in VIP and aerogels, low thermal conductivity values are possible to achieve with the materials already available when using lowered (near-vacuum) pressures. Once the low thermal conductivity values have been achieved, the most important issue in choosing insulators remains to be the long-term thermal performance. The concept of nano insulation materials (NIM) seem to represent a leap forward for the next generation of thermal insulation materials. One such example is found through the studies conducted by Gao et al. [12,17], Jelle et al. [5] and Sandberg et al. [6] where hollow silica nanospheres (HSNS) may be a possible foundation or stepping-stone for the development of the NIM of tomorrow. One distinctive advantage of HSNS NIM over conventional thermal insulators is the controllability of thermal properties by modifying their structural parameters like e.g. particle size, porosity, inner diameter and shell thickness. HSNS utilize physical principles such as the Knudsen effect to reduce the thermal conductivity of the material to a minimum. Nevertheless, it must be noted that turning the laboratory-made HSNS NIM into practical thermal insulation materials for building applications may require substantial research efforts dedicated to this field.

One may also imagine to apply hollow silica nanofibres (HSNF) in such NIMs, e.g. for increased mechanical strength purposes.

A thermal insulation material should be light-weight, and have a certain strength for transport and handling on the building site. Fibre reinforcing of aerogel is one principle that is well documented [10,11], and the right combination of fibre material and aerogel could result in a stronger and, at the same time, a material with a reduced thermal conductivity. Reinforcement often leads to a higher thermal conductivity, as seen from Table 1. Hence, a new material should consist of a homogenous, porous substance. To implement pores in already uniform materials would be an interesting research topic. Possible ways to perform this could be to implement closed pores individually using small valves or by implementing a membrane with holes of the desired size (which is removed at a later stage). Another solution may be to create a material that becomes open-porous when inflated. An inflation process, e.g. by chemical means, from within a bulk material creating a closed nanopore structure could also be imagined and feasible in the future.

In summary, one may categorize some of the promising experimental methods into membrane foaming, internal gas release and sacrificial template methods. The membrane foaming method is using a membrane to prepare a foam with nanoscale bubbles, followed by hydrolysis and condensation of a precursor within bubble walls to make a solid structure. The internal gas release method uses a controlled decomposition or evaporation of a component to form nanobubbles in a liquid system, followed by formation of a solid shell along the bubble perimeter. The sacrificial template method is based on the formation of a nanoscale liquid or solid structure, followed by reactions to form a solid shell along the template perimeter. The sacrificial template core is then chemically or thermally removed, thus resulting in a hollow sphere. Scanning electron microscope (SEM) images of the different steps in the template method when synthesizing HSNS are depicted in Fig.1, where polystyrene (PS) is used as the sacrificial template material.

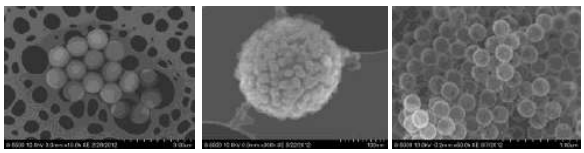

Figure 1. The different steps in the template method with SEM images (left to right) of PS templates, small silica particles coated around a spherical PS template, and HSNS after removal of PS.

6. Conclusions

There are many thermal insulation materials and solutions, both on the market and still at a research level. This study is briefly summarizing the information on today's high-performance thermal insulation for building applications. Aerogel and vacuum insulation panels (VIP) have several satisfying characteristics, such as low weight and low thermal conductivity. On the other hand, the challenges with brittle structures (aerogels) and loss of vacuum (VIP) will always be present with these solutions. Thus, risk of failures which then subsequently will lead to increased thermal conductivities and thus a higher heat transfer through the building envelope. The next generation of thermal insulation materials should be evolved so the various disadvantages are removed. A solution may be to manufacture a material with nanopores implemented by a controlled process.

Acknowledgements

This work has been supported by the Research Council of Norway within the Nano2021 program through the SINTEF and NTNU research project "High-Performance Nano Insulation Materials" (Hi-Per NIM).

References

[1] M. Pfundstein, R. Gellert, M.H. Spitzner, A. Rudolphi, 'Insulating materials: Principles, materials, applications', Birkhäuser, p. 112, 2008.

[2] B.P. Jelle, 'Traditional, state-of-the-art and future thermal building insulation materials and solutions -

Properties, requirements and possibilities', *Energy Build.*, **43**, 2549–2563, 2011.
[3] B. Notario, J. Pinto, E. Solorzano, J.A. de Saja, M. Dumon, M.A. Rodríguez-Pérez, 'Experimental validation of the Knudsen effect in nanocellular polymeric foams', *Polymer*, **56**, 57–67, 2015.
[4] R. Baetens, B.P. Jelle, A. Gustavsen, 'Aerogel insulation for building applications: A state-of-the-art review', *Energy Build.*, **43**, 761–769, 2011.
[5] B.P. Jelle, T. Gao, L.I.C. Sandberg, B.G. Tilset, M. Grancolas, A. Gustavsen, 'Thermal superinsulation for building applications - From concepts to experimental investigations', *International Journal of Structural Analysis and Design*, **1**, 43–50, 2014.
[6] L.I.C. Sandberg, T. Gao, B.P. Jelle, A. Gustavsen, 'Synthesis of hollow silica nanospheres by sacrificial polystyrene templates for thermal insulation applications', *Adv. Mater. Sci. Eng.*, **2013**, Article ID 483651, 2013.
[7] S. Schiavoni, F. D'Alessandro, F. Bianchi, F. Asdrubali, 'Insulation materials for the building sector: A review and comparative analysis', *Renew. Sustain. Energy Rev.*, **62**, 988–1011, 2016.
[8] Kommunal- og moderniseringsdepartementet, 'Forskrift om tekniske krav til byggverk (Byggteknisk forskrift) (Technical building regulations)'. Lovdata, Oslo, p. 39, 2010.
[9] N. Shukla, A. Fallahi, J. Kosny, 'Aerogel thermal insulation - Technology review and cost study for building enclosure applications', *ASHRAE Trans.*, **120**, 294–307, 2014.
[10] Z. Li, X. Cheng, S. He, X. Shi, L. Gong, H. Zhang, 'Aramid fibers reinforced silica aerogel composites with low thermal conductivity and improved mechanical performance', *Compos. Part A Appl. Sci. Manuf.*, **84**, 316–325, 2016.
[11] G. Hayase , K. Kanamori, K. Abe, H. Yano, A. Maeno. H. Kaji, K. Nakanishi, 'Polymethylsilsesquioxane–cellulose nanofiber biocomposite aerogels with high thermal insulation, bendability, and superhydrophobicity', *ACS Appl. Mater. Interfaces*, **6**, 9466–9471, 2014.
[12] T. Gao, B.P. Jelle, L.I.C. Sandberg, A. Gustavsen, 'Thermal conductivity of monodisperse silica nanospheres', *Journal of Porous Media*, **18**, 941–947, 2015.
[13] M.A. Mujeebu, N. Ashraf, A.H. Alsuwayigh, 'Effect of nano vacuum insulation panel and nanogel glazing on the energy performance of office building', *Appl. Energy*, **173**, 141–151, 2016.
[14] S.E. Kalnæs, B.P. Jelle, 'Vacuum insulation panel products: A state-of-the-art review and future research pathways', *Appl. Energy*, **116**, 355-375, 2014.
[15] R. Baetens, B.P. Jelle, J.V. Thue, M.J. Tenpierik, S. Grynning, S. Uvsløkk, A. Gustavsen, 'Vacuum insulation panels for building applications: A review and beyond', *Energy Build.*, **42**, 147–172, 2010.
[16] F. Isaia, S. Fantucci, A. Capozzoli, M. Perino, 'Thermal bridges in vacuum insulation panels at building scale', *Proc. of the Institution of Civil Engineers - Engineering Sustainability*, **170**, 47-60, 2017.
[17] T. Gao, B.P. Jelle, L.I.C. Sandberg, A. Gustavsen, 'Monodisperse hollow silica nanospheres for nano insulation materials: Synthesis, characterization and life cycle assessment', *ACS Appl. Mater. Interfaces*, **5**, 761-767, 2013.

Article III

Haakon Fossen Gangåssæter, Bjørn Petter Jelle, Sohrab Alex Mofid, **Synthesis of silica-based nano insulation materials for potential application in low-energy or zero emission buildings**, *Energy Procedia* 122 (2017) pp 949-954.

Available online at www.sciencedirect.com

ScienceDirect

Energy Procedia 122 (2017) 949–954

Energy Procedia

www.elsevier.com/locate/procedia

CISBAT 2017 International Conference – Future Buildings & Districts – Energy Efficiency from Nano to Urban Scale, CISBAT 2017 6-8 September 2017, Lausanne, Switzerland

Sustainable Building Envelopes (Ecobuildings, Retrofit, Performance Gap)

Synthesis of Silica-Based Nano Insulation Materials for Potential Application in Low-Energy or Zero Emission Buildings

Haakon Fossen Gangåssæter[a*], Bjørn Petter Jelle[ab], Sohrab Alex Mofid[a]

[a]*Norwegian University of Science and Technology (NTNU), Department of Civil and Environmental Engineering, NO-7491 Norway.*

[b]*SINTEF Building and Infrastructure, Department of Materials and Structures, NO-7465 Trondheim, Norway.*

Abstract

Sacrificial polystyrene (PS) templates have been used for synthesis of silica-based nano insulation materials (NIM). The PS was synthesized by a simple procedure where parameters as polyvinylpyrrolidone/styrene ratio and potassium persulfate amount were adjusted. Thereafter the PS templates were coated with silica by using tetraethyl orthosilicate (TEOS). The time used for adding TEOS was varied to investigate the effect on how the silica particles attached to the PS surface and the resulting silica spheres. By modifying the process, different PS templates were obtained. The thermal conductivity was measured for hollow silica spheres originating from the coating process of 198 nm PS templates, and the results showed thermal conductivities around 38 mW/(mK) for long-time measurements (160-640 s). Controlled synthesis of this silica-based NIM might be a stepping-stone on the path to a new generation of high-performance thermal insulation materials with low thermal conductivity, which can be used in the building envelope of low-energy or zero emission buildings in the future.

Peer-review under responsibility of the scientific committee of the CISBAT 2017 International Conference – Future Buildings & Districts – Energy Efficiency from Nano to Urban Scale

Keywords: Nano insulation material; NIM; Knudsen effect; Zero emission building; ZEB

* Corresponding author. Tel.: +47 922 03 869.
E-mail address: haakonfg@hotmail.com

1876-6102
Peer-review under responsibility of the scientific committee of the CISBAT 2017 International Conference – Future Buildings & Districts – Energy Efficiency from Nano to Urban Scale
10.1016/j.egypro.2017.07.435

1. Introduction

Increased global attention is given to environment in general, and especially sustainable development and energy use in buildings. This is regarded, in order to reach the goal set by the Intergovernmental Panel on Climate Change of limiting the global warming to 2 °C compared to pre-industrial level [1], as an important focus.

The building sector is often called the 40 % sector since it uses approximately 40 % of the materials and energy world-wide, and in addition accounts for 40 % of the annual global emissions of greenhouse gases (GHG) [2]. An important factor of the total energy use in a building is determined by the needs for heating and cooling, that has a varying share between 20 % and 80 %. This energy use is dependent on the building envelope. Thus, thermal insulation with significantly lower thermal conductivity than what is commonly used today may contribute to an overall reduced energy consumption in the building sector.

Today's commonly used solutions such as mineral wool and high-performance products as aerogel and vacuum insulation panels (VIP) all have their drawbacks. Mineral wool has a relatively high thermal conductivity, while aerogels are brittle and expensive and a VIP has the risk of puncture and in any case the inevitable vacuum loss over time due to diffusion of air and moisture into the VIP core, which can increase the thermal conductivity up to ten times the initial value. These disadvantages make it interesting to work with developing a new generation of thermal insulation materials.

A promising path to follow is to create nano insulation materials (NIM), where the goal is to utilize the Knudsen effect to reduce the thermal conductivity substantially [3]. NIM is proposed to be a homogenous structure with an overall conductivity of less than 4 mW/(mK). The structure can be both open or closed nanoporous [4]. For a VIP, the difference in thermal conductivity from pristine condition (4 mW/(mK)) to punctured (20 mW/(mK)) is entirely due to loss of vacuum, and therefore related to gaseous thermal conductivity. The heat transport within an insulation material is complex, but as VIPs illustrate may the gaseous thermal conductivity be of considerable importance. Reducing the pore diameter to nanoscale in a material may significantly reduce the thermal conductivity. An insulation material with considerable lower thermal conductivity than most commonly used materials today may not only save energy, but also money and space in every step from production and transport to installation, due to less material used.

The objective of this work is to attempt to have a controlled production of silica-based nanospheres using sacrificial polystyrene templates. Silica is used for many applications such as in medicine, electronics and water treatment on nano scale, and is shown to be a controllable and robust material [5–8]. Investigations for use in building envelopes, especially as core materials in VIPs, have also been conducted [9,10]. During the synthesis, several parameters are investigated in order to state their importance for the final product. Both the inner diameter of the spheres and the shell thickness may affect the thermal conductivity, and these are dependent on the size of the polystyrene spheres and the coating procedure, respectively. For the coating process may the time used for adding tetraethyl orthosilicate (TEOS) be important for the shell thickness.

2. Synthesis of silica-based nano insulation materials

The synthesis is carried out principally as described by Sandberg et al. [11], but with some modifications. The experimental work is explained in the following. The results from the different steps in the synthesis is showed in Figure 1.

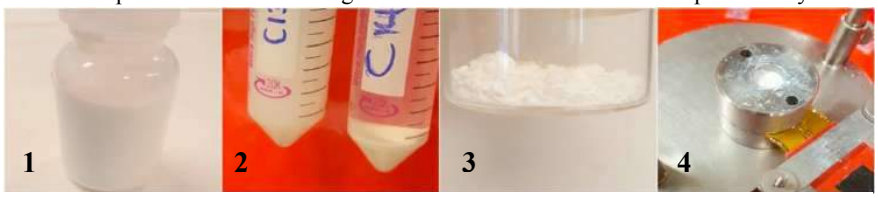

Figure 1: Results of the steps in the synthesis. The first and left photo shows the polystyrene templates produced (1), in the second photo the polystyrene spheres coated with silica particles are showed both before (left) and after (right) centrifuging (2), the third photo shows the dried silica spheres (3), and the fourth photo depicts the powder in the Hot Disk for measurement of thermal conductivity (4).

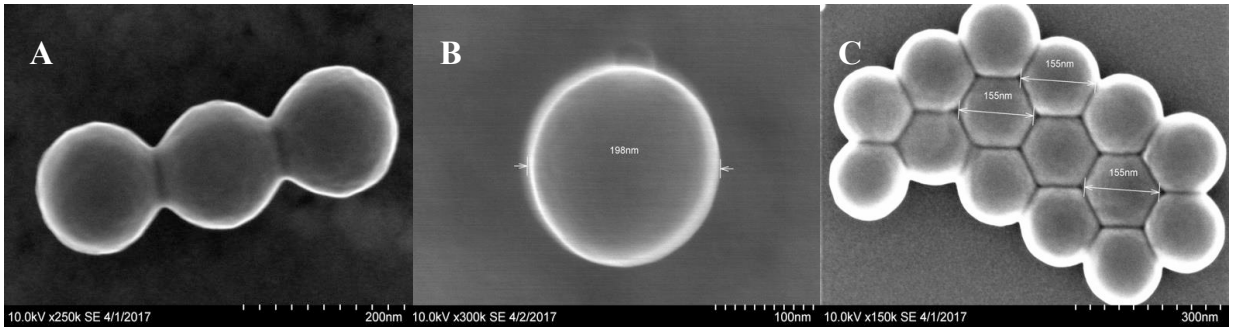

Figure 2: Scanning electron microscope (SEM) images of polystyrene templates A (160 nm), B (198 nm) and C (155 nm), dimensions referring to sphere diameter.

2.1. Materials

Polyvinylpyrrolidone (PVP), reagent grade styrene, potassium persulfate (KPS), tetraethyl orthosilicate (TEOS) as source for silica, ammonium hydroxide solution (NH_4OH, 28-30 wt%) and 96 % ethanol. Throughout the synthesis of the PS templates was distilled water used as a reaction medium.

2.2. Preparation of polystyrene templates

For the preparation of polystyrene (PS) templates, 10 g of styrene, 90 g of distilled water and a given amount of polyvinylpyrrolidone (PVP), were added in a single-neck round-bottom flask. The flask was immersed in an oil bath at 70 °C and magnetically stirred for 15 minutes before a KPS-water mixture (given amount of KPS in 10 g of distilled water) was added dropwise using a plastic pipette. The mixture was kept in the oil bath for approximately 24 hours, while magnetically stirred and heated at 70 °C. After this were the PS templates cooled down and stored at room temperature.

By varying the amount of KPS added, and the PVP/styrene-ratio, were different PS diameters achieved, see Table 1 and the scanning electron microscope (SEM) images in Figure 2.

Table 1: Average diameter of the polystyrene (PS) templates by varying the PVP/styrene-ratio and the amount of KPS.

Polystyrene sample	PVP/styrene-ratio	Amount of KPS (g)	Measured diameter (nm)
A	0.18	0.15	160
B	0.20	0.20	198
C	0.20	0.15	155

2.3. Coating of polystyrene templates

For coating of the PS spheres, 6 g of PS were added to 115 g of 96 % ethanol in a 500 ml round-bottom flask with extra horizontal opening for a syringe. The mixture was magnetically stirred at 500 rpm before 5 ml of NH_4OH was added. The flask was then closed with a ground glass stopper and vacuum grease to prevent evaporation. Then a 10 ml TEOS solution (5 ml TEOS and 5 ml 96 % ethanol) was added dropwise with the use of a syringe pump. The time used was adjusted to investigate possible changes. See Figure 3 for a photo of the setup. After the TEOS solution was added, the mixture was left over night while stirred. The solution was then centrifuged at 4500 rpm for 20 minutes to extract the silica coated PS templates. To remove the PS, was the sample dried at 475 °C for 12 hours.

Figure 3: TEOS solution added dropwise to the round bottom flask with the use of a syringe pump, a 10 ml syringe and a horizontal opening in the flask.

2.4. Characterization

Size and morphology were characterized using a Hitachi S-5500 scanning electron microscope (SEM), which also has a transmission electron microscope (TEM) mode. A small sample of the synthesized material was solved in ethanol and dripped onto a TEM grid. The ethanol was evaporated in air before the grid was inserted in the SEM.

Thermal conductivity of the NIM was measured by the use of Hot Disk TPS 2500 S Thermal Constant Analyser. The sensor used had a diameter of 6.403 mm.

3. Results and discussion

3.1. Polystyrene templates

The importance of the PVP/styrene ratio has been reported in several earlier publications [11,12]. Both size and monodispersity of the PS are dependent on this relation, but the effect is higher for smaller ratios [11]. This is shown by comparing sample A and C from this work, where the ratio was increased from 0.18 to 0.20 (≈ 11.1 %) and the diameter was reduced from 160 nm to 155 nm (≈ 3.2 %). For higher PVP/styrene ratios were there no monodispersity in the PS sample, which is important for creating a homogenous insulation material.

In this work, the effect of KPS was also investigated. It was found that for a PVP/styrene ratio of 0.20 and an increase in KPS, had a negative effect on the result. When increasing the amount of KPS from 0.15 to 0.20 (≈ 33.3 %), the diameter of the PS increased from 155 nm to 198 nm (≈ 27.7 %).

3.2. Coating of polystyrene templates

The time used for applying the TEOS solution for coating of the PS samples was adjusted in the range of 1–5 hours to investigate if the time had any effect, and the results showed that the time was not of significant importance.

More important is the surface characteristics of the PS sample. Since silica particles have a tendency of being in the negatively charged range will they not attach to the PS surface unless the PS surface is positively charged [13].

In Figure 4 one can see an SEM image of silica spheres produced by coating of PS sample B, which under investigation with SEM proved to be the most monodisperse material and was therefore used for measurement of thermal conductivity. For this image, the sacrificial polystyrene templates have been removed by drying the sample in the oven for 12 hours.

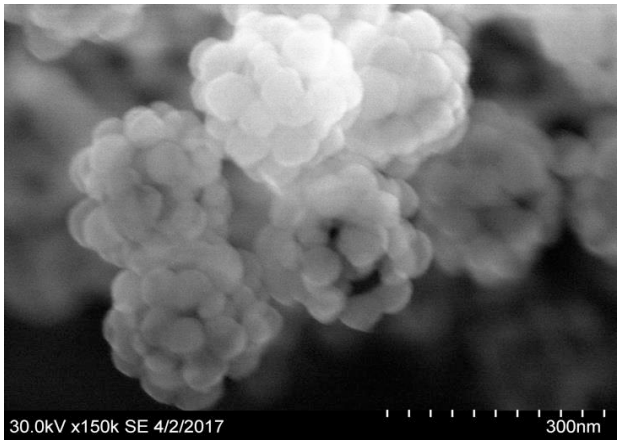

Figure 4: Scanning electron microscope (SEM) image of silica spheres produced by coating and drying of PS sample B.

3.3. Thermal conductivity measurements

The thermal conductivity measurements were carried out on silica spheres produced using the PS sample B as a sacrificial template. A SEM image can be seen in Figure 4. Four measurements were performed on the same sample where only the measurement time was varied. As seen in Table 2 the thermal conductivity was measured lower for longer measurement time. Since the start temperature (23 °C) and output power (50 mW) were the same for all the measurements it is assumed that the initial heating phase of the material has a minor role for longer measurements, hence the thermal conductivity measurement stabilizes in the range of 38 mW/(mK) over time. Naturally, for applications in building envelopes will these long-time measurement values represent the relevant performance. The value of 38 mW/(mK) is approximately 10 % higher than the lowest values for mineral wool in dry conditions (32-34 mW/(mK)) [14]. It is assumed that with smaller silica spheres, the exploitation of the Knudsen effect may be improved, thus lower thermal conductivity values may be obtained.

Table 2: Thermal conductivity measurements of insulation materials produced by coating of 198 nm PS spheres. The measurements were carried out by using a Hot Disk TPS 2500 S apparatus.

Measurement time (s)	Start temperature (K)	Output power (mW)	Thermal conductivity (mW/(mK))
80	296	50	42.1
160	296	50	38.9
320	296	50	38.0
640	296	50	37.9

An important notice for these measurements is that they are performed on the same sample, with the same packing density. The latter may affect the performance of the Hot Disk apparatus and alter the thermal conductivity measurements, and therefore also the obtained results. The influence of the packing density on the Hot Disk apparatus should be investigated in further studies.

4. Conclusions

The diameter of the polystyrene (PS) templates was adjusted by changes in the polyvinylpyrrolidone (PVP)/styrene ratio and potassium persulfate (KPS) amount used in the synthesis. A higher PVP/styrene ratio gave a smaller PS diameter, while an increase of KPS used gave an increase in the size of the PS templates.

For the coating process, it was discovered that the time used for adding the solution of tetraethyl orthosilicate (TEOS) and 96 % ethanol was not of significant importance and that the surface characteristics of the PS samples had a greater impact on the final results.

The thermal conductivity was measured to be in the range of 38 mW/(mK) when PS samples with sphere diameters of 198 nm were used. The thermal conductivity measurements were carried out over different time intervals, but on the same test sample with the same start temperature and the same output power for the Hot Disk TPS 2500 S apparatus. It is likely that the packing density of the silica powder can alter the thermal conductivity measurements in the Hot Disk apparatus. Hence, further studies should investigate the importance of this aspect.

Acknowledgements

This work has been supported by the Research Council of Norway within the NANO2021 program through the SINTEF and NTNU research project ”High-Performance Nano Insulation Materials” (Hi-Per NIM).

References

[1] IPCC. Climate change 2013 - The physical science basis, contribution of working group I to the fifth assessment report of the Intergovernmental panel on climate change. Cambridge, United Kingdom and New York, USA: Cambridge university press; 2013.
[2] Marszal AJ, Heiselberg P, Bourrelle JS, Musall E, Voss K, Sartori I, Napolitano A. Zero energy building – A review of definitions and calculation methodologies. Energy Build 2011;43:971–9.
[3] Notario B, Pinto J, Solorzano E, de Saja JA, Dumon M, Rodríguez-Pérez MA. Experimental validation of the Knudsen effect in nanocellular polymeric foams. Polymer (Guildf) 2015;56:57–67.
[4] Gao T, Sandberg LIC, Jelle BP, Gustavsen A. Nano insulation materials for energy efficient buildings: a case study on hollow silica nanospheres. vol. 1. 1st ed. Boca Raton, Florida: BrownWalker Press; 2012.
[5] Möller K, Bein T. Talented mesoporous silica nanoparticles. ACS - Chem Mater 2016;29:371–88.
[6] Mekaru H, Lu J, Tamanoi F. Development of mesoporous silica-based nanoparticles with controlled release capability for cancer therapy. Adv Drug Deliv Rev 2015;95:40–9.
[7] Fonoberov VA, Balandin AA. Phonon confinement effects in hybrid virus-inorganic nanotubes for nanoelectronic applications. Nano Lett 2005;5:1920–3.
[8] Montalti M, Prodi L, Rampazzo E, Zaccheroni N. Dye-doped silica nanoparticles as luminescent organized systems for nanomedicine. Chem Soc Rev 2014;43:4243–68.
[9] Li C, Li B, Pan N, Chen Z, Saeed MU, Xu T, Yang Y. Thermo-physical properties of polyester fiber reinforced fumed silica/hollow glass microsphere composite core and resulted vacuum insulation panel. Energy Build 2016;125:298–309.
[10] Shukla N, Fallahi A, Kosny J. Aerogel thermal insulation - Technology review and cost study for building enclosure applications. ASHRAE Trans 2014;120:294–307.
[11] Sandberg LIC, Gao T, Jelle BP, Gustavsen A. Synthesis of hollow silica nanospheres by sacrificial polystyrene templates for thermal insulation applications. Adv Mater Sci Eng 2013;2013:1–6.
[12] Cho Y-S, Shin CH, Han S. Dispersion polymerization of polystyrene particles using alcohol as reaction medium. Nanoscale Res Lett 2016;11:46:1–9.
[13] Nandiyanto ABD, Suhendi A, Ogi T, Umemoto R, Okuyama K. Size- and charge-controllable polystyrene spheres for templates in the preparation of porous silica particles with tunable internal hole configurations. Chem Eng J 2014;256:421–30.
[14] Abdou A, Budaiwi I. The variation of thermal conductivity of fibrous insulation materials under different levels of moisture content. Constr Build Mater 2013;43:533–44.

Article IV

Serina Ng, Bjørn Petter Jelle, Linn Ingunn Sandberg, Tao Gao and Sohrab Alex Mofid**, Hollow silica nanospheres as thermal insulation materials for construction: Impact of their morphologies as a function of synthesis pathways and starting materials**, *Construction and Building Materials,* 166 (2018) pp 72-80.

Construction and Building Materials 166 (2018) 72–80

Contents lists available at ScienceDirect

Construction and Building Materials

journal homepage: www.elsevier.com/locate/conbuildmat

Hollow silica nanospheres as thermal insulation materials for construction: Impact of their morphologies as a function of synthesis pathways and starting materials

Serina Ng [a,*], Bjørn Petter Jelle [a,b], Linn Ingunn Sandberg [b], Tao Gao [b], Sohrab Alex Mofid [b]

[a] SINTEF Building and Infrastructure, Department of Materials and Structures, NO-7465 Trondheim, Norway
[b] Norwegian University of Science and Technology (NTNU), Department of Civil and Environmental Engineering, NO-7491 Trondheim, Norway

HIGHLIGHTS

- Hollow silica nanospheres (HSNS) are promising thermal insulators for construction.
- Structural features, e.g. sizes and shell structures influence thermal conductivity.
- Formation of thermally insulating HSNS in general favoured by alkaline reaction.
- Synthesis route with tetraethyl orthosilicate (TEOS) was more robust.
- Water glass is a greener precursor for HSNS production.

ARTICLE INFO

Article history:
Received 21 March 2017
Received in revised form 15 November 2017
Accepted 8 January 2018
Available online 22 February 2018

Keywords:
Hollow silica nanosphere
HSNS
Nano insulation material
NIM
Thermal conductivity
Silica
Knudsen effect
Porosity
Green material

ABSTRACT

Hollow silica nanospheres (HSNS) show a promising potential to become good thermal insulators with low thermal conductivity values for construction purposes. The thermal conductivity of HSNSs is dependent on their structural features such as sizes (inner diameter and shell thickness) and shell structures (porous or dense), which are affected by the synthetic methods and procedures including reaction medium, polystyrene template, and silica precursor. Formation of thermally insulating HSNS was favoured by alkaline reaction, whereby highly porous silica shells were formed, promoting less silica per volume of material, thus a lower solid state thermal conductivity. The Knudsen effect is in general reducing the gas thermal conductivity including the gas and pore wall interaction for materials with pore diameters in the nanometer range, which is also valid for our HSNS reported here. Further decreasing the pore sizes would invoke a higher impact from the Knudsen effect. The additional insulating effect of the inter-silica voids (median diameter $D_{50} \approx 15$ nm) within the shell coating contributed also to the insulating properties of HSNS. The synthesis route with tetraethyl orthosilicate (TEOS) was more robust and produced more porous silica shells than the one with water glass (Na_2SiO_3, WG), although the latter might represent a greener synthetic method.

1. Introduction

According to the EU commission, heating and hot water alone account for 79% of total final energy use (192.5 Mtoe). While cooling is a fairly small share of total final energy use, demands from households and businesses such as food industry rise during the summer months. Therefore, in order to fulfil the EU's climate and energy goals of more than 20% energy savings by 2050, the heating and cooling sector must sharply reduce its energy consumption.

High-performance thermal insulation materials for buildings is one of the most direct methods to meet the demand of improved energy efficiency. Studies [1] have demonstrated that energy efficiency measures such as thermal insulation retrofit are the most cost-effective with respect to CO_2 emissions, whereas other measures e.g. solar photovoltaics and wind energy are far less cost-effective. Today, efforts are being put into moving from the common thermal insulation materials [2] to develop new materials with as low thermal conductivity as possible [3–9]. While this is the best solution for construction purposes, the current state-of-the-art thermal insulation materials are still in their infancy. Further work is needed before proper incorporation into the building industry could be achieved at an affordable cost.

* Corresponding author.
E-mail address: serina.ng@sintef.no (S. Ng).

https://doi.org/10.1016/j.conbuildmat.2018.01.054
0950-0618/

Both macro and micro scale developments have been conducted. The latest trend is to develop nanostructured thermal insulation materials, which can function and thermally insulate from the nano scale. A promising class of nanostructured thermal insulation materials are the nano-hybrid composite consisting of organic/inorganic particles and inorganic hollow particles. These materials have been investigated extensively in the context of chemistry and materials science. Principally, composite organic/inorganic particles can be classified as organic core with an inorganic shell or vice versa. Both polymer encapsulation of inorganic particles and coating of polymer particles with minerals can modify the properties of the precursor particles and lead to nanocomposite particles with tailored structures and morphologies [10,11]. Considerable research has been devoted to the preparation of mineral-coated polymer particles, and there are three main approaches: sol-gel nano-coating [12–16], hetero-coagulation [17] and layer-by-layer self-assembly [18]. By far, sol-gel synthesis is the most attractive for forming core-shell particles due to its ease of operation. Hollow nanospheres can be produced from hybrid nanoparticles, by extraction of the polymeric core through methods such as calcination, solvation, etc.

Among the different elements, silica is the most abundant chemical compound in the earth crust, most commonly found in nature as quartz and as the major constituent of sand. Its abundancy makes it a logical starting point material on the path to create nano insulation materials (NIM) for the future [19–21]. In parallel, our laboratory has been working on the development of new composite materials involving silica aerogel-concrete hybrids for both structural and thermal insulation properties so as to minimize the thickness of the material during construction [22–25]. Hollow silica nanospheres (HSNS) could potentially be a replacement material for silica aerogels. HSNS could also potentially be a replacement for thermal insulation materials such as expanded polystyrene (EPS) and extruded polystyrene (XPS), materials that may suffer from challenges related to fire, apart from their relatively large thermal conductivity values compared to silica aerogel [7].

This investigation thus aims to analyze the creation of thermally insulating hollow silica nanospheres (HSNS) for construction purposes. The current investigation is a follow-up on our investigations on the formation of HSNS based on a sacrificial polystyrene template and a silica precursor of tetraethyl orthosilicate (TEOS) [19–21]. We have previously shown that through such synthesis methods, thermally insulating materials with low thermal conductivity values of about 20–40 mW/(mK) can be produced [20,26], although the overall carbon footprint may be relatively high due to the use of organic silica precursor. It was then suggested that water glass (Na_2SiO_3, WG) can be an alternative for lowering the carbon footprint. The current investigation will thus explore the alternative synthesis route using water glass as the silica precursor. The synthesis of spherical polystyrene templates and formation of HSNS with TEOS will first be described to form the basis for a water glass based HSNS synthesis. Thereafter, a comparison of the differences in morphological formation of the silica network by applying TEOS and water glass as precursors will be discussed in relation to their thermal conductivity. The parameters affecting the formation, mode of formation and final product will be highlighted.

2. Materials and methods

2.1. Materials

Reagent grade styrene (St), polyvinvylpyrrolidone (PVP; Mw ≈ 40 k Da), potassium sulfate (KPS), ammonium hydroxide (NH_4OH, 28–30 wt%), tetraethyl orthosilicate (TEOS), ethanol (96%), water glass (sodium silicate solution, Na_2SiO_3, WG) and 1 M hydrochloric acid (HCl) were supplied by Sigma Aldrich.

2.2. Synthesis of polystyrene templates

Polystyrene (PS) templates based on varying PVP/St ratios were synthesized via emulsion polymerisation. In a typical synthesis, 10 g of styrene and required amount of PVP were homogenized in 90 g of distilled water at room temperature (RT) for 15 min in a 250 mL Erlenmeyer flask. The following eleven PVP/St ratios were employed: 0.0050, 0.0075, 0.0100, 0.0500, 0.1000, 0.1500, 0.2000, 0.2500, 0.3000, 0.4000 and 0.5000. 0.10 g of KPS dissolved in 10 g of distilled water was then added to the mixture maintained at a constant temperature of 70 ± 1 °C in an oil bath under stirring conditions of 300 rpm for 24 h before quenching by cooling in air at RT. The PS solutions are denoted as PS-ratio, e.g. PS-0.0050.

2.3. Coating PS templates with silica

2.3.1. TEOS as silica precursor

6 g of PS-0.1000 was dispersed in 95 g of 96% ethanol at 500 rpm for 15 min. 1.5 mL of NH_4OH was added (pH was about 13). The mixture was stirred for 15 min. 5 mL of TEOS in 5 mL of ethanol was added to the reacting pot in three manners: (1) TEOS-1: all at once, (2) TEOS-2: 1/5 of the TEOS/ethanol added at hourly interval over a period of 5 h and (3) TEOS-3: 1/100 of TEOS/ethanol added at 3 min interval over 5 h. The final mix was stirred at 500 rpm overnight at RT.

2.3.2. WG as silica precursor

20 g of PS-0.1500 (or PS-0.3000) were mixed with 3 g of WG in 240 g of distilled water. When further PS with lower PVP/St ratios were employed, no stable colloid could be formed at the original PS concentration. For synthesis purposes, an optimized diluted system was employed. To PS-0.0050 and PS-0.0075 samples, 5 g of PS was added to 1 g of WG in 50 g of distilled water. 1 M HCl was added to all samples until a pH of 2.0 was reached. The solutions were left stirring at 400 rpm overnight at RT.

All coated PS-silica samples were subjected to centrifugation at 8000 rpm for 10 min, air dried overnight and calcined at 500 °C for 5 h (heating rate = 5 °C/min) to remove the PS core.

2.4. Characterization

Microstructures of the obtained materials were analyzed by using a Hitachi S-5500 scanning transmission electron microscope (STEM). Analysis with secondary electrons employed an acceleration voltage of 10 kV and current of 7 μA while 30 kV was used in bright field transmission mode.

The thermal conductivity of unmodified PS-silica samples were determined by employing a Hotdisk Thermal Constants Analyzer (TPS 2500S). A transient plane source technique was applied [27,28] and the PS-silica were measured using the Kapton sensor with radius of 3.189 mm. The sensor is sandwiched between two well packed powder samples of PS-silica. The sensor acts both as a heat source, as well as to register the temperature increase in the samples. The temperature increase over time is recorded and used to calculate the thermal conductivity of the samples. The heating power and heating time can be varied independently to obtain the most appropriate testing conditions for each sample. The conductivity measurements were performed with a heating power ranging from 100 to 700 mW and a heating time of 320 s. All unmodified PS-silica samples were measured only after cooling to ensure equilibrium of the thermal conductivity. Repacking of the samples for measurements were employed and the final reported data are given as the arithmetic mean of 3–5 individual results, depending on the repeatability of the measurements.

3. Results and discussion

3.1. Size determination of PS templates

A nano insulation material (NIM) is a homogeneous, nanostructured material with closed or open nano-sized pores (Fig. 1). The overall thermal conductivity (λ_{tot}) of NIM can be attributed in a simplified form to the proximity of gases to solid interfaces, molecular collisions and the inherent materials properties for heat transfer within a specific area or volume as governed by the following expression:

$$\lambda_{tot} = \lambda_{solid} + \lambda_{gas} + \lambda_{rad} + \lambda_{conv} + \lambda_{coupling} \quad (1)$$

where λ_{tot} is the total overall thermal conductivity, λ_{solid} is the solid state thermal conductivity, λ_{gas} is the gas thermal conductivity, λ_{rad} is the radiation thermal conductivity, λ_{conv} is the convection thermal conductivity, commonly termed as part of the gas thermal conductivity and $\lambda_{coupling}$ is the thermal conductivity term accounting for second order effects between the various thermal conductivities

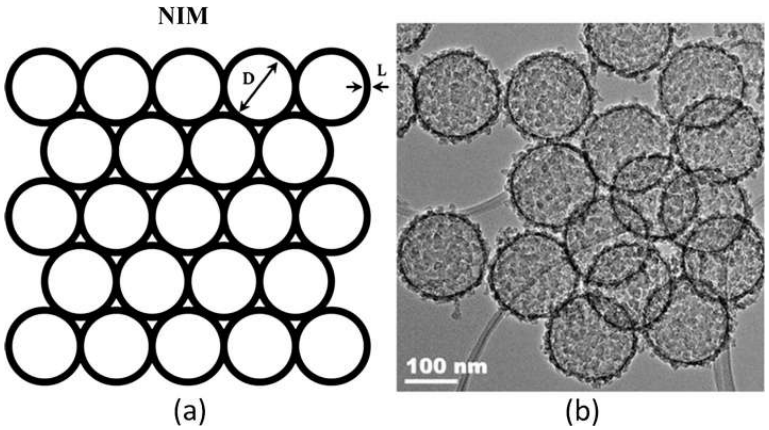

Fig. 1. (a) Conceptual model of a hollow nanosphere NIM with the pore size D and shell thickness L as dimensional characteristics and (b) TEM image of actual hollow silica nanospheres.

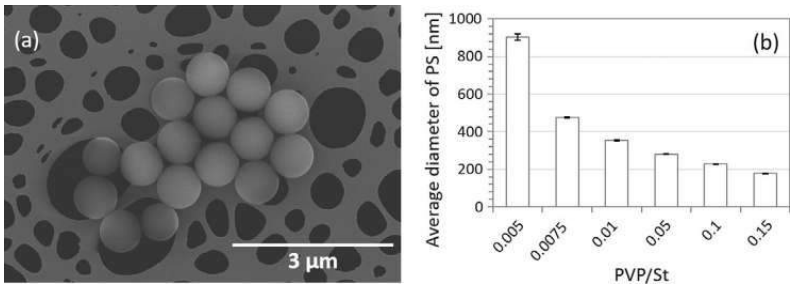

Fig. 2. (a) SEM images displaying monodisperse PS particles prepared with a PVP/St ratio of 0.0050, (b) D_{50} of PS particles as a function of PVP/St.

in Eq. (1). Generally, convection is not an issue in nanostructured thermal insulation materials. The three main determining factors are λ_{solid} and λ_{rad}, which are governed by the material bulk and surface properties, and λ_{gas}, which is exemplified by the Knudsen effect at nanometer levels [29]. In our investigations, the gas of concern is air at atmospheric pressure, since the air will be entrapped within the HSNS. λ_{gas} defined by the Knudsen equation is related to the mean free path of the gas or air molecules and the average diameter of the pores, which further includes the interaction between the gas molecules and the pore walls. It may be written as:

$$\lambda_{gas} = \frac{\lambda_{gas,0}}{1 + 2\beta Kn} \tag{2}$$

$$Kn = \frac{\sigma_{mean}}{\delta} = \frac{k_B T}{\sqrt{2}\pi d^2 \rho \delta} \tag{3}$$

where λ_{gas} is the thermal conductivity of the gas inside the nano-sized pores (also including gas and pore wall interaction); $\lambda_{gas,0}$ is the thermal conductivity of the gas at standard temperature and pressure (STP); β is the energy transfer (in)efficiency of the molecule-wall collisions (a unitless number between 1.5 and 2.0); Kn is the Knudsen number; σ_{mean} is the mean free path of the gas molecules; δ is the characteristic pore size of the material; d is the collision diameter of the gas molecules; p is the gas pressure inside the pores; k_B is the Boltzmann's constant; and T is the temperature. It should be noted that when the pores in a material are reduced to matter of nanometers, the Knudsen number becomes very large, which will result in a gas thermal conductivity that approaches zero. As the distance between the pore walls becomes small relative to the mean free path of the gas molecules, it becomes increasingly likely for the molecules to not hit other molecules before colliding with the pore walls, thus reducing the gas thermal conductivity, also including gas and pore wall interaction, within the pores substantially. Therefore, to ensure an effective Knudsen effect and very low thermal conductivity, controlling the size of PS templates (which influences the eventual length of flow space for air molecules in the insulator) would be a main criteria in determining the thermal conductivity values of HSNS. It has been calculated that the mean free path of ambient air is 68 nm [30], thus the Knudsen effect will be very large when the pore diameter is less than that. As a result, a pore size smaller than or in the range of 68 nm as determined by the smaller diameter of the PS template particles in the nanometer range, is desired in order to achieve a theoretically low thermal conductivity, assuming all other factors are constant.

Similar to other investigations [31], PVP was found to be the most important factor in determining the size of the PS particles, and in affecting the successful synthesis of PS/SiO_2 core-shell particles. The stabilizing and surfactant effect of PVP allow size control of the growing PS, resulting in uniformly distributed PS to be synthesized as a function of the PVP/St ratio. In the absence of PVP, PS particles of varying sizes (spherical to oblong) with high polydispersity and diameters up to micro-meters were formed, showing

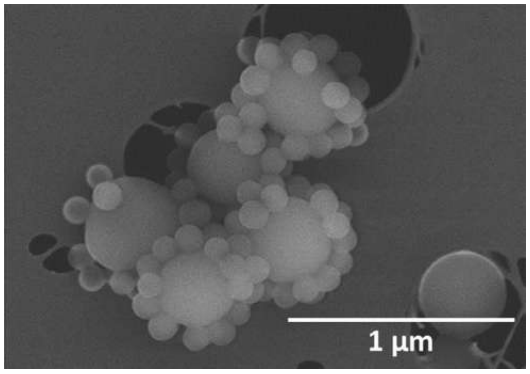

Fig. 3. SEM image displaying PS particles prepared at a PVP/St ratio of 0.3000.

susceptibility to slight variations in KPS and temperature during polymerisation. Upon the addition of PVP, the reaction stabilized and monodispersed PS particles with size dependency on PVP content was attained (Fig. 2a). The mean particle size distributions of the PS particles were calculated from the SEM images by averaging over hundreds of particles. It was found that the median particle diameter (D_{50}) of the PS particles decreased with increasing PVP amounts from 904 ± 17 nm at a PVP/St ratio of 0.0050 till an optimal PVP/St ratio of 0.1500 with a D_{50} of 180 ± 1 nm (Fig. 2b). The growth profile of the PS particles can be attributed to the stabilizing effect of the surfactant PVP on styrene, whereby incorporation of PVP on the surfaces of the PS particles mask the negative charges of the pi bonds of St, hence preventing propagation of polymerisation.

Further increase in PVP/St up to a ratio of 0.3000 resulted in the formation of bimodal PS particles (Fig. 3). The samples prepared at a PVP/St ratio of 0.3000 displayed a bimodal particle size distribution, with respective D_{50} of PS particles in the samples at approximately 450 μm and 120 μm. At PVP/St ratios of 0.4000 and 0.5000, no PS particles were detected, potentially due to the over-dispersing effectiveness of PVP on St, which increased the surface tension of PS particles and prevented the formation of spherical particles. For subsequent studies, PS-0.1500 and PS-0.1000 with an average diameter of ~200 nm, were mainly chosen for templating due to their sizes and stability in their respective mediums.

The D_{50} of PS templates for subsequent employment signified a diminishing Knudsen effect in the HSNS in our investigations.

The amphiphilic characteristic of PVP arising from the presence of the highly polar amide group within the pyrrolidone ring, polar methylene and methine groups in the ring [32,33] and along the backbone, allow modification of the PS surfaces to increase interfacial coupling with silica monomers or oligomers. Therefore, PS particles were subjected to direct coating with silica precursors through a modified Stöber process. A total of three different TEOS systems and one with WG were employed. The choice of WG can be boiled down mainly to the environmental friendliness of this material, where the medium was water. In the case of TEOS, ethanol was employed.

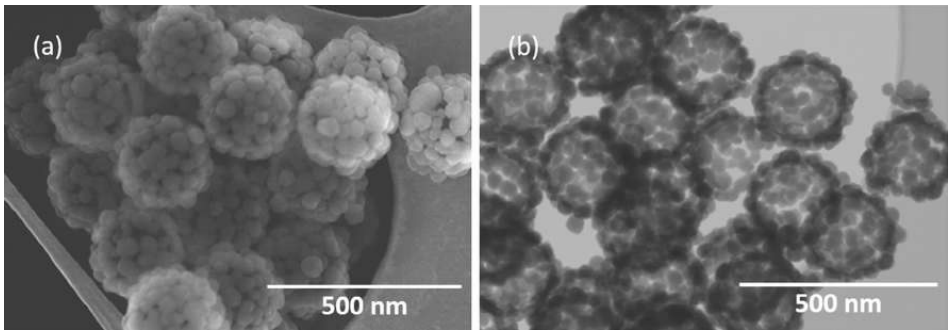

Fig. 4. HSNS prepared from PS-0.1000 and TEOS-1 after calcination (a) SEM image (b) TEM image.

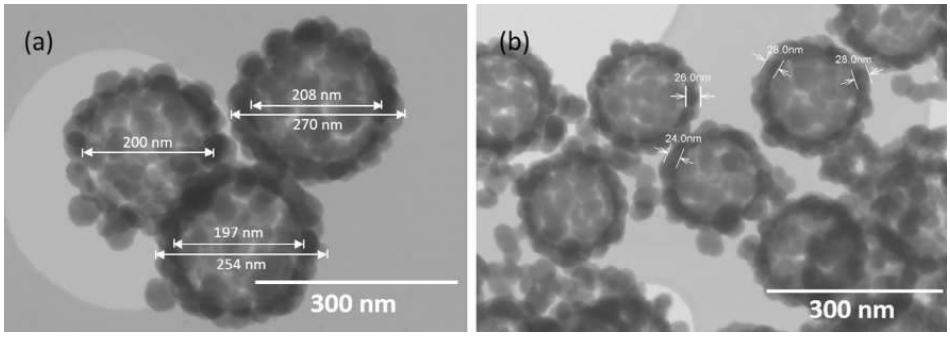

Fig. 5. Measured nanosilica globules prepared from PS-0.1000 and TEOS-1, demonstrating by measurement bars the (a) inner and outer circumferences and (b) size of individual silica particles.

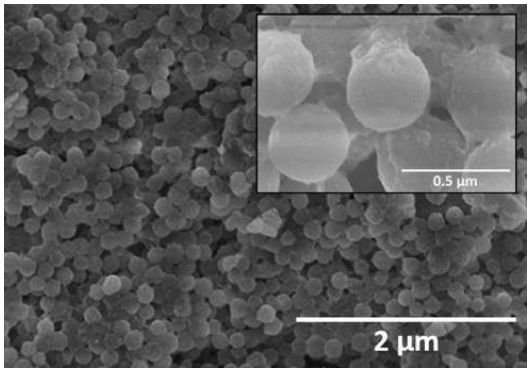

Fig. 6. Silica coated PS-0.1500 samples from water glass at pH = 2.0.

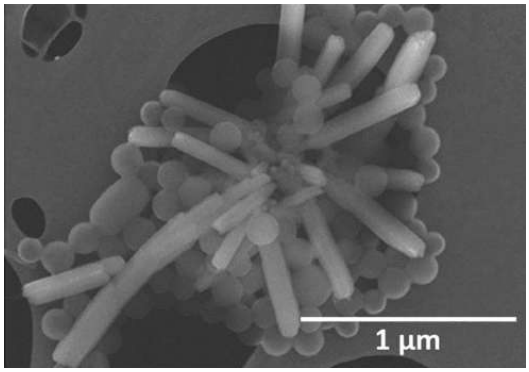

Fig. 7. By-products from WG-PS-0.1500 silica rods and non-reacted PS particles.

3.2. TEOS as silica precursor

Coating of PS-0.1000 under alkaline conditions by using TEOS as silica precursor was successful in all cases, and showed high repeatability and robustness in their formations. Nanospheres of ~270 nm were formed, showing a raspberry-like morphology. After calcination, all samples maintained the raspberry-like appearance with an average particle size of ~250 nm and appeared as monodispersed globules of consolidated silica nanoparticles. Under TEM imaging, these nanospheres/nanoclusters were hollow, confirming that the PS template had been successfully removed during calcination (Fig. 4, right).

The inner diameter of the globular particle was ~200 nm, 10% smaller than the original PS template indicating a coalescing effect of the silica nanoparticles upon calcination. This causes the loosely bound silica nanoparticles to be knitted more closely together. From the TEM image (Fig. 4b), it can be observed that gaps can still be observed between individual silica nanoparticles within each coating, indicating a highly porous shell structure. The thickness of the silica shell was approximately 50 nm in width (Fig. 5a). Each individual silica nanoparticle was dense and had a D_{50} of ~30 nm, independent of rate at which TEOS was added (Fig. 5b). This signified that a mono- to bilayer of silica nanoparticles was formed around the PS template during the coating process. The formation of individual silica nanoparticles may be attributed to the formation of highly branched discrete silicate oligomer species under alkaline conditions. The shapes and sizes of final products (solid core and hollow silica nanospheres) were independent of the mode of TEOS/ethanol addition, implying that the synthesis route of the silica monomers is more dependent on the size of the PS templates, surface tension of the forming silica nanoparticles and their interaction with the medium, than on kinetic parameters or conditions, indicating a robust formation pathway.

For determining the robustness of the synthesis route, a further experiment was performed to deduce the effect of the medium, i.e. addition of water on the hydrolysis rate of TEOS in forming the hollow nanospheres. It is known from literature that up to a threshold limit, increase in water content will favour hydrolysis of TEOS and gelation of silica [34]. In our investigations, when the purity of ethanol was altered from 96% to 100%, smaller silica nanoparticles of ~5% reduction in size were observed in the latter, indicating that despite the apparent effect of the hydrolytic consequence of water on the system, the overall medium dominated by the pH remains as the main determining factor in the formation of silica particles.

3.3. WG as silica precursor

Due to the low reactivity of water glass (WG), it was employed as a silica precursor at a low pH of about 2. This specific acidic condition was employed to promote electrostatic deposition onto PS as silica nanoparticles are positively charged below this isoelectric point [35]. Successfully coating of PS-0.1500 with WG depicts a rough, continuous layer of amorphous silica deposit after synthesis and initial air cooling (Fig. 6). This process of air drying was necessary to stabilize and retain the morphology of the silica structure. However, unlike its counter TEOS based formulation, by-products

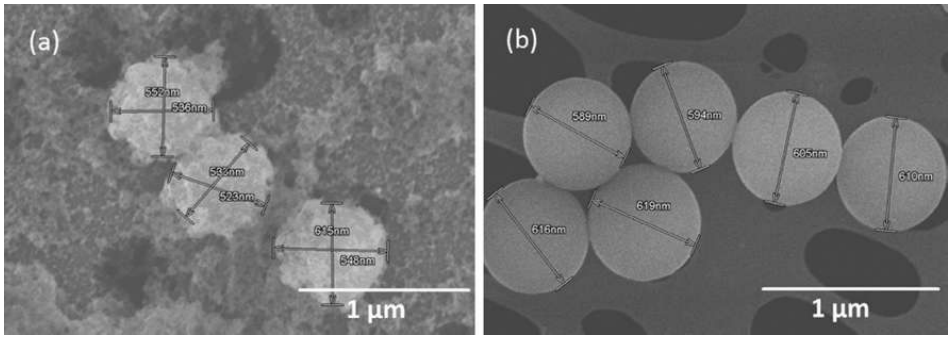

Fig. 8. PS-0.0075 (a) coated and (b) non-coated with silica from water glass, pH = 2.0.

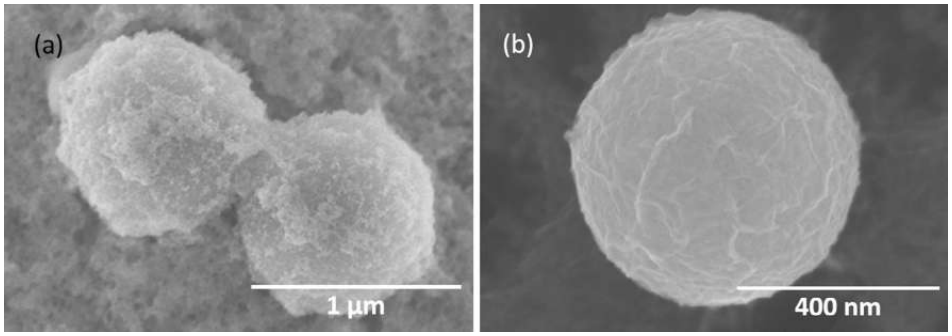

Fig. 9. (a) PS-0.0050 coated with silica from water glass pH = 2.0. (b) Appearance of the silica shell when coated by WG PS-0.005.

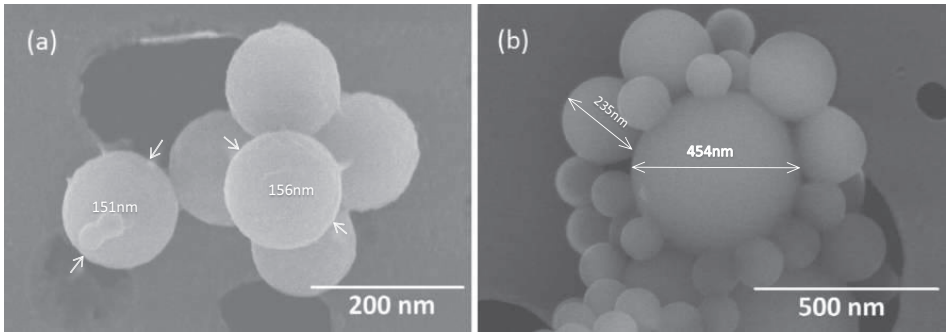

Fig. 10. (a) Coated PS-0.3000 particles and (b) non-coated PS-0.3000 particles in the presence of WG.

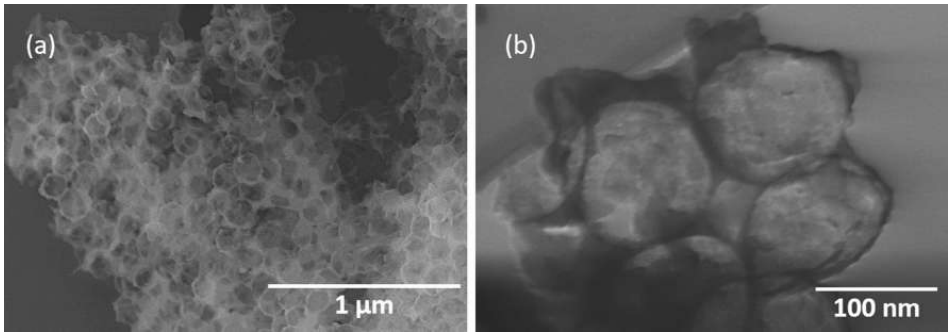

Fig. 11. Hollow WG based PS-0.1500 samples after calcination, pH = 2.0.

were often exhibited, such as silica rods (Fig. 7). The occurrence of these by-products increases proportionally as the amount of added HCl decreases, suggesting the electrostatic buffering effect of the PVP on the surfaces of PS particles, which suppressed the overall negative charge of the surfaces of PS particles. Further research efforts are obviously required to optimize the synthetic conditions to achieve better silica coatings from the WG system.

To verify the viability of WG as a silica precursor without the negative impact from PVP, further experiments were conducted with PS-0.0050 and PS-0.0075. According to extrapolation of values from Zou et al. [31], the amount of PVP exposed on the surfaces of PS particles would be less than 1% and 3% for PS-0.0050 and PS-0.0075, respectively (versus 25% for PS-0.1500). This renders the buffering effect of the PVP molecules to be insufficient to mask the negative charges on the PS particles arising from the sulfate groups. In this way, electrostatic attraction between PS and silica under acidic conditions can be promoted [36]. Samples containing WG and PS-0.0075 showed a blend of coated and non-coated (PS templates that are not successfully coated by silica during reaction) samples. The average diameter of the coated samples was between 500 nm and 600 nm (Fig. 8).

On the other hand, successful full coating of PS-0.0050 was observed. Particles with average diameters of between 600 and 1000 nm were produced (Fig. 9a), implying the instability of the

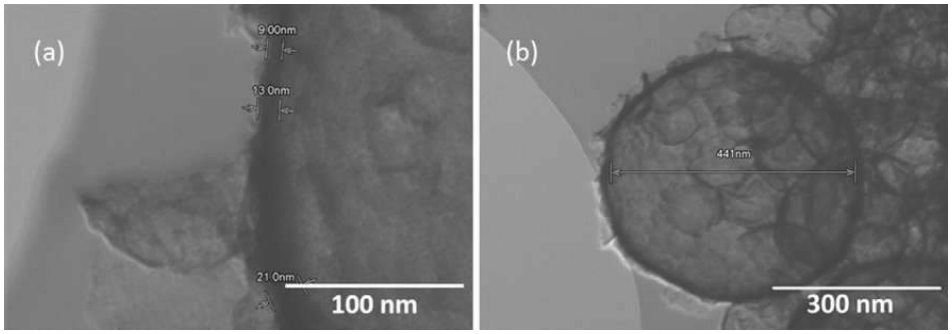

Fig. 12. (a) Shell thickness of silica layer (between 10 and 20 nm) and measured inner diameter of HSNS prepared with WG and PS-0.1500 (b) lower magnification of same sample.

Table 1
Thermal conductivities of HSNS and their corresponding median particle diameter (D_{50}) values (before and after coating).

No.	Sample name	Thermal conductivity [mW/(mK)]	$D_{50\ avg}$ [nm]		
			PS only	Coated	Inner D^
1	TEOS-1PS-0.1000 (96% EtOH)	46	220	250	200
2	TEOS-2PS-0.1000 (96% EtOH)	45	220	250	200
3	TEOS-3PS-0.1000 (96% EtOH)	45	220	250	200
4	TEOS-1PS-0.1000 (100% EtOH)	48	220	245	195
5	WG-PS-0.3000*	72	160**	150**	135
6	WG-PS-0.1500*	102	180	120	105
7	WG-PS-0.0075	56	500	Varied***	–
8	WG-PS-0.0050	44	900	Varied***	–

* Presence of non-reacted silica rods dispersed within sample: WG-PS-0.3000 > WG-PS-0.15000.
** Only the smaller PS particles were taken into account here and measurements for coated samples are taken before calcination. Most of the large PS particles remained non-coated and were burnt off during calcination.
*** Particle sizes varied between 400 and 1000 nm.
^ Estimated inner diameter based on silica layer thickness and final coated HSNS D_{50} values.

synthesis route, particularly when using these PS templates. The larger particles could potentially be formed due to coalescing of smaller PS particles together due to low amount of PVP stabilizer. On the other hand, smaller WG-PS particles are created in the same manner as the previous PS-WG hybrid, with shrinkage as a result of calcination. At higher magnifications, the surfaces of the resulting particles were unlike the silica shells of the TEOS based nanospheres, but resembled a large, continuous wrinkled sheet (Fig. 9b). This may be explained by the tendency of polymerisation to undergo slow hydrolysis at low pH, whereby the silica tends to form linear molecules that are occasionally cross-linked. These molecular chains can in turn entangle and form additional branches resulting in gelation and formation of a continuous layer, as amplified by Fig. 9.

On the other extreme, PS-0.3000 samples were coated with WG in a similar fashion as the former three samples and by-products of silica rods were found in higher amounts than that in PS-0.15000 scattered in the sample. While not all PS templates were coated, similar forms of continuous layers of silica coatings on the PS particles were observed. In such cases, the average particle sizes of coated samples were smaller than when PS-0.1500 was employed, standing at a value of ~150 nm. The larger PS on the other hand, were mostly non-coated (Fig. 10).

Upon calcination, compact mass clusters of nanospheres were detected. For samples prepared with PS-0.1500, the average D_{50} was ~ 120 nm (Fig. 11). Two points could be observed here. Firstly, not all PS from coated particles were successfully removed through calcination, potentially due to the impermeable continuous layer of silica deposit on the PS particles (Fig. 9). However, non-coated PS appeared to be removed during calcination. Secondly, the WG-PS particles were much smaller than the PS-0.1500 precursor (120 nm versus 180 nm, respectively), signifying a reduction of up to 35% in inner core space of the HSNS during calcination. A similar trend was observed for the other WG-PS samples. Higher magnification view of the silica layer displayed that no separation between single silica particles could be detected. Instead, a single continuous layer of between 10 and 20 nm of silica network could be detected (Fig. 12), approximately half to one-third the width of that from the TEOS systems.

3.4. Thermal conductivity of HSNS

Table 1 presents the thermal conductivities of the samples prepared from the TEOS and WG reaction systems. All samples were measured directly after calcination without further processing. Compared to the parent material of silica that possessed a thermal conductivity of ~1400 mW/(mK), the prepared HSNS were much lower in thermal conductivity.

All samples prepared with TEOS displayed thermal conductivity values of between 45 and 48 mW/(mK), which are much higher than the previously reported values [37]. This variation can be attributed to experimental uncertainties like e.g. variation in sample packing density during measurement, which can cause disturbances in the measured thermal conductivity. The consistent thermal conductivity values of TEOS prepared HSNS signified that slight variations in particle size and mode of formation did not affect the thermal conductivity of the final product.

Comparing the TEOS and WG formed HSNS, the reaction medium played a crucial role in determining the nature of the silica particles formed. When WG was employed, the thermal conductiv-

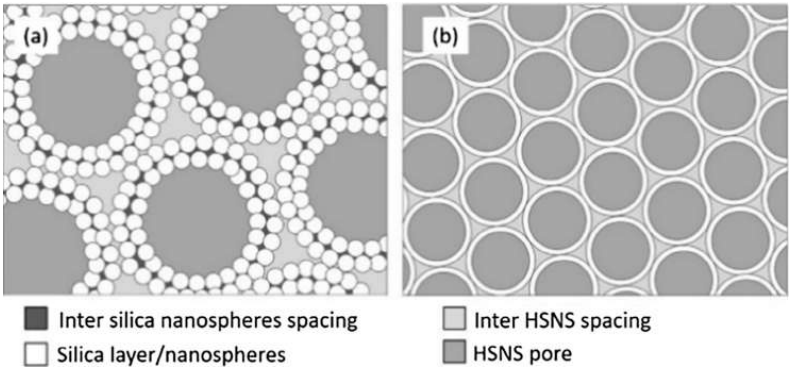

Fig. 13. Illustration of existing interspacing for the different HSNS samples based on (a) TEOS and (b) WG precursors. Close packing lattices for both systems are assumed (down to scale).

ity of the resulting products varied as a function of the PVP/St ratio of the PS templates, whereby the lowest thermal conductivity was registered for samples prepared with PS-0.0050 before attaining a maximum of 102 mW/(mK) with PS-0.1500, and finally stabilizing at 72 mW/(mK) for PS-0.3000. At first glance, it appeared that the variation in thermal conductivity was reversely proportional to the size of particles, which would act against the Knudsen effect, or in a broader sense the overall gas thermal conductivity. However, as observed in Eq. (1), the overall thermal conductivity is a function of many different parameters. The inverse trend may be explained by the amount of WG added at the onset of reaction. About 33% more WG was added to PS-0.1500 and PS-0.3000 as compared to PS-0.0075 and PS-0.0050. Therefore, a plausible explanation could be that the higher thermal conductivities were a result of the higher solid state conductivity. Additionally, the variation in packing sizes and densities for WG-PS-0.1500, WG-PS-0.0075 and WG-PS-0.3000 would cause slight variations among the samples.

The main discrepancy however, arose from the difference in thermal conductivity values between WG-PS-0.15000 and TEOS-PS samples. While TEOS based HSNS were twice as large in dimensions as the WG-PS based samples, the thermal conductivity was, however halved. This apparent discrepancy to the theory based on the gas thermal conductivity may be explained by the presence of inter-particle spaces between the silica nanospheres present in TEOS based HSNS (Fig. 13a), which were absent in the WG based samples (Fig. 13b). By assuming a close packing network of identically sized silica nanospheres, the average mass density of the silica nanoparticle layer made from the alkaline reaction with TEOS was ideally at a maximum fraction of 0.74 relative to total volume of the sample, regardless of the size of the particles. This implied that in reality, due to the porous nature of the silica layer from the TEOS synthesis, more than 25% of the TEOS based silica coating was made up of nanopores filled with air, bearing average lengths (pitch z) of ~15 nm. In this way, the coagulation of silica nanospheres to form the walls of the TEOS based HSNS resulted in an effective reduction of silica mass per volume of material and at the same time, increased the porosity (amount of air voids) within the sample. These two variations would cause a lower λ_{solid} and λ_{gas} for the TEOS based samples as compared to the WG based ones. The large number of nanopores with diameter less than the average mean free path of ambient air molecules (i.e. 68 nm) favored Knudsen effect and can effectively act as buffers for heat transfer, which further compensated for the difference in sizes between TEOS and WG based HSNS (HSNS core diameters: TEOS based 200 nm versus WG based 100 nm). In addition, a continuous connectivity existed between silica particles in the WG based HSNS, which was greatly minimized in the disconnected individually formed silica particles of the TEOS based HSNS. Due to the difference in morphological connectivity, the transmission of heat through the silica solid phase of WG based HSNS was more prevalent than that for TEOS based HSNS.

In this way, the overall thermal conductivity of the HSNS was a balance between the λ_{solid} of the amount of silica particles, the λ_{solid} of the heat transfer based on solid state connectivity and the overall gas conductivity λ_{gas}, which was governed by the λ_{gas} in the HSNS pores, the λ_{gas} in the intra-silica layer (HSNS shell) and the λ_{gas} in the inter-HSNS. Thus, the net thermal conductivity of WG based HSNS was as a result, higher than that of TEOS based HSNS. In the case of WG-PS-0.0075 and WG-PS-0.0050, no predictable explanations could be given due to the irregularity in the HSNS formed.

In general, the importance of the gas conductivity and the solid state and gas interaction as given by the Knudsen effect should not be downplayed as it plays a major role in the attempts to make the new superinsulation materials of tomorrow. Also note as stated by Kalnæs and Jelle [35] regarding vacuum insulation panels (VIP): "In the case of panel perforation, fumed silica will still have a rather low thermal conductivity of around 0.020 W/(mK) at atmospheric pressure. Note then that the difference between 0.004 W/(mK) (pristine condition) and 0.020 W/(mK) (punctured) of 0.016 W/(mK) is due entirely to gas thermal conductivity (not taking into account any changes to the solid core due to the loss of vacuum). That is, the combined solid state and radiation thermal conductivity of fumed silica is as low as 0.004 W/(mK) or in principle somewhat lower (as there is still a very small concentration of air inside a VIP a small part of the 0.004 W/(mK) value is due to gas conduction). Hence, as it is possible to make materials with such a very low solid state and radiation conductivity, there are rather good opportunities to make a high performance thermal insulation material functioning at atmospheric pressure by lowering the gas thermal conductivity."

4. Conclusions

A series of hollow silica nanospheres (HSNS) were synthesized with tetraethyl orthosilicate (TEOS) and water glass (Na_2SiO_3, WG) as silica precursors, in alkaline and acidic media, respectively. It was found that the production with TEOS was more robust and provided a lower thermal conductivity than samples prepared by WG due to increased porosity of the samples, which reduced the effective silica amount per volume of sample (and thus solid state

thermal conductivity) and gas thermal conductivity. The lowest thermal conductivity of 44 mW/(mK) of the HSNS samples reported within this study falls in the upper range of traditional thermal insulation materials. Further enhancement of the HSNS properties may be achieved by decreasing the size of the sacrificial templates to decrease the gas thermal conductivity as given by the Knudsen effect, thus making the HSNS a possible stepping-stone toward a viable, new thermal insulation material.

It may be inferred from this investigation that the choice of reaction medium is very important for effective production of thermally insulating HSNS. Therefore, for optimal production, deriving a new synthesis route by using WG as silica precursor may be a possible way to achieve a greener and more sustainable cost-effective method to produce HSNS.

Acknowledgements

This work has been supported by the Research Council of Norway and several partners through "The Research Centre on Zero Emission Buildings" (ZEB, project no. 193830) and by the Research Council of Norway through the research project "High-Performance Nano Insulation Materials" (Hi-Per NIM, project no. 250159) within the Nano2021 program. Furthermore, the Research Council of Norway is acknowledged for the support to the "Norwegian Micro- and Nano-Fabrication Facility" (NorFab, project no. 245963/F50).

References

[1] McKinsey, Pathways to a Low-carbon Economy. Version 2 of the Global Greenhouse Gas Abatement Cost Curve, McKinsey & Company, 2009.
[2] M.S. Al-Homoud, Performance characteristics and practical applications of common building thermal insulation materials, Build. Environ. 40 (2005) 353–366.
[3] A.M. Papadopoulos, State of the art in thermal insulation materials and aims for future developments, Energy Build. 37 (2005) 77–86.
[4] B.P. Jelle, A. Gustavsen, S. Grynning, E. Wegger, E. Sveipe, R. Baetens, Nanotechnology and possibilities for the thermal building insulation materials of tomorrow, in: Proceedings of the Renewable Energy Research Conference – Renewable Energy Beyond 2020, Trondheim, Norway, 7–8 June, 2010.
[5] B.P. Jelle, A. Gustavsen, R. Baetens, The path to the high performance thermal building insulation materials and solutions of tomorrow, J. Build. Phys. 34 (2010) 99–123.
[6] B.P. Jelle, A. Gustavsen, R. Baetens, The high performance thermal building insulation materials and solutions of tomorrow, in: Proceedings of the Thermal Performance of the Exterior Envelopes of Whole Buildings XI International Conference (Buildings XI), Clearwater Beach, Florida, U.S.A., 5–9 December, 2010.
[7] B.P. Jelle, B.G. Tilset, S. Jahren, T. Gao, A. Gustavsen, Vacuum and nanotechnologies for the thermal insulation materials of beyond tomorrow – from concept to experimental investigations, in: Proceedings of the 10th International Vacuum Insulation Symposium (IVIS-X), Ottawa, Canada, 15–16 September, 2011, pp. 171–178.
[8] B.P. Jelle, Traditional, state-of-the-art and future thermal building insulation materials and solutions – properties, requirements and possibilities, Energy Build. 43 (2011) 2549–2563.
[9] B.P. Jelle, T. Gao, L.I.C. Sandberg, B.G. Tilset, M. Grandcolas, A. Gustavsen, Thermal superinsulation for building applications – from concepts to experimental investigations, Int. J. Struct. Anal. Des. 1 (2014) 43–50.
[10] F. Caruso, Nanoengineering of Particle surfaces, Adv. Mater. 13 (2001) 11–22.
[11] G. Kickelbick, L.M. Liz-Marzán, in: H.S. Nalwa (Ed.), Encyclopedia of Nanoscience and Nanotechnology, vol. 2, American Scientific Publishers, Stevenson Ranch, CA, 2004, pp. 199–220.
[12] H. Bamnolker, B. Nitzan, S. Gura, S.J. Margel, New solid and hollow, magnetic and non-magnetic, organic-inorganic monodispersed hybrid microspheres: synthesis and characterisation, Mater. Sci. Lett. 16 (1997) 1412–1415.
[13] S. Margel, H.U.S. Bamnolker, Process for the Preparation of Microspheres and Microspheres Made Thereby, Patent 6,103,379, 2000.
[14] X. Ding, K. Yu, Y. Jiang, H. Hari-Bala, Z. Wang Zhang, A novel appraoch to the synthesis of hollow silica nanospheres, Mater. Lett. 58 (2004) 3618–3821.
[15] C. Graf, D.L.J. Vossen, A. Imhof, A. van Blaaderen, A general method to coat colloidal particle with silica, Langmuir 19 (2003) 6693–6700.
[16] Y. Chen, E. Kang, K. Neoh, A. Greiner, Preparation of hollow silica nanospheres by surface initiated atom transfer radical polymerization on polymer latex templates, Adv. Funct. Mater. 15 (2005) 113–117.
[17] N. Kawahashi, E.J. Matijević, Preparation and properties of uniform coated colloidal particles: V. Yittrium basic carbonate on polystyrene latex, Colloid Interface Sci. 138 (1990) 534–542.
[18] R.A. Caruso, A. Susha, F. Caruso, Multilayered titania, silica, and laponite nanoparticle coatings on polystyrene colloidal templates and resulting inorganic hollow spheres, Chem. Mater. 13 (2001) 400–409.
[19] T. Gao, B.P. Jelle, L.I.C. Sandberg, A. Gustavsen, Monodisperse hollow silica nanospheres for nano insulation materials: synthesis, characterization, and life cycle assessment, ACS Appl. Mater. Interfaces 5 (2013) 761–767.
[20] T. Gao, L.I.C. Sandberg, B.P. Jelle, Nano insulation materials: synthesis and life cycle assessment, Proc. CIRP 15 (2014) 490–495.
[21] L.I.C. Sandberg, T. Gao, B.P. Jelle, A. Gustavsen, Synthesis of hollow silica nanospheres by sacrificial polystyrene templates for thermal insulation applications, Adv. Mater. Sci. Eng. (2013).
[22] T. Gao, B.P. Jelle, A. Gustavsen, S. Jacobsen, Aerogel-incorporated concrete: an experimental study, Constr. Build. Mater. 52 (2014) 130–136.
[23] S. Ng, B.P. Jelle, T. Stæhli, Calcined clay as binder for thermal insulating and structural aerogel incorporated mortar, Cem. Concr. Compos. 72 (2016) 213–221.
[24] S. Ng, B.P. Jelle, Y.P. Zhen, O. Wallevik, Effect of storage and curing conditions at elevated temperatures on aerogel-incorporated mortar samples based on UHPC recipe, Constr. Build. Mater. 106 (2016) 640–649.
[25] S. Ng, B.P. Jelle, L.I. Sandberg, T. Gao, O. Wallevik, Experimental investigations of aerogel-incorporated ultra-high performance concrete, Constr. Build. Mater. 77 (2015) 307–316.
[26] R.D. Schlanbusch, B.P. Jelle, L.I.C. Sandberg, S.M. Fufa, T. Gao, Integration of life cycle assessment in the design of hollow silica nanospheres for thermal insulation applications, Build. Environ. 80 (2014) 115–124.
[27] S.E. Gustafsson, Transient plane source techniques for thermal conductivity and thermal diffusivity measurements of solid materials, Rev. Sci. Instrum. 62 (1991) 797–804.
[28] D.P. Bentz, Transient plane source measurements of the thermal properties of hydrating cement pastes, Mater. Struct 40 (2007) 1073–1080.
[29] S.E. Kalnæs, B.P. Jelle, Vacuum insulation panel products: a state-of-the-art review and future research pathways, Appl. Energy 116 (2014) 355–375.
[30] S. Jennings, The mean free path in air, J. Aerosol Sci. 19 (2) (1988) 159–166.
[31] H. Zou, S. Wu, Q. Ran, J. Shen, A simple and low-cost method for the preparation of monodisperse hollow silica spheres, J. Phys. Chem. C 112 (2008) 11623–11629.
[32] J.N. Smith, J. Meadows, P.A. Williams, Adsorption of polyvinvylpyrrolidone onto polystyrene latices and the effect on colloid stability, Langmuir 12 (1996) 3773–3778.
[33] P. Molyneux, Water-Soluble Synthetic Polymers: Properties and Behaviour, CRC Press Inc., Boca Raton, FL, 1983.
[34] M.A. Fardad, Catalysts and the structure of SiO_2 sol-gel films, J. Mater. Sci. 35 (2000) 1835–1841.
[35] M.C. Fuji, H. Takai, Imabeppu, X. Xu, Synthesis and shell structure design of hollow silica nanoparticles using polyelectrolyte as template, in: Tunisia-Japan Symposium: R and D of Energy and Material Sciences for Sustainable Society, TJS 2014, 596, 2015.
[36] X. Du, L. Yao, J. He, One-pot fabrication of noble-metal nanoparticles that are encapsulated in hollow silica nanospheres: dual roles of poly(acrylic acid), Chem. Eur. J. 18 (2012) 7878–7885;
S.E. Kalnæs, B.P. Jelle, Vacuum insulation panel products: a state-of-the-art review and future research pathways, Appl. Energy 116 (2014) 355–375.
[37] Y. Liao, X. Wu, H. Liu, Y. Chen, Thermal conductivity of powder silica hollow spheres, Thermochim. Acta 526 (2011) 178–184.

Article V

Sohrab Alex Mofid, Bjørn Petter Jelle, Tao Gao, **Utilization of hollow silica nanospheres for thermal insulation purposes**, *Proceedings of TechConnect World Innovation Conference* (2016) pp 259-262.

Utilization of Hollow Silica Nanospheres for Thermal Insulation Purposes

Sohrab Alex Mofid[a*], Bjørn Petter Jelle[ab] and Tao Gao[a]

[a]Norwegian University of Science and Technology (NTNU),
Department of Civil and Transport Engineering, NO-7491 Trondheim, Norway.
[b]SINTEF Building and Infrastructure,
Department of Materials and Structures, NO-7465 Trondheim, Norway.
[*]Corresponding author: sohrab.mofid@ntnu.no (e-mail), +47-93051989 (phone).

ABSTRACT

A great deal of attention has been paid to thermal insulation as it plays a significant role in improving the energy efficiency within the building and construction sector. There is an ever-increasing demand for advanced thermal insulation materials that show superior performance to that of the conventional ones. The state-of-the-art thermal insulation materials and solutions, such as vacuum insulation panels (VIP) and silica aerogels, and the emerging ones like nano insulation materials (NIM), are under rapid development and show a promising potential. Hollow silica nanospheres (HSNS) may be a promising candidate for achieving high performance super insulation materials (SIM). This study investigates synthesis parameters and properties of HSNS with the aim of reaching low thermal conductivity by exploiting the Knudsen effect. The experiments are carried out to optimize thermal performance based on variation of structural parameters like e.g. HSNS shell thickness and inner diameter.

Keywords: hollow silica nanosphere, HSNS, nano insulation material, NIM, thermal insulation.

1 INTRODUCTION

The last decades have witnessed a rapid growth of research and development activities applying nanotechnology in various fields including the construction industry that seek out a way to advance building materials/components by using a variety of nanomaterials [1-3]. It has been shown that the application of nanotechnology can significantly enhance important characteristics of building materials, such as durability and strength, and in addition enrich them with new useful properties [3-5], allowing the adaption of known theoretical principles in practice. Present-day worldwide effort is to limit the energy usage in the building sector by minimization of the heat loss and exacerbation of the requirements for thermal insulation. Enhancement of insulation properties within the building sector is a challenging task to fulfil and is associated with making compromises in both financial, functional and architectural areas. Therefore, new, innovative and more effective materials are currently being sought. Among them are insulation materials with super-low thermal conductivity and smaller dimensions which may revolutionize the development of high performance thermal insulation materials.

Conventional thermal insulation materials, like mineral wool, expanded polystyrene (EPS), extruded polystyrene (XPS) and polyurethane (PUR) foam have high thermal conductivities around 30-40 mW/(mK) (PUR: 20-30 mW/(mK)). Their application have not been fully satisfactory for several reasons, e.g. architechtural restrictions, safety issues and material consumption and costs. Traditional thermal insulators are distinguished by how they trap a gaseous material, i.e. in a fibrous, cellular or granular material [6].

New and improved state-of-the-art thermal insulation materials or solutions such as vaccum insulation panels (VIP) and silica aerogels may be more favourable to use due to their lower thermal conductivity. VIPs have a centre-of-panel thermal conductivity of typical 4 mW/(mK) in the pristine non-aged condition, wheres silica aerogels have values between 12-20 mW/(mK). However, both VIP and silica aerogels as well present certain weaknesses like fragility, perforation vulnerability (VIP), loss of vacuum by air and moisture diffusion (VIP) and relatively high costs. Similarly to the distinction in conventional thermal insulators, current state-of-the-art thermal insulators are distinguished by how they fulfil rarefaction of the gas, i.e. by a nanoporous solid structure or by application of a partial vaccum, in contrast to the fact that the best results may be obtained with the combination of both [6].

Hence, nanoengineering has been employed to study and demonstrate nano insulation materials (NIM) based on hollow silica nanospheres (HSNS) which have size-dependent thermal conduction and may be readily controlled over a large range [7]. Silica represents one of the best candidates for achieving HSNS as silica is the most abundant material in nature. This work gives an overview of the HSNS synthesis and characterizations and aim to reduce the thermal conductivity by modification of structural parameters such as the shell thickness of the hollow nanospheres.

2 EXPERIMENTAL

2.1 General

The materials used during the synthesis are summarized in Table 1 below.

Table 1: Materials used during the synthesis of HSNS (further details in the following section).

Raw materials	Volume (mL)	Mass (g)	Material supplier
Step 1: Synthesis of polystyrene nanospheres			
H_2O	110	110	In-place
Styrene	-	10	Sigma Aldrich
PVP	-	1.5	Sigma Aldrich
KPS	-	0.1	Sigma Aldrich
Step 2: Coating polystyrene nanospheres with silica			
Ethanol	332[a]	182	Sigma Aldrich
PS[b]	-	12	In-place
NH_4OH	12	-	Sigma Aldrich
TEOS	15	-	Sigma Aldrich

[a] Including ethanol used for washing the particles.
[b] PS nanosphere suspension.

2.2 Monodisperse PS Nanospheres

Monodisperse polystyrene (PS) nanospheres were first prepared and used as templates for the growth of silica coatings. The resulting PS spheres are depicted in the transmission electron microscope (TEM) images in Fig.1.

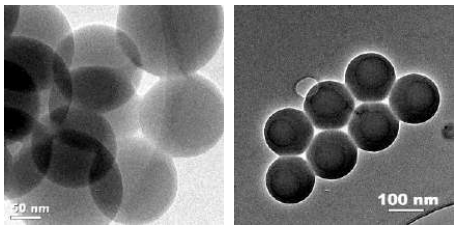

Figure 1: TEM images of monodisperse PS nanospheres with 150 nm diameter size.

For the particular synthesis, 1.5 g polyvinylpyrrolidone (PVP) was dissolved in 100 mL distilled water under ultrasonic irradiation, whereafter 10 g styrene solution was added to the mix. The obtained styrene/PVP solution was heated up to 70°C under constant stirring at 500 rpm. Afterwards, 10 mL potassium persulphate (KPS) solution (0.15 g KPS in 10 mL water) was added drop-wise into the PVP/styrene solution to initiate the polymerization reaction. The polymerization reaction was kept at around 70°C for 24 h. After the reaction took place, the obtained PS nanosphere suspension was cooled down to room temperature for further use.

2.3 Silica Nanospheres

For the particular synthesis, 6 g of as-prepared PS suspension and 4 mL NH_4OH solution were added into 120 mL ethanol under constant stirring at 500 rpm for two identical samples twice, Then, 10 mL tetraethyl orthosilicate (TEOS) ethanol solution (50 vol% TEOS in ethanol) was added drop-wise. For one of the two sample solutions, the suspension was divided into two equal portions and another 10 mL TEOS ethanol solution (50 vol% TEOS in ethanol) was added drop-wise to one of the solutions in order to grow thicker shell structures with silica, whereas the second equal solution remained unchanged. The reaction system was stirred for 10–24 h to prepare core-shell type PS@SiO_2 nanospheres. After the reaction, the solid product was separated from the mother solution by centrifugation. The obtained sediment was washed with ethanol once again and finally kept drying at room temperature. Hollow silica nanospheres were readily obtained by annealing the PS@SiO_2 nanospheres at 500°C in air for 5 h, with resulting HSNS as shown in the TEM images in Fig.2.

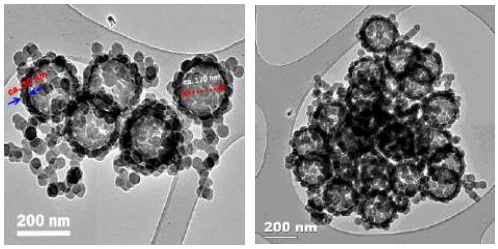

Figure 2: TEM images of HSNS with mean diameter of 150 nm and shell thickness of around 30 nm.

2.4 Characterization

Transmission electron microscope (TEM, JEM-2010) and scanning electron microscope (SEM, Hitachi S-5500) were employed to characterize the morphology and nanostructure of the as-synthesized items. Thermal conductivity of the obtained bulk materials was analyzed by using a Hot Disk Thermal Constants Analyzer (TPS 2500S). A disk-type Kapton Sensor 5465 with radius 3.189 mm was used. The sensor, which acts as heat source and temperature recorder, was sandwiched between two parts of powder samples. Temperature increase of the samples as a function of time was recorded to compute the thermal conductivity (uncertainty ~ 5%). The final thermal conductivity value reported was the arithmetic mean of four

individual measurements under different conditions (heating power 0.02–0.2 W; measurement time 1–320 s).

3 THERMAL PROPERTIES OF HSNS

The thermal conductivity of the HSNS can be understood by the size-dependent thermal conduction at nanometer scale [8,9]. Hence, the low thermal conductivity of the HSNS contributions from various thermal conduction mechanisms such as gaseous, solid, radiation and convection heat transport can determine the measured thermal conductivity of the HSNS.

3.1 Gaseous Thermal Conductivity

Gaseous thermal transport in a space with small dimensions can be explained by the Knudsen effect, where the mean free path of the gas molecules is larger than the pore diameter of the material. The gaseous thermal conductivity, including the gas and pore wall interaction, may according to the Knudsen effect be written as [10]:

$$\lambda_g = \frac{\lambda_{gas,0}}{1+2\beta Kn} \tag{1}$$

where

$$Kn = \frac{l_{mean}}{\delta} = \frac{k_B T}{\sqrt{2}\pi d^2 p \delta} \tag{2}$$

where λ_g is the gaseous thermal conductivity in the pores (W/(mK)), $\lambda_{g,0}$ is the gas thermal conductivity in the pores at standard temperature and pressure (STP), Kn is the Knudsen number indicating the ratio between the mean free path l_{mean} of gas molecules (m) (for air, $l_{mean} \approx 68$ nm at ambient condition) and δ the characteristic pore diameter (m), k_B is the Boltzmann's constant ($1.38 \cdot 10^{-23}$ J/K), T is the temperature (K), d is the gas molecule collision diameter (m), p is the gas pressure in the pores (Pa), β is a coefficient (between 1.5 and 2.0) characterizing the energy transfer (in)efficiency in terms of collision of gas molecules with the solid structure [7]. A lower pressure gives a longer mean free path which in turns gives a larger Knudsen number, i.e. a lower gaseous thermal conductivity. According to Eq.2, it is obvious that for pores with diameters of a few nanometers, the Knudsen effect becomes very large (small Knudsen number), thus resulting in reduced gaseous thermal conductivity. In this study, the synthesized HSNS have pore diameters of about 150 nm, which in turn can theoretically reduce the gaseous thermal conductivity down to10 mW/(mK).

3.2 Solid Thermal Conductivity

To further understand the measured thermal conductivity of HSNS due to variation in shell thickness, the solid-state conduction has to be taken into account. Theory of size-dependent thermal conductivity at nanoscale level for semiconductor systems is explained by Liang and Li [11]. Accordingly, the solid-state thermal conductivity of solid nanospheres λ_N can be given as:

$$\frac{\lambda_N}{\lambda_B} = p \cdot \exp\left(-\frac{l_0}{D}\right) \cdot \left[\exp\left(\frac{1-\alpha}{D/D_0 - 1}\right)\right]^{3/2} \tag{3}$$

where λ_B is the thermal conductivity of the bulk material, l_0 is the phonon mean free path at room temperature, D is the featured size (e.g. diameter of nanoparticles), D_0 and α are material constants, p is a factor reflecting the surface roughness, $0 \le p \le 1$, where $p \to 1$ represents a smoother surface which results in higher probability of specular phonon scattering, whereas $p \to 0$ corresponds to a rougher surface with higher probability of diffusive phonon scattering [12-13]. Related to our HSNS, given the same inner diameter, one may conclude that a thinner HSNS shell thickness, and thus smaller D in Eq.3, may result in lower solid-state thermal conductivity than a thicker shell thickness. In general, a more tortuous thermal conduction path leads to a lower solid-state thermal transport and conductivity. Although material-dependent parameters make it difficult to calculate an exact thermal conductivity value, as the contact area between adjacent spheres are typically within a few nanometers from each other [14], in general the contribution from the solid-state thermal conductivity in such materials is very small [15].

4 RESULTS AND DISCUSSION

This work gives an overview of the pathway of achieving NIM by based on HSNS. In general, the advantage of nanoporous materials' size-dependent thermal conduction at nanometer scale is the main reason for conducting such studies [16-17]. Thermal properties of HSNS may well depend on several structural parameters, such as the shell thickness of the hollow spheres, inner diameter, chemical composition of the shell materials and density of the hollow spheres [18]. Consequently, by modification of these structural parameters, the thermal performance of hollow spheres may be optimized and controlled over a large range.

HSNS can be prepared through different methods, of which the template-assisted approach represents presumably the most straightforward method with numerous advantages [19]. PS was chosen as the template material for the growth of HSNS because of the fact that PS nanospheres can be prepared with controlled diameters through varying the PVP/styrene weight ratio and surface properties [20-24]; furthermore, can be easily removed either by heating or dissolution [22-24]. In this study, PS nanospheres of 150 nm was prepared with a PVP/styrene ratio of 0.15. The small size and large surface-to-volume ratio, and that the PS nanosphere surfaces are very active, make PS nanospheres ideal nucleation sites for growth of silica. Considering the small size of PS nanospheres one could expect according to the Knudsen effect (Eq.1 and 2)

that the gaseous thermal conductivity may further be suppressed by reducing the inner pore diameter controlled by the PVP/styrene ratio.

The HSNS shells consist of silica nanoparticles produced from hydrolysis of TEOS that is captured and deposited on the surface of the PS nanospheres. The silica nano particle size may also depend on several experimental parameters such as NH_4OH and TEOS concentrations and reaction temperature [25].

Variation of thermal conductivity with respect to shell thickness is given in Table 2.

Table 2: Average thermal conductivity λ_{avg} for HSNS samples of different shell thicknesses L and constant inner diameter D.

Sample	λ_{avg} (mW/(mK))*	L (nm)	D (nm)
A	36 ± 1	10 ± 2	155 ± 5
B	45 ± 2	20 ± 3	162 ± 7
C	59 ± 3	30 ± 4	166 ± 9

*The uncertainty is calculated as two times the standard deviation of the mean, i.e. within a confidence interval of 95.45%.

It should be mentioned that variation of thermal conductivity values was obtained within one set of testing procedure, where values obtained from combinations of heating power and measurement time with Hot Disk apparatus were analysed, and hence finally an average of the conductivity values were calculated, each of them based on three samples.

5 CONCLUSIONS

Hollow silica nanospheres (HSNS) exhibit great flexibilities of modifying their properties by tuning the corresponding structural features. The structural features can be controlled by using the polystyrene (PS) nanosphere templates with different properties and/or use of different precursors like e.g., TEOS or Water glass as a structure for shell thickness growth. HSNS with inner pore diameters of ~ 150 nm and varying shell thicknesses of 10, 20 and 30 nm have been prepared. It was found that the thermal conductivity decreased with decreasing HSNS shell thickness which is in agreement with the theoritical background. Though experimentally challenging, future studies may be conducted in order to make PS nanospheres with reduced inner diameters, e.g. down to 30-50 nm, in an attempt to further lower the thermal conductivity according to the Knudsen equation. Due to the nature of HSNS and their properties for thermal insulation applications, further studies and development are worth pursuing.

ACKNOWLEDGEMENTS

We thank Yingda Yu (NTNU) for his contribution with the characterization by transmission electron microscopy.

REFERENCES

[1] Zhu, W.; Bartos, P. J. M.; Porro, A. *Mater. Struct.*, **37**, 649–658, 2004.
[2] Lee, J.; Mahendra, S.; Alvarez, P. J. J. *ACS Nano*, **4,** 3580–3590, 2010.
[3] Raki, L.; Beaudoin, J.; Alizadeh, R.; Makar, J.; Sato, T. *Materials*, **3***,* 918–942, 2010.
[4] Lee, J.; Mahendra, S.; Alvarez, P. J. J. *ACS Nano* , **4**, 3580–3590, 2010.
[5] Raki, L.; Beaudoin, J.; Alizadeh, R.; Makar, J.; Sato, T. *Materials*, **3**, 918–942, 2010.
[6] F.Pacheco-Torgal, M.V. Diamanti, A.Nazari, C-G Granqvist, "Nanotechnology in eco-efficient construction", 188-189, 2013.
[7] Jelle, B. P.; Gao, T.; Sandberg, L. I. C.; Tilset, B. G; Grandcolas, M.; Gustavsen, A. *International Journal of Structural Analysis and Design*, **1**, 43-50, 2014.
[8] Cahill, D. G.; Ford, W. K.; Goodson, K. E.; Mahan, G. D.; Majumdar, A.; Maris, H. J.; Merlin, R.; Philipot, S. R. *J. Appl. Phys.*, ***93***, 793–818, 2003.
[9] Heino, P.; Ristolainen, E. *Phys. Scripta* **,** *T114*, 171–174, 2004.
[10] Jelle, B. P. *Energy and Buildings*, **43**, 2549-2563, 2011.
[11] Liang, L.; Li, B. *Phys. Rev. B*, **73**, 153303, 2006.
[12] Liu, L.; Chen, X. *J. Appl. Phys.*, **107**, 033501, 2010.
[13] Teja, A. S.; Beck, M. P.; Yuan, Y.; Warrier, P. *J. Appl. Phys*., **107**, 114319, 2010.
[14] Desai, T. G. *Appl. Phys. Lett*., **98**, 193107, 2011.
[15] Liao, Y.; Wu, X.; Liu, H.; Chen, Y. *Thermochim. Acta*, **526**, 178–184, 2011.
[16] Cahill, D. G.; Ford, W. K.; Goodson, K. E.; Mahan, G. D.; Majumdar, A.; Maris, H. J.; Merlin, R.; Philipot, S. R. *J. Appl. Phys*., **93**, 793–818, 2003.
[17] Heino, P.; Ristolainen, E. *Phys. Scripta*, T**114**, 171–174, 2004.
[18] Gao, T.; Sandberg, L. I. C.; Jelle, B. P.; Gustavsen, A. In "Fuelling the Future: Advances in Science and Technologies for Energy Generation, Transmission and Storage"*,* Mendez-Vilas, A. A. (Ed.); *BrownWalker Press: Boca Raton*, 535–539, 2012.
[19] Guerrero-Martínez, A.; Pérez-Juste, J.; Liz-Marzán, L. M. *Adv. Mater*., **22**, 1182–1195, 2010.
[20] Yang, J.; Lind, J. U.; Trogler, W. C. *Chem. Mater*., **20**, 2875–2877, 2008.
[21] Du, X.; He, J. *J. Appl. Polym. Sci*., **108**, 1755–1760, 2008.
[22] Zou, H.; Wu, S.; Ran, Q.; Shen, J. *J. Phys. Chem. C*., **112**, 11623–11629, 2008.
[23] Chen, M.; Wu, L. M.; Zhou, S. X.; You, B. *Adv. Mater*., **18**, 801–806, 2006.
[24] Cao, S. S.; Jin, X.; Yuan, X. H.; Wu, W. W.; Hu, J.; Sheng, W.C. *J. Polym. Sci. Part A: Polym. Chem*., **48**, 1332–1338, 2010.
[25] Stöber, W.; Fink, A.; Bohn, E. *J. Colloid Interf. Sci*., **26**, 62-69, 1968.

Article VI

Bjørn Petter Jelle, Sohrab Alex Mofid, Tao Gao, Mathieu Grandcolas, Malin Sletnes and Espen Sagvolden, **Nano insulation materials exploiting the Knudsen effect**, IOP Conference Series: *Materials Science and Engineering*, IOP Publishing, 2019, p. 012003.

IOP Conf. Series: Materials Science and Engineering **634** (2019) 012003 doi:10.1088/1757-899X/634/1/012003

Nano insulation materials exploiting the Knudsen effect

B P Jelle[1,2,5], S A Mofid[1], T Gao[1], M Grandcolas[3], M Sletnes[2] and E Sagvolden[4]

[1]Norwegian University of Science and Technology (NTNU), Department of Civil and Environmental Engineering, NO-7491 Trondheim, Norway
[2]SINTEF Building and Infrastructure, Department of Materials and Structures, NO-7465 Trondheim, Norway
[3]SINTEF Industry, Department of Materials and Nanotechnology, NO-0314 Oslo, Norway
[4]SINTEF Industry, Department of Sustainable Energy Technology, NO-0314 Oslo, Norway

[5]E-mail: bjorn.petter.jelle@ntnu.no

Abstract. As the world's focus is turned even stronger toward miscellaneous energy efficiency and saving aspects, the development of new high-performance thermal insulation materials for building applications will play an important role in this regard. The aim of the presented study is to develop an understanding for the governing thermal transport mechanisms and utilize the Knudsen effect in nanoporous insulation materials through theoretical concepts and experimental laboratory explorations, thus being able to synthesize nano insulation materials (NIM) with very low thermal conductivity values as a major goal. NIMs based on hollow silica nanospheres (HSNS) have been synthesized by a sacrificial template method, where the idea is that the heat transport by gas conductance and gas/solid state interactions decreases with decreasing pore diameters in the nano range as predicted by the Knudsen effect. HSNS with reduced thermal conductivity compared to their solid counterparts have been prepared where the hollow sphere cavities and voids between the spheres are filled with air at atmospheric pressure, i.e. eliminating the need for various measures like e.g. protective metallized foils to maintain a vacuum or expensive low-conducting gases in the cavities and voids. Hence, HSNS represent a promising stepping-stone toward the future high-performance thermal insulation materials.

1. Introduction

In the years ahead there will probably be a continued increased attention and focus on energy efficiency and saving aspects alongside utilization of renewable and non-polluting energy sources. Miscellaneous energy sources and harvesting opportunities are being explored like e.g. solar cells and building integrated photovoltaics (BIPV) [1-10]. However, the energy you are not using you do not have to produce. In this respect, the development of new high-performance thermal insulation materials for building applications will be important [11-13]. A crucial property of these materials is the thermal conductivity, where it is an expressed goal to reach as low thermal conductivity as possible.

Traditional thermal insulation materials have thermal conductivity values typically in the range 20 to 50 mW/(mK) with cellulose and cork being in the higher end having values between 40 to 50 mW/(mK), mineral wool like glass wool and rock wool being in the middle range with values between 30 to 40 mW/(mK), polystyrene products like expanded polystyrene (EPS) and extruded polystyrene (XPS) also having values in the middle range between 30 to 40 mW/(mK), and polyurethane (PUR)

being in the lower end having values between 20 to 30 mW/(mK) [12]. In this respect, one should note that the thermal conductivity may increase to considerably higher values if the moisture content is increased in most of these materials. It should also be noted that even if PUR is safe in its intended use, it represents a potential serious health concern and hazard in case of a fire as PUR will when burning release poisonous gases of hydrogen cyanide (HCN) and isocyanates, where the HCN toxicity arises from the cyanide anion (CN^-) which prevents cellular respiration. These traditional thermal insulation materials may be cut and adjusted at the building site without any loss of thermal resistance, however, due to their relatively high thermal conductivities, walls, floors and roofs may become rather thick in order to achieve the desired thermal resistance of today's and the coming energy-efficient and zero emission buildings of the future.

Hence, there is a quest to make thermal insulation materials with substantially reduced thermal conductivity values.

State-of-the-art thermal insulation materials like vacuum insulation panels (VIP) [14-21], gas-filled panels (GFP) [22,23] and aerogels [24-29] have the potential of reaching substantially lower thermal conductivity values than the traditional thermal insulation materials. In addition, phase change materials (PCM) [30-32] may also become part of the thermal building envelope by absorbing and releasing energy when needed.

VIPs consist of an open-porous core surrounded by a laminate foil, where the laminate foil should have as low air and water vapour diffusion as possible in order to maintain a close-to-zero gas pressure, i.e. vacuum, inside the VIP core. Typically, VIPs with fumed silica cores have pristine (non-aged) thermal conductivity values between 3 to 4 mW/(mK), which with time will increase due to diffusion of air and moisture through the laminate foil and into the core (design values are often reported as 7 to 8 mW/(mK) taking into account diffusion/ageing effects and often also heat bridge effects caused by the enveloping laminate foil), and when perforated the thermal conductivity increases to about 20 mW/(mK). GFPs are in principle similar to VIPs, but with thermally low-conducting gases in their cores, where the pores in the GFPs are macroscopic pores and thus much larger than the VIP core pores which are in the micro and nano range. Although the potential of GFPs may seem high, they still have not come into relatively widespread use as e.g. VIPs, where currently VIPs may seem the better choice of these two. Note that both VIPs and GFPs can not be cut or adapted at the building site as that would cause a loss of vacuum and low-conducting gases, which none the less will also take place by diffusion in both VIPs and GFPs. Commercial aerogels as thermal insulation materials have thermal conductivity values typically in the range 12 to 20 mW/(mK), i.e. considerably higher values than for VIPs in their pristine condition and even than for typical VIP design values. Aerogels have an air content of 95 to 99 vol% and are thus mostly consisting of air by volume fraction, hence the aerogels are also very brittle. In addition, the aerogel products of today are very expensive. An advantage of aerogels is that they may be produced either as opaque, translucent or transparent materials, and they may also be cut and adjusted at the building site without any loss of thermal resistance.

Thus, there is a quest to make new thermal insulation materials as robust and flexible as the traditional thermal insulation materials and with as low thermal conductivity values as the state-of-the-art thermal insulation materials, more specifically as low as the VIPs in their pristine condition but with no increase of thermal conductivity during time.

The quest for making better thermal insulation materials is often concentrating the efforts around producing porous materials either filled with air, low-conducting gases (e.g. argon, krypton and xenon) or near-vacuum. A very interesting aspect in this regard is what happens when the pore diameters of the porous material are lowered into the nano range, i.e. that the thermal conductivity is substantially lowered due to the Knudsen effect, which basically is occurring when the pore diameter is reduced to a value smaller than the mean free path of the molecules in the pores [11-13]. For further details and elaborations around the Knudsen effect including the governing equations it is referred to the available literature within this research field.

In such a case and of immense significance is that very low values of the thermal conductivity can be reached even with air-filled pores at atmospheric pressure. Hence, by exploiting the Knudsen effect,

there is a large potential for being able to manufacture high-performance thermal insulation materials in form of nano insulation materials (NIM) [11-13] which will be robust towards any perforations and may be cut as desired at the building site without loss of performance due to the air-filled nanopores. The term super insulation materials (SIM) has also come into common usage within this field, with thermal conductivity values below 26 mW/(mK) (stagnant air value), 20 mW/(mK) or 10 mW/(mK) as examples of common borders for SIMs.

The objective of the work presented herein is to investigate the pathway of creating nano insulation materials by making hollow silica nanospheres (HSNS) by a sacrificial template method. In this method, templates of polystyrene (PS) are first fabricated, thereafter the PS templates are coated with a silica layer, and finally the PS templates are removed by burning them away by a diffusion process through the silica layer.

2. Experimental

Hollow silica nanospheres (HSNS) have been made by a sacrificial template method. Polystyrene (PS) template spheres were first fabricated and then coated with a silica layer. The silica precursor was either tetraethyl orthosilicate (TEOS) or water glass (Na_2SiO_3). The samples were placed in a heat incubator and the PS template spheres were burnt away by a diffusion through the enveloping silica layer. The final result was then the HSNS. Basically, the HSNS synthesis follows the schematic procedure as illustrated in figure 1. Further details and elaborations concerning the experimental conditions may be found in our earlier studies and a forthcoming one [13,33-38].

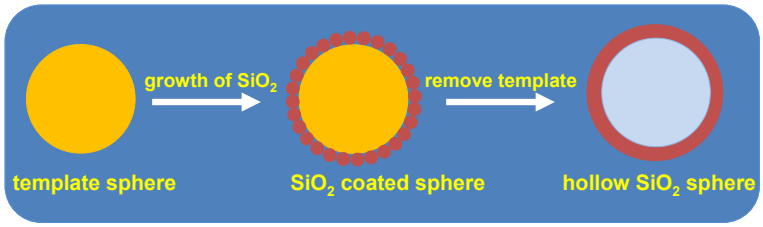

Figure 1. Illustration of the synthesis process when fabricating hollow silica nanospheres (HSNS) by the sacrificial template method.

The visual appearance of HSNS at nano level with their dimensional attributes were characterized by scanning electron microscopes (SEM) and transmission electron microscopes (TEM). Furthermore, the thermal conductivity λ of the HSNS was determined by calculation of the product $\lambda=\alpha\rho c_p$ where the diffusivity α was measured by a laser flash apparatus, the mass density ρ was calculated as $\rho=m/V$ from mass m and volume V measurements, and the specific heat capacity c_p was measured by differential scanning calometry (DSC). The details of these measurements and the corresponding HSNS syntheses will be published in a forthcoming and more extensive article [33]. In the following, a few excerpts and highlights will be given.

3. Results and discussion

The overall objective of this work is to gain insight into thermal transport mechanisms in nanoporous materials, thus enabling the opportunity of tailor-making materials with as low thermal conductivity as possible. That is, to fabricate nano insulation materials with the lowest possible thermal conductivity by utilizing the Knudsen effect.

The results presented herein are based on various syntheses of hollow silica nanospheres (HSNS) by the sacrificial template method [34-38], where polystyrene (PS) spheres have acted as sacrificial templates for these investigations. In general, the preparation of PS spheres with small dimensions and inner pore diameters well below 100 nm, which is needed in order to get the full effect of the Knudsen effect, has proven to be rather challenging in our experimental laboratory studies. Nevertheless, the

further below 100 nm in inner sphere diameter one may reach, the lower thermal conductivity values are expected, although other parameters like e.g. sphere shell thickness, sphere packing density and mesoporosity, may also influence this. However, the actually obtained and henceforth measured values may sometimes be quite different from the anticipated ones.

Examples of synthesized PS spheres are shown in the SEM images given in figure 2, depicting several spheres together and measurement of the diameter of a single sphere. In this particular case, these PS template spheres have diameters of 85 nm (figure 2).

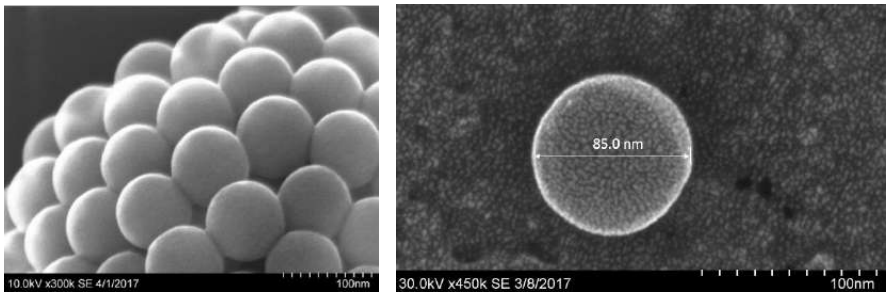

Figure 2. SEM images of PS template spheres with diameters of 85 nm.

After having prepared the PS template spheres, these templates were coated with a silica layer often consisting of small silica nanoparticles which give a relatively rough surface, whereas in some other cases the silica layer may look like a large, wrinkled silica sheet (not shown here), the wrinkled silica sheet surface being substantially smoother than the rough silica particle surface. These surface differences may greatly influence the interfacial interaction between the spheres when packed together, and hence also influence the thermal transport properties and the overall thermal conductivity.

Then, after the silica coating process, the PS template spheres were removed by heating the powder sample so that the PS could escape by diffusion through the silica shell, thereby leaving hollow silica nanospheres (HSNS) as the final result.

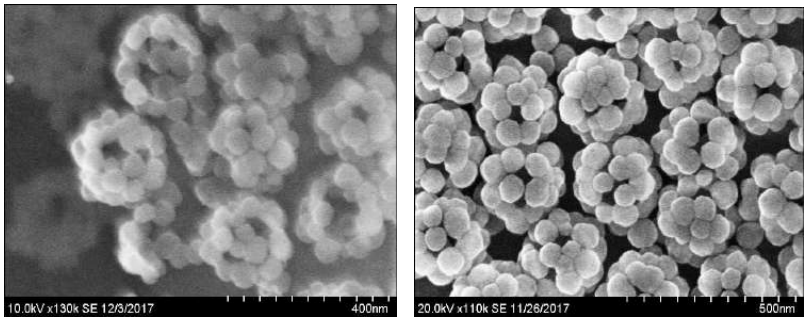

Figure 3. SEM images of HSNS with inner diameter 85 nm and two different shell thicknesses of 34 nm (left) and 67 nm (right).

Examples of the resulting HSNS are depicted in figures 3 and 4, the latter one also depicting the measurements of the silica nanoparticle diameters (shell thicknesses), where SEM images are given of HSNS with inner diameter 85 nm and two different shell thicknesses of 34 nm and 67 nm. As can be observed from the SEM images, the HSNS surfaces of these specific samples are rather rough and porous due to the relatively large silica particles constituting the HSNS shell.

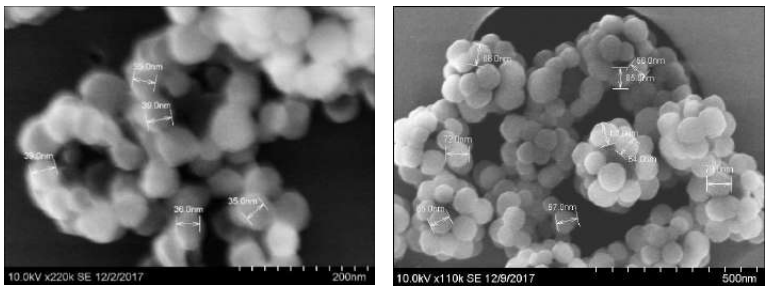

Figure 4. SEM images of HSNS with inner diameter 85 nm and two different shell thicknesses of 34 nm (left) and 67 nm (right), also depicting the measurements of the silica particle diameters.

In the study reported herein several different synthesis parameters have been varied in order to study their influence on the HSNS appearance (e.g. morphology) and their thermal conductivity. A detailed study of these aspects will be published in a more comprehensive and in-depth article [33]. As a main result and as anticipated, the thermal conductivity of HSNS was found to decrease with decreasing PS template sphere diameter and thus the resulting HSNS inner diameter. Here, the inner diameters of the synthesized HSNS were ranging between 85 to 213 nm. Correspondingly, the thermal conductivities of these HSNS have been measured (calculated based on measured values) between 14.3 to 29.7 mW/(mK). That is, the lowest measured thermal conductivity was found for the HSNS with the smallest inner diameters.

Thus, although a rather challenging task, one should attempt to make PS spheres as small as possible, i.e. with diameters well below 100 nm, e.g. down to 40 nm or even below. Success with the PS template preparation will probably lead to success with synthesizing HSNS with much lower thermal conductivities. The goal of manufacturing super insulation materials (SIM) would in such a case have been achieved, except from the commercial aspects in these matters. However, there are a lot of issues to be addressed and investigated much more in-depth in the field of making SIMs. In addition to specific synthesis aspects, general viewpoint issues like robustness assessment [39], durability and accelerated climate ageing [40], as well as life cycle analysis [41], should also be considered.

Nevertheless, to have reached as low value as 14.3 mW/(mK) in thermal conductivity, without having utilized very small inner sphere diameters and hence without having fully exploited the Knudsen effect (i.e. far below 100 nm), is promising with respect to forthcoming and future optimization attempts in the quest for SIMs.

4. Conclusions

Nano insulation materials (NIM) have been made as hollow silica nanospheres (HSNS) by utilizing the Knudsen effect with pore sizes, i.e. inner diameters of the HSNS, in the nano range.

The HSNS have been manufactured by employing a sacrificial template method, where the polystyrene (PS) templates have been removed from the silica spheres by heating and thus a subsequent diffusion process through the silica shell, hence leaving hollow silica spheres with inner diameters in the nano range as the result from the synthesis.

In the specific syntheses and experiments reported within this study, HSNS with inner diameters ranging between 85 to 213 nm have been made, with corresponding thermal conductivity values calculated to be between 14.3 to 29.7 mW/(mK), respectively, based on measured values of diffusivity, specific heat capacity, mass and volume, the two latter ones giving the mass density.

Acknowledgments

This work is supported by the Research Council of Norway within the Nano2021 program through the SINTEF and NTNU research project ”High-Performance Nano Insulation Materials” (Hi-Per NIM).

References

[1] Norton B, Eames P C, Mallick T K, Huang M J, McCormack S J, Mondol J D and Yohanis Y G 2011 Enhancing the performance of building integrated photovoltaics *Sol. Energy* **85** 1629-64
[2] Jelle B P, Breivik C and Røkenes H D 2012 Building integrated photovoltaic products: A state-of-the-art review and future research opportunities *Sol. Energy Mater. Sol. Cells* **100** 69-96
[3] Jelle B P 2013 The challenge of removing snow downfall on photovoltaic solar cell roofs in order to maximize solar energy efficiency - Research opportunities for the future *Energy Build.* **67** 334-51
[4] Breivik C, Jelle B P, Time B, Holmberget Ø, Nygård J, Bergheim E and Dalehaug A 2013 Large-scale experimental wind-driven rain exposure investigations of building integrated photovoltaics *Sol. Energy* **90** 179-87
[5] Fasana S and Nelva R 2013 Improvementt of the water resistancy in the integration of photovoltaic panels on traditional roofs *Constr. Build. Mater.* **48** 1081-91
[6] Jelle B P 2016 Building integrated photovoltaics: A concise description of the current state of the art and possible research pathways *Energies* **9** 1-30
[7] Jelle B P, Gao T, Mofid S A, Kolås T, Stenstad P M and Ng S 2016 Avoiding snow and ice formation on exterior solar cell surfaces - A review of research pathways and opportunities *Procedia Eng.* **145** 699-706
[8] Tripathy M, Sadhu P K and Panda S K 2016 A critical review on building integrated products and their applications *Renewable Sustainable Energy Rev.* **61** 451-65
[9] Andersson P-O, Jelle B P and Zhang Z 2017 Passive snow repulsion: A state-of-the-art review illuminating research gaps and possibilities *Energy Procedia* **132** 423-8
[10] Andenæs E, Jelle B P, Ramlo K, Kolås T, Selj J and Foss S E 2018 The influence of snow and ice coverage on the energy generation from photovoltaic solar cells *Sol. Energy* **159** 318-28
[11] Jelle B P, Gustavsen A and Baetens R 2010 The path to the high performance thermal building insulation materials and solutions of tomorrow *J. Build. Phys.* **34** 99-123
[12] Jelle B P 2011 Traditional, state-of-the-art and future thermal building insulation materials and solutions - Properties, requirements and possibilities *Energy Build.* **43** 2549-63
[13] Jelle B P, Gao T, Sandberg L I C, Tilset B G, Grandcolas M and Gustavsen A 2014 Thermal superinsulation for building applications - From concepts to experimental investigations *International Journal of Structural Analysis and Design* **1** 43-50
[14] Baetens R, Jelle B P, Thue J V, Tenpierik M J, Grynning S, Uvsløkk S and Gustavsen A 2010 Vacuum insulation panels for building applications: A review and beyond *Energy Build.* **42** 147-72
[15] Wegger E, Jelle B P, Sveipe E, Grynning S, Gustavsen A, Baetens R and Thue J V 2011 Aging effects on thermal properties and service life of vacuum insulation panels *J. Build. Phys.* **35** 128-67
[16] Sveipe E, Jelle B P, Wegger E, Uvsløkk S, Grynning S, Thue J V, Time B and Gustavsen A 2011 Improving thermal insulation of timber frame walls by retrofitting with vacuum insulation panels - Experimental and theoretical investigations *J. Build. Phys.* **35** 168-88
[17] Grynning S, Jelle B P, Uvsløkk S, Gustavsen A, Baetens R, Caps R and Meløysund V 2011 Hot box investigations and theoretical assessments of miscellaneous vacuum insulation panel configurations in building envelopes *J. Build. Phys.* **34** 297-324
[18] Alam M, Singh H and Limbachiya M C 2011 Vacuum insulation panels (VIPs) for building construction industry - A review of the contemporary developments and future directions *Appl. Energy* **88** 3592-602
[19] Haavi T, Jelle B P and Gustavsen A 2012 Vacuum insulation panels in wood frame wall constructions with different stud profiles *J. Build. Phys.* **36** 212-26
[20] Bouquerel M, Duforestel T, Baillis D and Rusaouen G 2012 Heat transfer modeling in vacuum insulation panels containing nanoporous silicas - A review *Energy Build.* **54** 320-36
[21] Kalnæs S E and Jelle B P 2014 Vacuum insulation panel products: A state-of-the-art review and

future research pathways *Appl. Energy* **116** 355-75
[22] Mills G L and Zeller C M 2008 The performance of gas filled multilayer insulation *Advances of Cryogenic Engineering: Transactions of the Cryogenic Engineering Conference* **53** 1475-82
[23] Baetens R, Jelle B P, Gustavsen A and Grynning S 2010 Gas-filled panels for building applications: A state-of-the-art review *Energy Build.* **42** 1969-75
[24] Baetens R, Jelle B P and Gustavsen A 2011 Aerogel insulation for building applications: A state-of-the-art review *Energy Build.* **43** 761-9
[25] Gao T, Jelle B P, Ihara T and Gustavsen A 2014 Insulating glazing units with silica aerogel granules: The impact of particle size *Appl. Energy* **128** 27-34
[26] Gao T, Jelle B P, Gustavsen A and He J 2014 Lightweight and thermally insulating aerogel glass materials *Applied Physics A: Materials Science & Processing* **117** 799-808
[27] Buratti C, Moretti E, Belloni E and Agosti F 2014 Development of innovative aerogel based plasters: Preliminary thermal and acoustic performance evaluation *Sustainability* **6** 5839-52
[28] Jelle B P, Baetens R and Gustavsen A 2015 Aerogel insulation for building applications *The Sol-Gel Handbook* Vol 3 D Levy and M Zayat eds (Weinheim, Germany: Wiley-VCH) pp 1385-412
[29] Sletnes M, Jelle B P and Risholt B 2017 Feasibility study of novel integrated aerogel solutions *Energy Procedia* **132** 327-32
[30] Demirbas M F 2006 Thermal energy storage and phase change materials: An overview *Energy Sources Part B* **1** 85-95
[31] Baetens R, Jelle B P and Gustavsen A 2010 Phase change materials for building applications: A state-of-the-art review *Energy Build.* **42** 1361-8
[32] Kalnæs S E and Jelle B P 2015 Phase change materials and products for building applications: A state-of-the-art review and future research opportunities *Energy Build.* **94** 150-76
[33] Mofid S A, Jelle B P, Zhao X, Gao T, Grandcolas M, Ng S and Yang R 2019 Utilization of size-tunable hollow silica nanospheres for building thermal insulation applications (To be published)
[34] Gao T, Jelle B P, Sandberg L I C and Gustavsen A 2013 Monodisperse hollow silica nanospheres for nano insulation materials: Synthesis, characterization, and life cycle assessment *ACS Appl. Mater. Interfaces* **5** 761-7
[35] Gao T, Jelle B P, Sandberg L I C and Gustavsen A 2015 Thermal conductivity of monodisperse silica nanospheres *Journal of Porous Media* **18** 941-7
[36] Gangåssæter H F, Jelle B P and Mofid S A 2017 Synthesis of silica-based nano insulation materials for potential application in low-energy or zero emission buildings *Energy Procedia* **122** 949-54
[37] Ng S, Jelle B P, Sandberg L I, Gao T and Mofid S A 2018 Hollow silica nanospheres as thermal insulation materials for construction: Impact of their morphologies as a function of synthesis pathways and starting materials *Constr. Build. Mater.* **166** 72-80
[38] Grandcolas M, Jasinski E, Gao T and Jelle B P 2019 Preparation of low density organosilica monoliths containing hollow silica nanospheres as thermal insulation materials *Mater. Lett.* **250** 151-4
[39] Jelle B P, Sveipe E, Wegger E, Gustavsen A, Grynning S, Thue J V, Time B and Lisø K R 2014 Robustness classification of materials, assemblies and buildings *J. Build. Phys.* **37** 213-45
[40] Jelle B P 2012 Accelerated climate ageing of building materials, components and structures in the laboratory *J. Mater. Sci.* **47** 6475-96
[41] Schlanbusch R D, Jelle B P, Sandberg L I C, Fufa S M and Gao T 2014 Integration of life cycle assessment in the design of hollow silica nanospheres for thermal insulation applications *Build. Environ.* **80** 115-24

Article VII

Sohrab Alex Mofid, Bjørn Petter Jelle, Xinpeng Zhao, Tao Gao, Mathieu Grandcolas, Bridget Cunningham, Serina Ng and Ronggui Yang, **Utilization of size-tunable hollow silica nanospheres for building thermal insulation applications**, *Journal of Building Engineering,* 31 (2020) 101336.

Journal of Building Engineering 31 (2020) 101336

Contents lists available at ScienceDirect

Journal of Building Engineering

journal homepage: http://www.elsevier.com/locate/jobe

Utilization of size-tunable hollow silica nanospheres for building thermal insulation applications

Sohrab Alex Mofid [a,b,*], Bjørn Petter Jelle [a,d], Xinpeng Zhao [b], Tao Gao [a], Mathieu Grandcolas [f], Bridget Cunningham [c], Serina Ng [d], Ronggui Yang [b]

[a] Norwegian University of Science and Technology (NTNU), Department of Civil and Environmental Engineering, NO-7491, Trondheim, Norway
[b] University of Colorado Boulder (CU-Boulder), Department of Mechanical Engineering, CO-80309, Colorado, USA
[c] University of Vermont (UVM), Department of Art and Art History, VT-05405, Vermont, USA
[d] SINTEF Building and Infrastructure, Department of Materials and Structures, NO-7465, Trondheim, Norway
[f] SINTEF Industry, Department of Materials and Nanotechnology, NO-0373, Oslo, Norway

ARTICLE INFO

Keywords:
Nano insulation material
Hollow silica nanosphere
HSNS
Superinsulation material
Thermal conductivity

ABSTRACT

Hollow silica nanospheres (HSNS) have been the subject of intense studies as a possible building block that may successfully bring about nano insulation materials (NIM) with substantially reduced thermal conductivity. The reported thermal conductivity values of the HSNS are currently ranged between 20 and 90 mW/(mK). In this work, we have investigated the thermal properties of HSNS as a function of the corresponding structural parameters such as inner pore diameter, porosity, shell thickness, and size of the silica nanoparticles constituting the shell of HSNS. HSNS with sizes less than 100 nm was specifically synthesized in an attempt to lower the expressed thermal conductivity values to be below 20 mW/(mK), which may be used as a potential target towards superinsulation materials used in building applications. Furthermore, synthetic approaches to gain insights into the mechanism and formation of HSNS, i.e., the influence of reaction parameters on the structural characteristics of HSNS, have been thoroughly discussed in this work.

1. Introduction

Hollow silica nanospheres (HSNS) have garnered much attention due to their unique properties such as low density, high porosity, large surface area to volume ratio and encapsulating ability [1,2], which have led to significant advances in applications for biomedical, electrical, and construction sectors [3–7]. HSNS may provide noticeable advantages to explore for miscellaneous thermal insulation applications [8]. For example, previous studies have demonstrated thermal insulation properties of HSNS, i.e., a reduced low thermal conductivity of about 20–90 mW/(mK), comparable to that of stagnant air of about 26 mW/(mK) [8–12]. It is intriguing that HSNS may potentially enable a new generation of nano-porous insulation materials with small pore sizes and low volume fraction of solid [13,14].

Distinctive advantages of HSNS for thermal insulation applications are amongst others, their controllability, i, e., thermal properties of HSNS being promptly modified by utilization of their structural characteristics, such as inner pore diameter and shell thickness. In general, HSNS can be classified as an air cavity enclosed by an inorganic shell with tailored structural features, where the voids are usually correlated to the use of sacrificial templates during the synthesis of HSNS [15]. Thus, the inner pore size of HSNS can be readily controlled by using the templates, e.g. polyacrylic acid (PAA) or polystyrene (PS), with different dimensions; the shell thickness of HSNS can be adjusted by a controlled growth and deposition of silica nanoparticles; and the shell morphology, depending on the reaction conditions, may be dense or porous. Therefore, it is possible to capitalize on the apparent structural features of HSNS to tailor their size-dependent thermal insulation properties.

Currently, the lowest reported thermal conductivity values of HSNS are typically of about 20 mW/(mK). For example, Liao et al. reported a thermal conductivity of ~20 mW/(mK) using 3ω method for HSNS powder with a typical inner diameter of ~200 nm and a shell thickness of ~40 nm. Gao et al. (2013) reported a thermal conductivity value of ~20 mW/(mK) using HotDisk measurement for HSNS powder with an inner pore diameter of about ~150 nm and a shell thickness of ~20 nm. Recently Li et al. (2014) presented a theoretical model to analyze the

* Corresponding author. Norwegian University of Science and Technology (NTNU), Department of Civil and Environmental Engineering, NO-7491, Trondheim, Norway.
E-mail address: sohrab.mofid@ntnu.no (S.A. Mofid).

https://doi.org/10.1016/j.jobe.2020.101336
Received 5 May 2019; Received in revised form 1 February 2020; Accepted 4 March 2020
Available online 7 March 2020

parameter variation on the thermal conductivity values of HSNS assemblies. They suggested that HSNS have the potential to reach a thermal conductivity as low as ~10 mW/(mK). Prior studies mostly account for thermal conductivity values of HSNS powder with pore sizes greater than 150 nm. However, the size effect on the thermal conductivity reduction becomes more prominent as the dimension reaches sub-100 nm range [16], where the pore size becomes comparable to the mean free path of the gas molecules (~70 nm, 300 K, 1.0 atm) that may well alter the gaseous thermal conductivity values. The existing 10 mW/(mK) gap between theoretical and experimental values may be bridged by investigating, say, inner pore diameter or shell thickness. However, it remains a significant challenge to experimentally validate the HSNS thermal properties.

The objective of this study is to optimize the thermal performance of HSNS with respect to parameter variations, specifically HSNS with inner pore sizes less than 100 nm, in an attempt to substantially lower the thermal conductivity far below 20 mW/(mK), which may present a less expensive alternative towards superinsulation materials (SIM).

2. Experimental

2.1. Chemicals and materials

Reagent grade styrene (St), polyvinylpyrrolidone (PVP; Mw ≈ 40k Da), potassium sulfate (KPS), ammonium hydroxide (NH_4OH, 28–30 wt %), tetraethyl orthosilicate (TEOS), ethanol (96%) and methanol (99.8%) were purchased from Sigma Aldrich and employed as as-supplied without additional purifications. Monodisperse polystyrene spheres (PS), with mean diameter of 46 nm (SD 5 nm) and 85 nm (SD 2 nm) were purchased from Corpuscular Inc., New York, USA and Micro Particles GmbH, Germany, respectively. The commercial PS spheres were used as received. The mean diameter of the PS purchased from Corpuscular Inc., New York, USA was remeasured using both Hitachi S-5500 SEM and Nanosight-LM10 nanoparticle analysis, and corrected at 79 nm (SD 5 nm) not the original 46 nm advertised by the manufacturer.

2.2. Methodology

Various fabrication methods of HSNS with details can be found from earlier studies [17–24]. In this study, HSNS was formed using the sacrificial-template method as depicted in transmission electron microscope (TEM) images given in Fig. 1. Polystyrene (PS) was used as template for providing the nucleation site for the growth of silica shell, which in theory can be any other material with suitable morphology, such as liquid droplets, solid particles [10] or gas bubbles [11,25]. Given the widespread knowledge that exists within silica-based materials, as well as possessing certain characteristics, e.g. abundance, low-cost, low thermal conductivity, non-flammable and environmentally friendliness of silica, it is considered as one of the best possible candidate materials for achieving the hollow nanospheres for thermal insulation purposes. Tetraethyl orthosilicate (TEOS) was used as the silica precursor to form the shell structure. It is worth to note that other silica source materials such as water glass (Na_2SiO_3) may also be used for successful synthesis of HSNS [24].

2.3. Synthesis of polystyrene templates

Polystyrene (PS) templates were synthesized via an emulsion polymerization process, where the ratio of PVP/St was varied to adjust the size of the obtained PS spheres. For a typical synthesis, 10 g of styrene and desired amount of PVP were homogenized in 100 mL of distilled water at room temperature (RT) for 10 min in a 250 mL Erlenmeyer round flask. The mixture was maintained at a constant temperature of ~70 °C applying a hotplate with heat-on block under stirring conditions of 450 rpm. Chosen KPS amount dissolved in 10 mL of distilled water was then added to the mixture slowly and the reaction solution was kept stirring for 24 h. The obtained PS solutions are designated as PS-size, e.g. PS-90, as shown in Table 1.

2.4. Coating of PS templates with TEOS and subsequent calcination

Tetraethyl orthosilicate (TEOS) was used as the silica precursor to form the shell structure. For a typical synthesis, 8 g of PS solution was dispersed in 140 mL of 96% ethanol at 450 rpm for 15 min. Then 4.5 mL of NH_4OH was added and pH value of the system was maintained at around 11. Afterwards, the mixture was stirred for 15 min. TEOS solution (5 mL TEOS in 5 mL of ethanol) was then added to the Erlenmeyer round flask using a Nexus 3000 syringe pump. Four different infusion pump rates were adopted, i.e. 15, 35, 160, and 450 μl/min. The final mix was left stirring at 450 rpm for 8 h at RT. All the coated PS-silica samples were subjected to centrifugation at 5000 rpm for 15 min, air dried overnight and calcined at 440 °C for 6–8 h (heating rate = 5 °C/min) to remove the PS template cores by calcination.

2.5. Characterization

The commercial Netzsch laser flash apparatus (LFA 457) and Netzsch differential scanning calorimetry (DSC 204 F1 Phoenix) were used for the thermal diffusivity α and the specific heat capacity c_p measurements, respectively. A special sample holder specifically designed for powder samples were used in the measurements. Thermal conductivity λ values of HSNS samples can be calculated by Refs. [26,27]:

Table 1
Obtained PS samples of different sizes as result of varying the PVP/St ratio and KPS amount.

Polystyrene-nm	PVP/Styrene Ratio	KPS	Weight/Volume (Aqueous Solution)
PS-213	0.1334	0.131	22%
PS-150	0.1612	0.142	22%
PS-100	0.1976	0.166	22%
Commercial PS-85 (Micro Particle GmbH, Germany)	–	–	5%
Commercial PS-79 (Corpuscular Inc, New York)	–	–	5%

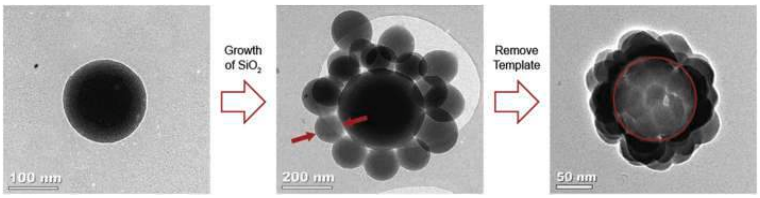

Fig. 1. TEM images showing (left) PS nanosphere used as the template, (middle) PS template coated with silica nanoparticles synthesized from hydrolysis of TEOS, and (right) well-defined core-shell structure of a hollow silica nanosphere after template removal through calcination at 440 °C.

$$\lambda = \alpha \rho c_p \quad (1)$$

The final thermal conductivity values were the result of arithmetic mean of four individual measurements under the same conditions. A transmission electron microscope (TEM, JEM-2010) and a scanning electron microscope (SEM, Hitachi S-5500) were employed to characterize the morphology and microstructures of the as-synthesized materials. Analysis with secondary electrons were employed at an acceleration voltage of 10 kV and emission current of 10 μA while 30 kV was employed for bright field transmission mode in S(T)EM mode. Nanosight-LM 10 with blue laser (405 nm wavelength) was adopted to keep track of the count and sizing of the nanoparticles on individual basis.

3. Results and discussion

3.1. Size determination of PS templates

Although a few articles have reported the synthesis of nano- or micro-sized PS spheres with respect to various chemical reaction conditions such as initiator types, stabilizer types and concentration and styrene concentrations [28–30]; synthesis of stable and highly monodispersed PS spheres with small sizes, e.g. less than 100 nm, remains challenging. In this study, a series of experiments were performed to investigate the role of the initiator system (KPS) in determining particle size distribution. Systematic synthesis of highly monodispersed PS spheres as a function of the PVP/St ratio can be found from our earlier study displayed in Fig. 2b. Fig. 2a presents newly achieved PS sizes in relation to varying PVP/St proportion. Smallest PS size (100 nm) was achieved for PVP/St: 0.1976 g shown in Table 1. In addition, we found that once the PVP concentration reached a certain value, i.e. PVP concentration 2.1 g in PVP/St: 0.21 g (Fig. 2a) size of the PS spheres no longer changed. On the contrary, further increase of PVP/St ratio prevented the formation of monodisperse PS spheres and resulted in the formation of bimodal PS particles. This may be due to the over-dispersing effectiveness of PVP on St. which increases the surface tension on PS particles and halts the formation of monodisperse particles. Furthermore, in the absence of PVP, polydisperse PS particles (spherical to oval) with varying sizes from nano to micron range were formed, leaving the PS particles exposed to the slightest variation in KPS and temperature during the polymerization process. PVP participates in polymerization reaction as a stabilizer or surfactant and the growth profile of the PS particles can be attributed to the stabilizing effect of the surfactant PVP on styrene. Further details concerning the effect of PVP on the size of PS particles can be found from our earlier study [24].

Therefore, the control over size and polydispersity is thus important because of the close relationship between properties of the polymer and the particle sizes. In this study, the mean particle size was determined using a scanning electron microscope (SEM, Hitachi S-5500) and the size distribution is precisely measured by a Nanosight-LM10 nanoparticle analysis system based on conventional optical microscope, using a blue laser (405 nm wavelength) source to illuminate nano-scale particles that appear individually as point-scatterers moving under Brownian motion. This way, the polydispersity and multimodal system are instantly recognisable and quantifiable. For example, the sample prepared at optimal PVP/St ratio of 0.1976 (Fig. 4) show a polydispersity index (PDI) of $\leq$0.1, confirming a narrow particle size distribution. Fig. 3 and Fig. 4 both display the polystyrene spheres with a mean diameter of 85 $\pm$ 2 nm and 100 $\pm$ 3 nm, respectively, which fulfils the goal of achieving $\leq$100 nm dimension.

3.2. The effect of the initiator system on particle size and distribution

Potassium persulfate (KPS) (an anionic type initiator), is one of the most commonly used initiators in the conventional emulsion polymerization in aqueous solutions [31–33]. In this work we used KPS for the polymerization of styrene in the presence of both distilled water and a mixture of distilled water and methanol as the co-solvent (20%). Addition of methanol reduces the surface interfacial tension between the aqueous phase and particles. Similar studies both by Adelnia et al. [34] and Kim et al. [35], shows that the addition of methanol causes an increase in medium viscosity which can facilitate the particle coagulation. Particle coagulation is a process that transpires during the particle nucleation/growth. Certain factors like e.g. viscosity of the media and reaction temperature directly influence this process [31,34]. The theory of Smith-Edwart (micellar theory) as well as a separate study by Sajjadi et al. [36], both anticipated that the particle number was proportional to the 0.40th and 0.39th power of the KPS concentration, respectively [37]. Both theories correlate the particle size with initiator concentration, suggesting that the particle size of the final medium decreases with increasing the initiator concentration. However, in our study we found out the particle size systematically increased with increasing of the initiator concentration (90, 135, 155, 195 nm at 0.13, 0.15, 0.174, 0.1968 g, respectively). Our result shows an opposite trend to that of standard emulsion polymerization. This is because as KPS concentration increased, a larger number of free radicals were formed, which in turn increased the number of polymer nuclei and promoted particle coagulation. In addition, an increase in the KPS concentration accelerated the growth of existing oligomers, nuclei and nanoparticles [38]. The particle sizes corresponding to different initiator concentrations are depicted in Fig. 5.

3.3. Coating of the PS templates with TEOS

To form a regular and uniform silica nanoparticles layer, tetraethyl orthosilicate (TEOS) was hydrolyzed and condensed on the PS sphere

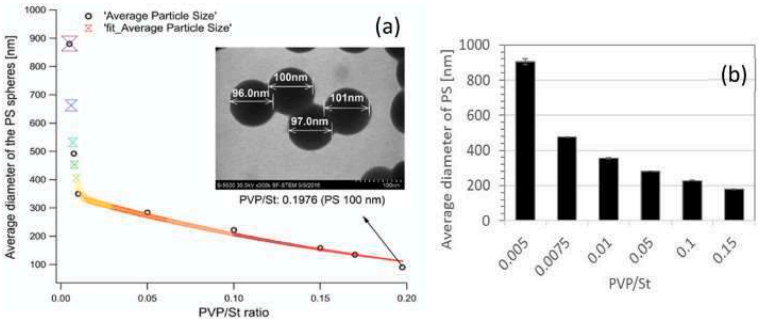

Fig. 2. (a) Graph embedded with the SEM image shows the smallest mean diameter of PS spheres in this work was achieved for PVP/St: 0.1976 at 100 nm, (b) Graph from our previous study by Ng et al. [24] displays dependence of PS particles as a function of PVP/St.

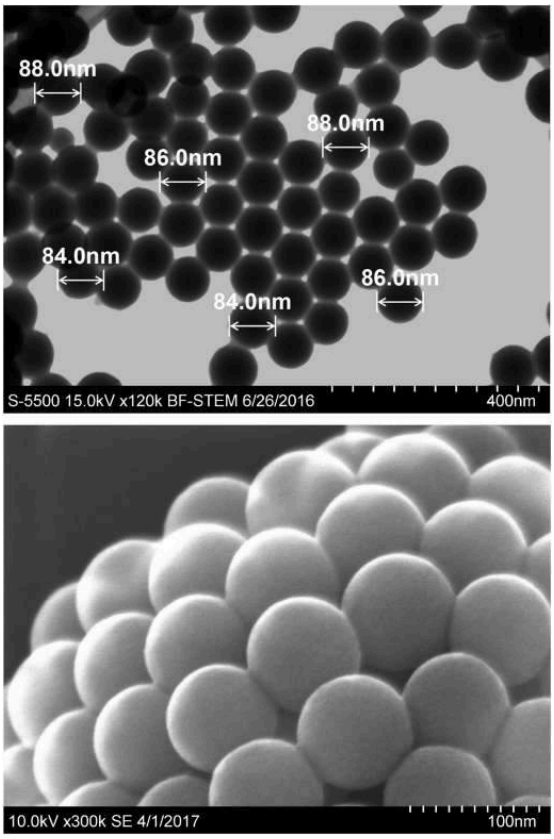

Fig. 3. SEM images displaying size of the polystyrene spheres, PS-85 (top) and it'surface morphology (bottom).

surface. Hollow SiO_2 spheres with mesoporous shells were then achieved after a thermal degradation process to remove the PS template core. In this study, coating of the samples through a modified Stöber approach under alkaline condition was successful and showed high reproducibility and stability in its formation. The nanospheres were formed demonstrating a raspberry-like morphology (Fig. 6). After calcination at 440 °C, the HSNS samples kept the same appearance and emerged as monodispersed globes of consolidated silica particles depicted in Fig. 6. Under SEM and TEM imaging, these nanospheres were found to be hollow, confirming the successful removal of the PS particle template after the calcination (Fig. 7, left).

From the TEM image it can be seen that upon calcination, the loosely bound silica particles are adhered more tightly together and there still remains gaps between individual silica nanospheres within each coating, exhibiting a highly porous structure. Usually, the shell thickness is measured from the projection in the TEM, which is given by black shaded ring that encircles the hollow core. However, in this study, the surface of the particles doesn't appear to be smooth and particles do make aggregates and clusters, in addition, no clear sintering necks between spheres or clusters can be observed in the TEM image. Therefore, to avoid confusion and for better precision, shell thickness is determined as the average size of silica nanoparticles forming a monolayer around the PS template after calcination; which accounts for average size of the individual silica nanoparticles along with the average size of the contact area between adjacent silica nanoparticles. Fig. 6 shows HSNS samples with the same inner pore diameter but with different shell thicknesses, where the variation of the shell thickness is directly due to the amount of TEOS used during the coating process.

To achieve complete coverage of the silica shell, TEOS concentration has to be higher than 0.2 M. This signified that a mono-to bilayer of nanosilica was formed around the PS template during the coating process. The synthetic system was sensitive to pH value. Relatively low pH values led to incomplete silica coating procedures while free silica particles and roughened SiO_2-shell surfaces were observed at higher pH-values ($\geq$10.0) as shown in Fig. 7, indicating that heterogeneous nucleation of the silica precursor occurred in the reaction medium. Creation of individual silica nanospheres may be attributed to the formation of largely segregated silicate oligomer species under alkaline conditions, which cannot undergo inter-penetration before drying. The shape and size of the final products are impartial to the mode of TEOS/ethanol addition, suggesting that the synthesis route of the silica monomers is particularly based on the size of the PS templates, surface

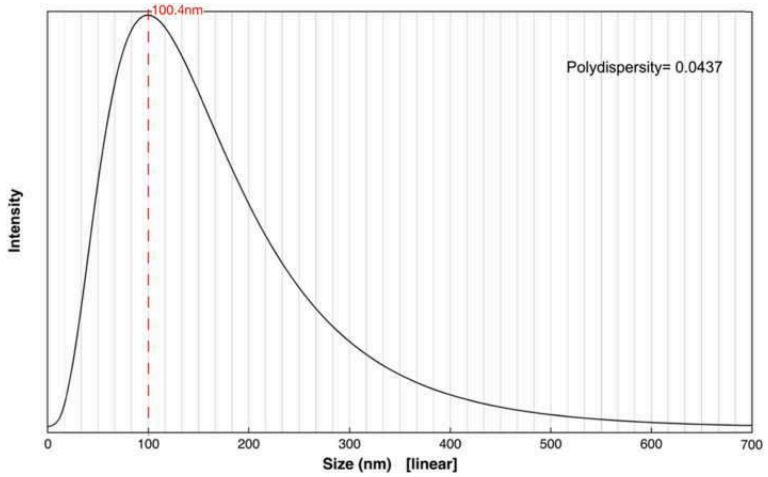

Fig. 4. Nanosight LM10 graph displays the unimodal result measured for the as-synthesized polystyrene sample with mean diameter 100.4 nm (PS-100) and Polydispersity Index 0.0437.

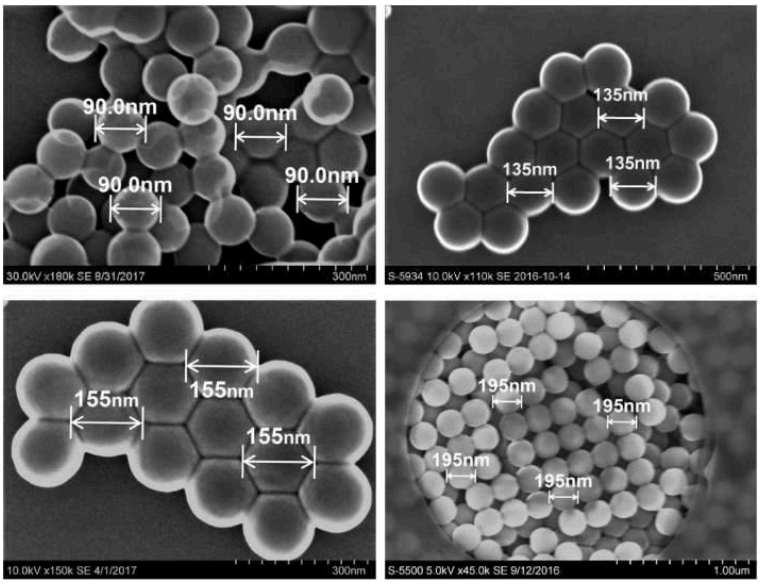

Fig. 5. SEM images of the measured PS particles prepared by one-step polymerization of styrene with various amount of KPS as the sole polymerization instigator parameter and methanol solution as co-solvent to the aqueous phase (weight ratio:20/80).

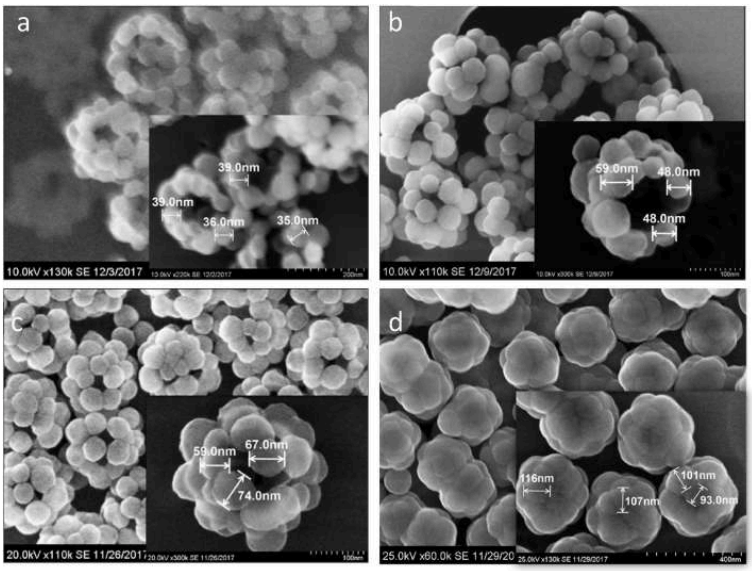

Fig. 6. SEM images display measured nanosilica particles prepared from (a) 4 mL, (b) 5 mL, (c) 7 mL and (d) 15 mL TEOS, forming mono-to bilayer around the PS template with average particle sizes (a) 34 nm, (b) 54 nm, (c) 67 nm and (d) 104 nm, defining the shell thickness.

tension of forming silica particles and their interaction with medium, rather than the kinetic parameters or condition, which points towards a robust formation pathway.

3.4. Thermal conductivity of HSNS

The effective thermal conductivity of HSNS is the coupling result of λ_{solid} – thermal conductivity of solid backbone of HSNS, λ_{gas} – thermal conductivity of gas is governed by both the gas inside the HSNS nanoscale pores and the gas in the inter-HSNS as depicted in Fig. 8. Here the contribution of infrared thermal radiation on the effective thermal conductivity can be ignored at room temperature according to the earlier studies [39,40]. It can be seen from the internal nanostructure shown in Fig. 8 that the structural parameters, such as shell thickness, contact area between neighboring nanoparticles, hollow spheres size and the packing density could influence the heat conduction of solid

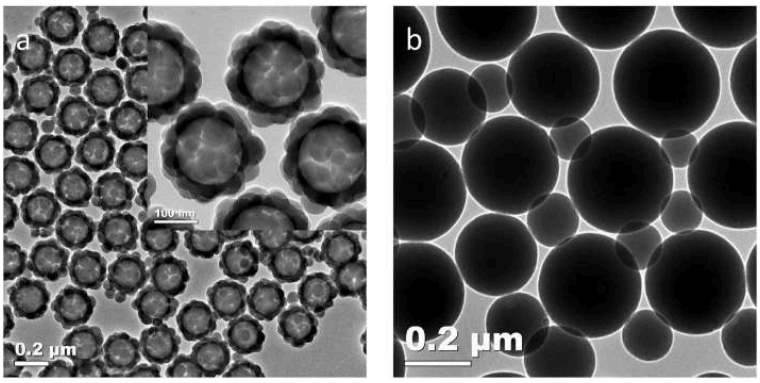

Fig. 7. (a) TEM image showing successful formation of uniformly coated and roughened SiO_2-shell surfaces of HSNS synthesized from PS-150 at pH-value 11.0, (b) randomly deposited and unsuccessful uniform coating of silica nanoparticles on the PS surface at lower pH-value 8.0.

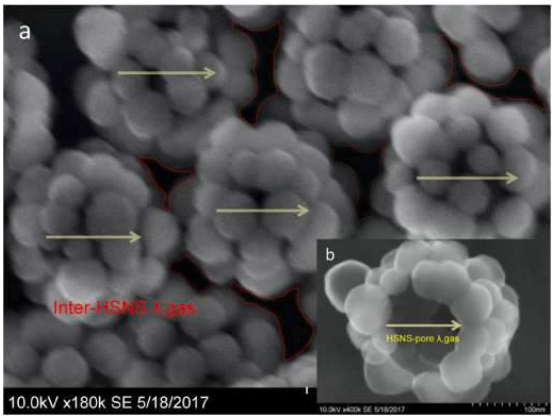

Fig. 8. Schematic illustration of various contributions to thermal conductivity in HSNS.

phase. For gaseous thermal conductivity λ_{gas}, as shown in Fig. 8, the spherical shells separate air in two ways, i.e. one enclosed in the spherical shell (yellow arrows in Fig. 8b), whose amount and pressure is controlled during synthesis, where the thermal conductivity is largely affected by the inner pore diameter inside the spherical shell [41]. The second one fills the inter-particle spaces between the silica nanospheres connecting to the ambient environment (red delimitations in Fig. 8a). The latter presents a similar situation as gas in open-cell porous medium such as aerogels [42], in which gaseous thermal conductivity is mainly determined by structural parameters such as packing density, and the outer diameter of the hollow spheres. Clearly the thermal conductivities of both gas and solid can be tailored by tuning the structural parameters of the HSNS during synthesis.

Fig. 9 displays the effective thermal conductivities of the samples measured using the laser flash method after calcination as function of inner diameter and shell thickness. The lowest thermal conductivity value is recorded for HSNS-2 sample with the smallest inner pore diameter (85 nm) and the largest structural density (Table 2). It is known that the solid thermal conductivity of the open-cell structure increases with the increase of the structural density [43–45]. The result indicates that the gaseous thermal conductivity of the sample HSNS-2 has been greatly suppressed due to a strong Knudsen effect inside the shell. The study by Wang et al. [46] shows thermal conductivity of air can be reduced to less than 10 mW/(mK) as the cell size decreased to 100 nm in an polymeric foam. Similar study by Notario et al. [47] also shows close correlation between the pore size and the thermal conductivity justified by a strong Knudsen effect. The Knudsen effect has been previously experimentally demonstrated in other porous materials, i.e., aerogels [48,49], ceramics [50], foams [47,51]; suggesting that reducing the pore size remains an effective way to substantially reduce the gaseous thermal conductivity which is the key contributor to the effective thermal conductivity of porous materials.

Furthermore, a measured ~6 mW/(mK) difference in thermal conductivity is also found between the HSNS-2 (5 mL TEOS, D = 85 nm, ST = **34** nm) and HSNS-2 (14 mL TEOS, D = 85 nm, ST = **104** nm) shown in Fig. 9. When the average shell particle size decreases e.g. in Fig. 6d (104 nm) and Fig. 6a (34 nm), the contact area is reduced, thus exhibiting larger porosity. According to the study by Lin et al. [52], smaller thermal contact resistance due to the enhanced contact between nanoparticles will lead to a higher thermal conductivity. Moreover, the numerical results by Li et al. [8] and Jia et al. [11] also show that, decreasing the spherical shell thickness or reducing the contact area can efficiently lower the contribution from the solid phase. The obtained values show consistency with the previous results, indicating that one possible reason behind reduction of the thermal conductivity is due to the reduced contact area inbetween adjacent silica nanoparticles and the shell thickness, which can lower the contribution from the solid phase. The trend of provided results proves that tuning the structural parameters such as inner pore diameter, shell thickness and contact area between neighboring nanoparticles can effectively reduce the effective thermal conductivity and enhance the overall thermal performance of HSNS assemblies.

4. Limitations and future work

In this work, we have experimentally validated that the reduction in thermal conductivity is only due to combination of the Knudsen effect and modification of the contribution of the solid phase. However, at a relative low density (0.1 g/cm^3) and reduced pore size (≤85 nm), further reducing the pore diameter and significant thinning of the shell thickness: 1- is very complicated to achieve experimentally, 2- doesn't ensure further reduction in effective thermal conductivity and better insulation performance. This may be due to significance of contribution from the thermal radiation as the pore, shell size become so thin compared to infrared electromagnetic radiation wavelength which will exhibit strong interference and scattering behaviours [46,53,54]. In another word, reduced thermal conductivity contributed by the thermal conduction can be compensated by an increased radiative thermal

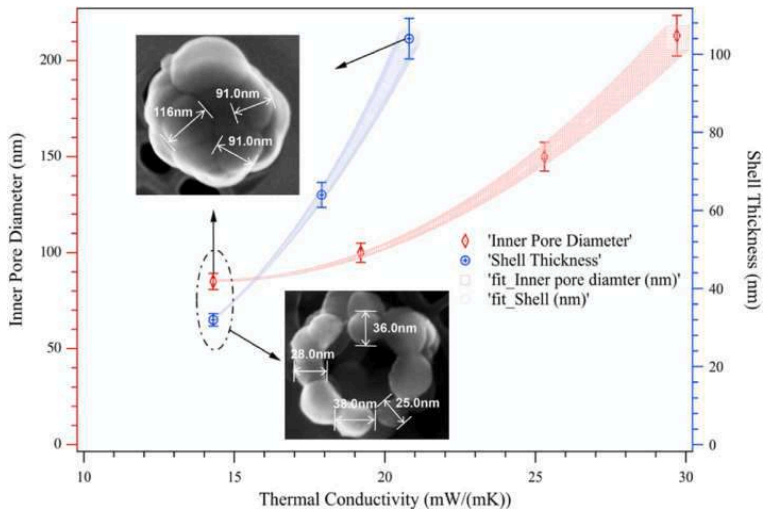

Fig. 9. Thermal conductivity in relation to varying inner pore diameter (constant shell thickness 34 nm) ranging from 85 nm to 213 nm (red line), and thermal conductivity in relation to varying shell thickness (constant inner pore diameter 85 nm) ranging from 34 nm to 104 nm (blue line). (For interpretation of the references to colour in this figure legend, the reader is referred to the Web version of this article.)

Table 2
Measured thermal conductivity values of HSNS samples with various inner pore diameters and constant shell thickness of ~34 nm.

Samples	Inner diameter$D_{100\ avg}$ (nm)	Thermal diffusivity (mm^2/s)	Density (g/cm^3)	Heat capacity(J/(gK))	Thermal conductivity (W/(mK))[d]
HSNS-1[a]	78 ± 2	–	–	–	–
HSNS-2[b]	85 ± 2	0.102	0.190	0.74	0.0143
HSNS-3	100 ± 3	0.144	0.180	0.74	0.0192
HSNS-4[c]	150 ± 5	0.195	0.175	0.74	0.0253
HSNS-5	213 ± 5	0.236	0.170	0.74	0.0297
Bulk silica	–				~1.4
Silica aerogel	–		0.12		~0.017[39]

[a] Size of the commercial polystyrene nanospheres (w/v 5% aqueous) by manufacturer Corpuscular Inc., New York, USA, D = 46 nm, was remeasured by us using Hitachi S-5500 SEM and Nanosight-LM10 nanoparticle analysis and corrected at, D = 79 nm. Polystyrene nanospheres could not be coated successfully, therefore thermal conductivity measurement and analysis wasn't performed for this sample.

[b] Commercial polystyrene nanospheres (w/v 5% aqueous) with mean diameter of 85 nm and standard deviation of 2 nm were purchased from Micro Particles GmbH, Germany.

[c] Monodisperse 150 nm PS nanospheres were chosen to be coated using 4, 5, 7 and 15 mL of TEOS, to achieve controlled proportion of shell thickness under stable conditions, the average between highest (213 nm) and lowest (79 nm) of PS size was chosen for shell thickness variations.

[d] The uncertainty of the measurement is evaluated based on the measurement errors and the systematic errors (~5.0%).

conductivity at lower densities in the nanoscale. The current transient methods, including the laser flash apparatus doesn't consider the thermal radiation in their theoretical models, but based on our calculation and an earlier study [46], we strongly believe that there exist an approximate 20% contribution from the thermal radiation at the nanoscale within the lower densities. Future work should emphasize on the addition of opacifier or reflecting agent to effectively block the infrared radiation and modulate the emissivity at different temperatures. In addition, hydrophobic treatment to further avoid vapor condensation, which in turn increases the thermal conductivity remains a crucial issue that has to be addressed in the future experimental study.

5. Conclusions

In this work, hollow silica nanospheres (HSNS) with varying inner pore diameter and shell thickness sizes have been successfully synthesized to study the influence of structural parameters on the effective thermal conductivity. The structural features of HSNS were controlled by applying different polystyrene (PS) sacrificial nanosphere templates in order to synthesize HSNS with different properties. The results showed that decreasing the size of the sacrificial template (polystyrene nanoparticles), from ~213 nm to 80 nm, can achieve a suppressed thermal conductivity of ≤20 mW/(mK), suggesting a strong Knudsen effect inside the shell which lowered the contribution of the gas phase. In addition, given the same inner pore diameter, we found that decreasing the average nanoparticle size, constituting shell thickness, from ~104 nm to 34 nm, showed a reduced ~6 mW/(mK) difference in thermal conductivity which exhibited a lowered contribution from the solid phase. Our study validated the size-dependent thermal conduction at the nanoscale and demonstrated that HSNS assemblies clearly yield thermal properties intermediate to those of gas and solid by tuning the structural parameters. Hence, due to the versatility in modifying their thermal properties, HSNS represent a foundation for the development of super-insulation material that can be used for thermal building insulation applications.

Declaration of competing interest

The authors declare no conflict of interest.

CRediT authorship contribution statement

Sohrab Alex Mofid: Conceptualization, Investigation, Data curation, Formal analysis, Writing - original draft. **Bjørn Petter Jelle:** Supervision, Formal analysis, Writing - original draft. **Xinpeng Zhao:** Formal analysis, Validation, Writing - original draft. **Tao Gao:** Methodology, Writing - original draft. **Mathieu Grandcolas:** Writing - review & editing. **Bridget Cunningham:** Visualization. **Serina Ng:** Writing - review & editing. **Ronggui Yang:** Formal analysis, Writing - original draft.

Acknowledgements

This work has been supported by the Research Council of Norway through the SINTEF and NTNU research project "High-Performance Nano Insulation Materials" (Hi-Per NIM, project no. 250159) within the NANO2021 program. Furthermore, the Research Council of Norway is acknowledged for the support to the" Norwegian Micro- and Nano-Fabrication Facility" (NorFab, project no. 245963/F50). We would like to further thank Yinda Yu from Material Science and Engineering Department for his help with transmission electron microscope.

References

[1] X. Wang, J. Feng, Y. Bai, Q. Zhang, Y. Yin, Synthesis, properties, and applications of hollow micro-/nanostructures, Chem. Rev. 116 (18) (2016) 10983–11060.
[2] T. Sugama, B. Lipford, Hydrothermal light-weight calcium phosphate cements: use of polyacrylonitrile-shelled hollow microspheres, J. Mater. Sci. 32 (13) (1997) 3523–3534.
[3] J. Sun, J. Zhang, M. Zhang, M. Antonietti, X. Fu, X. Wang, Bioinspired hollow semiconductor nanospheres as photosynthetic nanoparticles, Nat. Commun. (2012) 1139.
[4] A. Liberman, N. Mendez, W.C. Trogler, A.C. Kummel, Synthesis and surface functionalization of silica nanoparticles for nanomedicine, Surf. Sci. Rep. 69 (2–3) (2014) 132–158.
[5] Z.-Z. Li, L.-X. Wen, L. Shao, J.-F. Chen, Fabrication of porous hollow silica nanoparticles and their applications in drug release control, J. Contr. Release 98 (2) (2004) 245–254.
[6] F.-P. Chang, Y. Hung, J.-H. Chang, C.-H. Lin, C.-Y. Mou, Enzyme encapsulated hollow silica nanospheres for intracellular biocatalysis, ACS Appl. Mater. Interfaces 6 (9) (2014) 6883–6890.
[7] B.P. Jelle, T. Gao, L.I.C. Sandberg, B.G. Tilset, M. Grandcolas, A. Gustavsen, Thermal superinsulation for building applications-From concepts to experimental investigations, Int. J. Struct. Anal. 1 (2014) 43–50.
[8] Y.-H. Li, Z.-Y. Li, W.-Q. Tao, An ideal nano-porous insulation material: design, modeling and numerical validation, Appl. Therm. Eng. 72 (1) (2014) 34–40.
[9] T. Gao, B.P. Jelle, L.I.C. Sandberg, A. Gustavsen, Monodisperse hollow silica nanospheres for nano insulation materials: synthesis, characterization, and life cycle assessment, ACS Appl. Mater. Interfaces 5 (3) (2013) 761–767.
[10] Y. Liao, X. Wu, H. Liu, Y. Chen, Thermal conductivity of powder silica hollow spheres, Thermochim. Acta 526 (1) (2011) 178–184.
[11] Z. Jia, Z. Wang, D. Hwang, L. Wang, Prediction of the effective thermal conductivity of hollow sphere foams, ACS Appl. Energy Mater. 1 (3) (2018) 1146–1157.
[12] Haakon Fossen Gangåssæter, Bjørn Petter Jelle, Sohrab Alex Mofid, Synthesis of Silica-Based Nano Insulation Materials for Potential Application in Low-Energy or Zero Emission Buildings, Energy Procedia 122 (2017) 949–954.
[13] M. Wang, N. Pan, Predictions of effective physical properties of complex multiphase materials, Mater. Sci. Eng. R Rep. 63 (1) (2008) 1–30.
[14] Haakon Fossen Gangåssæter, Bjørn Petter Jelle, Sohrab Alex Mofid, Tao Gao, Air-filled nanopore based high-performance thermal insulation materials, Energy Procedia 132 (2017) 231–236.
[15] M. Fuji, C. Takai, H. Imabeppu, X. Xu, Synthesis and shell structure design of hollow silica nanoparticles using polyelectrolyte as template, in: Journal of Physics: Conference Series, IOP Publishing, 2015, 012007.
[16] D.R. Boverhof, C.M. Bramante, J.H. Butala, S.F. Clancy, M. Lafranconi, J. West, S. C. Gordon, Comparative assessment of nanomaterial definitions and safety evaluation considerations, Regul. Toxicol. Pharmacol. 73 (1) (2015) 137–150.
[17] M. Chen, L. Wu, S. Zhou, B. You, A method for the fabrication of monodisperse hollow silica spheres, Adv. Mater. 18 (6) (2006) 801–806.
[18] I. Tissot, J. Reymond, F. Lefebvre, E. Bourgeat-Lami, SiOH-functionalized polystyrene latexes. A step toward the synthesis of hollow silica nanoparticles, Chem. Mater. 14 (3) (2002) 1325–1331.
[19] Y. Wan, S.-H. Yu, Polyelectrolyte controlled large-scale synthesis of hollow silica spheres with tunable sizes and wall thicknesses, J. Phys. Chem. C 112 (10) (2008) 3641–3647.
[20] S. Yoon, J. Kim, J. Kim, S. Park, C. Lee, J.-S. Yu, Template synthesis of nanostructured silica with hollow core and mesoporous shell structures, Curr. Appl. Phys. 6 (6) (2006) 1059–1063.
[21] Q. Sun, P.C. Magusin, B. Mezari, P. Panine, R.A. van Santen, N.A. Sommerdijk, The formation of gigantic hollow silica spheres from an EO 76–PO 29–EO 76/butanol/ethanol/H 2 O quaternary system, J. Mater. Chem. 15 (2) (2005) 256–259.
[22] B. Jelle, B. Tilset, S. Jahren, T. Gao, A. Gustavsen, Vacuum and nanotechnologies for the thermal insulation materials of beyond tomorrow–From concept to experimental investigations, in: Proceedings of the 10th International Vacuum Insulation Symposium, IVIS-X), 2011, pp. 171–178.
[23] Z. Deng, M. Chen, S. Zhou, B. You, L. Wu, A novel method for the fabrication of monodisperse hollow silica spheres, Langmuir 22 (14) (2006) 6403–6407.
[24] S. Ng, B.P. Jelle, L.I. Sandberg, T. Gao, S.A. Mofid, Hollow silica nanospheres as thermal insulation materials for construction: impact of their morphologies as a function of synthesis pathways and starting materials, Construct. Build. Mater. 166 (2018) 72–80.
[25] Q. Yue, Y. Li, M. Kong, J. Huang, X. Zhao, J. Liu, R.E. Williford, Ultralow density, hollow silica foams produced through interfacial reaction and their exceptional properties for environmental and energy applications, J. Mater. Chem. 21 (32) (2011) 12041–12046.
[26] D. Zhao, X. Qian, X. Gu, S.A. Jajja, R. Yang, Measurement techniques for thermal conductivity and interfacial thermal conductance of bulk and thin film materials, J. Electron. Packag. 138 (4) (2016), 040802.
[27] Xinpeng Zhao, Sohrab A. Mofid, Majed R. Al Hulayel, Gabriel W. Saxe, Bjørn Petter Jelle, Ronggui Yang, Reduced-scale hot box method for thermal characterization of window insulation materials, Applied Thermal Engineering 160 (2019).
[28] X. Du, J. He, Facile size-controllable syntheses of highly monodisperse polystyrene nano-and microspheres by polyvinylpyrrolidone-mediated emulsifier-free emulsion polymerization, J. Appl. Polym. Sci. 108 (3) (2008) 1755–1760.
[29] D.-S. Yun, H.-S. Lee, H.-G. Jang, J.-W. Yoo, Controlling size and distribution for nano-sized polystyrene spheres, Bull. Kor. Chem. Soc. 31 (5) (2010) 1345–1348.
[30] J. Lee, J.U. Ha, S. Choe, C.-S. Lee, S.E. Shim, Synthesis of highly monodisperse polystyrene microspheres via dispersion polymerization using an amphoteric initiator, J. Colloid Interface Sci. 298 (2) (2006) 663–671.
[31] B. Liu, Y. Wang, M. Zhang, H. Zhang, Initiator systems effect on particle coagulation and particle size distribution in one-step emulsion polymerization of styrene, Polymers 8 (2) (2016) 55.
[32] C. Chern, Emulsion polymerization mechanisms and kinetics, Prog. Polym. Sci. 31 (5) (2006) 443–486.
[33] J.P. Rao, K.E. Geckeler, Polymer nanoparticles: preparation techniques and size-control parameters, Prog. Polym. Sci. 36 (7) (2011) 887–913.
[34] H. Adelnia, S. Pourmahdian, Soap-free emulsion polymerization of poly (methyl methacrylate-co-butyl acrylate): effects of anionic comonomers and methanol on the different characteristics of the latexes, Colloid Polym. Sci. 292 (1) (2014) 197.
[35] G. Kim, S. Lim, B.H. Lee, S.E. Shim, S. Choe, Effect of homogeneity of methanol/water/monomer mixture on the mode of polymerization of MMA: soap-free emulsion polymerization versus dispersion polymerization, Polymer 51 (5) (2010) 1197–1205.
[36] S. Sajjadi, Extending the limits of emulsifier-free emulsion polymerization to achieve small uniform particles, RSC Adv. 5 (72) (2015) 58549–58560.
[37] I. Capek, Emulsion polymerization of butyl acrylate IV. Effects of initiator type and concentration, Polym. J. 26 (1994) 1154.
[38] Z. LI, S.-B. WANG, Investigation of hollow silica spheres with controllable size and shell thickness, 无机材料学报 26(8), 2011.
[39] S. Zeng, A. Hunt, R. Greif, Mean free path and apparent thermal conductivity of a gas in a porous medium, J. Heat Tran. 117 (3) (1995).
[40] Z.-Y. Li, H. Liu, X.-P. Zhao, W.-Q. Tao, A multi-level fractal model for the effective thermal conductivity of silica aerogel, J. Non-Cryst. Solids 430 (2015) 43–51.
[41] M.G. Kaganer, Thermal Insulation in Cryogenic Engineering, 1969.
[42] H. Liu, Z.-Y. Li, X.-P. Zhao, W.-Q. Tao, Investigation of the effect of the gas permeation induced by pressure gradient on transient heat transfer in silica aerogel, Int. J. Heat Mass Tran. 95 (2016) 1026–1037.
[43] X. Zhao, C. Huang, Q. Liu, I.I. Smalyukh, R. Yang, Thermal conductivity model for nanofiber networks, J. Appl. Phys. 123 (8) (2018), 085103.
[44] J. Fricke, X. Lu, P. Wang, D. Büttner, U. Heinemann, Optimization of monolithic silica aerogel insulants, Int. J. Heat Mass Tran. 35 (9) (1992) 2305–2309.
[45] M. Bouquerel, T. Duforestel, D. Baillis, G. Rusaouen, Heat transfer modeling in vacuum insulation panels containing nanoporous silicas—a review, Energy Build. 54 (2012) 320–336.
[46] G. Wang, C. Wang, J. Zhao, G. Wang, C.B. Park, G. Zhao, Modelling of thermal transport through a nanocellular polymer foam: toward the generation of a new superinsulating material, Nanoscale 9 (18) (2017) 5996–6009.
[47] B. Notario, J. Pinto, E. Solorzano, J.A. de Saja, M. Dumon, M.A. Rodríguez-Pérez, Experimental validation of the Knudsen effect in nanocellular polymeric foams, Polymer $V 56 (2015) 57–67.
[48] X. Lu, R. Caps, J. Fricke, C. Alviso, R. Pekala, Correlation between structure and thermal conductivity of organic aerogels, J. Non-Cryst. Solids 188 (3) (1995) 226–234.
[49] O.-J. Lee, K.-H. Lee, T.J. Yim, S.Y. Kim, K.-P. Yoo, Determination of mesopore size of aerogels from thermal conductivity measurements, J. Non-Cryst. Solids 298 (2–3) (2002) 287–292.
[50] B. Nait-Ali, K. Haberko, H. Vesteghem, J. Absi, D. Smith, Thermal conductivity of highly porous zirconia, J. Eur. Ceram. Soc. 26 (16) (2006) 3567–3574.
[51] G. Wang, J. Zhao, L.H. Mark, G. Wang, K. Yu, C. Wang, C.B. Park, G. Zhao, Ultra-tough and super thermal-insulation nanocellular PMMA/TPU, Chem. Eng. J. 325 (2017) 632–646.

[52] Z.-Z. Lin, C.-L. Huang, W.-K. Zhen, Z. Huang, Enhanced thermal conductivity of metallic nanoparticle packed bed by sintering treatment, Appl. Therm. Eng. 119 (2017) 425–429.
[53] H. Song, L. Guo, Z. Liu, K. Liu, X. Zeng, D. Ji, N. Zhang, H. Hu, S. Jiang, Q. Gan, Nanocavity enhancement for ultra-thin film optical absorber, Adv. Mater. 26 (17) (2014) 2737–2743.
[54] M.A. Kats, R. Blanchard, P. Genevet, F. Capasso, Nanometre optical coatings based on strong interference effects in highly absorbing media, Nat. Mater. 12 (1) (2013) 20.

Article VIII

Xinpeng Zhao, Sohrab A. Mofid, Majed R. Al Hulayel, Gabriel W. Saxe, Bjørn Petter Jelle and Ronggui yang, **Reduced-scale hotbox method for thermal characterization of window insulation materials.** *Applied Thermal Engineering,* 160 (2019) 114026.

Applied Thermal Engineering 160 (2019) 114026

Contents lists available at ScienceDirect

Applied Thermal Engineering

journal homepage: www.elsevier.com/locate/apthermeng

Research Paper

Reduced-scale hot box method for thermal characterization of window insulation materials

Xinpeng Zhao[a], Sohrab A. Mofid[a,b], Majed R. Al Hulayel[a], Gabriel W. Saxe[a], Bjørn Petter Jelle[b,c], Ronggui Yang[a,*]

[a] Department of Mechanical Engineering, University of Colorado, Boulder, CO 80309, USA
[b] Department of Civil and Environmental Engineering, Norwegian University of Science and Technology, NO-7491 Trondheim, Norway
[c] Department of Materials and Structures, SINTEF Building and Infrastructure, NO-7465 Trondheim, Norway

HIGHLIGHTS

- A reduced-scale hot box is built to measure window insulation materials.
- The built system can measure the specimens with sizes $< 0.2\,m \times 0.2\,m$ accurately.
- The thermal conductivity and U-value of transparent porous aerogel are measured.

ARTICLE INFO

Keywords:
Hot box method
Laser flash apparatus
Window
Thermal insulation
Thermal transmittance
Thermal conductivity

ABSTRACT

Highly transparent and low thermal conductivity materials have attracted great interest for the applications in window insulation in recent years. Accurate characterization of the thermal properties including thermal transmittance (U-value) and thermal conductivity of window insulation materials is very important for developing next-generation materials. The conventional hot box method, which is commonly used to measure the U-values of building materials, requires sample sizes $> 1.0\,m^2$ to minimize the influence of parasitic heat loss on the measurement accuracy. This characterization challenge hinders the development of novel window materials which are not yet available for large-scale deployment. To address this issue, a reduced-scale hot box system (RHS) was designed to measure both the U-value and the thermal conductivity of specimens that can be more readily made, with sizes $< 0.2\,m \times 0.2\,m$. The developed reduced-scale hot box system has a very simple testing system and can avoid the challenging thermal insulation requirement of the conventional hot box. The fast turnaround of the reduced-scale hot box system can help facilitate the development of novel insulating materials for energy-efficient windows.

1. Introduction

The commercial and residential buildings account for ~40% of the total energy use today in the United States, and this number is likely to reach more than 45% by 2035 [1,2]. Heating, cooling, ventilation, and air-conditioning (HVAC) systems use ~50% of the total building energy consumption [2]. In comparison to other building envelope materials (e.g. walls and roofs), windows are the weakest thermal barrier between the indoor and outdoor environments, and are responsible for 40–60% of the total energy loss from buildings [3,4]. Previous studies [4–6] have shown that the utilization of transparent insulation materials for windows can significantly reduce energy loss while maintaining the visible light transmission. According to an evaluation by the U.S. Department of Energy [7], an energy-efficient window retrofit for the existing single-pane windows can reduce 1.2 quads (1.266×10^{18} J) of domestic energy consumption in the United States per year. In recent years, several transparent insulation materials, such as aerogels [4,6,8], polymer foams [9], and hollow microcapsule embedded polymers [10], have been developed for window insulation. Generally, the thermal conductivity and the thermal transmittance are the two parameters used to select the type and thickness of insulation materials and evaluate economic performance in the building construction/renovation industry [11–13]. Thus, accurate characterization of the thermal conductivity and the thermal transmittance is very important for the design, evaluation, and adoption of new window insulation materials. The objective of this work is to develop a convenient

* Corresponding author.
E-mail address: ronggui.yang@colorado.edu (R. Yang).

https://doi.org/10.1016/j.applthermaleng.2019.114026
Received 21 February 2019; Received in revised form 21 June 2019; Accepted 26 June 2019
Available online 29 June 2019
1359-4311/

Nomenclature

c_p	heat capacity (J/(kgK))
d	sample thickness (m)
h_c	heat transfer coefficient of chamber side (W/m^2)
h_r	heat transfer coefficient of room side (W/m^2)
k	thermal conductivity (W/(mK))
Q	heat flux (W/(m^{2}K))
R_c	contact resistance ((m^{2}K)/W)
$t_{1/2}$	measured time (s)
T_c	chamber temperature (°C)
T_r	room temperature (°C)
T_{sc}	inner surface temperature (°C)
T_{sr}	outer surface temperature (°C)
U	U-value (W/(m^{2}K))

Symbols

Δ	uncertainty

Greeks

α	thermal diffusivity (m^2/s)
ρ	mass density (kg/m^3)

tool that can be used to characterize the thermal transmittance and thermal conductivity of transparent window insulation materials, especially during early stages of material development when large size samples are not yet available.

In practice, the thermal transmittance coefficient (W/(m^{2}K)), namely the U-value, is used to quantify the overall heat exchange between the interior and exterior environments through a building envelope [14]. The hot box method has been extensively used to measure the U-values of various building materials, such as aluminum framed windows [14], hollow block walls [15], vacuum glazings [16], and aerogel insulation blankets [17,18]. The thermal conductivities of specimens can also be obtained if the inner and outer surface temperatures of the samples are monitored during the hot box measurements [17,19]. In the conventional hot box system, a metering chamber and a climate chamber are used to simulate the indoor and outdoor environments, respectively. The net heat flow through the specimen is calculated according to the heat input/removal to/from the metering chamber [14,20]. To reduce the influence of heat loss through the metering chamber wall on the accuracies of the measurements, in conventional hot box measurements, the metering wall loss are controlled to be as low as 1–2%, and the minimum specimen area should be larger than 1.0 m^2 according to ASTM C1363-11 [20]. However, during the early stages of material development, samples of 1.0 m^2-scale are usually difficult or too costly to make, especially for nanostructured materials. If one aims to measure a sample with the much smaller size (e.g. 0.2 m × 0.2 m) using the conventional hot box method, the parasitic heat loss should be much less (~1/25) in order to have the similar accuracy as in the cases of 1.0 m^2-scale samples, which brings a great challenge to the thermal insulation of the metering chamber. Thus, a simple and fast U-value measurement setup with small sizes (< 0.2 m × 0.2 m) is highly desirable, especially when the material is not yet available for a large-scale deployment.

In this work, a reduced-scale hot box system (RHS) is developed to measure the thermal transmittances and the thermal conductivities of window insulation materials. Unlike the conventional hot box method in which the net heat flow through the specimen is evaluated according to heat input/removal to/from the metering chamber, the net heat flow through the specimen is measured using a heat flux transducer directly. The commercially available thermal insulation materials having known thermal conductivities are first used to validate the measurement of U-values and thermal conductivity values. Then, the RHS is used to measure the U-values and thermal conductivities of the recently developed transparent porous aerogel [8] exposed to controlled conditions. The measured thermal conductivities of transparent porous aerogel from our RHS are further validated using the laser flash method. The measured results show that the transparent porous window insulation aerogel has a thermal conductivity of 0.018 W/(mK) at room temperature, and the aerogel with a thickness of ~4.0 mm can reduce the U-value of single pane window by ~50%. The RHS method developed in this work can facilitate the development of next-generation window insulation materials.

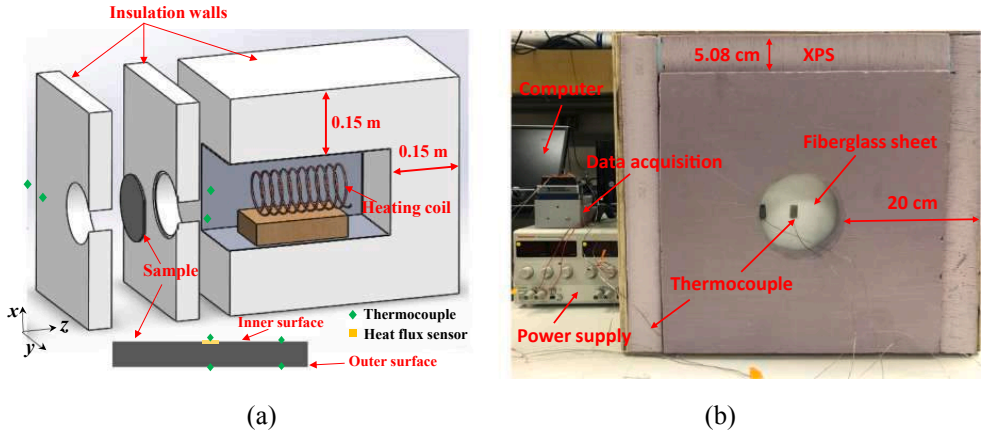

Fig. 1. Setup of the reduced-scale hot box system. (a) Schematic of the reduced-scale hot box system. The heating coil inside the chamber is used to control the temperature inside the chamber. (b) Snapshot of the assembled experimental setup, in which the thickness of the insulation XPS wall is 0.15 m, and the sample diameter is 0.14 m.

2. System description and measurements

2.1. Development of reduced-scale hot box

In the conventional hot box method, the net heat flow through the metered specimen is determined by heat input/removal to/from the metering chamber, corrected for the heat loss through the metering chamber walls and flanks [20]. To make sure that the uncertainty of parasitic heat loss correction to the net heat flow is less than 0.5% of the net heat flow through the specimen, the heat loss through the walls and flank of the hot box are controlled as low as 2–3% of the heat flow through the specimen, and the minimum sample size is required to be larger than 1.0 m^2 according to ASTM C1363-11 [20]. The above-mentioned requirements make the conventional hot box very bulky. To reduce the hot box size and acquire the heat flow going across the specimen directly, the heat flow meters are usually adopted by the newly designed smaller size hot boxes [21–23]. Following the same idea, a heat flux transducer is adopted to measure the heat flow through the specimen in our design. As a result, the influence of heat loss through the surrounding walls of our designed RHS becomes insignificant and the testing system is greatly simplified. Moreover, because the room environment (e.g. temperature and humidity) is stable and the sample size is very small compared to the size of the experimental room, it is reasonable to choose the exterior room environment as a cold chamber. Following this concept, a simplified reduced-scale hot box has been designed, constructed and calibrated.

Fig. 1(a) shows the layout of the designed hot box. The overall dimensions of the hot box are 0.5 m × 0.5 m × 0.6 m (*x*–*y*–*z* directions). The insulating walls are built using commercially available extruded polystyrene foam (XPS, ~0.035 W/(m K)) with a wall thickness of 0.15 m. The inner chamber dimensions are 0.2 m × 0.2 m × 0.35 m (*x*–*y*–*z* directions) to provide easy access to the inner components such as sensors and the heating coils. The specimen to be measured is placed in the opening of the chamber, which separates the hot chamber from the cold room environment. Fourteen (14) T-type thermocouples (Omega, accuracy ± 0.5 °C or 0.4%) are used to monitor the surface temperatures of the specimen, insulating walls, air temperatures inside the hot chamber and the room environment (part of them can be seen in Fig. 1(a)). A heat flux meter (HFM) with dimensions 3.0 cm × 3.0 cm × 3.0 cm (greenTEG gSKIN®-XO, ± 3%) is used to measure the heat flow through the specimen. The thermocouples and HFM are connected to a multiple channel data acquisition system (National Instruments, NI-9213). The measured temperatures and heat flux are recorded by LabVIEW software. Fig. 1(b) shows a snapshot of the experimental setup for U-value measurements of thermal insulation materials. The temperature inside the chamber can vary from room temperature to ~80.0 °C. The room temperature is set to be the cold chamber temperature.

The specimen is placed between the chamber and room environment and the air inside the chamber is heated using the heating coil (Fig. 1(a)). To make sure that the heat transfer across the measured specimen is one-dimensional (1D), the following strategies are adopted: (1) an engraved slot shown in Fig. 1(a) is designed to provide specimen support and reduce the edge heat loss. At least 20.0 cm thick insulating layer is used to make the edge heat loss be smaller than 0.75% of the heat flowing across the sample (Fig. 1(b)). Considering the heat flux transducer/chamber size, and insulation requirement, the optimal sample size is in the range of 0.06–0.2 m (diameter or length) for both circular and square shapes. (2) The position of the heating coil with respect to the measured sample has been adjusted to make sure that the hot air reaching the inner surface of the sample is uniform. (3) The inner walls of the chamber and the heating coils are all covered by a low emissivity aluminum foil to reduce the influence of thermal radiation on the measurements. When both the air temperature inside the hot chamber and the heat flow through the specimen become constant or fluctuate around constant values, the system reaches steady-state. Assuming the heat transfer is 1D, the U-value (W/(m^2K)) of the specimen can be determined by the ratio between the heat flux Q (W/m^2) through the element versus the temperature difference between the hot chamber and the cold room environment, i.e. shown in the following:

$$U = \frac{Q}{T_c - T_r} \tag{1}$$

where T_c is the chamber temperature and T_r is the room temperature. The RHS can also be used to measure the thermal conductivity of the specimen. If the inner surface temperature T_{sc} and the outer surface temperature T_{sr} of the specimen with a thickness of d are monitored, the thermal conductivity k (W/(mK)) of the material can be calculated according to Fourier's law of heat conduction as follows:

$$k = \frac{Qd}{T_{sc} - T_{sr}} \tag{2}$$

2.2. Uncertainty analysis

The uncertainties of the measured U-value and thermal conductivity k depend on many factors, such as the accuracies of thermocouples and heat flux sensors, edge heat loss, geometry (e.g. shape, thickness) and thermal properties of specimens. According to the uncertainty propagation formula and Eq. (1), the uncertainty of the U-value can be

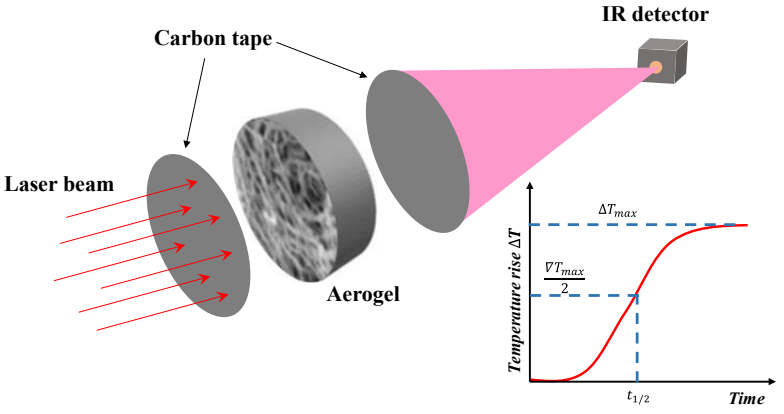

Fig. 2. The principle of the laser flash apparatus method.

determined by [14,24]

$$\frac{\Delta U}{U} = \sqrt{\left(\frac{\Delta Q}{Q}\right)^2 + \left(\frac{\Delta T_c}{T_c - T_r}\right)^2 + \left(\frac{\Delta T_r}{T_c - T_r}\right)^2} \quad (3)$$

where ΔQ is the uncertainty of the heat flux going across the measured samples, and ΔT_h and ΔT_r are the uncertainties associated with the air temperature in the chamber and the room environment. For ΔQ, it consists of both the intrinsic uncertainty of the HFM and the edge heat loss which is closely related to the insulation conditions, geometry and thermal conductivities of the specimen. Here, the up limit (~0.75% of Q) is used to evaluate the uncertainty induced by the edge heat loss. For ΔT_h and ΔT_r, the thermal contact resistance between the thermocouple and sample surface and the heat loss through thermocouple leads are neglected. Thus, only the uncertainty measurement of the thermocouples are considered. In Eq. (3), it is shown that the uncertainty of the U-value decreases as the temperature difference increases. Therefore, to reduce the uncertainty, it is best to carry out the measurements under large temperature differences. Following the same procedure, the uncertainty of the thermal conductivity in Eq. (2) could also be determined. Similarly, a large temperature difference is desirable in order to reduce the uncertainty of measured thermal conductivity.

2.3. Thermal conductivity measurements using laser flash apparatus method

Generally, the steady methods, such as heat flow meter [25] and guarded hot plate [26], are used for the thermal conductivity characterization of insulation materials, however, they usually require long measurement time (~several hours). Recent studies have shown that laser flash apparatus (LFA) can also be used to determine the thermal properties of thermal insulation materials, such as xonotlite-type calcium silicate [27], silica powders [28], foams [29,30], and nanoporous wood [31] and aerogels [32–34]. To calibrate the measured thermal conductivity from the RHS and provide a fast thermal conductivity measurement method for small size insulation materials (~1.0 cm × 1.0 cm), the commercial Netzsch laser flash apparatus (LFA 457) and Netzsch differential scanning calorimetry (DSC 204 F1 Phoenix) are used for the thermal diffusivity and specific heat capacity measurements respectively, and the thermal conductivity was then

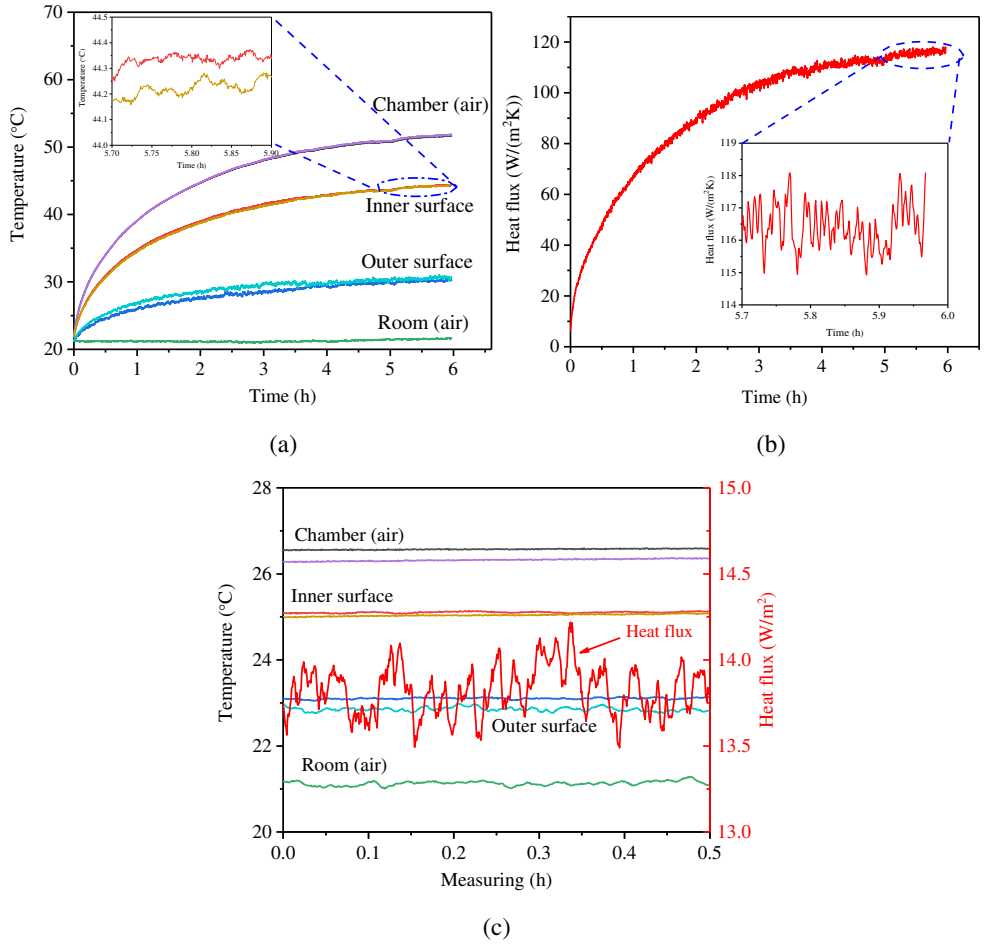

Fig. 3. Measured parameters during the reduced-scale hot box measurements. (a) Chamber temperature, surface temperatures of fiberglass sheet and room temperature as a function of time. (b) Heat flux going through the fiberglass sheet as a function of time. (c) Chamber temperature, surface temperatures of black aerogel sheet, room temperature and heat flux going through the black aerogel sheet in steady state. The positions of the thermocouples and heat flux sensor are given in Fig. 1(a).

calculated accordingly. As shown in Fig. 2, during the LFA measurement, an instantaneous light is used as heat source to heat up the front side of the sample, and an infrared detector records the temperature response from the rear side of the sample. Under the assumption that the heat transfer is one-dimensional, the thermal diffusivity α (m^2/s) is determined by [35]

$$\alpha = \frac{1.38d^2}{\pi^2 t_{1/2}} \quad (4)$$

where d is the thickness of the sample (m) and $t_{1/2}$ is the measured time (s) that takes for the sample to heat to one half of the maximum temperature on the rear surface. The thermal conductivity k (W/(mK)) is then calculated by

$$k = \alpha \rho c_p \quad (5)$$

where ρ is the mass density (kg/m^3) and $c_p$is the specific heat capacity (J/(kgK)). In general, the two surfaces of the specimen are coated by graphite or black carbon spray to absorb the laser light on the front side and enhance the emission intensity on the rear side [28,30,36]. For the highly porous and transparent insulation materials, a thin layer of metal, such as gold [34,37] or iron [27], is usually first deposited on both surfaces of the samples to eliminate the radiative penetration and ensure a rapid planar heat distribution upon laser incidence. However, because the metallic coating would destroy the internal porous nanostructures of materials such as aerogels [38], in this work the highly thermally conductive carbon tapes are applied to both top and bottom of the aerogel samples to prevent laser light transmission and convert the laser radiation into heat (Fig. 2). The carbon tape has a thickness of ~160 μm along with the following properties: mass density 708.5 kg/m^3, specific heat 1500.0 J/(kgK) and thermal conductivity ~1.0 W/(mK). It is obvious that the measured thermal conductivity includes the effect of contact resistance between the aerogel and the carbon tapes. To eliminate the contribution of the contact resistances to the measured conductivity, 5–10 identical samples with different thicknesses are measured. The magnitude of the contact resistance can then be extracted and accounted for based on the following equations: $L_1/k_1 = L_{1s}/k_s + 2L_t/k_t + 2R_c$ and $L_2/k_2 = L_{2s}/k_s + 2L_t/k_t + 2R_c$ where L_1 and L_2 are the thicknesses of the two stacked sandwich structures, k_1 and k_2 are the corresponding thermal conductivities, L_{1s} and L_{2s} are the thicknesses of the aerogel materials, L_t is the thickness of the carbon tape, k_s and k_t are the thermal conductivies of the samples and carbon tapes, and R_c is the contact resistance between the conductive carbon tape and the insulation material. Moreover, the thickness of the measured samples using LFA are all in the range of 0.5–1.0 mm to make sure that the corresponding temperatures on the rear sides of the sample surfaces can be detected accurately. The uncertainty of the measurement is then evaluated on the basis of the measurement errors and the systematic errors.

3. Results and discussion

In this work, the commercially available materials are used to calibrate the reduced-scale hot box system (RHS) first. The developed method is then adopted to measure the thermal conductivities and U-values of transparent porous aerogel under different conditions.

3.1. Calibration of the reduced-scale hot box system

The data reduction assumes that heat transfer across the specimen is one-dimensional (1D). During the measurements, the chamber temperature and the specimen surface temperatures are monitored at different locations (Fig. 1(a)) to check whether the heat transfer is 1D or not. Fig. 3(a) and (b) display the variation of chamber temperature, specimen (fiberglass sheet) surface temperatures, room temperature and heat flux across the fiberglass sheet as a function of time. After about 5.5 h, the measured temperatures and heat flux become constant, showing the measurement reaches steady-state. The inset figure in Fig. 3(a) shows that the temperature difference between two different locations on the inner surface is smaller than 0.2 ℃ which is within the uncertainty range of T-type thermocouple (± 0.5 ℃). Similar results can also be seen from Fig. 3(c) in which the commercial black aerogel sheet is measured. Therefore, it can be concluded that the heat transfer is 1D in our designed hot box system. Besides the temperatures, the fluctuation of the heat flux is also checked during the measurements. As shown in Fig. 3(b), the measured heat flux across the fiberglass sheet fluctuates around a constant value when the system reaches steady-state. The inset figure shows that the fluctuation of the heat flux is within ± 2.0 W/m^2 when the average heat flux is at 116.1 W/m^2 as given in Table 1. Additionally, from Fig. 3(c), it is seen that the fluctuation of the heat flux through black aerogel sheet decreases when the measured heat flux is small (13.8 W/m^2, Table 1). Overall, the fluctuation is within the uncertainty range of the heat flux sensor (± 3.0%). Note that each measured value in Table 1 is the time-averaged results during steady-state from two independent thermocouples at different locations (Fig. 1). According to Eqs. (1) and (2), the measured U-values and thermal conductivities can be calculated using the inputs from Table 1.

According to Eqs. (1) and (2), for the developed RHS, the measurement accuracy of heat flux plays an important role in determining both the thermal conductivity and the U-value of a material. Here, the specimens with known thermal properties are used to calibrate the accuracy of the heat flux measured by the heat flux transducer (Eq. (2)). As shown in Fig. 4(a), two commercially available insulation materials (fiberglass sheet (0.029 W/(mK) at 24 ℃) and black aerogel sheet (0.014 W/(mK) at 24 ℃) which is made of silica and reinforcing fibers) from McMaster-Carr are used for the calibration of the RHS. As shown in Fig. 4(a), the measured thermal conductivities of both the fiberglass sheet and the black aerogel sheet are consistent with the results

Table 1
The time-averaged temperature and heat flux from the reduced-scale hot box method in steady-state.

Specimen	Chamber air temperature T_c (℃)	Inner surface temperature T_{sc} (℃)	Outer surface temperature T_{sr} (℃)	Room air temperature T_r (℃)	Heat flux Q (W/m^2)
Fiberglass (d=3.1 mm)	38.7	34.1	26.3	22.1	62.3
	51.6	44.2	30.4	21.2	116.1
	74.2	62.1	37.2	21.8	223.6
Black aerogel (d=2.0 mm)	26.6	25.2	23.0	21.8	13.8
	45.2	39.5	28.0	21.1	78.6
	66.8	57.0	34.2	21.6	156.9
Window pane (d=3.0 mm)	31.2	/	/	25.1	29.2
	38.7	/	/	25.4	71.8
	53.4	/	/	25.3	175.7
TOCN-PMSQ aerogel (d=2.7 mm)	33.0	30.8	27.7	26.3	20.5
	42.1	37.2	29.7	25.5	52.3
	62.8	52.8	35.3	25.8	130.0

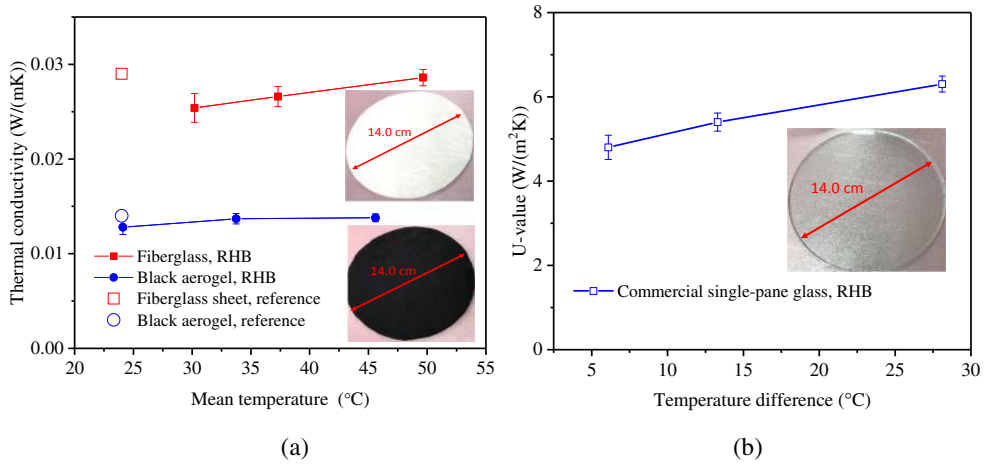

Fig. 4. Measured thermal conductivities and U-values of commercially available insulation materials using the reduced-scale hot box system. (a) Thermal conductivities of the fiberglass sheet and the black aerogel sheet as a function of mean temperature. (b) U-values of the window glass pane as a function of temperature difference. The measured data is given in Table 1.

provided by the supplier, demonstrating that the measured heat fluxes by the RHS are correct. In Fig. 4(a), the mean temperature (x-axis) is the average result ($(T_{sc} + T_{sr})/2$) of the outer and inner surface temperatures. Due to the influence of the radiative heat transfer, it is found that the measured thermal conductivities increase slightly as the temperature difference tends to increase. Fig. 4(b) shows the measured U-values of commercially available single glass pane with thickness 3.0 mm, where the temperature difference (x-axis) is the difference between chamber temperature and room temperature. The U-value of single glass pane increases from 4.5 to 6.1 W/(m^{2}K) as the temperature difference increases from 5.5 to 30.0 °C, which also agrees with the results (5.8–6.1 W/(m^{2}K)) given in the literature [39–41]. All the measured data are given in Table 1.

3.2. Measured thermal property of transparent aerogels

Fig. 5 compares the measured thermal conductivities of highly porous transparent TOCN-PMSQ (TEMPO-oxidized cellulose nanofiber-polymethylsilsesquioxane) aerogel samples from both LFA measurements (1.0 cm × 1.0 cm sample) and RHS (8.0 cm × 8.0 cm sample). The preparation method and optical properties can be found in Liu et al. [8]. The mass density and specific heat capacity of the TOCN-PMSQ aerogel samples are measured to be 0.069 ± 0.0008 g/cm^3 and 992.2 ± 49.6 J/(kgK), respectively. In Fig. 5, the temperatures in the RHS are the mean results of the inner and outer surface temperatures given in Table 1, and the temperatures in LFA method are the environment temperatures of the testing chamber where the measurements are performed. By comparing the measured thermal conductivities from the RHS and the LFA method, it is found that the differences between the two methods are within 10%, hence suggesting that the measured thermal conductivities of transparent porous insulation materials from the developed RHS are accurate and reliable.

Fig. 6(a) shows the measured U-values of transparent TOCN-PMSQ aerogel samples. Comparing Fig. 6(a) with Fig. 4(b), it is seen that the U-values of aerogels are much smaller than those of commercial windows. When the temperature difference is ~40 °C, the aerogels with thickness of 2.7 mm could reduce the U-values of single pane windows by ~40%. It is known that the U-value depends not only on the thermal conductivity and the thickness of a material, but also on the surface emissivity of the material, and the indoor/outdoor conditions (temperature, wind speed). To find the optimal thickness of the aerogel materials used for the window insulations, the U-values of transparent aerogels as a function of aerogel thickness under different outdoor wind speeds displayed in Fig. 6(b) have been calculated, where $h_r = Q/(T_{sr} - T_r)$and $h_c = Q/(T_c - T_{sc})$ represent the effective heat transfer coefficients including both convection and thermal radiation of the room side and chamber side, respectively. Here it is assumed that h_r and h_c are constant with respect to the variation of the aerogel thickness. According to Table 1, $h_r \approx h_c \approx 13.0$ W/(m^{2}K) are obtained when the temperature difference between the room and the chamber reaches ~40 °C without the influence of wind flow (almost calm). Note that the values of h_r and h_c ae very specific related to the RHS developed in our work. For a windy day (~5.0 m/s), it is assumed that the room side keeps constant ($h_r \approx 13.0$ W/(m^{2}K)) while $h_c \approx 25.0$ W/(m^{2}K) is evaluated according to Ref. [42]. It is seen from Fig. 6(b) that the U-value decreases by > 50% when the TOCN-PMSQ aerogel with a thickness d close to 4.0 mm is applied to a single glass window pane in both a calm and a windy day. If the thickness of the aerogel material

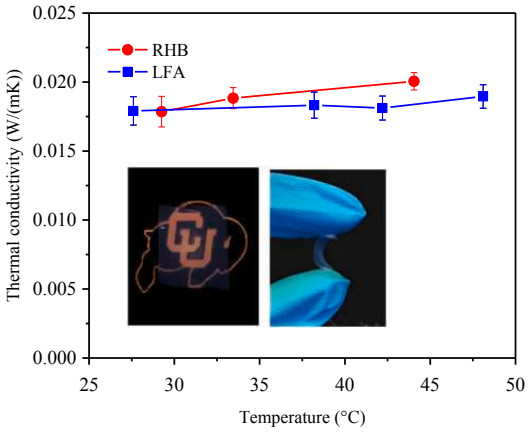

Fig. 5. Comparison of the measured thermal conductivities of highly porous transparent aerogel from laser flash apparatus and reduced-scale hot box. The inset figures show the snapshots of the measured aerogel samples synthesized by Liu et al. [8]. The measured data are given in Table 1.

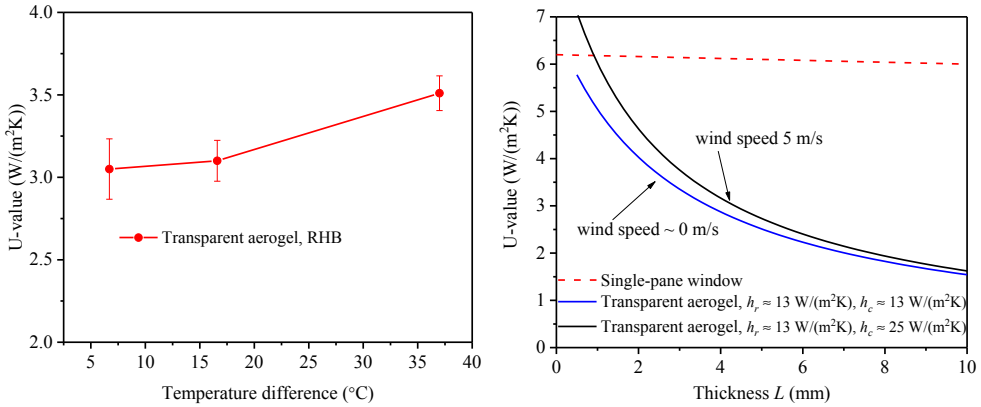

Fig. 6. U-values of transparent porous aerogels. (a) Measured U-values under the calm condition as a function of temperature difference. (b) Calculated U-values under both calm and windy conditions as a function of aerogel thickness.

continues to increase, the heat flow through the window glass pane becomes less influenced by its thickness L, and hence become more dominant based on the values of h_r and h_c. In practical application, more efforts should be devoted to reduce h_r and h_c for further reducing the U-value, including applying low emissivity films, curtains, and blinds.

4. Conclusions

In summary, this work focuses on the thermal property characterizations of highly transparent thermal barriers utilized in window applications. A reduced-scale hot box system (RHS) is designed to measure the thermal transmittance coefficient (U-value) and the thermal conductivity of window insulation materials, in which the obtained results are compared to the values of the commercially available materials to validate our proposed characterization method. In order to avoid the challenging heat insulation requirements, in our design, the net heat flow through the specimens are measured directly using a heat flux transducer, which greatly simplifies the test system. The commercial laser flash technique is also used to measure the thermal conductivity of window insulation materials ($< 1.0\,\text{cm} \times 1.0\,\text{cm}$), confirming that the measurements using the RHS is accurate. According to our measurements, the U-value of a single pane window could be reduced by > 50% when the thickness of the transparent porous TOCN-PMSQ aerogel reaches 4.0 mm. The developed measurement methods for the thermal properties of small-sized window insulation materials may in turn help facilitate the development of novel materials for energy-efficient buildings.

Acknowledgements

This research was supported by the U.S. Department of Energy's Advanced Research Projects Agency-Energy (ARPA-E) under award number DE-AR0000743. The involvement of researchers from Norway has been supported by the Research Council of Norway within the Nano2021 program through the SINTEF and NTNU research project "High-Performance Nano Insulation Materials" (Hi-Per NIM, Project No. 250159). X.P. Zhao acknowledges the fruitful discussions with Dr. D.L. Zhao, Dr. P.Q. Jiang and Dr. X. Qian.

References

[1] K. Amasyali, N.M. El-Gohary, A review of data-driven building energy consumption prediction studies, Renew. Sustain. Energy Rev. 81 (2018) 1192–1205.
[2] Office of Energy Efficiency and Renewable Energy, Buildings Energy Data Book, 2017.
[3] B.P. Jelle, A. Hynd, A. Gustavsen, D. Arasteh, H. Goudey, R. Hart, Fenestration of today and tomorrow: a state-of-the-art review and future research opportunities, Sol. Energy Mater. Sol. Cells 96 (2012) 1–28.
[4] T. Gao, B.P. Jelle, T. Ihara, A. Gustavsen, Insulating glazing units with silica aerogel granules: the impact of particle size, Appl. Energy 128 (2014) 27–34.
[5] Y. Sun, R. Wilson, Y. Wu, A review of Transparent Insulation Material (TIM) for building energy saving and daylight comfort, Appl. Energy 226 (2018) 713–729.
[6] C. Buratti, E. Moretti, Glazing systems with silica aerogel for energy savings in buildings, Appl. Energy 98 (2012) 396–403.
[7] ARPA-E, Single-pan highly insulating efficient lucid designs (SHIELD) program overview, 2016.
[8] Q. Liu, A.W. Frazier, X. Zhao, A. Joshua, A.J. Hess, R. Yang, I.I. Smalyukh, Flexible transparent aerogels as window retrofitting films and optical elements with tunable birefringence, Nano Energy 48 (2018) 266–274.
[9] S. Liu, J. Duvigneau, G.J. Vancso, Nanocellular polymer foams as promising high performance thermal insulation materials, Eur. Polym. J. 65 (2015) 33–45.
[10] C.B. Kim, N.H. You, M. Goh, Hollow polymer microcapsule embedded transparent and heat-insulating film, RSC Adv. 8 (17) (2018) 9480–9486.
[11] R. Ricciu, L.A. Besalduch, A. Galatioto, G. Ciulla, Thermal characterization of insulating materials, Renew. Sustain. Energy Rev. (2017).
[12] M. Ozel, Influence of glazing area on optimum thickness of insulation for different wall orientations, Appl. Therm. Eng. 147 (2019) 770–780.
[13] A. Gounni, M.T. Mabrouk, M. El Wazna, A. Kheiri, M. El Alami, A. El Bouari, O. Cherkaoui, Thermal and economic evaluation of new insulation materials for building envelope based on textile waste, Appl. Therm. Eng. 149 (2019) 475–483.
[14] F. Asdrubali, G. Baldinelli, Thermal transmittance measurements with the hot box method: Calibration, experimental procedures, and uncertainty analyses of three different approaches, Energy Build. 43 (7) (2011) 1618–1626.
[15] Y. Gao, J. Roux, C. Teodosiu, L. Zhao, Reduced linear state model of hollow blocks walls, validation using hot box measurements, Energy Build. 36 (11) (2004) 1107–1115.
[16] Y. Fang, P.C. Eames, B. Norton, T.J. Hyde, Experimental validation of a numerical model for heat transfer in vacuum glazing, Sol. Energy 80 (5) (2006) 564–577.
[17] Á. Lakatos, Comprehensive thermal transmittance investigations carried out on opaque aerogel insulation blanket, Mater. Struct. 50 (1) (2017) 2.
[18] U. Berardi, L. Ákos, Thermal bridges of metal fasteners for aerogel-enhanced blankets, Energy Build. 185 (2019) 307–315.
[19] C. Buratti, E. Belloni, L. Lunghi, M. Barbanera, Thermal conductivity measurements by means of a new 'Small Hot-Box'Apparatus: manufacturing, calibration and preliminary experimental tests on different materials, Int. J. Thermophys. 37 (5) (2016) 47.
[20] ASTM C1363-11: Standard Test Method for Thermal Performance of Building Materials and Envelope Assemblies by Means of a Hot Box Apparatus, 2011.
[21] R. Bruno, P. Bevilacqua, G. Cuconati, N. Arcuri, An innovative compact facility for the measurement of the thermal properties of building materials: first experimental results, Appl. Therm. Eng. 143 (2018) 947–954.
[22] X. Meng, T. Luo, Y. Gao, L. Zhang, Q. Shen, E. Long, A new simple method to measure wall thermal transmittance in situ and its adaptability analysis, Appl. Therm. Eng. 122 (2017) 747–757.

[23] I. Simões, N. Simões, A. Tadeu, J. Riachos, Laboratory assessment of thermal transmittance of homogeneous building elements using infrared thermography, in: Proceedings of the 12th International Conference on Quantitative InfraRed Thermography, Bordeaux, France, 2014, pp. 7–12.
[24] S. Yuan, G. Russell, W. Goss, Uncertainty analysis of a calibrated hot box, Insulation Materials: Testing and Applications: 4th Volume, ASTM International, 2002.
[25] R.H. Nosrati, U. Berardi, Hygrothermal characteristics of aerogel-enhanced insulating materials under different humidity and temperature conditions, Energy Build. 158 (2018) 698–711.
[26] D. Salmon, Thermal conductivity of insulations using guarded hot plates, including recent developments and sources of reference materials, Meas. Sci. Technol. 12 (12) (2001) R89.
[27] G. Wei, X. Zhang, F. Yu, K. Chen, Thermal diffusivity measurements on insulation materials with the laser flash method, Int. J. Thermophys. 27 (1) (2006) 235–243.
[28] T.W. Lian, A. Kondo, M. Akoshima, H. Abe, T. Ohmura, W.H. Tuan, M. Naito, Rapid thermal conductivity measurement of porous thermal insulation material by laser flash method, Adv. Powder Technol. 27 (3) (2016) 882–885.
[29] Y.H. Zhao, Z.K. Wu, S.L. Bai, Thermal resistance measurement of 3D graphene foam/polymer composite by laser flash analysis, Int. J. Heat Mass Transf. 101 (2016) 470–475.
[30] J. Zajas, P. Heiselberg, Determination of the local thermal conductivity of functionally graded materials by a laser flash method, Int. J. Heat Mass Transf. 60 (2013) 542–548.
[31] T. Li, J. Song, X. Zhao, Z. Yang, G. Pastel, S. Xu, C. Jia, J. Dai, C. Chen, A. Gong, F. Jiang, Y. Yao, T. Fan, B. Yang, L. Wågberg, R. Yang, L. Hu, Anisotropic, lightweight, strong, and super thermally insulating nanowood with naturally aligned nanocellulose, Sci. Adv. 4 (3) (2018) eaar3724.
[32] M. Wiener, G. Reichenauer, S. Braxmeier, F. Hemberger, H.-P. Ebert, Carbon aerogel-based high-temperature thermal insulation, Int. J. Thermophys. 30 (4) (2009) 1372–1385.
[33] J. Feng, J. Feng, Y. Jiang, C. Zhang, Ultralow density carbon aerogels with low thermal conductivity up to 2000 C, Mater. Lett. 65 (23–24) (2011) 3454–3456.
[34] M.A.B. Meador, L.A. Capadona, L. McCorkle, D.S. Papadopoulos, N. Leventis, Structure-property relationships in porous 3D nanostructures as a function of preparation conditions: isocyanate cross-linked silica aerogels, Chem. Mater. 19 (9) (2007) 2247–2260.
[35] D. Zhao, X. Qian, X. Gu, S.A. Jajja, R. Yang, Measurement techniques for thermal conductivity and interfacial thermal conductance of bulk and thin film materials, J. Electron. Packag. 138 (4) (2016) 040802.
[36] I. Abdulagatov, Z. Abdulagatova, S. Kallaev, A. Bakmaev, P. Ranjith, Thermal-diffusivity and heat-capacity measurements of sandstone at high temperatures using laser flash and DSC methods, Int. J. Thermophys. 36 (4) (2015) 658–691.
[37] W. Lin, J. Shang, W. Gu, C. Wong, Parametric study of intrinsic thermal transport in vertically aligned multi-walled carbon nanotubes using a laser flash technique, Carbon 50 (4) (2012) 1591–1603.
[38] H. Liu, Z.Y. Li, X.P. Zhao, W.Q. Tao, Investigation of the effect of the gas permeation induced by pressure gradient on transient heat transfer in silica aerogel, Int. J. Heat Mass Transf. 95 (2016) 1026–1037.
[39] U. Berardi, The development of a monolithic aerogel glazed window for an energy retrofitting project, Appl. Energy 154 (2015) 603–615.
[40] M. Rubin, Calculating heat transfer through windows, Int. J. Energy Res. 6 (4) (1982) 341–349.
[41] T. Chow, C. Li, Z. Lin, Innovative solar windows for cooling-demand climate, Sol. Energy Mater. Sol. Cells 94 (2) (2010) 212–220.
[42] I. Nardi, D. Paoletti, D. Ambrosini, T. De Rubeis, S. Sfarra, U-value assessment by infrared thermography: a comparison of different calculation methods in a Guarded Hot Box, Energy Build. 122 (2016) 211–221.

Article IX

Dianxun Hou, Tian Li, Xi Chen, Shuaiming He, Jiaqi Dai, Sohrab A. Mofid, Deyin Hou, Arpita Iddya, David Jassby, Ronggui Yang, Liangbing Hu and Zhiyong Jason Ren, **Hydrophobic nanostructured wood membrane for thermally efficient distillation**, *Science Advances,* 5(8) (2019) eaaw3203.

ENGINEERING

Hydrophobic nanostructured wood membrane for thermally efficient distillation

Dianxun Hou[1], Tian Li[2], Xi Chen[1,3], Shuaiming He[2], Jiaqi Dai[2], Sohrab A. Mofid[4,5], Deyin Hou[6], Arpita Iddya[7], David Jassby[7], Ronggui Yang[4], Liangbing Hu[2]*, Zhiyong Jason Ren[1,3]*

Current membrane distillation (MD) is challenged by the inefficiency of water thermal separation from dissolved solutes, controlled by membrane porosity and thermal conductivity. Existing petroleum-derived polymeric membranes face major development barriers. Here, we demonstrate a first robust MD membrane directly fabricated from sustainable wood material. The hydrophobic nanowood membrane had high porosity (89 ± 3%) and hierarchical pore structure with a wide pore size distribution of crystalline cellulose nanofibrils and xylem vessels and lumina (channels) that facilitate water vapor transportation. The thermal conductivity was extremely low in the transverse direction, which reduces conductive heat transport. However, high thermal conductivity along the fiber enables efficient thermal dissipation along the axial direction. As a result, the membrane demonstrated excellent intrinsic vapor permeability (1.44 ± 0.09 kg m^{-1} K^{-1} s^{-1} Pa^{-1}) and thermal efficiency (~70% at 60°C). The properties of thermal efficiency, water flux, scalability, and sustainability make nanowood highly desirable for MD applications.

INTRODUCTION

Water scarcity is a worldwide grand challenge. The United Nations reported this year that nearly half of the global population (~3.6 billion) are currently living in potential water-scarce regions at least 1 month per year. This number could increase to between 4.8-5.7 billion by 2050 (*1*). This problem is exacerbated by climate change and rapid urbanization, evidenced by extensive periods of drought and more frequent wildfires in California and other regions (*2*–*4*). Desalination can help alleviate water stress by extracting fresh water from a range of saline or contaminated sources including seawater, brackish groundwater, or wastewater (*5*, *6*), and the development of desalination has been greatly boosted by nanotechnology and advanced manufacturing (*7*, *8*). However, although reaching its energy efficiency limit (~50%), current water desalination processes such as reverse osmosis are still energy intensive [2 to 4 kilowatt-hour m^{-3}] (*9*, *10*). However, in many regions that can benefit from the technology, an increasing supply of renewable yet intermittent solar energy in the format of heat or electricity generates great opportunities for solar desalination, which also mitigate challenges in energy storage. By taking advantage of this low-cost and sometimes excess supply of heat or electrical energy, water desalination can become more cost effective (*11*–*13*).

Membrane distillation (MD) is an emerging thermally driven separation process with great potential for high-salinity water desalination using solar, thermal or other renewable sources (*10*). Driven by difference in temperature and vapor pressure. Water evaporates at the hot feed side of MD cells and diffuses through a porous hydrophobic membrane before condensing at the cold permeate side (*14*–*16*). MD can be operated using low-grade heat such as condenser cooling water from thermal power plants or, increasingly, from renewable sources such as solar thermal or geothermal plants (*17*–*19*). During MD, the transport of water vapor leads to the convective heat transfer, where the heat partially conducts through the membrane materials thereby reducing temperature gradient and lowering the driving force for mass transfer across the membrane (*20*, *21*). Thermal efficiency is an important parameter in MD and is defined as the convective heat flux across the membrane divided by the total heat flux (*22*). Accordingly, an ideal MD membrane would have a desired combination of characteristics, such as large pore size, low pore tortuosity, low thermal conductivity, high porosity, optimized thickness, good mechanical strength, cost competitiveness, and low environmental impacts (*10*, *22*–*24*).

Current commercial MD membranes are made of synthetic polymers such as polytetrafluoroethylene (PTFE), polyvinylidene fluoride (PVDF), and polypropylene (PP) (*16*, *25*–*27*). In general, these membranes have porosities lower than 0.80, thermal conductivities higher than 0.050 W m^{-1} K^{-1}, and thermal efficiency up to 60% (*10*, *15*, *16*, *22*, *25*, *28*). For example, the microporous PTFE membranes are widely used in MD modules owing to their high hydrophobicity and stability (*26*), but many of these membranes are typically isotropic (fig. S4) and not ideal for highly effective thermal insulation (*29*–*31*). In addition, these polymer materials are derived from petroleum products, and their use and disposal generate environmental concerns due to low biodegradability (*32*). Therefore, MD membranes made from natural and low-cost materials with high thermal stability and hydrophobicity are highly desired, yet not available. Recently, Leitch *et al.* (*24*) presented a new bacterial nanocellulose aerogel MD membrane with high porosity (>98%) and low thermal conductivity (<0.03 W m^{-1} K^{-1}), demonstrating how membranes could be fabricated using natural materials.

In this study, we developed the first robust MD membrane directly from a sustainable wood material. Nanocellulose is an earth-abundant and, oftentimes, waste biomass source that has been used in products with minimal environmental and health impacts such as construction materials, body armor, biofuels, or water filters (*33*–*39*). Most nanocellulose-based products, such as paper (fig. S4), are from wood

[1]Department of Civil, Environmental, and Architectural Engineering, University of Colorado Boulder, Boulder, CO 80303, USA. [2]Department of Materials Science and Engineering, University of Maryland, College Park, MD 20742, USA. [3]Department of Civil and Environmental Engineering, Princeton University, Princeton, NJ 08544, USA. [4]Department of Mechanical Engineering, University of Colorado Boulder, Boulder, CO 80309, USA. [5]Department of Civil and Environmental Engineering, Norwegian University of Science and Technology, NO-7491 Trondheim, Norway. [6]State Key Laboratory of Environmental Aquatic Chemistry, Research Center for Eco-Environmental Sciences, Chinese Academy of Sciences, Beijing 100085, China. [7]Department of Civil and Environmental Engineering, University of California, Los Angeles, Los Angeles, CA 90095, USA.
*Corresponding author. Email: binghu@umd.edu (L.H.); zjren@princeton.edu (Z.J.R.)

pulp, where degraded cellulose fibers are randomly mixed together to form an isotropic structure with high density (1.20 g cm^{-3}) and lower mechanical strength (0.25 to 0.30 MPa) (*40*, *41*). In contrast, this new wood membrane was made by directly removing lignin and semicellulose via chemical treatment and freeze-drying, which allowed the preservation of the anisotropic microstructure and hierarchical alignment of wood fibers. As a result, the wood can be prepared into an anisotropic and thermally insulating bulk material with extremely high porosity (~90%), low thermal conductivity (~0.04 W m^{-1} K^{-1}), and good mechanical strength (18 MPa), making it an ideal substrate for MD membrane. In this study, we report a nanostructured wood (i.e., nanowood) from natural American basswood followed by silane coating, which resulted in a hydrophobic nanowood membrane with high porosity yet very low thermal conductivity. The highly porous structure with naturally formed pores either amid the nanofibrils or growing on the wood vessels and fibril tracheid lumens (pits) reduces the water vapor transfer resistance and provides good water flux (20.8 ± 0.8 kg m^{-2} $hour^{-1}$ at 60°C) in direct contact MD (DCMD) tests (Fig. 1). The anisotropic property can allow heat to spread along the nanofibril direction and reduce the conductive heat transfer, while the high intrinsic permeability enhances water vapor transfer and, thus, convective heat transfer. Together, these grant the membrane excellent thermal efficiency (71 ± 2% at 60°C) with one of the highest values among all the reported MD membranes in literature (*22*). The hydrophobic wood membranes were also compared with commercial membranes in terms of membrane structures [e.g., pore size distribution (PSD) and thermal conductivity] and MD performance (i.e., flux, vapor permeability, and thermal efficiency). Figure 1B shows a large piece of the nanowood membrane with a length of 18 cm, which demonstrates the scalability of the wood membrane fabrication process. To the best of our knowledge, this is the first report on a hydrophobic MD membrane made from a sustainable wood material.

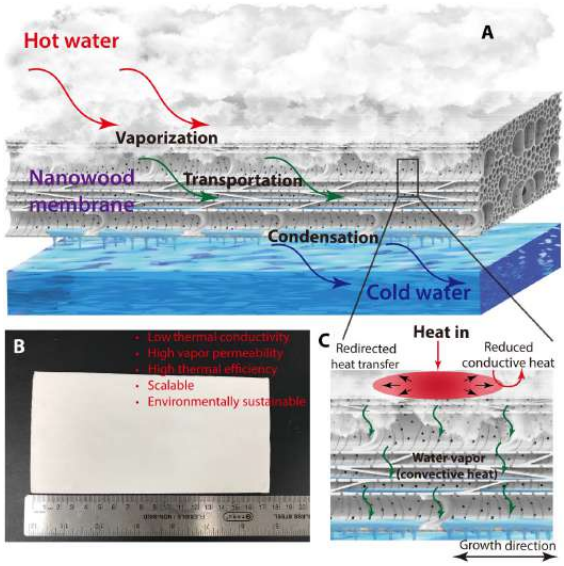

Fig. 1. The process schematic of nanowood membranes for MD. (**A**) Schematic of MD using the wood membrane. (**B**) Digital photograph of the nanowood and the corresponding beneficial properties for MD applications. (**C**) Schematic of the water (vapor) and heat transfer in the wood membrane during MD. Photo credit: T. Li, University of Maryland.

RESULTS AND DISCUSSION

The unique porous structure of the hydrophobic nanostructure wood as a highly efficient membrane

The hydrophobic wood membranes (Fig. 2, A, B and C and Fig. 3, A and B) were directly derived from natural American basswood, in which amorphous lignin and hemicellulose are intertwined with cellulose nanofibrils (*42*). After chemical treatment and purification, as described in Materials and Methods, we preserved the wood microstructure and the hierarchical alignment. For the nanowood membrane, lignin and hemicellulose were removed, while the naturally aligned cellulose nanofibrils isolated from each other along the growth direction can be directly observed with the aid of scanning electron microscopy (SEM) (Fig. 2, D to H). The removal of intermixed lignin and hemicellulose for the nanowood membrane greatly reduced the linkage and interaction among cellulose fibrils and the fibril aggregates within the fibril wall, which greatly increased flexibility and porosity (*39*). The resulting aligned crystalline cellulose nanofibrils were held together by intermolecular hydrogen bonds and van der Waals forces (*43*). Presumably, this aligned structure with weakened interactions would reduce the thermal conductivity in the transverse direction, thereby mitigating the heat loss via the conductive heat transfer during MD.

Different from commercial membranes with vertical pores (e.g., finger-like structure; fig. S7) (*26*), the wood membranes presented a unique pore structure with naturally formed xylem vessels and lumina (channels) in parallel to the membrane surface (Fig. 2D). The channel diameters ranged from 10 to 100 μm, and the channel pores granted the hydrophobic natural wood membrane a porous structure with a porosity of 21 ± 3%. Impressively, the removal of intermixed lignin and hemicellulose contributed to ~70% mass loss in the wood structure and, thus, further improved the porosity more than four times from 21 ± 3 to 89 ± 3% for the hydrophobic nanowood membrane. Note that the porosity of the hydrophobic nanowood membrane was also larger than that of commercial membranes, of which the porosity ranged from 41 to 85% (Table 1) (*10*, *15*, *22*, *25*, *28*). In addition to porosity augmentation, the removal of lignin and hemicellulose greatly shifted the PSD to the right (Fig. 2I) and increased the average pore size by ~56% from 0.18 ± 0.02 to 0.28 ± 0.03 μm (Table 1). We observed the obtained pore structure of the hydrophobic nanowood membrane using SEM (Fig. 2, D to H). Along the cross-sectional direction, we also detected micropores amid the crystalline cellulose nanofibrils (<100 nm; Fig. 2F). Apart from the pores between nanofibrils, we also observed a large amount of mesopores (pits) growing on the xylem vessels and lumina (5 to 10 μm; Fig. 2, E, G, and H), which were used for water and nutrient delivery during tree growth. This study takes advantage of the gas transportation property of these pores located either between the nanofibrils or on the channel walls for water vapor transportation. The unique pore structure of the hydrophobic nanowood membrane resulted in the nonuniform PSD with several peaks, which were totally different from the commercial PP and PTFE membranes with very uniform PSDs (fig. S6). Benefiting from the large porosity, the theoretical thermal conductivity of the hydrophobic nanowood membrane was decreased from 0.210 to 0.040 W m^{-1} K^{-1} at 25°C (section S12), which would contribute to conductive heat loss reduction.

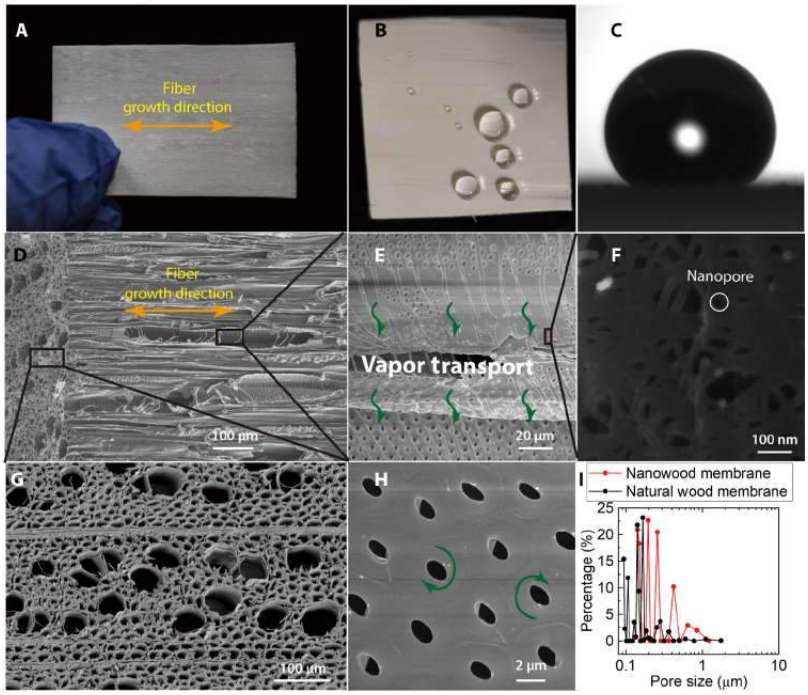

Fig. 2. Structural characterization of the nanowood membrane. (**A**) Photo of the hydrophobic nanowood membrane. (**B**) Photo that shows hydrophobicity after silane treatment. (**C**) Water contact angle of the nanowood membrane. (**D**) SEM images of the nanowood surface that exhibit aligned texture, xylem vessels, and lumina (channels). (**E**) SEM images that exhibit mesopores [(**G**) cross section and (**H**) pits] growing on the walls of the xylem vessels and lumina. (**F**) SEM images that exhibit microsized pores amid the cellulose fibers. (**I**) PSD of the hydrophobic natural wood and nanowood membranes. Photo credit: D. Hou, University of Colorado.

Moreover, different from the commercial membranes with isotropic structures and intertwined fibers (fig. S7), the aligned and high–aspect ratio nanofibril channels led to anisotropic heat flow along the alignment direction rather than the cross-sectional direction, which can further prevent the heat transfer across the wood membrane (*39*). In addition, the increased pore size and porosity were hypothesized to improve vapor permeability and enhance water flux (section 12), thereby increasing convective heat transfer (*10*).

As shown in Fig. 2C and fig. S8, both the hydrophobic nanowood membrane and natural wood membrane had water contact angles greater than 140°, indicating that the initially highly hydrophilic wood substrate (i.e., no measurable water contact angle) was successfully modified to be hydrophobic after surface fluorination. The hydrophobicity of the treated wood membranes was better than those commercial membranes with PTFE or PP substrate, where the contact angles were lower than 130° (Table 1) (*22*, *26*). The excellent hydrophobicity of the wood membranes was attributed to fluoroalkylsilane (FAS) treatment, which has super low surface energy (13.1 mN m^{-1}) compared to PTFE (20 mN m^{-1}) and PP (30 mN m^{-1}) (*26*, *44*). Note that the surface morphologies and pore structure did not change before and after surface fluorination by FAS (fig. S2). Owing to the good hydrophobicity and relatively small pore size, the nanowood membrane demonstrated decent liquid entry pressure (LEP; ~74.7 ± 0.5 kPa), suggesting a better resistance to membrane wetting than the commercial PP membranes. However, it was noted that the nanowood membrane showed smaller LEP than the PTFE membrane (~130 kPa). This is due to the wide PSD of the nanowood membrane, as larger pores (>0.4 μm) may exert negative effects (*45*).

Thermal conductivity characterization of the nanowood membrane

To demonstrate the thermal insulation capabilities of the fabricated hydrophobic nanowood membrane, we tested the specimens under a conductive heat source to simulate the DCMD. We measured the temperature with an infrared radiation (IR) camera (Fig. 3). Five different temperatures were applied, and the results show that the hydrophobic nanowood membrane yielded lower backside temperature than the hydrophobic natural wood membrane, attributed to its low thermal conductivity and anisotropic property (*39*).

The thermal conductivity of both nanowood and natural wood increased gradually from 0.210 to 0.270 W m^{-1} K^{-1} and from 0.040 to 0.049 W m^{-1} K^{-1}, respectively, with the escalation of the heat source temperature from 40° to 60°C (Fig. 3E). This is assumed because of the increase in conductivity of the cell wall substances rather than the increase in gas phase conductivity or the radiative conductivity (*46*). The trend was more notable for the natural wood (29%) than for nanowood (23%) due to the presence of hemicellulose and lignin, which are of less thermal stability (*47*). The measured thermal conductivity was comparable to the theoretical values (section S12), which are 0.184 and 0.037 W m^{-1} K^{-1} at 25°C for natural wood and nanowood membranes, respectively. The nanowood membrane showed lower thermal conductivity than most of the commercial membranes, whose

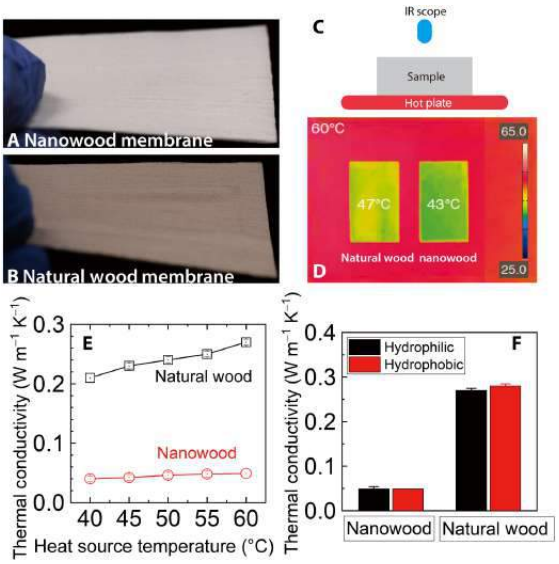

Fig. 3. Thermal conductivity characterization of the wood membranes. (**A**) Photo of the hydrophobic nanowood membrane. (**B**) Photo of the hydrophobic natural wood membrane. (**C**) Schematic representation of contact heat source measurement. IR thermographs of (**D**) the wood membranes. (**E**) Measured thermal conductivity of the wood membranes from 40° to 60°C. (**F**) Comparison of the thermal conductivity of the woods at 60°C before and after hydrophobic silane treatment. Error bars represent the SDs based on three independent experiments. Photo credit: D. Hou, University of Colorado.

thermal conductivity is generally higher than 0.045 W m^{-1} K^{-1}. This lower thermal conductivity was believed to reduce the conductive heat loss during MD and maintain the effective temperature gradient across the membrane. When heated by a conductive heat source at 60°C, it was shown that the stabilized backside temperature of the hydrophobic natural wood was 47°C, whereas that of the hydrophobic nanowood was 43°C, under 200 mW cm^{-2} (Fig. 3D). This directly indicated that the nanowood exhibited better thermal insulation property or less conductive heat loss than the natural wood. Accordingly, the thermal conductivity of the nanowood membrane was 0.049 ± 0.002 W m^{-1} K^{-1} at 60°C (Fig. 3E), which was only 18% of the thermal conductivity of the natural wood membrane (0.270 ± 0.005 W m^{-1} K^{-1} at 60°C). This significantly lower thermal conductivity of nanowood membrane was attributed not only to the higher porosity (89 ± 3% versus 21 ± 3%) but also to bigger pore size (0.28 ± 0.03 μm versus 0.18 ± 0.02 μm). Previous study indicated that higher interspacing (pore size) between fibers than the mean free path of air can mitigate thermal conduction through air. The reduction of microsized and nanosized pores is appreciable for further reduction of thermal conductivity (*39*). Furthermore, hemicellulose (0.34 W m^{-1} K^{-1}) and lignin (0.39 W m^{-1} K^{-1}) carried higher thermal conductivity than the nanocrystalline cellulose (0.26 W m^{-1} K^{-1}). Therefore, the removal of intermixed lignin and hemicellulose greatly reduced the bulk thermal conductivity of nanowood. Note that the hydrophobic treatment with FAS did not result in significant change of the thermal conductivity of the wood (Fig. 3F).

Thermally efficient desalination of the nanowood membrane

Figure 4 shows the water (vapor) flux through the hydrophobic wood membranes. Accompanied by the increase in feed temperature from

Table 1. Characteristic comparisons of the new wood membranes and commercial polymeric membranes. LEP, liquid entry pressure; ECTFE, ethylene chlorotrifluoroethylene.

Membrane	Manufacturer	Active layer	Support material	Pore size (μm)	Thickness (μm)	Porosity (%)	Contact angle (°)	LEP (kPa)	Intrinsic permeability (×10^{-10} kg m^{-1} s^{-1} Pa^{-1})	Thermal conductivity (W m^{-1} K^{-1})*	Thermal efficiency (%)†	Reference
ECTFE	3M	ECTFE	–	0.43‡	46	67	118	–	0.39	~0.034	~60	(*22*)
0.45PP	3M	PP	–	0.79‡	110	85	130	–	0.95	0.048	~58	(*22*)
QM902	Clarcor	ePTFE	–	0.45‡	–	70-85	–	–	–	–	~51	(*22*)
2400	Celgard	PP	–	0.043‡	25	41	138	–	0.02	0.111	<3	(*22*)
0.22PP	Tisch	PP	–	1.79 ± 0.10§	196 ± 18	72 ± 3	119	42.7 ± 0.3	0.64 ± 0.02	0.066	44 ± 1	This study
0.45PP	Tisch	PP	–	2.65 ± 0.24§	175 ± 4	72 ± 1	125	38.6 ± 0.5	0.68 ± 0.04	0.066	39 ± 3	This study
0.22PTFE	Tisch	PTFE	PP	0.33 ± 0.00§	188 ± 5	75 ± 4	121	126 ± 2	1.21 ± 0.22	0.082	53 ± 0	This study
0.45 PTFE	Tisch	PTFE	PP	0.36 ± 0.00§	156 ± 11	78 ± 2	117	133 ± 5	1.15 ± 0.21	0.075	59 ± 2	This study
Natural wood		Cellulose	–	0.18 ± 0.02§	540 ± 15	21 ± 3	142	98.5 ± 0.8	0.20 ± 0.04	0.210	12 ± 2	This study
Nanowood		Cellulose	–	0.28 ± 0.03§	502 ± 35	89 ± 3	144	74.7 ± 0.5	1.44 ± 0.09	0.040‖	71 ± 2	This study

*The theoretical values were based on the assumption of isotropic thermal property (in this table and section S12) (*39*, *47*, *59*). However, the real nanowood is anisotropic with a measured, while the anisotropic thermal conductivity in *x* (fiber growth direction), *y*, and *z* (transverse direction) directions was 0.060, 0.030, and 0.030 W m^{-1} K^{-1}, respectively. †The experimental feed temperature and distillate temperature were 60° and 20°C, respectively. ‡Nominal pore size. §Averaged pore size. ‖Theoretical thermal conductivity at room temperature.

40° to 60°C, water flux through the hydrophobic natural wood and nanowood membranes raised from 1.4 ± 0.2 to 3.4 ± 0.5 kg m^{-2} $hour^{-1}$ and from 5.1 ± 0.1 to 20.8 ± 0.8 kg m^{-2} $hour^{-1}$, respectively. Although the hydrophobic nanowood membrane was comparable in thickness to the hydrophobic natural wood membrane, it demonstrated up to ~6.1 times higher water flux, owing to the increase in porosity (4.2 times) and pore size (1.6 times), which substantially reduced the vapor transfer resistance. At feed and distillate temperatures of 60° and 20°C, respectively, the water flux through the hydrophobic nanowood membrane (20.8 ± 0.8 kg m^{-2} $hour^{-1}$) was close to that of the commercial PP membranes (~22.5 kg m^{-2} $hour^{-1}$) (Fig. 4A and fig. S10). The comparable flux was attributed to the much higher porosity (89 ± 3%) over the PP (~72%) membrane, which compensated for the disadvantage of higher thickness (502 ± 35 μm versus ~180 μm). It was not unusual that all the PTFE membranes exhibited far better water flux (up to 54.2 ± 3.1 kg m^{-2} $hour^{-1}$ for 0.45 PTFE at 60°C) than the wood membranes. The better water flux should be attributed to the much smaller thickness (~130 μm versus ~500 μm of nanowood membrane), which greatly reduced the vapor transfer resistance. However, when normalized by thickness, the nanowood membrane demonstrated a very high intrinsic permeability (1.44 ± 0.09 kg m^{-1} K^{-1} s^{-1} Pa^{-1}), which was ~2 times and ~1.2 times better than that of the PP (~0.65 kg m^{-1} K^{-1} s^{-1} Pa^{-1}) and PTFE (~1.2 kg m^{-1} K^{-1} s^{-1} Pa^{-1}) membranes, respectively (Fig. 4C). The higher permeability was attributed to the much higher porosity (89 ± 3%) over the PP (~72%) and PTFE (~75%) membranes. The experimental permeability was supported by the theoretical values based on the dusty gas model, which indicated that the vapor permeation through the wood and PTFE membranes with smaller pore sizes (<1.4 μm; 100 times the mean free path of water vapor at 50°C) was dominated by the Knudsen and ordinary molecular diffusion (*48*, *49*). This was different from the PP membrane (pore size, >1.7 μm) with viscous diffusion as the primary transport mechanism. In concordance with the results of other studies, the intrinsic permeability of both the nanowood and commercial membranes was generally higher than the theoretical permeability (fig. S13), which assumed cylindrical nonconnected pores with uniform size (section S15) (*23*, *24*). It was hypothesized that the enhanced ordinary molecular diffusion through the large pores amid cellulose fibers and viscous diffusion in the interconnected nanowood channels attributed to the 26% higher intrinsic permeability compared to that of the PTFE membranes (*23*, *24*). Another contributing factor might be the anisotropic thermal property of the nanowood membrane (section S5), which was believed to facilitate heat transfer along the membrane, thereby helping maintain the temperature gradient and promote flux. Although the nanowood demonstrated ~20% higher porosity and intrinsic permeability, the advantages were offset by disadvantages of its higher thickness and smaller pore size (0.28 ± 0.03 μm versus ~0.34 μm of PTFE membranes) (*10*). Therefore, thinner wood membranes should be fabricated for better flux in future studies (*10*). Figure S16 shows the water flux of wood membrane (salt rejection, >99.8%) kept stable for at least 6 hours before declining because of wetting. However, the performance recovered after deionized (DI) water and ethanol rinsing, followed by drying. Improved silane treatment such as adding silica nanoparticles may help extend the membrane's longevity without changing the wood structure (*44*, *50*).

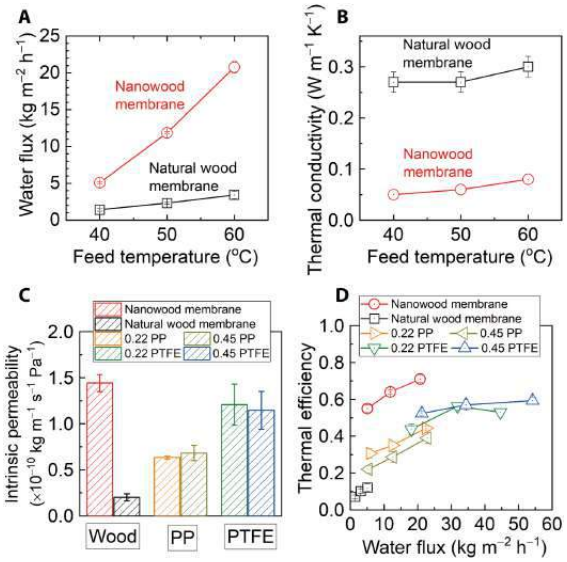

Fig. 4. MD performance of the wood and commercial membranes. (**A**) Water flux and (**B**) experimental thermal conductivities for the hydrophobic wood membranes with feed temperature continuously varying between 40° and 60°C and distillate temperature of 20°C. (**C**) Intrinsic permeability of the membranes. (**D**) Thermal efficiency versus water flux of the wood membranes and commercial membranes. Error bars represent the SDs based on three independent experiments.

The thermal efficiency is a performance parameter in determining the energy efficiency (*10*, *22*). Thermal efficiency can indicate how effectively the membrane uses thermal gradient for vapor transfer as compared to conductive heat loss (*22*). A higher thermal efficiency results from higher convective heat transfer and/or less conductive heat transfer through the membrane material (*10*). For the membranes in the study, the thermal efficiency has a substantial dependence on water flux (feed temperature; Fig. 4D). The thermal efficiency of both nanowood and natural wood membranes increased along with the heat source temperature increased from 40° to 60°C. This is believed to be associated with the faster evolution of convective heat transfer than conductive heat transfer. Moreover, the hydrophobic nanowood membrane demonstrated a good thermal efficiency of up to 71 ± 2% at 60°C, representing one of the highest values achieved in MD so far (*22*). In contrast, the hydrophobic natural wood membrane had a very limited thermal efficiency of 12 ± 2%. As a result, this membrane would require six times more energy for operation compared to the hydrophobic nanowood membrane. The good thermal efficiency of the hydrophobic nanowood membrane was ascribed not only to its super low thermal conductivity (0.080 versus 0.30 ± 0.02 W m^{-1} K^{-1} for natural wood membrane at 60°C) but also to its high porosity (89 ± 3% versus 21 ± 3%) and bigger pore size (0.28 ± 0.03 μm versus 0.18 ± 0.02 μm). The low membrane thermal conductivity reduced the conductive heat transfer through a membrane material, while the high porosity and bigger pore size reduced water transfer resistance, thereby enhancing water flux and convective heat transfer (*10*, *21*, *22*). The superior thermal insulation property prevented conductive heat loss and offset the limitation of low water flux and convective heat transfer. Benefiting from low thickness and higher porosity, the commercial 0.45 PTFE membrane exhibited the highest water flux among all membranes tested. However, note that the 0.45 PTFE membrane demonstrated a lower intrinsic permeability (1.15 ± 0.16 × 10^{-10} kg m^{-1} s^{-1} Pa^{-1}) than

that of the nanowood membrane ($1.44 \pm 0.09 \times 10^{-10}$ kg m^{-1} s^{-1} Pa^{-1}) at 60°C, indicating comparatively limited convective heat transfer (*24*). In addition, suffering from higher thermal conductivity and, thereby, higher conductive heat transfer, its thermal efficiency (59 ± 2%) was lower than that of the nanowood membrane, meaning that the nanowood membrane produced 1.2 times the freshwater permeate of the commercial PTFE membranes per kilojoule of heat energy at 60°C. Although the commercial PP membranes show smaller thermal conductivity than the PTFE membranes, the limited intrinsic permeability (~0.65×10^{-10} kg m^{-1} s^{-1} Pa^{-1}) restricted the convective heat flux and, thus, resulted in low thermal efficiency (up to 44 ± 1% for 0.22PP; Table 1) at 60°C. The intrinsic permeability of nanowood in this study was comparable to that of a fibrous cellulose aerogel membrane (~1.4×10^{-10} kg m^{-1} s^{-1} Pa^{-1}) with a high porosity of 98% (*24*). This suggests that owing to a unique structure with larger pore size and wider PSD, the nanowood membrane offsets the disadvantage from lower porosity (*23*). However, note that the effect of the unique anisotropic structure with large PSD on the heat and mass transfer is still unclear and requires further investigation.

IMPLICATIONS AND FUTURE WORK

Completely derived from abundant and sustainable natural wood, the newly developed hydrophobic nanowood membrane demonstrated superior properties and potential in MD for water desalination. The membrane exhibited good water flux (water vapor transportation) and excellent thermal efficiency (up to 70%), comparable or even higher than commercial polymeric membranes that are made of petroleum products. The exceptional thermal efficiency was attributed to its high intrinsic permeability (1.44 ± 0.09 kg m^{-1} K^{-1} s^{-1} Pa^{-1}) and super low thermal conductivity (0.040 W m^{-1} K^{-1}), which promoted convective and conductive heat transfer, respectively. In addition, the anisotropic thermal property of the nanowood membrane was believed to facilitate the heat transfer along the membrane, thereby helping to maintain the temperature gradient and promote flux. However, to quantify these benefits, localized temperature differences will need to be measured and compared. Instead of using complex fabrication processes such as those for PP and PTFE manufacturing, the nanowood membrane can be fabricated by a scalable top-down approach via simple chemical treatments. As a proof of concept for scalability, we have constructed pieces of the nanowood membrane with a length larger than 15 cm and a thickness less than 500 μm. The newly developed nanowood membrane as a thermally efficient membrane carries great potential to use low-grade heat from different sources for water desalination. Optimizations of the pore size and thickness can be achieved by selecting other wood species and using microtomes. Future bio-based wood membrane with this unique pore structure may also be engineered using nanocellulose fibers via electrospinning. Because of the hydrophilic nature of nanocellulose materials, further improvements are needed to increase hydrophobic treatment efficacy and membrane durability under high temperature and chemical conditions. In addition, fabrication methods need to be improved to generate thinner and larger membrane materials.

MATERIALS AND METHODS

Materials and chemicals

All working solutions were prepared using American Chemical Society–grade chemicals (Thermo Fisher Scientific, Waltham, MA) and Milli-Q water (18.2 megohm·cm) throughout the study, unless otherwise stated. The lignin removal solution contained 2.5 M NaOH and 0.4 M Na_2SO_3, and the bleaching solution was 2.5 M H_2O_2. A mixture of 95 weight % (wt %) ethanol, 2 wt % FAS (perfluorodecyltriethoxysilane, $C_{16}H_{19}F_{17}O_3Si$; Sigma-Aldrich), and 3 wt % Milli-Q water (pH adjusted at pH 5.0 with acetic acid) was prepared and used as the silane solution for hydrophobic treatment. The mixture was magnetically stirred for 24 hours for silane hydrolysis. The mechanism of silane treatment can be found in section S1 (*50*). Commercial hydrophobic membranes (Table 1 and fig. S5) in comparison tests were purchased from Tisch Scientific, North Bend, OH.

Nanowood membrane preparation and characterization

The base wood used in this study was American basswood purchased from Walnut Hollow Company. Two types of woods were prepared for membrane fabrication. One type of membrane was made from natural wood without lignin treatment, and another was constructed using treated nanowood, which underwent lignin removal process to increase flexibility and porosity. The nanowood was prepared from natural wood slices (thickness, 2 mm) by boiling the wood along cellulose fiber direction for 12 hours, followed by rinsing in hot distilled water three times to remove residuals (*51*, *52*). The product was subsequently immersed in the boiling bleaching solution until the wood turned white (Fig. 3, A and B). Last, each wood sample was rinsed with cold water and freeze-dried to preserve the nanoporous structure of the delignified wood (*39*).

Similar procedures were used on pieces of nanowood and natural wood for membrane fabrication. After the above treatment, the average thickness of the nanowood was 502 ± 35 μm, while the average thickness of natural wood was 540 ± 15 μm (fig. S3). Wood consists of naturally aligned cellulose fibers with abundant hydroxyl functional groups that allow surface modification via silane chemistry (fig. S1). The nanowood was dipped into the FAS solution with gentle agitation for 10 hours to enable full infiltration before thorough ethanol rinse. Then, the FAS-treated wood was subjected to heat treatment at 120°C for 4 hours in a vacuum oven (−80 kPa). After this treatment, the hydrophilic wood membranes became hydrophobic with FAS loadings of wood (71.3 ± 5.4 mg FAS g^{-1}). The membrane samples were characterized using SEM, contact angle measurements, PSD, porosity, and thermal conductivity (*24*, *39*, *53*–*55*), and the performance in desalination was compared with commercial MD membranes.

Contact angle and LEP measurements

Contact angle measurements were performed using a contact angle goniometer (Model 250, ramé-hart, Netcong, NJ) via sessile drop method (*54*). The measurements were performed by placing the sample on the measurement platform coupled with a camera lens to capture the image. A 3-μl DI water droplet was deposited by a syringe placed above the surface. The contact angle was measured and analyzed using the built-in software. At least three measurements were conducted on each of the three different locations for one membrane sample, and the data were averaged.

The LEP was measured using a stainless membrane cell (Sartorius), where DI water was placed on the membrane and the pressure in the sample holder was increased by flowing nitrogen gas. The pressure at which the gas flow was detected by a flow meter was reported as the LEP.

PSD and porosity measurements

The PSD of the prepared membranes was determined using a capillary flow porometer (CFP; Porolux 1000, IB-FT GmbH, Germany). The

membrane was fully wetted with Porefil, followed by measurements described by Nakao (*53*) and Khayet and Matsuura (*56*). The PSD was obtained with the aid of the coupled CFP software.

Membrane porosity was determined using the gravimetric method (*24*, *55*). Specifically, a piece of membrane was dried at 40°C for 5 hours in an oven and subsequently weighed using an analytical balance (Denver PI-214A). The sample was then fully immersed into 2-propanol for 1 day for complete alcohol infiltration. After wetting, the sample was cleaned to remove residue from the surface and weighed. The porosity (ε) was estimated using the equation

$$\varepsilon = \frac{V_{\text{pore}}}{V_{\text{total}}} = \frac{m_{\text{IPA}} / \rho_{\text{IPA}}}{V_{\text{total}}} \quad (1)$$

where V, m, and ρ are the volume, mass, and density, respectively, and IPA indicates 2-propanol. Three independent measurements were performed on each sample.

Thermal property measurements

The thermal properties of the membranes were characterized using a conductive heat source with a contact area of 4 mm by 4 mm via conductive thermal paste. IR thermographs were taken using an IR camera (T630sc from FLIR). Steady state was reached before the data were recorded at room temperature (21°C). The thermal conductivity of woods was measured using the laser flash apparatus (LFA), during which an instantaneous laser pulse was used to heat up one side of the sample, and the response of temperature on the other side was recorded by a detector. The thermal conductivity κ of the sample was calculated according to Li *et al.* (*39*). Briefly, an instantaneous laser pulse was irradiated on one side of the sample, and the response of temperature on the other side was recorded by an LFA 457 detector (NETZSCH, Burlington, MA) for thermal diffusivity measurement. Differential scanning calorimetry method with a sapphire reference was used to determine the heat capacity. The thermal conductivity k can then be calculated by multiplying the thermal diffusivity and the heat capacity together with the material bulk density (0.13 ± 0.03 g cm^{-3}). The samples were stored at 25°C and 20% humidity for a minimum of 24 hours before measurement.

MD reactor and operation

Membrane performance was evaluated using a laboratory-scale DCMD apparatus (fig. S9). The membranes were inserted into the custom-built acryl cell with an effective membrane area of 8 cm^2 (4-cm length by 2-cm width). Hot feed [NaCl (1 g liter^{-1})] and cold distillate (DI) streams were circulated using two variable gear pumps (Cole-Parmer, Vernon Hills, IL), and temperature was controlled using two recirculating water baths (Polystat Standard, Cole-Parmer, Vernon Hills, IL). Diamond-shaped polyester spacers were inserted in both feed and distillate channels to support and maintain membrane geometry in the cell. During operation, cocurrent flow, which was parallel to the fiber growth direction of the wood membrane, was adopted with a flow rate of 220 ml min^{-1} (equivalent to a cross flow velocity of 8.0 cm s^{-1}) for both feed and distillate. Water vapor flux, J_w, across the membrane was measured by monitoring the increase in distillate mass using a digital balance (NVT6200, OHAUS, Parsippany, NJ). The distillate weight gain was recorded in a laptop at 1-min intervals. Salt passage was monitored by measuring the salt concentration in distillate using a calibrated conductivity meter (OAKTON Instruments, Vernon Hills, IL) at 1-min intervals. Membrane performance for every sample was measured for three different sets of feed temperatures (40°, 50°, and 60°C), while the distillate temperature was fixed at 20°C. Each temperature set was operated for 30 min. The experimental thermal conductivity and intrinsic permeability were calculated according to a modified Schofield method (section S14) (*22*). The transport mechanism and theoretical permeability of water vapor through the membrane (section S15) were simulated using the widely adopted "dusty gas model," which considered viscous diffusion, ordinary molecular diffusion, and Knudsen diffusion (*23*, *24*, *57*, *58*).

SUPPLEMENTARY MATERIALS

Supplementary material for this article is available at http://advances.sciencemag.org/cgi/content/full/5/8/eaaw3203/DC1

Section S1. The hydrophobic silane treatment mechanism
Section S2. The nanowood membrane before and after hydrophobic treatment
Section S3. The natural wood membranes
Section S4. Comparison of the wood membranes and common papers
Section S5. Anisotropic thermal insulation property of the nanowood membrane and the potential benefits
Section S6. Commercial hydrophobic membranes
Section S7. Pore size distribution of the commercial membranes
Section S8. Morphology and pore structure of the commercial membranes
Section S9. Surface hydrophobicity/hydrophilicity
Section S10. DCMD reactors and configurations
Section S11. Water flux of commercial membranes
Section S12. Theoretical thermal conductivity estimation
Section S13. Thermal insulation of commercial membranes
Section S14. Experimental thermal conductivity and membrane permeability
Section S15. Theoretical permeability coefficient and intrinsic permeability
Section S16. Wood membrane durability
Section S17. Wood membrane application and fouling
Fig. S1. Schematics of hydrophobic treatment of wood membranes using silane coupling agent (*50*).
Fig. S2. Surface morphologies and pore size distribution of the nanowood membrane before and after hydrophobic treatment.
Fig. S3. Visual images of the hydrophobic natural wood membrane after silane treatment.
Fig. S4. Temperature plots of isotropic and anisotropic thermal insulators from a point heat source.
Fig. S5. Visual images of the commercial hydrophobic membranes purchased from Tisch Scientific (North Bend, Ohio).
Fig. S6. PSD of the commercial membranes.
Fig. S7. SEM images of the surface and cross-section of the commercial membranes.
Fig. S8. Water contact angles of the commercial and hydrophobic natural wood membranes.
Fig. S9. Schematics, images, and control interface of the apparatus for direct contact membrane distillation (DCMD).
Fig. S10. Water flux of the commercial polymeric membranes in DCMD with feed [NaCl (1 g liter^{-1})] temperature continuously varying between 40° and 60°C and distillate (DI water) temperature of 20°C.
Fig. S11. IR thermographs of the commercial membranes with the heat source temperature of 60°C.
Fig. S12. Temperature plots of anisotropic nanowood and isotropic commercial membranes from a point heat source.
Fig. S13. Comparison of experimentally measured intrinsic (thickness-normalized) membrane permeability of the wood and commercial membranes.
Fig. S14. Water flux of the hydrophobic wood membranes in DCMD with feed [NaCl (1 g liter^{-1})] and distillate (DI water) temperatures controlled at 60° and 20°C, respectively.
Fig. S15. Water flux of the hydrophobic nanowood membrane in DCMD with [NaCl (35 g liter^{-1}) and synthetic wastewater] and distillate (DI water) temperatures controlled at 60° and 20°C, respectively.
Table S1. Comparison between nanowood and common paper.

REFERENCES AND NOTES

1. United Nations World Water Assessment Programme, "The United Nations world water development report 2018: Nature-based solutions for water" (United Nations Educational, Scientific and Cultural Organization, 2018).

2. G. M. MacDonald, Climate change and water in southwestern North America special feature: Water, climate change, and sustainability in the southwest. *Proc. Natl. Acad. Sci. U.S.A.* **107**, 21256–21262 (2010).
3. W. N. Adger, J. Barnett, K. Brown, N. Marshall, K. O'Brien, Cultural dimensions of climate change impacts and adaptation. *Nat. Clim. Chang.* **3**, 112–117 (2012).
4. A. AghaKouchak, D. Feldman, M. Hoerling, T. Huxman, J. Lund, Water and climate: Recognize anthropogenic drought. *Nature* **524**, 409–411 (2015).
5. M. A. Shannon, P. W. Bohn, M. Elimelech, J. G. Georgiadis, B. J. Mariñas, A. M. Mayes, Science and technology for water purification in the coming decades. *Nature* **452**, 301–310 (2008).
6. M. Elimelech, W. A. Phillip, The future of seawater desalination: Energy, technology, and the environment. *Science* **333**, 712–717 (2011).
7. C. Forrestal, Z. Stoll, P. Xu, Z. J. Ren, Microbial capacitive desalination for integrated organic matter and salt removal and energy production from unconventional natural gas produced water. *Environ. Sci. Water Res. Technol.* **1**, 47 (2015).
8. D. Jassby, T. Y. Cath, H. Buisson, The role of nanotechnology in industrial water treatment. *Nat. Nanotechnol.* **13**, 670–672 (2018).
9. A. Al-Karaghouli, L. L. Kazmerski, Energy consumption and water production cost of conventional and renewable-energy-powered desalination processes. *Renew. Sustain. Energy Rev.* **24**, 343–356 (2013).
10. A. Deshmukh, C. Boo, V. Karanikola, S. Lin, A. P. Straub, T. Tong, D. M. Warsinger, M. Elimelech, Membrane distillation at the water-energy nexus: Limits, opportunities, and challenges. *Energ. Environ. Sci.* **11**, 1177–1196 (2018).
11. P. Denholm, M. O'Connell, G. Brinkman, J. Jorgenson, *Overgeneration from Solar Energy in California. A Field Guide to the Duck Chart* (National Renewable Energy Laboratory, 2015).
12. A. V. Dudchenko, C. Chen, A. Cardenas, J. Rolf, D. Jassby, Frequency-dependent stability of CNT Joule heaters in ionizable media and desalination processes. *Nat. Nanotechnol.* **12**, 557–563 (2017).
13. P. Tao, G. Ni, C. Song, W. Shang, J. Wu, J. Zhu, G. Chen, T. Deng, Solar-driven interfacial evaporation. *Nat. Energy* **3**, 1031–1041 (2018).
14. A. Alkhudhiri, N. Darwish, N. Hilal, Membrane distillation: A comprehensive review. *Desalination* **287**, 2–18 (2012).
15. B. L. Pangarkar, M. G. Sane, S. B. Parjane, M. Guddad, Status of membrane distillation for water and wastewater treatment—A review. *Desalin. Water Treat.* **52**, 5199 (2013).
16. E. Drioli, A. Ali, F. Macedonio, Membrane distillation: Recent developments and perspectives. *Desalination* **356**, 56–84 (2015).
17. A. P. Straub, N. Y. Yip, S. Lin, J. Lee, M. Elimelech, Harvesting low-grade heat energy using thermo-osmotic vapour transport through nanoporous membranes. *Nat. Energy* **1**, 16090 (2016).
18. P. D. Dongare, A. Alabastri, S. Pedersen, K. R. Zodrow, N. J. Hogan, O. Neumann, J. Wu, T. Wang, A. Deshmukh, M. Elimelech, Q. Li, P. Nordlander, N. J. Halas, Nanophotonics-enabled solar membrane distillation for off-grid water purification. *Proc. Natl. Acad. Sci. U.S.A.* **114**, 6936–6941 (2017).
19. P. Zhang, J. Li, L. Lv, Y. Zhao, L. Qu, Vertically aligned graphene sheets membrane for highly efficient solar thermal generation of clean water. *ACS Nano* **11**, 5087–5093 (2017).
20. M. Qtaishat, T. Matsuura, B. Kruczek, M. Khayet, Heat and mass transfer analysis in direct contact membrane distillation. *Desalination* **219**, 272–292 (2008).
21. A. Deshmukh, M. Elimelech, Understanding the impact of membrane properties and transport phenomena on the energetic performance of membrane distillation desalination. *J. Memb. Sci.* **539**, 458–474 (2017).
22. J. Vanneste, J. A. Bush, K. L. Hickenbottom, C. A. Marks, D. Jassby, C. S. Turchi, T. Y. Cath, Novel thermal efficiency-based model for determination of thermal conductivity of membrane distillation membranes. *J. Memb. Sci.* **548**, 298–308 (2018).
23. M. Khayet, Membranes and theoretical modeling of membrane distillation: A review. *Adv. Colloid Interface Sci.* **164**, 56–88 (2011).
24. M. E. Leitch, C. Li, O. Ikkala, M. S. Mauter, G. V. Lowry, Bacterial nanocellulose aerogel membranes: Novel high-porosity materials for membrane distillation. *Environ. Sci. Technol. Lett.* **3**, 85–91 (2016).
25. A. M. Alklaibi, N. Lior, Membrane-distillation desalination: Status and potential. *Desalination* **171**, 111–131 (2005).
26. P. Wang, T.-S. Chung, Recent advances in membrane distillation processes: Membrane development, configuration design and application exploring. *J. Memb. Sci.* **474**, 39–56 (2015).
27. D. Hou, A. Iddya, X. Chen, M. Wang, W. Zhang, Y. Ding, D. Jassby, Z. J. Ren, Nickel-based membrane electrodes enable high-rate electrochemical ammonia recovery. *Environ. Sci. Technol.* **52**, 8930–8938 (2018).
28. M. Gryta, Osmotic MD and other membrane distillation variants. *J. Memb. Sci.* **246**, 145–156 (2005).
29. T. Borca-Tasciuc, S. Vafaei, D.-A. Borca-Tasciuc, B. Wei, R. Vajtai, P. Ajayan, Anisotropic thermal diffusivity of aligned multiwall carbon nanotube arrays. *J. Appl. Phys.* **98**, 054309 (2005).
30. L. Guo, J. Wang, Z. Lin, S. Gacek, X. Wang, Anisotropic thermal transport in highly ordered TiO_2 nanotube arrays. *J. Appl. Phys.* **106**, 123526 (2009).
31. B. Wicklein, A. Kocjan, G. Salazar-Alvarez, F. Carosio, G. Camino, M. Antonietti, L. Bergstrom, Thermally insulating and fire-retardant lightweight anisotropic foams based on nanocellulose and graphene oxide. *Nat. Nanotechnol.* **10**, 277–283 (2015).
32. N. Lucas, C. Bienaime, C. Belloy, M. Queneudec, F. Silvestre, J. E. Nava-Saucedo, Polymer biodegradation: Mechanisms and estimation techniques. *Chemosphere* **73**, 429–442 (2008).
33. Y. Habibi, L. A. Lucia, O. J. Rojas, Cellulose nanocrystals: Chemistry, self-assembly, and applications. *Chem. Rev.* **110**, 3479–3500 (2010).
34. L. Hu, G. Zheng, J. Yao, N. Liu, B. Weil, M. Eskilsson, E. Karabulut, Z. Ruan, S. Fan, J. T. Bloking, M. D. McGehee, L. Wågberg, Y. Cui, Transparent and conductive paper from nanocellulose fibers. *Energ. Environ. Sci.* **6**, 513–518 (2013).
35. L.-F. Chen, Z.-H. Huang, H.-W. Liang, W.-T. Yao, Z.-Y. Yu, S.-H. Yu, Flexible all-solid-state high-power supercapacitor fabricated with nitrogen-doped carbon nanofiber electrode material derived from bacterial cellulose. *Energ. Environ. Sci.* **6**, 3331–3338 (2013).
36. Y. H. Jung, T.-H. Chang, H. Zhang, C. Yao, Q. Zheng, V. W. Yang, H. Mi, M. Kim, S. J. Cho, D. W. Park, H. Jiang, J. Lee, Y. Qiu, W. Zhou, Z. Cai, S. Gong, Z. Ma, High-performance green flexible electronics based on biodegradable cellulose nanofibril paper. *Nat. Commun.* **6**, 7170 (2015).
37. F. Chen, A. S. Gong, M. Zhu, G. Chen, S. D. Lacey, F. Jiang, Y. Li, Y. Wang, J. Dai, Y. Yao, J. Song, B. Liu, K. Fu, S. Das, L. Hu, Mesoporous, three-dimensional wood membrane decorated with nanoparticles for highly efficient water treatment. *ACS Nano* **11**, 4275–4282 (2017).
38. Z. Huang, A. Gong, D. Hou, L. Hu, Z. J. Ren, A conductive wood membrane anode improves effluent quality of microbial fuel cells. *Environ. Sci. Water Res. Technol.* **3**, 940–946 (2017).
39. T. Li, J. Song, X. Zhao, Z. Yang, G. Pastel, S. Xu, C. Jia, J. Dai, C. Chen, A. Gong, F. Jiang, Y. Yao, T. Fan, B. Yang, L. Wagberg, R. Yang, L. Hu, Anisotropic, lightweight, strong, and super thermally insulating nanowood with naturally aligned nanocellulose. *Sci. Adv.* **4**, eaar3724 (2018).
40. S. A. Lavrykov, B. V. Ramarao, Thermal properties of copy paper sheets. *Drying Technol.* **30**, 297–311 (2012).
41. PaperOnWeb, "Properties of paper"; https://paperonweb.com/paperpro.htm.
42. R. H. White, Effect of lignin content and extractives on the higher heating value of wood. *Wood Fiber Sci.* **19**, 446 (1987).
43. P. T. Larsson, E. L. Hult, K. Wickholm, E. Pettersson, T. Iversen, CP/MAS 13C-NMR spectroscopy applied to structure and interaction studies on cellulose I. *Solid State Nucl. Magn. Reson.* **15**, 31–40 (1999).
44. C. Boo, J. Lee, M. Elimelech, Engineering surface energy and nanostructure of microporous films for expanded membrane distillation applications. *Environ. Sci. Technol.* **50**, 8112–8119 (2016).
45. A. Franken, J. Nolten, M. Mulder, D. Bargeman, C. A. Smolders, Wetting criteria for the applicability of membrane distillation. *J. Memb. Sci.* **33**, 315–328 (1987).
46. B. M. Suleiman, J. Larfeldt, B. Leckner, M. Gustavsson, Thermal conductivity and diffusivity of wood. *Wood Sci. Technol.* **33**, 465–473 (1999).
47. J. Eitelberger, K. Hofstetter, Prediction of transport properties of wood below the fiber saturation point—A multiscale homogenization approach and its experimental validation: Part I. Thermal conductivity. *Compos. Sci. Technol.* **71**, 134–144 (2011).
48. K. W. Lawson, D. R. Lloyd, Membrane distillation. *J. Memb. Sci.* **124**, 1–25 (1997).
49. R. W. Field, H. Y. Wu, J. J. Wu, Multiscale modeling of membrane distillation: Some theoretical considerations. *Ind. Eng. Chem. Res.* **52**, 8822–8828 (2013).
50. S. Lin, S. Nejati, C. Boo, Y. Hu, C. O. Osuji, M. Elimelech, Omniphobic membrane for robust membrane distillation. *Environ. Sci. Technol. Lett.* **1**, 443–447 (2014).
51. M. Zhu, J. Song, T. Li, A. Gong, Y. Wang, J. Dai, Y. Yao, W. Luo, D. Henderson, L. Hu, Highly anisotropic, highly transparent wood composites. *Adv. Mater.* **28**, 5181–5187 (2016).
52. T. Li, M. Zhu, Z. Yang, J. Song, J. Dai, Y. Yao, W. Luo, G. Pastel, B. Yang, L. Hu, Wood composite as an energy efficient building material: Guided sunlight transmittance and effective thermal insulation. *Adv. Energy Mater.* **6**, 1601122 (2016).
53. S.-i. Nakao, Determination of pore size and pore size distribution. *J. Memb. Sci.* **96**, 131–165 (1994).
54. Y. Yuan, T. R. Lee, Contact angle and wetting properties, in *Surface Science Techniques*, G. Bracco, B. Holst, Eds. (Springer, 2013), pp. 3–34.
55. E. Shaulsky, S. Nejati, C. Boo, F. Perreault, C. O. Osuji, M. Elimelech, Post-fabrication modification of electrospun nanofiber mats with polymer coating for membrane distillation applications. *J. Memb. Sci.* **530**, 158–165 (2017).
56. M. Khayet, T. Matsuura, Preparation and characterization of polyvinylidene fluoride membranes for membrane distillation. *Ind. Eng. Chem. Res.* **40**, 5710–5718 (2001).
57. E. A. Mason, A. P. Malinauskas, *Gas Transport in Porous Media: The Dusty-Gas Model*, vol. 17 of *Chemical Engineering Monographs*, A. P. Malinauskas, Ed. (Elsevier, 1983).

58. J. Phattaranawik, R. Jiraratananon, A. G. Fane, Effect of pore size distribution and air flux on mass transport in direct contact membrane distillation. *J. Memb. Sci.* **215**, 75–85 (2003).
59. M. G. Kaganer, *Thermal Insulation in Cryogenic Engineering* (Israel Program for Scientific Translations, 1969).

Acknowledgments: We thank X. Zhao (University of Colorado Boulder), W. Gan, R. Mi (University of Maryland, College Park), and Z. Wang (Yale University) for great assistance in membrane characterizations. **Funding:** We appreciate the financial support from the U.S. Department of Agriculture (2017-67022-26135) and Office of Naval Research (N000141612210). The work at University of Maryland is supported by the A. James & Alice B. Clark Foundation and the A. James School of Engineering at the University of Maryland. **Author contributions:** D.X. Hou, T.L., L.H., and Z.J.R. wrote the manuscript. D.X. Hou, T.L., L.H., and Z.J.R. conceived experiments. X.C. conducted part of MD experiment and flux characterization. S.H. and J.D. performed SEM measurements. S.A.M., D.Y. Hou, and R.Y. performed part of thermo measurements. A.I. and D.J. performed part of membrane characterizations. **Competing interests:** L.H., T.L., and S.H. are inventors on an international patent application related to this work filed by the University of Maryland, College Park (no. PCT/US2018/051091, filed 14 September 2018). All other authors declare that they no competing interests.
Data and materials availability: The white wood materials were made at the University of Maryland. Requests for these materials should be submitted to the University of Maryland, Office of Technology Commercialization. All data needed to evaluate the conclusions in the paper are present in the paper and/or the Supplementary Materials. Additional data related to this paper may be requested from the authors.

Submitted 13 December 2018
Accepted 27 June 2019
Published 2 August 2019
10.1126/sciadv.aaw3203

Citation: D. Hou, T. Li, X. Chen, S. He, J. Dai, S. A. Mofid, D. Hou, A. Iddya, D. Jassby, R. Yang, L. Hu, Z. J. Ren, Hydrophobic nanostructured wood membrane for thermally efficient distillation. *Sci. Adv.* **5**, eaaw3203 (2019).

Hydrophobic nanostructured wood membrane for thermally efficient distillation

Dianxun Hou, Tian Li, Xi Chen, Shuaiming He, Jiaqi Dai, Sohrab A. Mofid, Deyin Hou, Arpita Iddya, David Jassby, Ronggui Yang, Liangbing Hu and Zhiyong Jason Ren

Sci Adv **5** (8), eaaw3203.
DOI: 10.1126/sciadv.aaw3203

Article X

Xinpeng Zhao, Sohrab Alex Mofid, Bjørn Petter Jelle, Gang Tan, Xiabo Yin and Ronggui Yang, **Optically-switchable thermally insulating VO_2-PMMA aerogel hybrid film for window retrofits**, *Applied Energy,* 278 (2020) 115663.

Applied Energy 278 (2020) 115663

Contents lists available at ScienceDirect

Applied Energy

journal homepage: www.elsevier.com/locate/apenergy

Optically-switchable thermally-insulating VO_2-aerogel hybrid film for window retrofits

Xinpeng Zhao [a], Sohrab Alex Mofid [b,c], Bjørn Petter Jelle [c,d], Gang Tan [e], Xiaobo Yin [b], Ronggui Yang [a,*]

[a] School of Energy and Power Engineering, Huazhong University of Science and Technology, Wuhan, Hubei 430074, China
[b] Department of Mechanical Engineering, University of Colorado Boulder, Boulder, CO 80309, USA
[c] Department of Civil and Environmental Engineering, Norwegian University of Science and Technology (NTNU), NO-7491 Trondheim, Norway
[d] Department of Materials and Structures, SINTEF Community, NO-7465 Trondheim, Norway
[e] Department of Civil and Architectural Engineering, University of Wyoming, Laramie, WY 82071, USA

HIGHLIGHTS

- An optically-switchable thermally-insulating VO_2-aerogel hybrid film was proposed.
- A coupled heat conduction and solar radiation heat transfer model was developed.
- The U-value of the film is ~50% less than the value of single-pane windows.
- The solar modulation ability of the film is ~20%.
- This film can improve thermal comfort, avoid moisture condensation and overheating.

ARTICLE INFO

Keywords:
Window retrofit
Aerogel
VO_2 nanoparticle
Thermochromic
Building energy saving

ABSTRACT

Developing easy-to-install energy-efficient window retrofitting materials is important for reducing the heating and cooling loads of buildings. However, it is very challenging to achieve window retrofits that are simultaneously thermally insulating, visible-light transparent, and dynamically switchable in solar transmission. Here, a visibly transparent and thermally insulating film was proposed to reduce the energy loss through windows. By embedding insulator–metal phase transition vanadium dioxide (VO_2) nanoparticles inside an ultralow thermal conductivity aerogel film, the thermal insulation performance is greatly improved in such thermochromic film while the solar transmission can be dynamically switched in response to ambient conditions. A coupled heat conduction and solar radiation heat transfer model was developed to evaluate the effect of geometric features such as film thickness, nanoparticle size, and concentration on the thermal and optical performance of the proposed films. It was shown that a 3.0 mm thick film could achieve a low U-value of ~ 3.0 W/(m^2K), and a high luminous transmittance of > 60% and a solar modulation ability of ~ 20%. This film improves the performance of single-pane windows by reducing the energy loss, improving thermal comfort, and avoiding moisture condensation in cold climates and overheating in hot climates.

1. Introduction

Due to the relatively high thermal conductivity (~ 1.0 W/(mK)), in comparison with 0.04–0.1 W/(mK) of building insulation materials, such as mineral wool, extruded polystyrene and cork, and the high infrared emissivity (~ 0.84) of float glass, 40% ~ 60% of the energy loss from buildings is through windows [1,2]. For single-pane windows, the energy loss rate is in the range of 60–250 W/m^2 according to the ASHRAE standard [3]. During the daytime, glass windows transmit as high as ~ 800 W/m^2 solar energy [4,5], which significantly reduces the heating demands in cold climates. However, the extra solar irradiance shedding in a room also increases the cooling demands and causes glare in hot climates. Moreover, the low thermal resistance of the single-pane window causes thermal discomfort and moisture condensation in cold climates. According to the analysis of ARPA-E [6], a fully successful

* Corresponding author.
E-mail address: ronggui@hust.edu.cn (R. Yang).

https://doi.org/10.1016/j.apenergy.2020.115663
Received 25 February 2020; Received in revised form 29 July 2020; Accepted 4 August 2020
Available online 19 August 2020

Nomenclatures

a	inner diameter, [nm]
b	outer diameter, [nm]
a_n, b_n	Mie scattering coefficients, [-]
h	heat transfer coefficient, [W/(m^{2}K)]
I_λ	radiation intensity, [W/(m^{2}Srμm)]
k	thermal conductivity, [W/(mK)]
$K_{lum,\lambda}$	standard luminous efficiency, [-]
L	thickness, [mm]
m_1,m_2	complex refractive index, [-]
N	nanoparticle number, [-]
M	total discrete direction, [-]
Q	efficiency factor, [-]
q_r	radiative heat flux, [W/m^2]
T	temperature, [°C]
U	U-value, [W/(m^{2}K)]
V_f	volume fraction, [-]
v	wind speed, [m/s]
w	quadrature weight, [-]
z	cartesian coordinate, [m]

Greeks

β	extinction coefficient, [m^{-1}]
λ	wavelength, [μm]
τ	transmittance, [-]
ρ	reflectance, [-]
ε	emissivity, [-]
μ,μ'	direction cosine, [-]
ω	scattering albedo, [-]
σ	Stefan-Boltzmann's constant, [W/(m^{2}K^4)]
θ	polar angle, [°]
φ_s	solar incidence angle, [°]
ϕ	azimuth angle, [°]
γ_s	solar azimuth angle, [°]
Δ	difference

Subscripts

a	ambient or aerogel
abs	absorption
all	overall
a-vah	air/VAH interface
b	blackbody
c	critical phase transition
ext	extinction
g-a	glass/air interface
gla	glass
g-vah	glass/VAH interface
i	inside
lum	luminous
o	outside
p	nanoparticle
r	room or radiation
scat	scattering
sol	solar
vah	VO_2-aerogel hybrid
λ	wavelength dependent

Superscripts

+	forward
–	backward

Abbreviations

VAH	VO_2-aerogel hybrid
DNI	direct normal irradiance
DHI	diffusive horizontal irradiance
RTE	radiative transfer equation
DOM	discrete coordinates method

single-pane retrofit will save 1.3% of the domestic energy use in the United States.

In order to reduce the heat loss through windowpanes, several kinds of transparent insulation materials have been explored to provide a high thermal resistance while retaining solar transmission [7]. Silica aerogels with low thermal conductivity (~ 0.02 W/(mK)) and high optical transmittance (~ 0.9) [8,9] were considered as a good candidate material for window insulation [2,10–13]. However, silica aerogels are very fragile. Significant enhancement in the mechanical performance has been reported in the recently synthesized flexible and transparent aerogels using organic–inorganic cross-linked structures [14,15] or cellulose nanofibers [16,17], showing great potential for window insulation applications. Some other visibly-transparent thermally insulating materials, including polymer nanofoams [18] and hollow microcapsule embedded polymers [19,20], have also been explored. However, most of the existing transparent insulation materials can only reduce the heat loss through windows and cannot dynamically respond to solar heat gain when the temperature changes.

Chromogenic materials are of great interest as they can dynamically modulate solar transmission (visible and infrared) by up to ~ 60% [21–23] when the environment changes. For example, WO_3 based electrochromic windows could change from transparent to a dark blue color because of cathodic Faradaic charge injection under an external voltage [24,25]. Windows made of the liquid crystal [26,27] and the suspended particle (e.g., polymer particle) [28] could switch between transparent and translucent states due to molecular/particle alignments. Unfortunately, most of the currently available electrochromics are cost-prohibitive for window retrofits. Compared with electrochromics, thermochromic windows are relatively more competitive due to their unique characteristics, including low cost and automatic response to temperature change [29,30]. Depending on the climates, the thermochromic windows could save 5–84.7% of the heating and cooling energy consumption in comparison to the normal windows [31]. Vanadium dioxide (VO_2) has demonstrated a promising regulation ability of solar transmission in the near-infrared range (780–2500 nm wavelength) through a reversible insulator–metal structural transformation at 68 °C [32–34]. By doping with other elements such as magnesium [35] or tungsten [36], the phase transition temperature of doped VO_2 can be tailored down to room temperature. However, the VO_2 thin films usually have very low solar modulation ability (< 10%) and luminous transmittance (< 40%) [33,37,38]. Recently, both theoretical model [37] and experimental measurement [39] showed that dielectric hosts embedded with dilute VO_2 nanoparticles could considerably improve the luminous transmittance to above 50% and the solar modulation ability to around 20%. However, switchable VO_2 nanoparticles can easily be oxidized to non-switchable V_2O_5 by the vapor and oxygen in the ambient [40]. Therefore, an addition of environmentally stable material such as SiO_2 [41], ZnO [39], and TiO_2 [42] was adopted as a protection layer to enhance anti-oxidation and anti-acid ability of VO_2 nanoparticles. The addition of a chemically stable shell layer does not prevent the reversible insulator–metal structural transformation behavior of VO_2. On the contrary, it may enhance the luminous transmittance of VO_2 nanoparticle-based films. For example, Li *et al.* [41] showed that compared to the visible transmittance of ~ 31.7% for VO_2(M), the VO_2(M)@SiO_2 exhibits a visible transmittance of ~ 46%, with an increase of ~ 13.4%. Although a chromogenic thin film may substantially

change the thermal-radiative properties, e.g., solar absorbance, transmittance, reflectance, and infrared-emissivity, the electrochromic and thermochromic films alone cannot block the heat loss due to low thermal resistance in the thin film form. In previous studies [43,44], the opacifier particles such as carbon, SiC, TiO_2, and ZrO_2 have been embedded into the aerogel matrix to improve the absorption coefficient in the infrared range of 3–8 μm, making silica aerogel a promising candidate for high-temperature thermal insulation applications (> 600 K). The above-mentioned strategies indicate that combining thermochromic nanoparticles together with transparent thermal insulation materials may be an effective way towards thermally-insulating window retrofits which is switchable to solar radiation.

In this work, an optically-switchable thermally-insulating VO_2-aerogel hybrid (VAH) film is proposed for energy-efficient window retrofits, by embedding VO_2 nanoparticles into the aerogel film, which can both dynamically manipulate the solar transmission when temperature change and achieve a high thermal resistance due to the low thermal conductivity of aerogels. The effects of the film thickness, the size, and concentration of the nanoparticles on the thermal and optical performance of the VAH film were analyzed using a coupled heat conduction and solar radiation heat transfer model. It was found that a 3.0 mm thick VAH film embedded with a 0.01 vol% core–shell structure VO_2/SiO_2 with an inner diameter of 25 nm and an outer diameter of 40 nm could achieve a thermal transmittance (U-value) of ~ 3.0 W/(m^2K), which approximately ~ 50% less than the value of single-pane windows, a luminous transmittance of 0.7 (0.6) in cold (hot) climates, and a solar modulation ability of ~ 20%. The modeling results also showed that employing the VAH film could not only reduce the heat loss but also greatly improve the performance of single-pane windows by improving thermal comfort and avoiding moisture condensation in cold climates and overheating in hot climates.

2. Modeling approach

2.1. Structure of thermochromic VO_2-aerogel hybrid film

Fig. 1(a) illustrates the heat transfer and solar radiation transfer across a windowpane where the single-pane glass is externally covered by a VAH retrofitting film. Fig. 1(b) shows the detailed structure of the proposed thermochromic VO_2-aerogel hybrid (VAH) film. Transparent aerogel with ultralow thermal conductivity (~ 0.018 W/(mK)) is adopted to increase the conductive thermal resistance of the windowpane and to reduce the energy loss. Here the transparent aerogel can be silica aerogels or other recently synthesized mechanically enhanced aerogels such as liquid-crystalline nanocellulose aerogel [16], and organic–inorganic crosslinked hybrid aerogels [14,17], as long as nanoparticles can be embedded. Core-shell VO_2/SiO_2 nanoparticles are randomly dispersed in the transparent aerogel matrix to regulate solar transmission in response to the ambient conditions. Here the SiO_2 coating increases the environmental durability of the VO_2 nanoparticles (preventing the transformation of VO_2 to V_2O_5 due to natural oxidation) [39,45] and increases the optical performance [41]. When the temperature of the VO_2 nanoparticles T is lower than the critical phase transition temperature T_c ($T < T_c$), VO_2 nanoparticles are in the electrically-insulating state, and the hybrid film is transparent to solar radiation. When $T > T_c$, VO_2 nanoparticles transform to the metallic phase, the visible light can transmit while the near-infrared part of the solar irradiance is blocked [32]. The temperature of the VO_2 nanoparticles (T) inside the VAH film is regulated by the external and internal temperature of the window, along with solar radiation. The phase change temperature of VO_2 nanoparticles (T_c) could be tuned by doping with other elements (e.g., magnesium, and tungsten [35,36]). The optimized T_c is determined by both the weather conditions and the optical performance of VAH film.

2.2. Optical transmittance of VO_2-aerogel hybrid film

The optical performance of the thermochromic VAH film is characterized by the luminous transmittance and solar modulation ability. The mean luminous (380–780 nm) transmittance τ_{lum} is defined as [32,46],

$$\tau_{lum} = \frac{\int_{380\ nm}^{780\ nm} K_{lum,\lambda}\tau_\lambda d\lambda}{\int_{380\ nm}^{780\ nm} K_{lum,\lambda} d\lambda} \quad (1a)$$

where $K_{lum,\lambda}$ is the standard luminous efficiency for vision [47,48], and τ_λ is the transmittance of radiation at wavelength λ. The solar modulation ability $\Delta\tau_{sol}$ is defined by the difference of solar transmittance (280–2500 nm) before and after the phase transition,

$$\Delta\tau_{sol} = \tau_{sol}(T < T_c) - \tau_{sol}(T > T_c) \quad (1b)$$

where τ_{sol} is the mean solar (280–2500 nm) transmittance, which is defined by,

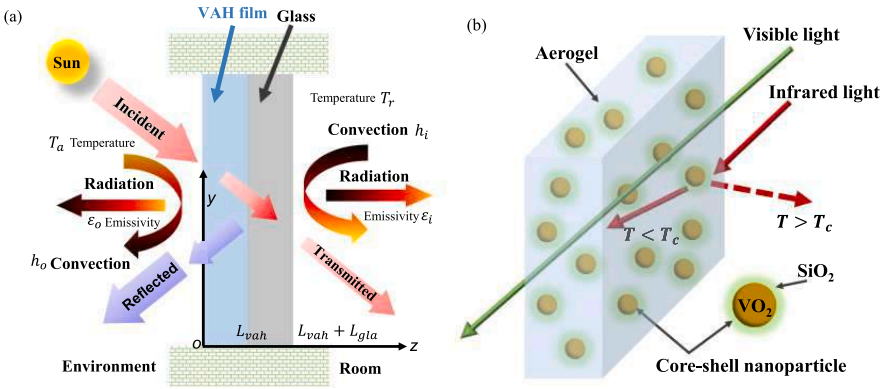

Fig. 1. Schematic of a single-pane window covered by a thermochromic VO_2-aerogel hybrid (VAH) retrofitting film. (a) Illustration of heat transfer and solar radiation transfer across a windowpane covered with a VAH film. (b) Structure of the VO_2-aerogel hybrid film. Transparent aerogel film with ultralow thermal conductivity is used to reduce conductive heat loss. The randomly dispersed metal-to-insulator phase-transition VO_2 nanoparticles coated with SiO_2 are embedded in the aerogel so that the solar transmission can be dynamically modulated in response to the ambient temperature and solar irradiance.

$$\tau_{sol} = \frac{\int_{280\ nm}^{2500\ nm} I_{AM15,\lambda}\tau_\lambda d\lambda}{\int_{280\ nm}^{2500\ nm} I_{AM15,\lambda} d\lambda} \tag{1c}$$

where $I_{AM15,\lambda}$ is the solar spectrum of air mass 1.5 (AM 1.5), which corresponds to the sun standing 37° above the horizon [49]. In Eqs. (1a)–(1c), the luminous transmittance τ_{lum} and solar modulation ability $\Delta\tau_{sol}$ of the thermochromic VAH film are determined by the size and volume fraction of the core–shell VO_2/SiO_2 nanoparticles, and the thickness of the aerogel film.

According to Ref. [37], a 5.0 μm thick film with ~ 1% volume fraction of VO_2 nanoparticles has luminous transmission τ_{lum} of ~ 0.7. In order to achieve similar optical performances (τ_{lum} = 0.6 ~0.7), the volume fraction of the VO_2/SiO_2 nanoparticles needs to remain very low (≪1%) as the hybrid film thickness is expected to be around several millimeters to be an effective thermal barrier. The low volumetric fraction guarantees that each VO_2/SiO_2 nanoparticle inside the VAH film can be considered as an individual scattering center. According to the Lorenz-Mie theory [48], when a single core–shell particle with inner diameter a and outer diameter b interacts with an electromagnetic wave with wavelength λ, the thermal radiative properties of the core–shell particle are governed by the complex refractive index of the core (shell) material $m_1(m_2)$, and the size parameters $x = \pi a/\lambda$ and $y = \pi b/\lambda$. The scattering (Q_{sca}), extinction (Q_{ext}) and absorption (Q_{abs}) efficiency factors of a single core–shell nanoparticle are evaluated by [50],

$$Q_{sca,\lambda} = \frac{2}{x^2}\sum_{n=1}^{\infty}(2n+1)\left(|a_n|^2 + |b_n|^2\right) \tag{2a}$$

$$Q_{ext,\lambda} = \frac{2}{x^2}\sum_{n=1}^{\infty}(2n+1)\mathrm{Re}(a_n + b_n) \tag{2b}$$

$$Q_{abs,\lambda} = Q_{ext,\lambda} - Q_{sca,\lambda} \tag{2c}$$

where a_n and b_n are the Mie scattering coefficients and functions of x, y, m_1, and m_2, and Re (·) denotes the real part of a complex number. The details of a_n and b_n can be found in Ref. [50].

Since the VO_2/SiO_2 core/shell nanoparticles are randomly dispersed inside the VAH film, assuming the total number of nanoparticles per volume is N, then the spectrum extinction coefficient $\beta_{p,\lambda}$ (m^{-1}) can be expressed as the summation of the scattering cross-section of all the particles [51],

$$\beta_{p,\lambda} = N\frac{1}{4}\pi b^2 Q_{ext,\lambda} = \frac{3}{2}\frac{V_f Q_{ext,\lambda}}{b} \tag{3}$$

where V_f is the volume fraction of the core–shell nanoparticles. Because the volume fraction of the nanoparticles is very low, and the aerogel matrix is dielectric, the interaction between the embedded nanoparticles and the aerogel matrix is ignored. Thus, the spectral extinction coefficient β_λ of the VAH film is evaluated by [52],

$$\beta_\lambda \approx \beta_{p,\lambda} + \beta_{a,\lambda} \tag{4}$$

where $\beta_{a,\lambda}$ is the spectrum extinction coefficient of the aerogel matrix. The spectral transmittance τ_λ of the VAH film with a thickness L_{vah} is given by the Beer-Lambert law [48],

$$\tau_\lambda = e^{-\beta_\lambda L_{vah}} \tag{5}$$

With the spectral transmittance calculated using Eq. (5), the luminous transmittance (Eq. (1a)) and the solar modulation ability (Eqs. (1b) and (1c)) of the VAH films can then be calculated.

2.3. Heat transfer through VO_2-aerogel hybrid film

Since the thermochromic VAH film can greatly reduce the temperature difference between the inside surface of windowpane and the room environment, the thermal comfort and condensation resistance of single-pane windows may be improved remarkably. In general, the thermal comfort concerns the satisfaction of occupants with the thermal environment [53]. As the temperature difference between the occupants and the innermost surface of windows leads to "radiant temperature asymmetry" [54], a human body would lose thermal energy through infrared thermal radiation, which in turn affects the thermal comfort in the buildings. Moisture condensation would occur when the surface temperature of the windowpanes reaches the dew point of the interior environment. Moisture condensation not only reduces the clear view of windows, but also limits the humidity level inside the building, which is a big concern for indoor air quality.

To evaluate the thermal comfort, condensation resistance, and energy loss of single-pane windows employing a thermochromic VAH film, the heat transfer across both the VAH film and the glass pane needs to be calculated. As shown in Fig. 1(a), the temperature distribution across the window (VAH film and glass pane) is affected by many factors such as room/ambient temperature, outside wind speed, inside natural convection, surface emissivity and absorption of solar radiation by the window materials. Assuming the length and width of a windowpane are much larger than its thickness and the contact resistance between the VAH film and glass can be ignored, one-dimensional (1D) heat transfer equation across the VAH film and the glass pane are written as [55],

$$k_{vah}\frac{d^2T(z)}{dz^2} - \frac{dq_r(z)}{dz} = 0, \quad z \leqslant L_{vah} \tag{6a}$$

$$k_{gla}\frac{d^2T(z)}{dz^2} - \frac{dq_r(z)}{dz} = 0, \quad L_{vah} < z \leqslant L_{vah} + L_{gla} \tag{6b}$$

where, k_{vah} and k_{gla} are the thermal conductivities of the thermochromic VAH film and the glass, respectively. L_{vah} and L_{gla} are the thicknesses of the VAH film and glass, $T(z)$ represents the temperature distribution along the z-direction, and $dq_r(z)/dz$ is the solar radiation absorbed in the VAH film and glass per unit volume. The boundary conditions of Eqs. 6 (a-b) can be written as,

$$q_o|_{z=0} = h_o(T_a - T_{z=0}) + \sigma\varepsilon_o\left(T_a^4 - T_{z=0}^4\right) \tag{7a}$$

$$-k_{vah}\frac{dT_{z=L_{vah}^-}}{dz} = -k_{gla}\frac{dT_{z=L_{vah}^+}}{dz} \tag{7b}$$

$$q_i|_{z=L_{vah}+L_{gla}} = h_i\left(T_{z=L_{vah}+L_{gla}} - T_r\right) + \sigma\varepsilon_i\left(T_{z=L_{vah}+L_{gla}}^4 - T_r^4\right) \tag{7c}$$

where T_a and T_r are the external ambient temperature and internal room temperature, respectively,h_o, ε_o and h_i, ε_i are the convective heat transfer coefficients and average surface emissivities of outside and inside, and σ is the Stefan-Boltzmann's constant.

To determine the local heat flux distribution $q_r(z)$ in Eqs. (6a)–(6b), the radiative transfer equation (RTE) of solar radiation needs to be solved. By assuming that radiation scattering is isotropic, the one-dimensional RTE in the z-direction across the window can be written as [48],

$$\frac{\mu}{\beta_\lambda}\frac{dI_\lambda(z,\mu)}{dz} = -I_\lambda(z,\mu) + (1-\omega_\lambda)I_{b,\lambda}(z) + \frac{\omega_\lambda}{2}\int_{-1}^{1} I_\lambda(z,\mu')d\mu' \tag{8}$$

where $\mu = cos\theta$ is the directional cosine and θ is the polar angle away from z direction, I_λ is the radiation intensity, $I_{b,\lambda}$ is the intensity of the black body radiation at position z, $\omega_\lambda \approx Q_{sca,\lambda}/Q_{ext,\lambda}$ is the scattering albedo, and $\mu' = \mu$. In Eq. (8), the local blackbody emission $I_{b,\lambda}$ within the range of 280–2500 nm (solar band) can be ignored due to the low temperature inside the VAH film and the glass (cold medium), according to Planck's law [48]. According to the propagation direction of the radiation, the radiation can be divided into forward ($I_\lambda^+(z,\mu)$) and

backward ($I_\lambda^-(z,\mu)$) radiation,

$$I_\lambda(z,\mu)=\begin{cases} I_\lambda^-(z,\mu), -1<\mu<0 \\ I_\lambda^+(z,\mu), 0<\mu<+1 \end{cases} \tag{9}$$

In this work, the discrete coordinates method (DOM) is adopted to solve the RTE, then Eq. (8) could be rewritten as [48],

$$\frac{\mu_i}{\beta_\lambda}\frac{dI_\lambda^+(z,\mu_i)}{dz}=-I_\lambda^+(z,\mu_i)+\frac{\omega_\lambda}{2}\sum_{j=1}^{M/2}w_j\left(I_\lambda^+(z,\mu_j)+I_\lambda^-(z,\mu_j)\right) \tag{10a}$$

$$-\frac{\mu_i}{\beta_\lambda}\frac{dI_\lambda^-(z,\mu_i)}{dz}=-I_\lambda^-(z,\mu_i)+\frac{\omega_\lambda}{2}\sum_{j=1}^{M/2}w_j\left(I_\lambda^+(z,\mu_j)+I_\lambda^-(z,\mu_j)\right) \tag{10b}$$

where $\mu_i=cos\theta_i$ is the discrete direction cosine as shown in Fig. 2, M is the total discrete direction, and $w_i(w_j)$ is the quadrature weight associated with the direction $\mu_i(\mu_j)$, Once $I_\lambda^+(z,\mu_i)$ and $I_\lambda^-(z,\mu_i)$ are determined, the local heat flux in Eq. (6) can be calculated by [48,55],

$$q_r(z)=2\pi\int_0^\infty\int_{-1}^{1}\left(I_\lambda^+(z,\mu)-I_\lambda^-(z,\mu)\right)\mu d\mu d\lambda=2\pi\int_0^\infty\sum_{i=1}^{M/2}w_i\left(I_\lambda^+(z,\mu_i)-I_\lambda^-(z,\mu_i)\right)d\lambda \tag{11}$$

The boundary conditions of Eqs. (10a) and (10b) are shown in Fig. 2. At the air-VAH interface ($z=0$), the radiation $I_\lambda^+(z=0^+,\mu_i)$ in the VAH film side is the sum of the reflected radiation incident on VAH and the transmitted solar radiation,

$$I_\lambda^+(z=0^+,\mu_i)=\rho_{a-vah,\lambda}I_\lambda^-(z=0^+,\mu_i)+\tau_{a-vah,\lambda}I_{solar,\lambda}(\mu_i) \tag{12a}$$

where $I_{solar,\lambda}(\mu_i)$ is the intensity of solar radiation in the direction μ_i, $\rho_{vah-a,\lambda}$ is the reflectance from the VAH film side to air side, and $\tau_{a-vah,\lambda}$ is the transmittance from air side to the VAH film side. In this work, we assume that all the solar radiation is in the discrete direction of $\mu_i\approx 1$. For the VAH-glass interface at $z=L_{vah}$ (Fig. 2), where L_{vah} is the VAH film thickness, the radiation going inside the window glass is the sum of the radiation transmitted through the interface and reflected off radiation by the interface,

$$I_\lambda^+\left(z=L_{vah}^+,\mu_i\right)=\rho_{g-vah,\lambda}I_\lambda^-\left(z=L_{vah}^+,\mu_i\right)+\tau_{vah-g,\lambda}I_\lambda^+\left(z=L_{vah}^-,\mu_i\right) \tag{12b}$$

where $\rho_{g-vah,\lambda}$ is the reflectance from the glass to the VAH film, and $\tau_{vah-g,\lambda}$ is the transmittance from the VAH film to the glass under a specific incident angle. At the glass-air interface ($z=L_{vah}+L_{gla}$, Fig. 2), the backward radiation equals the reflected radiation at the glass-air interface,

$$I_\lambda^-\left(z=\left(L_{vah}+L_{gla}\right)^-,\mu_i\right)=r_{g-a,\lambda}I_\lambda^+\left(z=\left(L_{vah}+L_{gla}\right)^-,\mu_i\right) \tag{12c}$$

where $\rho_{g-a,\lambda}$ is the reflectance from glass to air. The interface reflectances and transmittances in Eqs. (12a)–(12c) are calculated using Snell's law, and the Fresnel equations [56].

Eqs. (6)–(12) together show that the heat conduction and thermal radiation are coupled, which are needed to be solved numerically. Because the boundary conditions shown in Eqs. (7a)–(7c) are determined by the temperature distribution in the windowpane, an initial temperature distribution is given first. The simplified RTE (Eqs. (10a) and (10b)) and heat transfer equations (Eqs. (6a) and (6b)) are then discretized and solved iteratively using the finite volume method (FVM) to obtain the new temperature field and heat flux distribution [57]. The new temperature field is then used to update the thermal boundary conditions (Eqs. (7a)–(7c)). The iteration continues until the converged criterion ($\max|T_{N+1}(z)-T_N(z)|<10^{-5}$ K) is satisfied, where N is the number of iterations. For clear and uncoated float glass, the thermal conductivity and average surface emissivity are assumed to be $k_{gla}=0.96$ W/(mK) and $\varepsilon_i\approx 0.84$, respectively [21,58]. According to the effective medium theory [59], the influence of core–shell VO_2/SiO_2 nanoparticles on the thermal resistance of the VAH film is negligible when their concentrations are very low (<0.1%). The thermal conductivity and average surface emissivity of the transparent aerogel film are assumed to be $k_{vah}=0.018$ W/(mK) and $\varepsilon_o\approx 0.84$, respectively [17]. The convective heat transfer coefficient towards inside is assumed to be $h_i=3.6$ W/(m^{2}K) and the convective heat transfer coefficient towards outside can be evaluated by and $h_o=(10+4.1v)$ W/(m^{2}K), where v (m/s) is the wind speed [21]. The spectral transmittances of aerogel and glass are taken from Ref. [60] and Ref. [21], respectively (Fig. 3(a)). The spectral refractive complex indices of VO_2 in the insulating phase and the metallic phase (Fig. 3(b)) are found from the available literature [37]. The refractive index of SiO_2 is set as 1.5 [21].

To validate the coupled heat conduction and solar radiation heat transfer model in this work, we calculated the heat transfer from the hot ambient (35 °C) to a cold room (24 °C) [61], across the single-pane window with different thickness (3–8 mm). Here the thermal conductivity of glass pane is $k_{gla}=0.96$ W/(mK), the indoor and outdoor

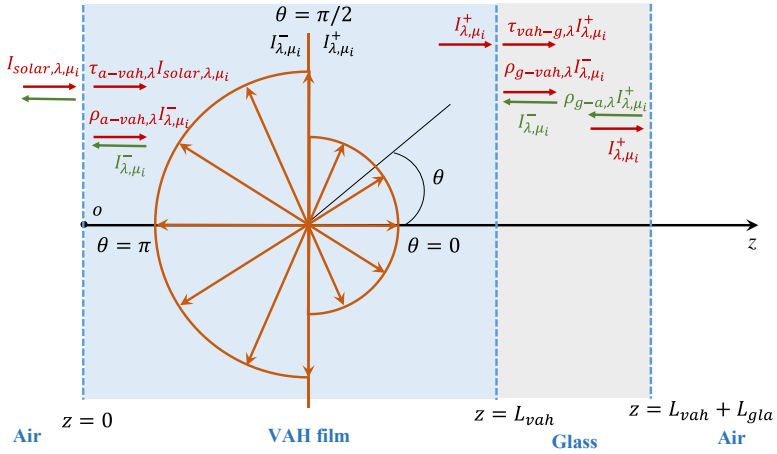

Fig. 2. Schematic of the one-dimensional radiation transfer in the VO_2-aerogel hybrid film and the glass. The radiation intensity $I_\lambda(z,\mu)$ is divided into forward radiation $I_\lambda^+(z,\ 0<\mu<+1)$ and backward radiation $I_\lambda^-(z,\ -1<\mu<0)$ according to the polarization angle away from the z-direction, where $\mu=cos\theta$.

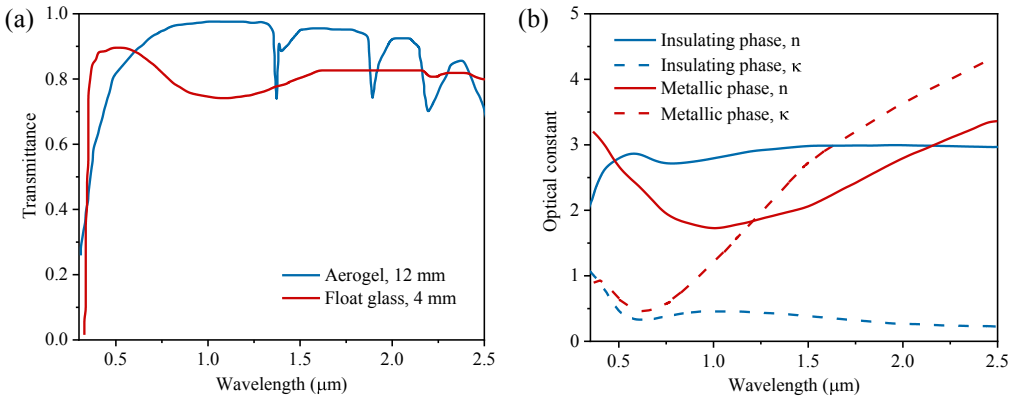

Fig. 3. Optical parameters used in the calculations. (a) Spectral transmittances of aerogel [60] and float glass [21]. (b) Complex refractive indices of VO_2 in both insulating phase and metallic phase [37].

surface convective heat transfer coefficients are $h_i = 3.6\ \mathrm{W/(m^2K)}$ and $h_o = 18\ \mathrm{W/(m^2K)}$, respectively, and the indoor and outdoor surface emissivities are $\varepsilon_i = \varepsilon_o = 0.84$. The calculated conductive heat transfer without solar radiation was compared with the results from Ismail *et al.* [61], as shown in Fig. 4(a). Solar radiation and solar absorption of the windowpane is then included by the coupled heat conduction and solar radiation model (Fig. 4(b)). A good agreement between our work and Ismail *et al.* [61] is observed, confirming that the coupled heat conduction and solar radiation heat transfer model used in our work is accurate.

3. Results and discussion

3.1. Effect of aerogel film thickness

The thickness of the aerogel matrix influences both the thermal insulation performance and the solar transmission of the VO_2-aerogel hybrid (VAH) film (Eqs. (1a) and (1c)). Here, the thermal performance of the VAH film is approximately evaluated by the overall heat transfer coefficient, namely U-value, which is defined as [21],

$$\frac{1}{U} = \frac{1}{h_{o,all}} + \frac{1}{k_{vah}/L_{vah} + k_{gla}/L_{gla}} + \frac{1}{h_{i,all}} \tag{13}$$

where k_{vah} and L_{vah} are the thermal conductivity and thickness of VAH film, k_{gla} and L_{gla} are the thermal conductivity and thickness of glass, $h_{i,all}$ and $h_{o,all}$ are the overall heat transfer coefficients of VAH film towards outside and insider in which both the convective and radiative heat transfer are included. Note that Eq. (13) does not consider the solar absorption, and the radiative heat transfer between the VAH films and the environments was evaluated by Stefan-Boltzmann law. From Eq. (13), increasing the thickness of the aerogel matrix (L_{vah}) can improve the thermal insulation performance of the VAH film.

Fig. 5(a) compares the U-values of a single-pane window (3.0 mm) covered by the thermochromic VAH film, a single-pane window and an air-filled double-pane window [62] exposed to winter climates as a function of thickness, where the external temperature is $T_a = -18\ ^\circ\mathrm{C}$, the internal temperature is $T_r = 21\ ^\circ\mathrm{C}$, and the wind speed is 5.5 m/s (ASHRAE standard) [3]. It is found that 3.0 mm thick aerogel could reduce the energy loss of a single-pane window by ~ 50%, which is close to the insulation performance of an air-filled double-pane window (Fig. 5(a)). However, it is also noted that the decrease of U-value is nonlinear, and the decreasing rate becomes slower as the thickness of

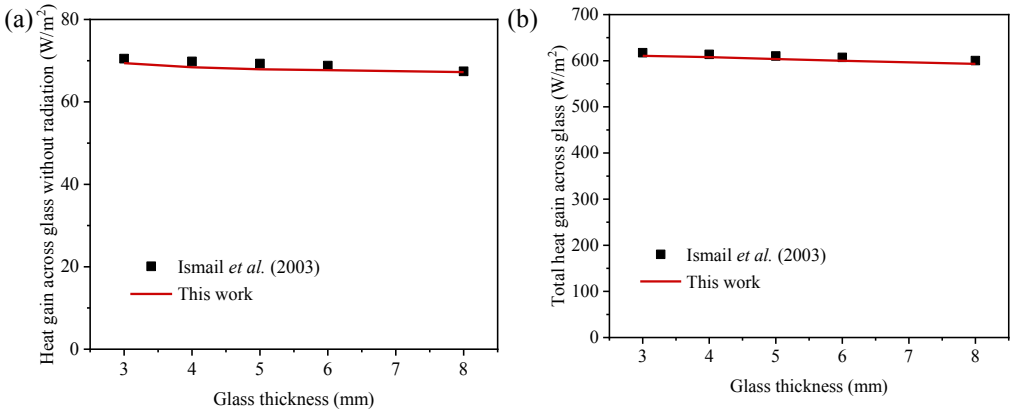

Fig. 4. Validation of the developed heat transfer model. (a) Comparison of the conductive heat flux across a single-pane window as a function of thickness between this work and Ref. [61] when the solar radiation is not included. (b) Comparison of the total heat flux across a single-pane window as a function of thickness between this work and Ref. [61] when both solar radiation and heat conduction are considered simultaneously.

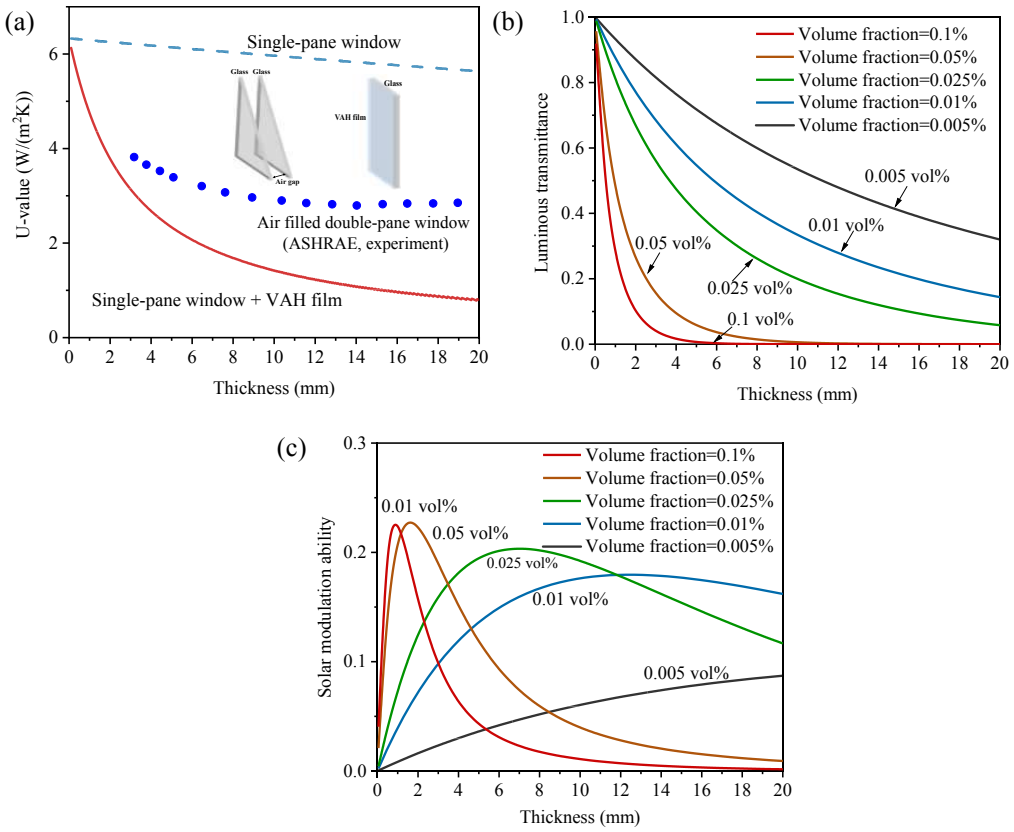

Fig. 5. Influence of film thickness on the thermal and optical performance of VO_2-aerogel hybrid film. (a) U-value of VO_2-aerogel hybrid film as a function of aerogel thickness calculated based on (Eq. (13)). The corresponding heat transfer coefficients are evaluated according to Ref. [21]. (b) Luminous transmittance of VO_2-aerogel hybrid film in the insulating state as a function of the thickness of aerogel matrix (Eq. (1a)). (c) Solar modulation ability of VO_2-aerogel hybrid film as a function of the thickness of aerogel matrix (Eqs. (1b) and (1c)). In (b) and (c), the inner and outer diameters (VO_2/SiO_2) are a = 50 nm, and b = 80 nm, respectively.

the aerogel matrix increases. This is because the U-values are dominated by the convective/radiative heat transfer between the window surfaces and the room and ambient environments (Eq. (13)) when the conductive thermal resistance of the windowpane increases. Fig. 5(b-c) show the results of the luminous transmittance and solar modulation ability as a function of the aerogel thickness and the volume fraction of VO_2/SiO_2 nanoparticles calculated based on Eqs. (1)–(5), where the inner and outer diameters are assumed to be $a = 50$ nm, and $b = 80$ nm, respectively. As shown in Fig. 5(b), the luminous transmittance of the VAH film decreases with the increase of aerogel thickness. The transparency of the VAH film can be improved by decreasing the volume fraction of core–shell VO_2/SiO_2 nanoparticles, but the solar modulation ability also decreases (Fig. 5(c)). Fig. 5(b-c) show that there exist an optimal film thickness and a volume fraction to achieve relatively large luminous transmittance and solar modulation ability for the core–shell VO_2/SiO_2 with a specific size. In this work, we aim to make the thermal insulation performance of single-pane windows to be close to the air-filled double-pane windows (Fig. 5(a)). Therefore, a 3.0 mm VAH thickness is used in our calculations in the following sections.

3.2. Effect of size and concentration of VO_2/SiO_2 nanoparticles

The optical performance of the thermochromic VAH film is closely related to the concentration, size, and distribution of the core–shell VO_2/SiO_2 nanoparticles. According to the recent progress [40,63,64], the diameters of pure crystalline VO_2 nanoparticles fabricated under different synthesis routes vary between 5 and 80 nm. In order to enhance durability and prevent oxidation, the VO_2 nanoparticles may be coated with a thin layer of oxides such as SiO_2, ZnO, and TiO_2 ranging from 3 nm to 200 nm, to form the core–shell structure nanoparticles [39,45,65,66]. Therefore, in this work, the VO_2 nanoparticle with a diameter in the range of 10–50 nm (interval is 1 nm), and the SiO_2 shell with a thickness of 5–50 nm (interval is 0.5 nm) are modeled for optimizing the luminous transmittance and solar modulation ability. The volume fraction of the VO_2/SiO_2 in the VAH film varies from 0.001% to 0.05% (interval is 0.001%).

Fig. 6(a-b) show the results of the luminous transmittance of a 3.0 mm thick VAH film in both the insulating phase and the metallic phase as a function of inner diameter, shell thickness, and volume fraction of the VO_2/SiO_2 in the VAH film calculated based on Eqs. (1)–(5). It is found that, for the VO_2 nanoparticles in both the insulating phase and the metallic phase, the luminous transmittances τ_{lum} of the VAH film decreases while the solar modulation ability $\Delta\tau_{solar}$ becomes larger as the size of the VO_2 nanoparticle increases (Fig. 6(c)). This indicates that the luminous transmittance τ_{lum} needs to be sacrificed in order to achieve a larger solar modulation ability $\Delta\tau_{solar}$. Here, the recommended $\tau_{lum} = 0.7$ and $\tau_{lum} = 0.6$ are used for winter and summer, respectively [67]. In Fig. 6(d), we show the optimized size and concentration of VO_2

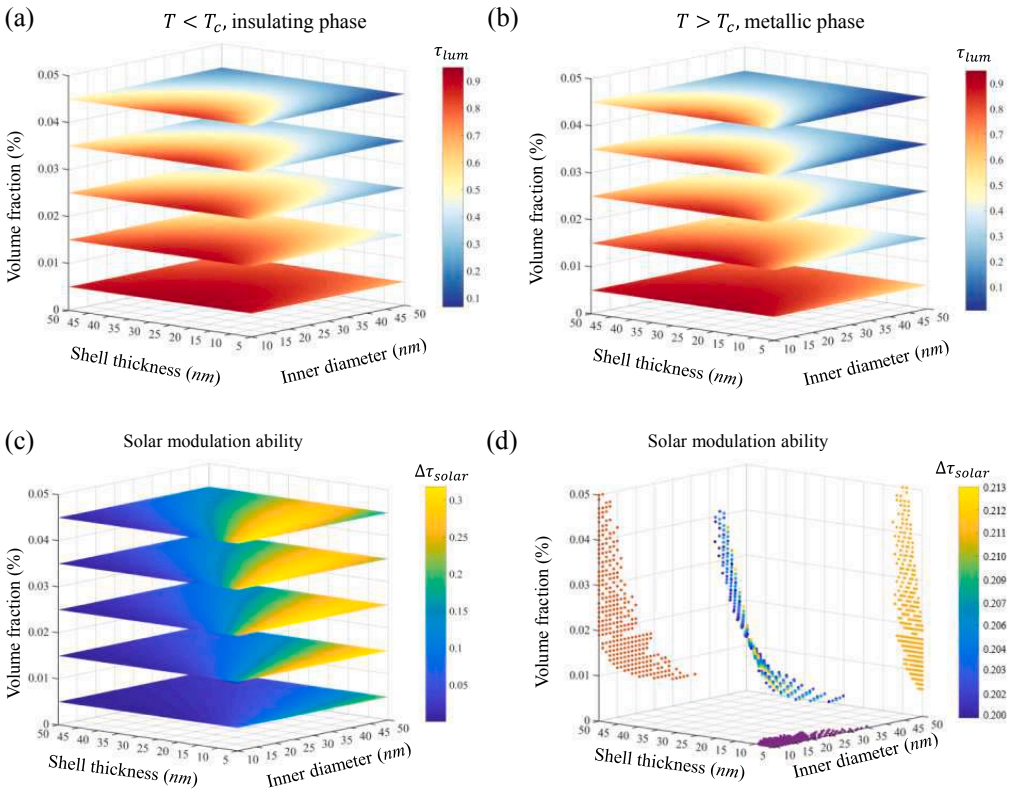

Fig. 6. Influence of the size and the volume fraction of core–shell VO_2/SiO_2 nanoparticles on the thermochromic performance of an aerogel with the film thickness of 3 mm. (a) Luminous transmittance of VO_2-aerogel hybrid film when VO_2 is in the insulating phase ($T < T_c$). (b) Luminous transmittance of VO_2-aerogel hybrid film when VO_2 is in the metallic phase ($T > T_c$). (c) The difference of solar energy transmittance (solar modulation ability) between insulating and metallic phase VO_2. The luminous transmittance and solar modulation ability are calculated based on Eqs. (1)–(5). (d) Optimized size and concentration of VO_2/SiO_2 core–shell nanoparticles embedded in the VAH film with $\tau_{lum} > 0.7$ (0.6) in insulating (metallic) phase and $\Delta\tau_{solar} > 0.2$.

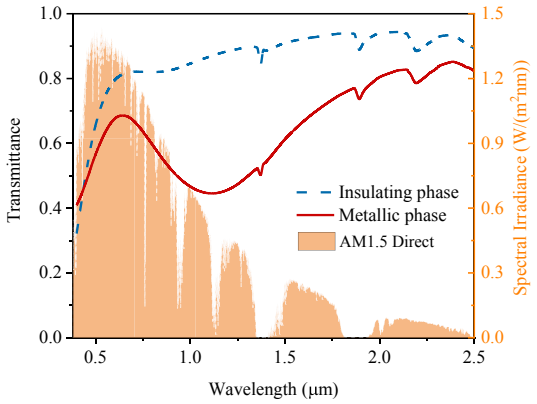

Fig. 7. Spectral transmittances of single-pane glass and VO_2-aerogel hybrid (VAH) film in both insulating and metallic phases, where the aerogel thickness is 3 mm and the VO_2/SiO_2 nanoparticle concentration is 0.01 vol%. The inner and outer diameters (VO_2/SiO_2) are a = 25 nm, and b = 40 nm, respectively.

core–shell nanoparticles embedded in the VAH film with $\tau_{lum} > 0.7$ (0.6) in insulating (metallic) phase and $\Delta\tau_{solar} > 0.2$. It is seen that the optimal inner diameter and the shell thickness are within the range of 10–35 nm and 5–10 nm, respectively. Fig. 7 shows the spectral transmittances of the VAH film in both hot and cold climates with $\Delta\tau_{solar}$ of ~ 20.2%, in which the diameter of VO_2 nanoparticle is 25 nm, outer diameter is 40 nm (SiO_2 shell thickness of 7.5 nm), and the volume fraction of VO_2/SiO_2 nanoparticles is 0.01%. It is important to note that the spectral absorptivity of VAH film roughly equals (1-τ_λ) due to the large extinction coefficient of VO_2 (Fig. 3(b)). As expected, the NIR transmittance of the VAH films exhibits a strong dependence on the phase state of the VO_2 nanoparticles, while the luminous transmittance almost keeps constant

3.3. Thermal insulation performance of VO_2-aerogel hybrid film

Fig. 8(a) shows the relative position between a south-facing single-pane window and the sun, where $\mathbf{n}_w$, pointing to the south, is the normal direction of the window, ϕ is the azimuth angle, φ_s is the solar incidence angle, and γ_s is the solar azimuth angle. Here, the intensity of the solar irradiation reaching the external surface of the windowpane (Eq. (12a)) is evaluated according to the solar incidence angle φ_s which is the angle between the incident beam radiation and the normal direction of the windowpane. The solar azimuth angle γ_s is the angular displacement measured eastward from north to the projection of beam radiation on

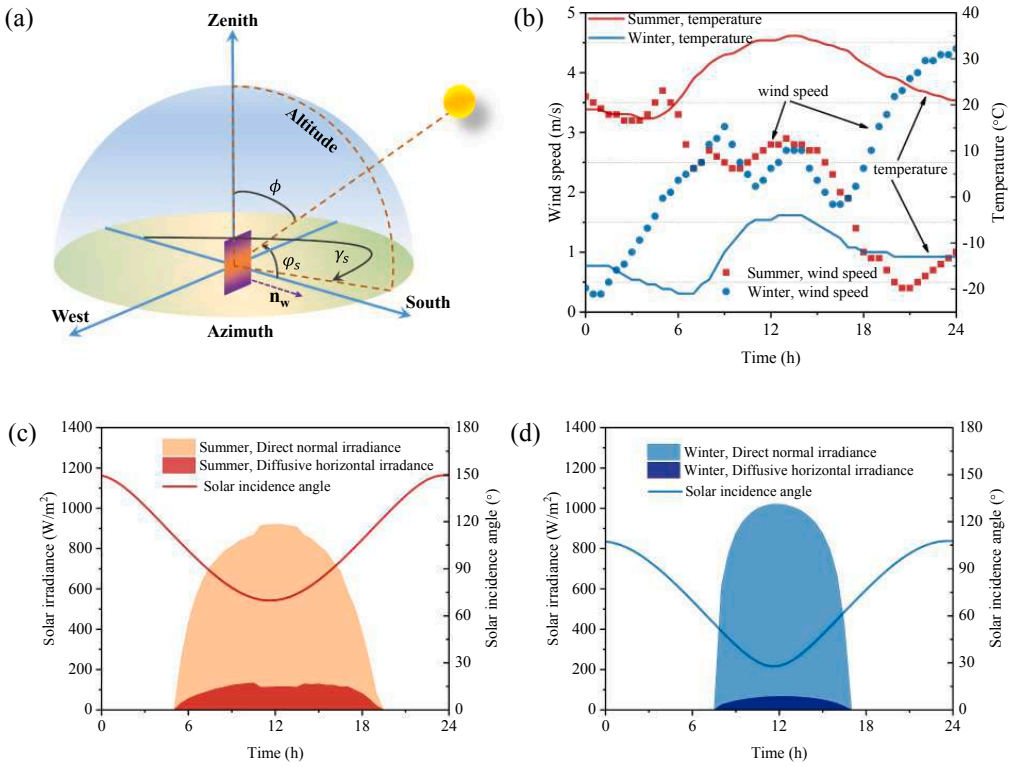

Fig. 8. The weather conditions used for evaluating the thermal insulation performance of a south-facing single-pane window employing VAH film during a winter day and a summer day. (a) Schematic of the relative position between a south-facing window and the sun. (b) The variations of outdoor temperatures and wind speeds as a function of time on a winter day and a summer day. (c) The variations of direct normal irradiance (DNI), diffusive horizontal irradiance (DHI), and solar incidence angle of a south-facing window as a function of time on a summer day. (d) The variations of DNI, DHI, and solar incidence angle of a south-facing window as a function of time on a winter day. The selected dates of the winter day and summer day are (6th of January 2017) and (24th of July 2017) in Boulder, CO, USA (40.0150° N, 105.2705° W, 1655 m altitude). The weather conditions are acquired from the NSRDB Data Viewer [68].

the horizontal plane [69]. Fig. 8(b-c) show the outdoor temperatures and wind speeds and solar irradiances in one of the hottest days in summer (24th of July 2017) and one of the coldest days in winter (6th of January 2017) days in Boulder, CO, USA. The solar incidence angle θ in Fig. 8(c-d) is calculated based on the solar position algorithm developed in Ref. [69].

In Fig. 9(a), we calculated the overall heat gain/loss across a single-pane window with VO_2-aerogel hybrid film as a function of the critical phase change temperature of VO_2 nanoparticles, in which the positive/negative sign represents the heat gain/loss. Here we assumed that the heat loss through window increases the heating demands, while the solar heating reduces the heating demands in winter days, and both the heat gain through heat conduction and solar radiation increase cooling demands in summer days. The optimal phase change temperature (T_c) is found to be ~ 28 °C which is higher than the room temperature (21 °C). Note that the optimal phase change temperature in Fig. 9(a) was calculated based on the selected winter and summer days. Fig. 9(b-e) compare the thermal insulation performances of a south-facing single-pane window and a south-facing single-pane window employing VAH film under the weather conditions shown in Fig. 8 (Eqs. (6–12)), in which $T_c = 28^{\circ}$C. As shown in Fig. 9(b), employing the VAH film can reduce ~ 50% heat loss through a single-pane window caused by the temperature difference between outside and inside environments at nighttime during winter. In addition, the inside surface temperature of windowpane also rises considerably (Fig. 9(c)), which greatly reduces the heat loss through infrared thermal radiation (wavelength peaks at ~ 10 μm at room temperature) from the human body and improves the thermal comfort of the single-pane window. In Fig. 9(c), it is also seen that employing the VAH film may prevent moisture condensation even when the indoor relative humidity level reaches ~ 50%, which is much higher than that of the single-pane windows. During the daytime, the single-pane window allows more solar irradiance to transmit through (Fig. 9(b)), but thermal discomfort and moisture condensation remain issues due to the low surface temperature (Fig. 9(c)). When the VAH film is adopted, the VO_2/SiO_2 nanoparticles in the VAH film can absorb solar irradiance and convert into heat that can be transferred to the room environments through heat conduction. Thus, it is seen that the inside window surface temperature is much higher (Fig. 9(c)), and there is heat flow from the window surfaces to the indoor environments through heat conduction during the time of ~ 9 a.m.–15 p.m. (Fig. 9(b)). Fig. 9(d) shows the heat flow from the external environment to the room due to temperature difference and solar irradiation in the hot climates, where positive/negative signs show heat flow into/out of the room environment. It is seen that the VO_2 nanoparticles reach the phase change temperature at ~ 8:30 a.m. due to high external ambient temperatures and absorbed solar irradiance. Solar irradiance transmitting through the window drops, which reduces the sun's glare and cooling demands caused by the extra solar heating. As the direct solar irradiance decreases and ambient temperature decreases, the VO_2 changes from the metallic phase to the insulating phase (occurs in nighttime). Fig. 9(e)

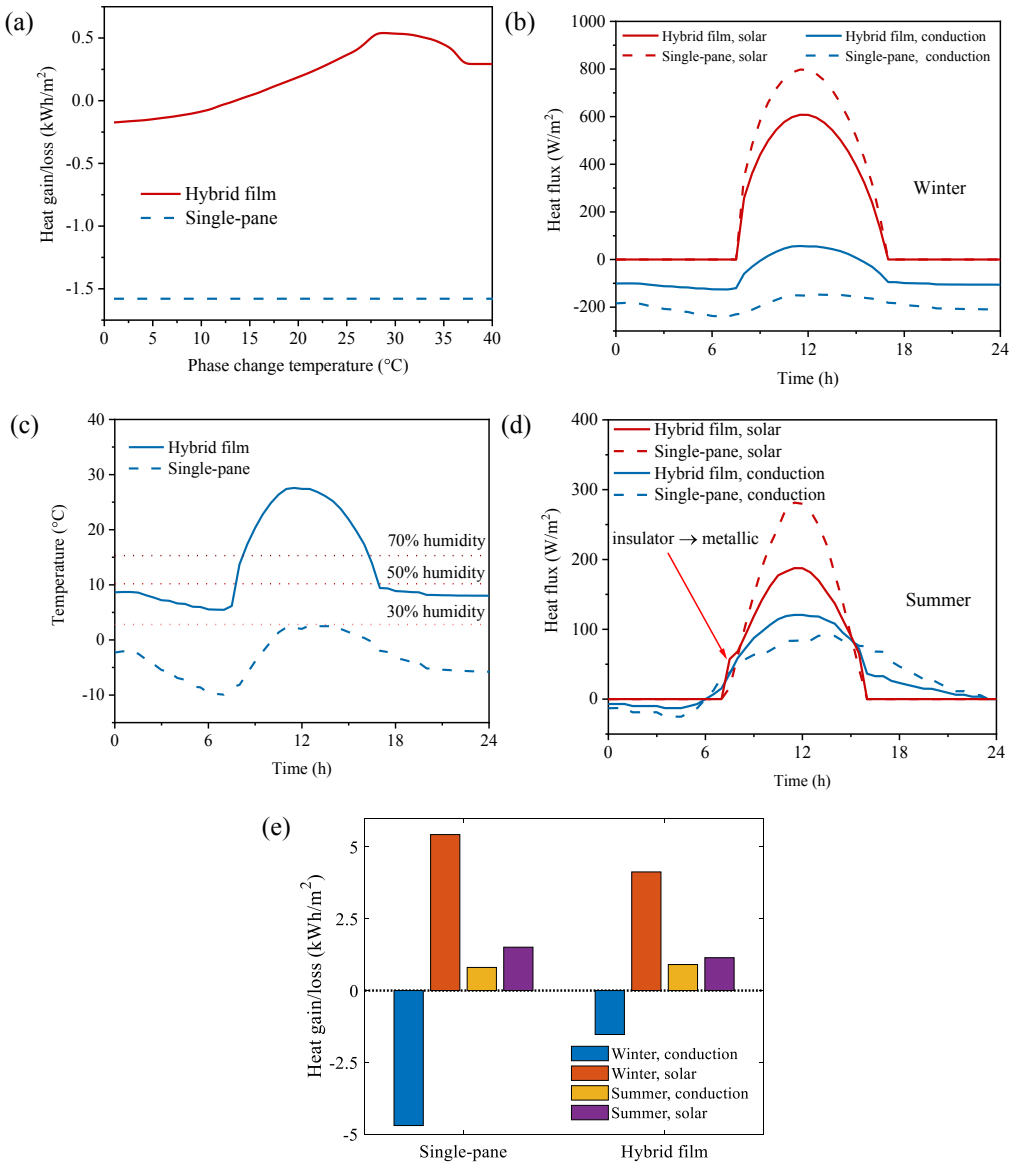

Fig. 9. Thermal insulation performance of a south-facing window under practical weather conditions. (a) Overall heat loss/gain through a single-pane window covered with VO_2-aerogel hybrid film as a function of critical phase change temperature of VO_2. (b) Heat loss/gain through single-pane windows with/without VO_2-aerogel hybrid film on a winter day. (c) Inside surface temperatures of a single-pane window with/without the VO_2-aerogel hybrid film on a winter day. (d) Heat loss/gain through a single-pane window with/without VO_2-aerogel hybrid film on a summer day. (e) Total heat loss/gain on a winter day and a summer day when the critical phase change temperature is 28 °C. Here the positive/negative value represents the heat gain/loss. In winter days, the heat loss through window increases the heating demands, while the solar heating reduces the heating demands. In summer days, both the heat gain through heat conduction and solar irradiation increase cooling demands.

shows the average heat loss/gain of a south-facing window on the simulated winter and summer days. When heat loss/gain in both winter and summer days are considered together, the heating/cooling demands of a south-facing single-pane window stands at ~ 1.58 kWh/m^2, while employing VAH film could gain energy (~ 0.54 kWh/m^2) from the ambient. The above results show that employing the VAH film could not only significantly reduce the heating and cooling loads of single-pane windows but also improve the thermal comfort and indoor humidity level.

4. Conclusions

In summary, an optically switchable and thermally insulating thermochromic VO_2-aerogel hybrid (VAH) film has been proposed as a

window retrofit for reducing energy loss through single-pane windows. A theoretical model coupling heat conduction with solar radiation heat transfer was developed to evaluate the thermal insulation performance and solar regulation ability of the designed window retrofitting films. The results have shown that a 3.0 mm thick aerogel film embedded with 0.01 vol% VO_2/SiO_2 with an inner diameter of 25 nm and an outer diameter of 40 nm can achieve: a U-value of ~ 3.0 W/(m^2K) which is ~ 50% reduction in U-value from the single-pane value of about 6.0 W/(m^2K), a luminous transmittance of 0.7 in cold climates and 0.6 in hot climates, and a solar transmittance modulation of ~ 20%. In cold climates, the thermochromic VAH film not only reduces the heat loss due to the temperature difference but also improves thermal comfort and condensation resistance of the windows. In hot climates, the VO_2-aerogel hybrid film can reduce the sun's glare and cooling demands caused by the extra solar heating through the phase change of VO_2 nanoparticles. The proposed thermochromic VO_2-aerogel hybrid film with a relatively low U-value, a relatively high luminous transmission, and a dynamic solar transmission can minimize the energy loss without blocking out the useful energy and daylight from the sun, which has a great application potential as a retrofit for increasing the energy efficiency of single-pane windows.

Author contributions

X.P. Zhao and R.G. Yang designed the research and modeling approach. X.P. Zhao carried out the computation and analyzed the data. X.P. Zhao, S.A. Mofid, B.P. Jelle, G. Tan, X.B. Yin, and R.G. Yang wrote the manuscript. All authors participated in the discussion of the research.

Declaration of Competing Interest

The authors declare that they have no known competing financial interests or personal relationships that could have appeared to influence the work reported in this paper.

Acknowledgments

The involvement of researchers from Norway has been supported by the Research Council of Norway within the Nano 2021 program through the SINTEF and NTNU research project "High-Performance Nano Insulation Materials" (Hi-Per NIM, Project No. 250159).

References

[1] Jelle BP, Hynd A, Gustavsen A, Arasteh D, Goudey H, Hart R. Fenestration of today and tomorrow: A state-of-the-art review and future research opportunities. Sol Energy Mater Sol Cells 2012;96:1–28.
[2] Gao T, Jelle BP, Ihara T, Gustavsen A. Insulating glazing units with silica aerogel granules: The impact of particle size. Appl Energy 2014;128:27–34.
[3] ASHRAE Standard: Thermal Environmental Conditions for Human Occupancy: ASHRAE; 2010.
[4] Ismail KAR, Henriquez JR. Thermally effective windows with moving phase change material curtains. Appl Therm Eng 2001;21(18):1909–23.
[5] Temps RC, Coulson KL. Solar radiation incident upon slopes of different orientations. Sol Energy 1977;19(2):179–84.
[6] ARPA-E. Single-pan highly insulating efficient lucid designs (SHIELD) programoverview; 2014.
[7] Sun Yanyi, Wilson Robin, Wu Yupeng. A review of transparent insulation material (TIM) for building energy saving and daylight comfort. Appl Energy 2018;226:713–29.
[8] Soleimani Dorcheh A, Abbasi MH. Silica aerogel; synthesis, properties and characterization. J Mater Process Technol 2008;199(1-3):10–26.
[9] Gurav Jyoti L, Jung In-Keun, Park Hyung-Ho, Kang Eul Son, Nadargi Digambar Y. Silica aerogel: synthesis and applications. J Nanomater 2010;2010:1–11.
[10] Baetens Ruben, Jelle Bjørn Petter, Gustavsen Arild. Aerogel insulation for building applications: A state-of-the-art review. Energy Build 2011;43(4):761–9.
[11] Buratti C, Moretti E. Silica nanogel for energy-efficient windows. Nanotechnology in eco-efficient construction: Elsevier; 2013. p. 207–35.
[12] Reim M, Körner W, Manara J, Korder S, Arduini-Schuster M, Ebert H-P, Fricke J. Silica aerogel granulate material for thermal insulation and daylighting. Sol Energy 2005;79(2):131–9.
[13] Berardi Umberto. The development of a monolithic aerogel glazed window for an energy retrofitting project. Appl Energy 2015;154:603–15.
[14] Shimizu Taiyo, Kanamori Kazuyoshi, Nakanishi Kazuki. Silicone-based organic-inorganic hybrid aerogels and xerogels. Chem Eur J 2017;23(22):5176–87.
[15] Zu Guoqing, Shimizu Taiyo, Kanamori Kazuyoshi, Zhu Yang, Maeno Ayaka, Kaji Hironori, et al. Transparent, superflexible doubly cross-linked polyvinylpolymethylsiloxane aerogel superinsulators via ambient pressure drying. ACS Nano 2018;12(1):521–32.
[16] Kobayashi Yuri, Saito Tsuguyuki, Isogai Akira. Aerogels with 3D ordered nanofiber skeletons of liquid-crystalline nanocellulose derivatives as tough and transparent insulators. Angew Chem 2014;126(39):10562–5.
[17] Liu Qingkun, Frazier Allister W, Zhao Xinpeng, De La Cruz Joshua A, Hess Andrew J, Yang Ronggui, et al. Flexible transparent aerogels as window retrofitting films and optical elements with tunable birefringence. Nano Energy 2018;48:266–74.
[18] Liu Shanqiu, Duvigneau Joost, Vancso G Julius. Nanocellular polymer foams as promising high performance thermal insulation materials. Eur Polym J 2015;65:33–45.
[19] Kim Chae Bin, You Nam-Ho, Goh Munju. Hollow polymer microcapsule embedded transparent and heat-insulating film. RSC Adv 2018;8(17):9480–6.
[20] Hu Feng, Wu Siyu, Sun Yugang. Hollow-structured materials for thermal insulation. Adv Mater 2019;31(38):1801001. https://doi.org/10.1002/adma.v31.3810.1002/adma.201801001.
[21] Jelle Bjørn Petter. Solar radiation glazing factors for window panes, glass structures and electrochromic windows in buildings—Measurement and calculation. Sol Energy Mater Sol Cells 2013;116:291–323.
[22] Papaefthimiou S. Chromogenic technologies: Towards the realization of smart electrochromic glazing for energy-saving applications in buildings. Adv Build Energy Res 2010;4(1):77–126.
[23] Zhang Y, Tso CY, Iñigo JS, Liu S, Miyazaki H, Chao Christopher YH, et al. Perovskite thermochromic smart window: Advanced optical properties and low transition temperature. Appl Energy 2019;254:113690. https://doi.org/10.1016/j.apenergy.2019.113690.
[24] Wang Yang, Runnerstrom Evan L, Milliron Delia J. Switchable materials for smart windows. Annu Rev Chem Biomol Eng 2016;7(1):283–304.
[25] Runnerstrom Evan L, Llordés Anna, Lounis Sebastien D, Milliron Delia J. Nanostructured electrochromic smart windows: traditional materials and NIR-selective plasmonic nanocrystals. Chem Commun 2014;50(73):10555–72.
[26] Kim Mingyun, Park Kyun Joo, Seok Seunghwan, Ok Jong Min, Jung Hee-Tae, Choe Jaehoon, et al. Fabrication of microcapsules for dye-doped polymer-dispersed liquid crystal-based smart windows. ACS Appl Mater Interfaces 2015;7(32):17904–9.
[27] Cupelli Daniela, Pasquale Nicoletta Fiore, Manfredi Sabrina, Vivacqua Marco, Formoso Patrizia, De Filpo Giovanni, Chidichimo Giuseppe. Self-adjusting smart windows based on polymer-dispersed liquid crystals. Sol Energy Mater Sol Cells 2009;93(11):2008–12.
[28] Ghosh Aritra, Norton Brian, Duffy Aidan. Measured overall heat transfer coefficient of a suspended particle device switchable glazing. Appl Energy 2015;159:362–9.
[29] Ke Yujie, Zhou Chengzhi, Zhou Yang, Wang Shancheng, Chan Siew Hwa, Long Yi. Emerging thermal-responsive materials and integrated techniques targeting the energy-efficient smart window application. Adv Funct Mater 2018;28(22):1800113. https://doi.org/10.1002/adfm.v28.2210.1002/adfm.201800113.
[30] Qian Z, Wang Z, Zhao N, Xu J. Aerogels derived from polymer nanofibers and their applications. Macromol Rapid Commun 2018;1700724.
[31] Aburas Marina, Soebarto Veronica, Williamson Terence, Liang Runqi, Ebendorff-Heidepriem Heike, Wu Yupeng. Thermochromic smart window technologies for building application: A review. Appl Energy 2019;255:113522. https://doi.org/10.1016/j.apenergy.2019.113522.
[32] Cui Yuanyuan, Ke Yujie, Liu Chang, Chen Zhang, Wang Ning, Zhang Liangmiao, et al. Thermochromic VO_2 for energy-efficient smart windows. Joule 2018;2(9):1707–46.
[33] Gao Yanfeng, Luo Hongjie, Zhang Zongtao, Kang Litao, Chen Zhang, Du Jing, et al. Nanoceramic VO_2 thermochromic smart glass: A review on progress in solution processing. Nano Energy 2012;1(2):221–46.
[34] Wang Shancheng, Owusu Kwadwo Asare, Mai Liqiang, Ke Yujie, Zhou Yang, Hu Peng, et al. Vanadium dioxide for energy conservation and energy storage applications: Synthesis and performance improvement. Appl Energy 2018;211:200–17.
[35] Li Shu-Yi, Niklasson Gunnar A, Granqvist Claes G. Thermochromic undoped and Mg-doped VO_2 thin films and nanoparticles: Optical properties and performance limits for energy efficient windows. J Appl Phys 2014;115(5):053513. https://doi.org/10.1063/1.4862930.
[36] Hu Lingting, Tao Haizheng, Chen Guohua, Pan Ruikun, Wan Meinan, Xiong Dehua, et al. Porous W-doped VO_2 films with simultaneously enhanced visible transparency and thermochromic properties. J Sol-Gel Sci Technol 2016;77(1):85–93.
[37] Li S-Y, Niklasson GA, Granqvist CG. Nanothermochromics: Calculations for VO_2 nanoparticles in dielectric hosts show much improved luminous transmittance and solar energy transmittance modulation. J Appl Phys 2010;108(6):063525. https://doi.org/10.1063/1.3487980.
[38] Kang Litao, Gao Yanfeng, Luo Hongjie, Chen Zhang, Du Jin, Zhang Zongtao. Nanoporous thermochromic VO_2 films with low optical constants, enhanced luminous transmittance and thermochromic properties. ACS Appl Mater Interfaces 2011;3(2):135–8.
[39] Chen Yunxiang, Zeng Xianzhe, Zhu Jingting, Li Rong, Yao Heliang, Cao Xun, et al. High performance and enhanced durability of thermochromic films using VO_2@ZnO Core–Shell nanoparticles. ACS Appl Mater Interfaces 2017;9(33):27784–91.

[40] Zhao XP, Mofid SA, Gao T, Tan G, Jelle BP, Yin XB, et al. Durability-enhanced vanadium dioxide thermochromic film for smart windows. Mater Today Phy 2020; 13:100205. https://doi.org/10.1016/j.mtphys.2020.100205.

[41] Li Rong, Ji Shidong, Li Yamei, Gao Yanfeng, Luo Hongjie, Jin Ping. Synthesis and characterization of plate-like VO_2(M)@SiO_2 nanoparticles and their application to smart window. Mater Lett 2013;110:241–4.

[42] Li Yamei, Ji Shidong, Gao Yanfeng, Luo Hongjie, Jin Ping. Modification of mott phase transition characteristics in VO_2@TiO_2 Core/Shell nanostructures by misfit-strained heteroepitaxy. ACS Appl Mater Interfaces 2013;5(14):6603–14.

[43] Zeng SQ, Hunt A, Greif R. Theoretical modeling of carbon content to minimize heat transfer in silica aerogel. J Non-Cryst Solids 1995;186:271–7.

[44] Zhao Jun-Jie, Duan Yuan-Yuan, Wang Xiao-Dong, Zhang Xue-Ren, Han Yun-He, Gao Ya-Bin, et al. Optical and radiative properties of infrared opacifier particles loaded in silica aerogels for high temperature thermal insulation. Int J Therm Sci 2013;70:54–64.

[45] Zhu Jingting, Zhou Yijie, Wang Bingbing, Zheng Jianyun, Ji Shidong, Yao Heliang, et al. Vanadium dioxide nanoparticle-based thermochromic smart coating: high luminous transmittance, excellent solar regulation efficiency, and near room temperature phase transition. ACS Appl Mater Interfaces 2015;7(50):27796–803.

[46] Li Xin-Hao, Liu Chang, Feng Shien-Ping, Fang Nicholas Xuanlai. Broadband light management with thermochromic hydrogel microparticles for smart windows. Joule 2019;3(1):290–302.

[47] Wyszecki G, Stiles WS. Color science. New York: Wiley; 1982.

[48] Modest MF. Radiative heat transfer. Academic Press; 2013.

[49] Riordan C, Hulstron R. What is an air mass 1.5 spectrum? (Solar cell performance calculations). IEEE Conference on Photovoltaic Specialists: IEEE 1990:1085–8.

[50] Bohren CF, Huffman DR. Absorption and scattering of light by small particles. John Wiley & Sons 2008.

[51] Zhu Chuan-Yong, Li Zeng-Yao, Pang Hao-Qiang, Pan Ning. Design and optimization of core/shell structures as highly efficient opacifiers for silica aerogels as high-temperature thermal insulation. Int J Therm Sci 2018;133:206–15.

[52] Wang Xiao-Dong, Sun Duo, Duan Yuan-Yuan, Hu Zi-Jun. Radiative characteristics of opacifier-loaded silica aerogel composites. J Non-Cryst Solids 2013;375:31–9.

[53] Taleghani Mohammad, Tenpierik Martin, Kurvers Stanley, van den Dobbelsteen Andy. A review into thermal comfort in buildings. Renew Sustain Energy Rev 2013;26:201–15.

[54] Lyons P, Arasteh D, Huizenga C. Window performance for human thermal comfort. Trans-Am Soc Heating Refrigerating Air Conditioning Engineers 2000;106: 594–604.

[55] McEnaney Kenneth, Weinstein Lee, Kraemer Daniel, Ghasemi Hadi, Chen Gang. Aerogel-based solar thermal receivers. Nano Energy 2017;40:180–6.

[56] Born M, Wolf E. Principles of optics: electromagnetic theory of propagation, interference and diffraction of light. Elsevier 2013.

[57] Eymard R, Gallouët T, Herbin R. Finite volume methods. Handbook of Numerical Analysis 2000;7:713–1018.

[58] Zhao Xinpeng, Mofid Sohrab A, Al Hulayel Majed R, Saxe Gabriel W, Jelle Bjørn Petter, Yang Ronggui. Reduced-scale hot box method for thermal characterization of window insulation materials. Appl Therm Eng 2019;160:114026. https://doi.org/10.1016/j.applthermaleng.2019.114026.

[59] Nan Ce-Wen, Birringer R, Clarke David R, Gleiter H. Effective thermal conductivity of particulate composites with interfacial thermal resistance. J Appl Phys 1997;81 (10):6692–9.

[60] Nordgaard A, Beckman WA. Modelling of flat-plate collectors based on monolithic silica aerogel. Sol Energy 1992;49(5):387–402.

[61] Ismail K. Modeling and simulation of a simple glass window. Sol Energy Mater Sol Cells 2003;80(3):355–74.

[62] 2001 ASHRAE Handbook: Fundamentals. ASHRAE, Atlanta, USA; 2001.

[63] Nguyen Thanh-Dinh, Do Trong-On. Solvo-hydrothermal approach for the shape-selective synthesis of vanadium oxide nanocrystals and their characterization. Langmuir 2009;25(9):5322–32.

[64] Yu Long, Zhang Xiaogang. Hydrothermal synthesis and characterization of vanadium oxide/titanate composite nanorods. Mater Chem Phys 2004;87(1): 168–72.

[65] Gao Yanfeng, Wang Shaobo, Luo Hongjie, Dai Lei, Cao Chuanxiang, Liu Yiliao, et al. Enhanced chemical stability of VO_2 nanoparticles by the formation of SiO_2/VO_2 core/shell structures and the application to transparent and flexible VO_2-based composite foils with excellent thermochromic properties for solar heat control. Energy Environ Sci 2012;5(3):6104. https://doi.org/10.1039/c2ee02803d.

[66] Li Yamei, Ji Shidong, Gao Yanfeng, Luo Hongjie, Kanehira Minoru. Core-shell VO_2@TiO_2 nanorods that combine thermochromic and photocatalytic properties for application as energy-saving smart coatings. Sci Rep 2013;3(1). https://doi.org/10.1038/srep01370.

[67] Rezaei Soroosh Daqiqeh, Shannigrahi Santiranjan, Ramakrishna Seeram. A review of conventional, advanced, and smart glazing technologies and materials for improving indoor environment. Sol Energy Mater Sol Cells 2017;159:26–51.

[68] https://maps.nrel.gov/nsrdb-viewer/.

[69] Reda Ibrahim, Andreas Afshin. Solar position algorithm for solar radiation applications. Sol Energy 2004;76(5):577–89.

Article XI

Xinpeng Zhao, Sohrab Alex Mofid, Tao Gao, Gang Tan, Bjørn Petter Jelle, Xiabo Yin and Ronggui Yang, **Durability-enhanced vanadium dioxide thermochromic films for smart windows**, *Materials Today Physics,* 13 (2020) 100205.

Materials Today Physics 13 (2020) 100205

Contents lists available at ScienceDirect

Materials Today Physics

journal homepage: https://www.journals.elsevier.com/materials-today-physics

Durability-enhanced vanadium dioxide thermochromic film for smart windows

X.P. Zhao [b, g], S.A. Mofid [b, c, g], T. Gao [c], G. Tan [d], B.P. Jelle [c, e, ***], X.B. Yin [b, **], R.G. Yang [a, f, *]

[a] School of Energy and Power Engineering, Huazhong University of Science and Technology, Wuhan, Hubei, 430074, China
[b] Department of Mechanical Engineering, University of Colorado, Boulder, CO, 80309, USA
[c] Department of Civil and Environmental Engineering, Norwegian University of Science and Technology (NTNU), NO-7491, Trondheim, Norway
[d] Department of Civil and Architectural Engineering, University of Wyoming, Laramie, WY, 82071, USA
[e] Department of Materials and Structures, SINTEF Community, NO-7465, Trondheim, Norway
[f] State Key Laboratory of Coal Combustion, Huazhong University of Science and Technology, Wuhan, Hubei, 430074, China

ARTICLE INFO

Article history:
Received 13 February 2020
Received in revised form
3 March 2020
Accepted 3 March 2020
Available online xxx

Keywords:
VO_2 nanoparticle
Cross-linking
Thermochromic film
Environmental stability

ABSTRACT

Vanadium dioxide (VO_2)–based thermochromic films are of great interest for energy-saving smart windows as they can dynamically change the solar transmittance as the ambient temperature changes. However, VO_2 is thermodynamically unstable and could be easily oxidized by the oxygen and moisture in the ambient air. In this work, a durability-enhanced VO_2 nanoparticle-polymer thermochromic film was proposed and fabricated using the blade coating method where the cross-linked and highly entangled poly(methyl methacrylate) (PMMA) chains with a molecular weight (~ 950,000) was adopted to block gas diffusion in the polymer matrix. It was shown that the developed VO_2 nanoparticle film kept ~30% of its solar modulation ability after ~900 h of accelerated durability test in the aging environment with a temperature at 60 °C and ~95% relative humidity. This is ~4 times of the lifetime of the VO_2 nanoparticles which are embedded in the non–cross-linked PMMA matrix with low molecular weight (~15,000). The cross-linked PMMA-VO_2 film also showed a high luminous transmittance of ~50%, a high solar modulation ability of ~17%, and a low haze of ~11%. Our method provides an easy and effective strategy to improve the lifetime of VO_2 nanoparticles, showing a promising pathway toward environmentally stable and easily scalable thermochromic films for energy-efficient smart windows.

1. Introduction

With a high solar transmittance >90%, as much as ~800 W/m^2 solar irradiance reaches the indoor environment through windows during daytime [1,2]. The transmitted solar energy greatly reduces the energy consumption for heating in cold climates. However, the excessive solar heating would result in increased cooling loads in hot climates, especially in summer. Smart windows that could dynamically adjust the transmittance of solar radiation have been thought of as one of the most promising techniques to reduce energy consumption of buildings [3,4]. In particular, there are a lot of interests in vanadium dioxide (VO_2) nanoparticle and transparent polymer matrix based thermochromic films in recent years, especially due to the relatively high luminous transmittance of ~50% and solar modulation ability of ~20% [5–11]. However, pristine VO_2 is thermodynamically unstable and can be easily oxidized to V_2O_5 when exposed to air for several months [12,13], which in turn dramatically reduces the solar modulation ability. A humid environment would also greatly accelerate the oxidation process. Previous studies [8,14–16] showed that the thermochromic performance of VO_2 decreased noticeably when exposed to relatively high humidity for only ~ 24 h, deterring the practical deployment of VO_2 based smart windows.

To improve the antioxidation ability and increase the lifetime of VO_2 nanoparticles, core-shell nanoparticles have been proposed, where the environmentally stable materials are used as a protection layer to prevent VO_2 from water and oxygen exposure and hence to decrease the oxidation rate. For example, the previous study showed that using aluminum oxide–based shells could

* Corresponding author.
** Corresponding author.
*** Corresponding author.
E-mail addresses: bjorn.petter.jelle@ntnu.no (B.P. Jelle), xiaobo.yin@colorado.edu (X.B. Yin), ronggui@hust.edu.cn (R.G. Yang).
[g] These authors contribute equally.

https://doi.org/10.1016/j.mtphys.2020.100205
2542-5293/

increase the lifetime of VO_2 from ~3 days to more than ~20 days under accelerated aging tests with a 60 °C temperature and 90% relative humidity [16]. In addition, other environmentally stable oxides such as SiO_2 [10], TiO_2 [17], and ZnO [8] have been used to increase the durability of VO_2 nanoparticles. However, in practical applications, when VO_2 nanoparticles transit periodically from monoclinic (M, $a_M = 5.75$ Å, $b_M = 4.52$ Å, $c_M = 5.38$ Å, $\beta = 122.6°$) structure to tetragonal rutile (R, $a_R = b_R = 4.55$ Å, $c_R = 2.86$ Å) structure [6], the interface stress between VO_2 cores and oxide protection shells induced by the lattice structure transformation of VO_2 nanoparticles may result in formation of microcracks at the interface. A recent study [18] has shown that cracks occur in VO_2-based multilayer thin films after ~ 1000 times of reversible phase transitions. In addition, cracks were even found in SiO_2 [19] and TiO_2 shells [8,17] during synthesis process. The accelerated aging tests at 60 °C temperature and 90% relative humidity showed that the lifetime of the SiO_2-coated VO_2 nanoparticles was only ~72 h because of the appearance of such cracks [8]. It is also worthwhile to note that although the introduction of a shell layer potentially enhances the durability of VO_2 nanoparticles and improves the solar luminous transmittance, it may lower the solar modulation ability of the film. For example, the experimental results by Li et al. [17] showed that the solar modulation ability decreased ~50% when the VO_2 nanoparticles were coated by ~7 nm thick TiO_2 shells. Besides the core-shell nanoparticle structures, blocking the diffusion of oxygen and moisture in polymer matrix may also delay the oxidation process of VO_2 nanoparticles. In general, increasing the molecular weight (length) of polymer chain and generating chemical cross-links between neighboring polymer chains are two effective ways to reduce gas diffusion in polymer matrix because the mobility of polymer chains can be restricted by the highly entangled polymer chains and the ionic or covalent bonds between neighboring polymer chains [20–24]. A previous study by Berens and Hopfenberg [25] showed that the diffusivity of organic vapors (e.g., $(CH_3)_2CO$, $CHCl_3$) was decreased by a factor of ~10 when the molecular weight of polystyrene increased from 10,000 to 300,000. Klinger et al. [26] showed that a 0.45% mole of cross-links in poly(methyl methacrylate) (PMMA) could reduce the oxygen diffusion coefficient by ~ 30%. These together imply that highly cross-linked high molecular weight polymers may provide a simple yet effective pathway to protect the randomly dispersed VO_2 nanoparticles from oxidation.

Considering high transparency, structural stability, and cross-linking ability of PMMA, a cross-linked high molecular weight PMMA film (~950,000) embedded with VO_2 nanoparticles with a size of 50–80 nm was demonstrated in this work. The developed PMMA-VO_2 film with a thickness of ~4 μm has a relatively high luminous transmittance of ~50%, solar modulation ability of ~17.1%, and a low haze of ~11%. The accelerated aging test at 60 °C temperature and a relative humidity of ~95% shows that the lifetime of the VO_2 nanoparticles dispersed in the cross-linked high molecular weight PMMA film (~950,000) is more than 900 h, which is much longer than that of VO_2 nanoparticles in the non–cross-linked low molecular weight (~15,000) PMMA, around 200 h. The lifetime of VO_2 nanoparticles in the cross-linked and entangled PMMA matrix is significantly longer than the reported VO_2 nanoparticles coated by SiO_2 (~72 h), $Al(OH)_3$ (~120 h), and VO_2 thin film protected by Al_2O_3 (~100 h) [14] and is comparable with the VO_2 nanoparticles coated by Al_2O_3 (>480 h) [16] and VO_2 thin film protected by SiN_x (~600 h) [18]. The fatigue test shows that the thermochromic performance of the developed PMMA-VO_2 films keeps the same after 3000 times of continuous reversible phase transitions. The analysis also shows that the developed PMMA-VO_2 film could greatly reduce the cooling demands in hot climates and improve the thermal comfort and condensation resistance in cold climates.

2. Materials and methods

2.1. Synthesis

2.1.1. Chemicals and materials

Vanadium pentoxide (V_2O_5, 99.99%, Sigma-Aldrich), oxalic acid dihydrate ($H_2C_2O_4 \cdot 2H_2O$, 99%, Sigma-Aldrich), PMMA (molecular weight ~15,000 (15 K), Sigma-Aldrich), anisole (C_7H_8O, 99.7%, Sigma-Aldrich), and PMMA A4 (molecular weight ~950,000 (950 K), MicroChem Corp) resists in anisole and were purchased and used as as-supplied without additional purifications.

2.1.2. Synthesis of monoclinic VO_2

Various synthesis methods of monoclinic VO_2 (M) could be found in the earlier studies [8,10,27–29]. In this work, VO_2 nanoparticles were synthesized by the hydrothermal method [8]. For a typical synthesis, 2.0 g of V_2O_5 powder was added to 40.0 ml deionized water and was stirred for 20 min and then 3.4 g of oxalic acid dihydrate was added to the mixture and further stirred until a clear light green/blue slurry was formed. The suspension was then moved to a 150 ml Teflon-lined stainless-steel autoclave. The autoclave was kept at 260 °C for 24.0 h and then air cooled to room temperature. The resulting black precipitates were collected and washed with deionized water and ethanol 3 times, respectively, then dried with a vacuum furnace at 120 °C for 5.0 h. A schematic illustrating the synthesis process could be found in Fig. 1(a).

2.2. Measurements

The commercial Netzsch differential scanning calorimetry (DSC 204 F1 Phoenix) was used to determine the phase transition properties of the synthesized VO_2 powder over the temperature range from 0 to 100 °C and the heat absorption of the PMMAs from 0 to 550 °C, respectively. The heating/cooling rate was set at 10 °C/min. The crystalline phase of the VO_2 powder was identified using X-ray diffraction (XRD, MiniFlex600, Rigaku, Japan) with Cu Kα radiation ($\lambda = 1.5418$) at a voltage 40 kV and a current of 40 mA. Transmission electron microscope (JEM-2010) was used to characterize the morphology and microstructure of the nanoparticles. Optical performance, including spectral transmittance and haze of the films, was measured using a ultraviolet (UV)-vis-near-IR spectrophotometer (Shimadzu UV-3101) together with a temperature control unit including black anodized aluminum 6061 plate and a variac (2 A, 120 V). A helium-neon (HeNe) laser (SIEMENS) and a programmable stage temperature controller (LINKAM TMS 94) together with a heating/freezing microscope stage (LINKAM MDS600) with a microscope objective lens (NIKON, Plan Fluor ELWD 20x/0.45) was assembled to measure the reflectance spectrum of the film with a ~100 nm silver coating in 633 nm at 25 °C and 90 °C with a ramping rate of 10 °C/min. A TPS (TENNEY) environmental chamber was used to create a steady-state temperature and humidity (60 °C, relative humidity ~ 95%) for the durability test of the fabricated PMMA-VO_2 films.

3. Results and discussion

3.1. Fabrication and characterization of PMMA-VO_2 film

PMMA is a non-toxic, inexpensive thermoplastic with high optical transparency, high mechanical strength and durability, excellent thermal stability, and weather resistance [30]. PMMA with different molecular weights (chain length and entanglement) could

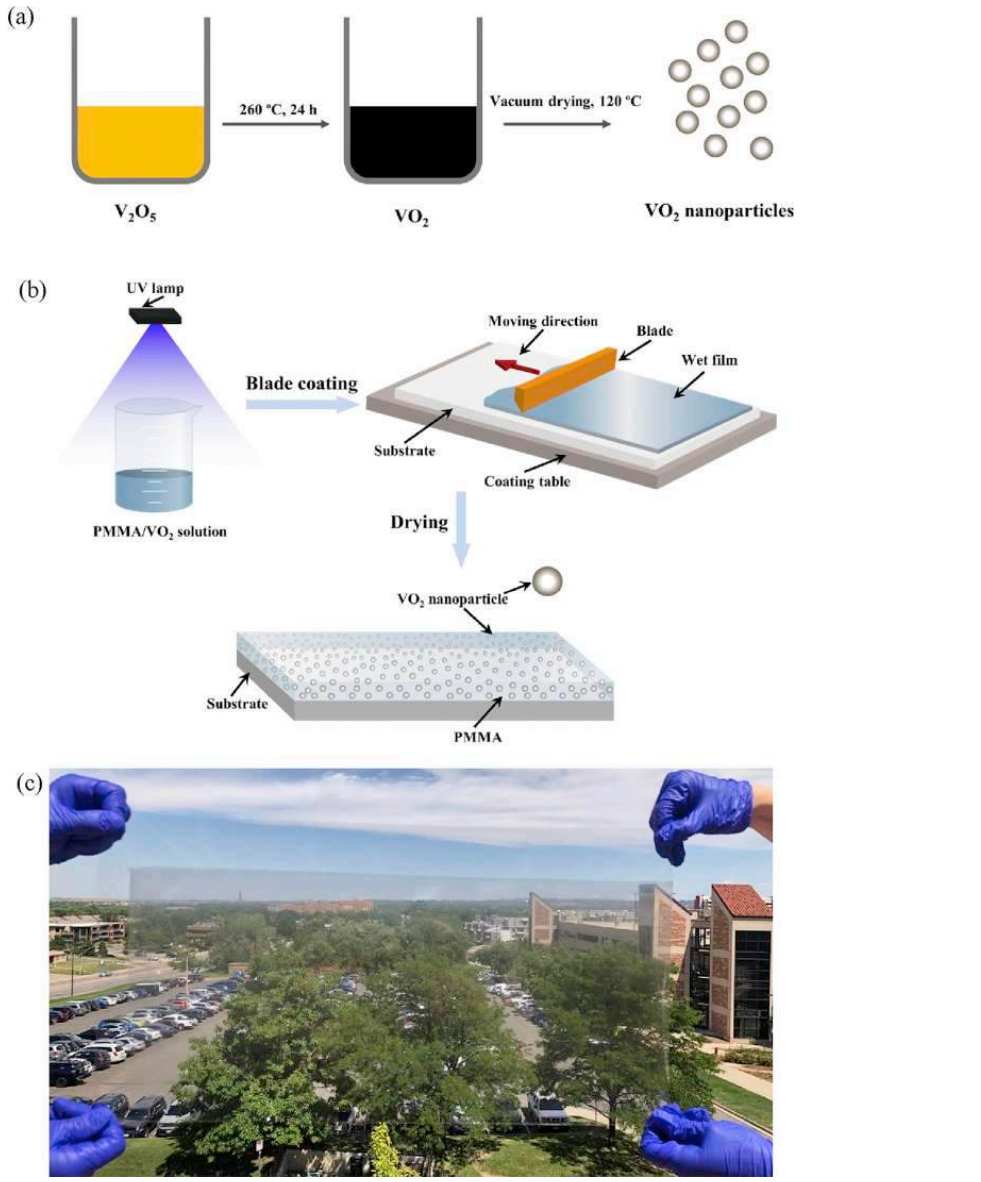

Fig. 1. Fabrication of durability-enhanced PMMA-VO_2 thermochromic film for smart windows. (a) Synthesis process of VO_2 nanoparticles using the hydrothermal method. (b) Schematic of the fabrication process of the meter-scale durability-enhanced PMMA-VO_2 film. The PMMA-VO_2 solution was first exposed to ultraviolet (UV) rays. Then, the wet PMMA-VO_2 film was fabricated using the blade coating method. After drying, the PMMA-VO_2 composite film was obtained. (c) Snapshot of the PMMA-VO_2 film with a size of 600 mm × 300 mm (length × width) manufactured using the blade coating method, in which a ~4.0 μm thick PMMA-VO_2 film is coated on a 50 μm thick BoPET film. BoPET, biaxially oriented polyethylene terephthalate; PMMA, poly(methyl methacrylate); VO_2, vanadium dioxide.

be obtained and processed easily [31]. Moreover, the influence of the near-UV from solar radiation on PMMA is minor because PMMA is only sensitive to high energy radiation such as electron beam, x-rays, and UV radiation with wavelengths shorter than 300 nm [31,32]. Thus, PMMA was adopted as the polymer matrix in this work. As shown in Fig. 1(b), the desired amount of as-synthesized crystalline monoclinic VO_2 nanoparticles was dispersed ultrasonically into 40 ml of PMMA 950 K A4. The solution was then stirred at room temperature for 12 h. Generally, the molecule chains of PMMA could be interlinked using several methods, including free radical polymerization, condensation reaction, small molecule crosslinking, and radiation [33]. Wochnowski et al. [32] showed that the 248 nm wavelength UV irradiation could cross-link two neighboring PMMA molecules by establishing an oxygen

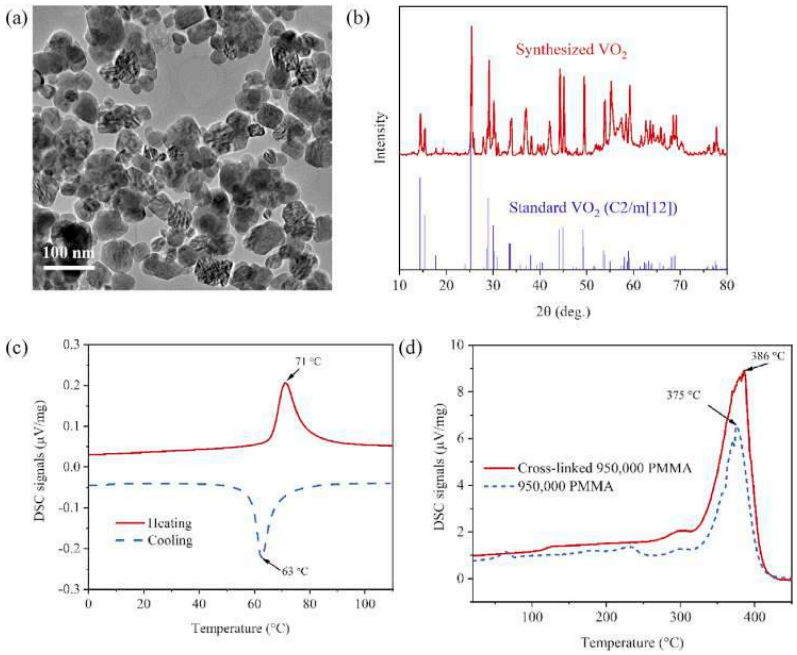

Fig. 2. Characterization of the synthesized VO_2 nanoparticles. (a) Transmission electron microscopy (TEM) image of the VO_2 nanoparticles. (b) X-ray diffraction (XRD) pattern of the VO_2 nanoparticles. (c) Differential scanning calorimetry (DSC) of the VO_2 nanoparticles, where the heating/cooling rate is set at 10 °C/min. (d) Comparison of the DSC thermograms of cross-linked and non−cross-linked PMMA with molecular weight ~950,000. The positive peak represents an endothermic process, and the negative peak represents an exothermic process. PMMA, poly(methyl methacrylate); VO_2, vanadium dioxide.

bridge between ester side chains or connecting the two carbonyl groups. The degree of cross-linking of PMMA matrix could be controlled by both the dose and the duration of UV irradiation. A higher degree of cross-linking usually has a higher endothermic peak, which can be evaluated by the DSC measurements. The radiation dose needs to be less than 2.0 J/cm^2 to prevent the brittleness of PMMA film after cross-linking [34]. Here the PMMA-VO_2 solution was irradiated by the UV radiation (220−380 nm, ADJ Products) for 10 h in the room environment while being stirred at 300 rpm to generate cross-links in the PMMA matrix. The final mixture was maintained at a constant temperature of ~75 °C on a hotplate for 40 min. The solution was then loaded onto a ~50 μm thick transparent and chemically stable biaxially oriented polyethylene terephthalate (BoPET) sheet laminated on a piece of float glass using the blade coating method as shown in Fig. 1(b). The final thickness of the dried PMMA-VO_2 film is determined by the concentration of PMMA, the moving speed of the blade, and the gap between the blade tip and the substrate. Here, the film was formed using blade coating at a speed of 15 mm/s. After the wet film was fabricated, the film was dried in a fume hood for 2 h. Finally, a thin film with an area of 600 mm × 300 mm (length × width) and a thickness of ~4 μm was obtained as shown in Fig. 1(c), in which the PMMA-VO_2 film was coated on a 50 μm thick BoPET film. No obvious variation of the film brittleness was observed.

Fig. 2(a) shows the morphology of the synthesized VO_2 nanoparticles from transmission electron microscopy. It is seen that most of the nanoparticles have an approximately spherical shape, and the diameter of the VO_2 nanoparticles mainly lies in the range of 50−80 nm. Fig. 2(b) presents the XRD measurement of the VO_2 nanoparticles, where the diffraction peaks indicate that the VO_2 nanoparticles are in the monoclinic phase (M2, C2/m) [12]. The phase transition temperature of the VO_2 nanoparticles was determined by the DSC measurements using a heating/cooling rate of 10 °C/min in the temperature range from 0 to 110 °C. Because the insulator-to-metal transformation of VO_2 is a first-order phase transition [35], the discontinuous variation of entropy results in the release or absorption of latent heat. As shown in Fig. 2 (c), when VO_2 transits from the monoclinic (M) phase to the rutile (R) phase during the heating cycle, an endothermic (positive) peak with a peak temperature of ~ 71 °C is observed. A corresponding exothermic (negative) peak, representing metal-to-insulator transition, occurs in the cooling cycle, where the peak temperature is ~63 °C. This DSC curve is similar to that reported in the literature [8,11,36]. Because the cross-linking process could generate new chemical bondings between neighboring chains, the cross-linked PMMA polymers are expected to have a higher endothermic peak and a larger maximum decomposition temperature [37]. Fig. 2(d) compares the DSC thermographs of cross-linked PMMA and non−cross-linked PMMA with molecular weight ~ 950,000. Compared to the non-UV exposed 950,000 PMMA, the 950,000 PMMA under UV exposure presents a higher endothermic peak (from ~6.0 μV/mg to ~ 9.5 μV/mg) and a larger maximum decomposition temperature (from 375 °C to 386 °C), indicating that the cross-links were generated.

3.2. Optical performances of PMMA-VO_2 film

To evaluate the thermochromic performance of the fabricated PMMA-VO_2 film, the total transmittance and haze were both measured using a commercial UV-vis-near-IR spectrophotometer

(Shimadzu UV-3101). The total transmittance ($\tau_{\lambda,tot}$) was measured by placing the PMMA-VO_2 film and a diffuse reflector at the inlet and outlet of the integrating sphere, respectively. The measured total spectral transmittances of the PMMA-VO_2 film at low temperature (~25 °C) and high temperature (~90 °C) are shown in Fig. 3(a). Because the metallic phase VO_2 blocks the near-infrared solar radiation, it is found that the transmittance of the PMMA-VO_2 film in the range of 800–2500 nm is much smaller when the temperature of the PMMA-VO_2 film is ~ 90 °C. The mean luminous (380–780 nm) transmittance τ_{lum} and mean solar (280–2500 nm) transmittance τ_{sol} are calculated as follows:

$$\tau_{lum} = \frac{\int_{380\ nm}^{780\ nm} I_{lum,\lambda}\tau_{\lambda,tot}d\lambda}{\int_{380\ nm}^{780\ nm} I_{lum,\lambda}d\lambda} \quad (1)$$

$$\tau_{sol} = \frac{\int_{280\ nm}^{2500\ nm} I_{sol,\lambda}\tau_{\lambda,tot}d\lambda}{\int_{280\ nm}^{2500\ nm} I_{sol,\lambda}d\lambda} \quad (2)$$

where $I_{lum,\lambda}$ is the standard luminous efficiency function for vision [38], $I_{sol,\lambda}$ is the solar radiation intensity of air mass 1.5 (AM1.5) corresponding to the sun standing 37° above the horizon [39], and $\tau_{\lambda,tot}$ is the total transmittance of radiation at wavelength λ shown in Fig. 3(a). The solar modulation ability $\Delta\tau_{sol}$ is defined by the difference of solar transmittance before and after the phase transition, that is,

$$\Delta\tau_{sol} = \tau_{sol}(T < T_c) - \tau_{sol}(T > T_c) \quad (3)$$

where T_c is the critical phase change temperature of VO_2. According to Eqs. (1) and (2), the luminous transmittance at low temperature and solar modulation ability are calculated to be ~50% and ~17.1%, respectively. Besides, we have also checked the uniformity of the coating by measuring the transmittance of the PMMA-VO_2 film at several different locations. The difference of the solar transmittances among different points was found to be less than 1%.

Haze is used to characterize the percentage of the transmitted light whose propagation direction deviates a specific angle from the direction of the incident beam. According to the ASTM D1003-13 [40], haze is defined as follows:

$$H_\lambda = \frac{\tau_{dif,\lambda}}{\tau_{tot,\lambda}} = \frac{\tau_{dif,\lambda}}{\tau_{dif,\lambda} + \tau_{dir,\lambda}} \quad (4)$$

where $\tau_{dif,\lambda}$ refers to the light scattered more than 2.5° off from the incident light [40] and $\tau_{dir,\lambda}$ is the transmitted light within the angle of 2.5°. The diffuse transmittance can be measured by replacing the diffuse reflector at the outlet of the integrating sphere with a light trap to prevent the direct transmittance from influencing the measurement signal. Because the VO_2 nanoparticle size (50–80 nm) is much smaller than the wavelength of the light in visible range (380–780 nm), the scattering of the light passing through the PMMA-VO_2 films can be described by Rayleigh scattering approximately [41]. Therefore, it is seen that the haze value decreases as wavelength increase in Fig. 3(b). The averaged haze value in the visible range is calculated as follows:

$$H = \frac{\int_{380\ nm}^{780\ nm} H_\lambda I_{lum,\lambda}d\lambda}{\int_{380\ nm}^{780\ nm} I_{lum,\lambda}d\lambda} \quad (5)$$

where H_λ is the measured haze value at wavelength λ. According to Eq. (5), the averaged haze in the luminous range is ~11%, as shown in Fig. 3(b). Note that the haze of the developed film could be lowered by reducing the size of the VO_2 nanoparticles [41]. In short, we have fabricated a large-sized PMMA-VO_2 film with high luminous transmittance (~50%), large solar modulation ability (~17.1%), and relatively low haze visibly (~11%).

3.3. Durability of PMMA-VO_2 film

Oxygen and moisture in the ambient air could diffuse into polymer matrix and oxidize the phase-switchable VO_2 to the non-switchable V_2O_5, resulting in the loss of solar modulation ability. It is thus desirable to reduce the diffusion capacity of gas molecules in polymer matrix. The previous studies have shown that the thermal stability [37], surface hardness, and chemical resistance [42] of polymer matrix could be improved significantly using entangled and cross-linked molecular chains, which is also directly related to a smaller gas diffusion coefficient. In practice, the natural oxidation of VO_2 is a long process, and an obvious variation of the thermochromic property in the ambient conditions may only be observed after a few months [12]. Thus, accelerated environmental tests were performed to evaluate the durability of VO_2 nanoparticles [43,44]. The tests were conducted at 60 °C temperature and the relative humidity ~95%, similar to the testing conditions reported in the previous

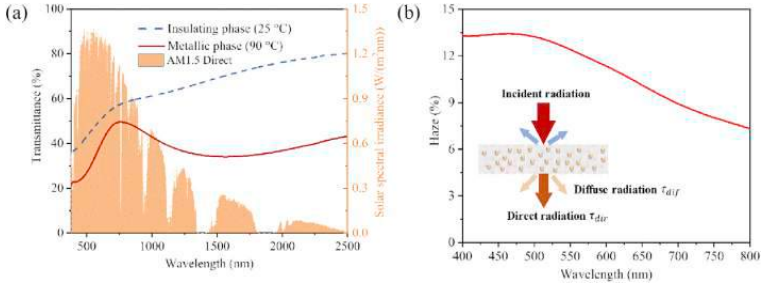

Fig. 3. Optical performance of the PMMA-VO_2 film. (a) Spectral transmittance of the PMMA-VO_2 film in the solar spectrum, where the luminous transmittance is ~50% and the solar modulation ability is ~17.1%, respectively. (b) Spectral haze of the PMMA-VO_2 film in the visible range with wavelength of 400–800 nm, the averaged haze is ~11%. PMMA, poly(methyl methacrylate); VO_2, vanadium dioxide.

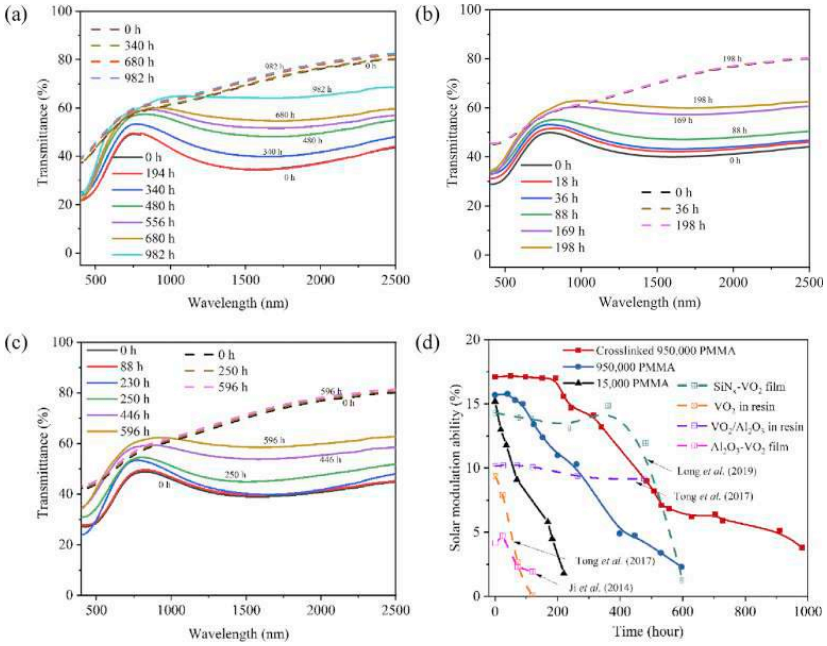

Fig. 4. Durability performance of the PMMA-VO_2 films. (a) Variation of the spectral optical transmittance of VO_2 nanoparticles embedded in the cross-linked 950,000 PMMA matrix as a function of aging time. (b) Variation of the spectral optical transmittance of VO_2 nanoparticles embedded in the non−cross-linked 150,000 PMMA matrix as a function of aging time. (c) Variation of the spectral optical transmittance of VO_2 nanoparticles embedded in the non−cross-linked 950,000 PMMA matrix as a function of aging time. (d) Comparison of the solar modulation ability of the VO_2 nanoparticles embedded in non−cross-linked 150,000 PMMA, non−cross-linked 950,000 PMMA, cross-linked 950,000 PMMA matrixes, and previous studies [14,16,18]. The low and high temperatures for the optical measurements are 25 °C (insulating phase) and 90 °C (metallic phase), respectively. The aging tests were performed in a accelerated aging chamber with the temperature at 60 °C, and the relative humidity is ~95%. PMMA, poly(methyl methacrylate); VO_2, vanadium dioxide.

studies [8,18]. Systematic measurements of spectral transmittance at both low temperature (25 °C, insulating phase) and high temperature (90 °C, metallic phase) were recorded as a function of time to determine the variation of the thermochromic performance of the PMMA-VO_2 films. Each measurement was then repeated at least three times to ensure the testing reliability. To investigate the influence of cross-linking and entanglement on the durability of the PMMA-VO_2 film, the cross-linked (950,000) and non−crossed-linked PMMA-VO_2 films with two different molecular weights (950,000 and 15,000) were measured. It is seen that the cross-linked PMMA film with molecular weight ~950,000 exhibits no noticeable change in optical transmittance after ~200 h, as shown in Fig. 4 (a). The thermochromic performance of the cross-linked PMMA-VO_2 film with molecular weight ~950,000 begins to deteriorate after ~450 h exposure while still maintaining more than 60% of its solar modulation ability (~10%). After ~900 h, the solar modulation ability decreases from ~17.1% to ~5.0%, indicating that a large part of the VO_2 nanoparticles has been oxidized. For comparison, the durability performances of the non−cross-linked PMMA with molecular weights ~15,000 (Fig. 4(b)) and ~950,000 (Fig. 4(c)) were also tested under the same accelerated testing conditions (60 °C, relative humidity ~ 95%). Fig. 4(d) gives the variation of solar modulation abilities of the aforementioned three PMMA-VO_2 films as a function of time. It is seen that the decreasing rate of the non−cross-linked film with molecular weight ~15,000 is much faster than that of the non−cross-linked PMMA with molecular weight ~950,000, which is close to decreasing rate of the uncoated VO_2 in the matrix of the resin [16]. The thermochromic performance of the VO_2 in the non−cross-linked PMMA with molecular weights ~15,000 disappears after ~200 h. Furthermore, it is found that the lifetime of the cross-linked 950,000 PMMA is approximately 350 h longer than of the non−-cross-linked 950,000 PMMA at ~600 h. This indicates that the entangled and cross-linked polymer matrix can substantially improve the lifetime of VO_2 nanoparticles. Fig. 4(d) shows that the lifetime of the PMMA-VO_2 film developed in this work is better than the previously reported values of VO_2 nanoparticles coated by SiO_2 (~72 h) [8], $Al(OH)_3$ (~120 h) [8], and VO_2 thin film protected by Al_2O_3 (~100 h) [14] and is comparable with the performances of VO_2 nanoparticles coated by Al_2O_3 (>480 h) [16] and VO_2 thin film protected by SiN_x (~600 h) [18]. Clearly we have demonstrated here an alternative pathway to effectively improve the lifetime of VO_2 nanoparticles, avoiding the emergence of cracks induced by the periodic insulator-to-metal phase transition found in the core-shell structures.

Fatigue tests are used to determine the number of cycles (fatigue life) that a material or structure can withstand under cyclic loadings. The emergence of cracks in VO_2-based films or complete fractures may occur due to the lattice transformation of VO_2 during many cycles of phase transitions from the insulating state to the metallic state. Therefore, a fatigue test was performed to study the stability of the developed PMMA-VO_2 thermochromic film. The design of the fatigue test can be seen in Fig. 5(a). The PMMA-VO_2 sample coated with a ~100 nm thick bottom silver layer was placed on a programmable stage with a temperature control unit (LINKAM MDS600), where the ramping rate was 10 °C/min and an extra 45 s delay was assigned to stabilize the temperature of the film at both 25 °C and 90 °C. Meanwhile, the film was constantly exposed to a 633 nm focused laser beam from

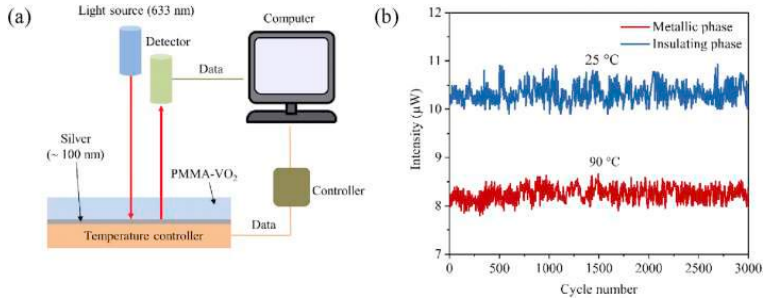

Fig. 5. Fatigue test and performance of the PMMA-VO_2 film. (a) Schematic of the setup for the fatigue measurements. The temperatures of the insulating phase and metallic phase VO_2 were set at 25 °C and 90 °C, respectively. (b) Variation of the transmittance of the durability-enhanced PMMA-VO_2 film as a function of cycle number. PMMA, poly(methyl methacrylate); VO_2, vanadium dioxide.

the HeNe laser (SIEMENS). The intensity of the transmitted light (μW) was then recorded by the detectors at both low temperature (25 °C, insulating phase) and high temperature (90 °C, metallic phase) to complete a cycle. Fig. 5(b) shows no noticeable change in the transmitted laser intensity in both the metallic and insulator phase after 3000 continuous cycles, indicating that the solar modulation ability of the cross-linked PMMA-VO_2 remained constant. To ensure the reliability of the test, the measurements were repeated at another two sample locations during each cycle and the results in Fig. 5(b) are the arithmetic average of the three tested points. Note that because incident light traveled across the film twice, the difference between the metallic phase (25 °C) and the insulator phase (90 °C) in Fig. 5(b) is approximately twice as larger than that of Fig. 3(a).

3.4. Thermal comfort and energy saving of PMMA-VO_2 film in different regions

To evaluate the energy-saving performance of the PMMA-VO_2 film in different climates and regions, a heat transfer model was developed. Fig. 6(a) depicts the heat and solar radiation transfer across a window pane, where PMMA-VO_2 film with a thickness of ~4 μm is used. The spectral transmittance of the PMMA-VO_2 film in both the insulating phase and the metallic phase is shown in Fig. 3(a). Because the thickness of a windowpane is much smaller than its width and length, the heat transfer in the z-direction can be treated as one dimensional. Thus, the heat transfer in the z-direction can be described as follows:

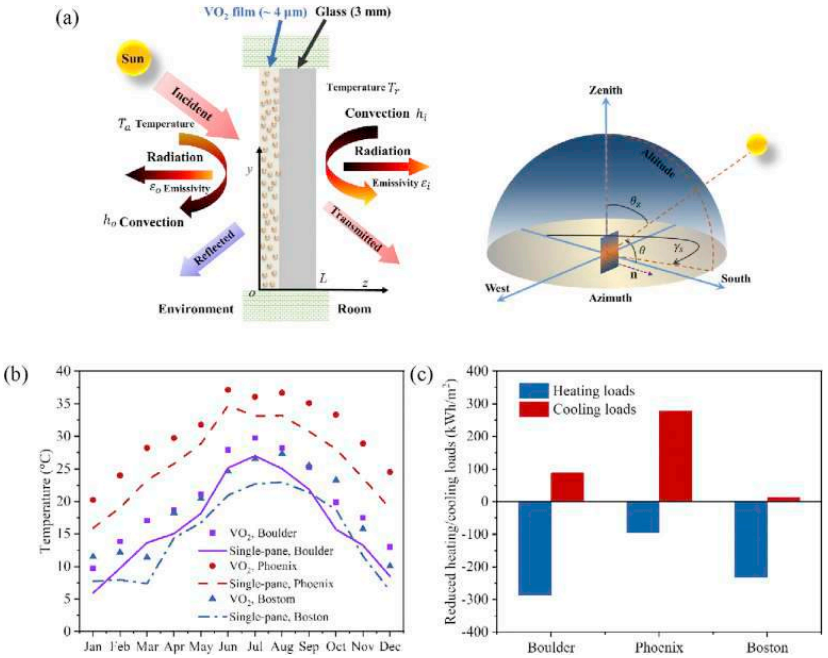

Fig. 6. Thermal comfort and energy savings of the PMMA-VO_2 film in selected cities: Boulder (CO), Phoenix (AZ), and Boston (MA). (a) Schematic of heat and radiation energy transfer across a south-facing single-pane window covered by the PMAA-VO_2 film. (b) Influence of PMMA-VO_2 film on the inside surface temperature of a glass window. (c) Comparison of reduced annual heating/cooling loads of a south-facing window. PMMA, poly(methyl methacrylate); VO_2, vanadium dioxide.

$$k_{gla}\frac{d^2T(z)}{dz^2}-\frac{dI(z)}{dz}=0 \tag{6}$$

where k_{gla} is the thermal conductivity of the float glass, $T(z)$ is the temperature at position z, $dI(z)/dz$ is the solar radiation absorped in glass per unit volume (W/m^3). $I(z)$ can be written as follows:

$$I(z)=\tau_{sol}I_o e^{-\beta_{gla}z} \tag{7}$$

where I_o is the incident solar energy, τ_{sol} is the solar transmittance of the PMMA-VO_2 film, and β_{gla} is the extinction coefficient of the float glass. Compared to the thickness of float glass (3 mm), the thickness of the PMMA-VO_2 film (~ 4 μm) can be ignored. Thus, the boundary conditions at $z=0$ and $z=L_{gla}$ are as follows:

$$q_{z=0}=h_o(T_a-T_{z=0})+\sigma\varepsilon_o\left(T_a^4-T_{z=0}^4\right)+Q_{abs} \tag{8}$$

$$q_{z=L_{gla}}=h_i\left(T_{z=L_{gla}}-T_r\right)+\sigma\varepsilon_i\left(T_{z=L_{gla}}^4-T_r^4\right) \tag{9}$$

where T_a and T_r are the external ambient temperature and internal room temperature, respectively, h_o, h_i and ε_o, ε_i are the outside and inside convective heat transfer coefficients and average outside and inside surface emissivities, $\sigma=5.67\times10^{-8}$ (Wm)/K^4 is the Stefan-Boltzmann's constant, $Q_{abs}=\alpha_{sol}I_o$, is the absorbed solar irradiation by the PMMA-VO_2 film, and α_{sol} is the solar absorbance of the PMMA-VO_2 film. Here, Eq. (6) was solved by the finite volume method [45]. The thermal conductivity and average surface emissivity of the float glass are assumed to be $k_g=0.96$ W/(mK) and $\varepsilon_o\approx0.84$ according to reference[46]. The surface emissivity of the PMMA-VO_2 film is $\varepsilon_o\approx0.9$. From Fig. 3(a), the solar transmittances (τ_{sol}) of the PMMA-VO_2 film in the insulating phase and metallic phase are 0.57 and 0.40, respectively. The reflectances (r_{sol}) of the PMMA-VO_2 film in both insulating and metallic phases were measured as 0.05. Thus, the absorbance can be calculated by $\alpha_{sol}=1-\tau_{sol}-r_{sol}$. The inside and external convective heat transfer coefficients can be evaluated by $h_i=3.6$ W/(m^{2}K) and $h_o=(10+4.1v)$ W/(m^{2}K), where v (m/s) is the wind speed [46]. The weather conditions including ambient temperature (T_o), window speed (v), and solar radiation density (I_o) are acquired from the National Solar Radiation Database (NSRDB) Data Viewer [47].

The inside surface temperatures of the single-pane window with and without the PMMA-VO_2 film are compared in Fig. 6(b). After using the PMMA-VO_2 film, the inside surface temperature of the single-pane window is ~5 °C higher than that of the single-pane window without the PMMA-VO_2 film, indicating that the PMMA-VO_2 film can reduce the temperature difference between the occupants and the innermost surface of windows, which indeed improves the thermal comfort and condensation resistance of the single-pane window in cold climates significantly [48]. Because the solar transmittance of the PMMA-VO_2 film (0.57–0.4, Fig. 3(a)) is smaller than that of the single-pane window (~92%), applying the PMMA-VO_2 film increases the heating loads in cold climates and reduces the cooling loads in hot climates. Fig. 6 (c) compares the reduced annual heating/cooling loads of a south-facing window in different regions, where the positive/negative sign represents the reduced/increased energy. For simplicity, it is assumed that the transmitted solar energy decreases (increases) the heating (cooling) loads when the external ambient temperature is higher (lower) than the internal room temperature (21 °C). Note that the transmitted solar energy includes both the directly transmitted solar irradiance and the absorbed solar energy by window pane and subsequently transferred toward the indoor room environment through heat conduction. Clearly, the cooling demands in the hot areas (e.g., Phoenix) are significantly reduced. However, in the cold areas (e.g., Boston), the increased heating loads in winter are much higher than the reduced cooling loads in summer, indicating that using PMMA-VO_2 film would increase the annual energy cost.

4. Conclusions

In summary, a thermochromic film based on VO_2 nanoparticles and PMMA matrix was proposed and fabricated using the blade coating method. The area and thickness of the fabricated film are 600 mm × 300 mm (length × width) and ~4 μm, respectively. It is shown that the PMMA-VO_2 film has a luminous transmittance of ~50%, a solar modulation ability of ~17.1%, and a haze of ~11%. The solar modulation ability of the PMMA-VO_2 film is higher than that of most previous studies which are usually less than 10%. The lifetime of the VO_2 nanoparticles was greatly improved by the cross-linked polymer matrix with high molecular weight. The durability tests were performed in a accelerated aging chamber whose environmental temperature is 60 °C and relative humidity is ~95%. It was shown that the lifetime of the VO_2 nanoparticles embedded in the cross-linked PMMA matrix with molecular weight ~950,000 is ~900 h, which is much longer than that (~200 h) of the VO_2 in the non−cross-linked PMMA matrix with low molecular weight (~15,000). The lifetime of the VO_2 nanoparticles in the highly entangled and cross-linked polymer matrix is close to or longer than the lifetime of thermochromic films made of VO_2 protected by environmental stable materials (e.g., aluminum oxide and SiN_x), indicating that cross-linked polymer chains with high molecular weight could improve the durability of VO_2 remarkably. It was shown that there is no decay of the solar modulation ability after ~3000 cycles of the fatigue test. The analysis also showed that the PMMA-VO_2 film could greatly reduce the cooling demands in hot climates and improve the thermal comfort in cold climates.

Author contributions

R.G. Yang, X.B. Yin, and B.P. Jelle designed the research. S.A. Mofid and X.P. Zhao conceived the experiments, characterization, and modeling. X.P. Zhao, S.A. Mofid, T. Gao, G. Tan, B.P. Jelle, X.B. Yin, and R.G. Yang wrote the manuscript. All authors participated in the discussion of the research.

Declaration of competing interest

The authors declare no conflict of interest.

Acknowledgments

X.P. Zhao and S.A. Mofid acknowledge the help of Dr. L.H. Shen., Dr. Y. Zai, and Mr. A. Aili for the synthesis of VO_2 nanoparticles and the fabrication of PMMA-VO_2 films, Mr. H.D. Zhao. and Prof. G. Cao for the XRD measurements, Mr. D. Alchenberger and Mr. M. Cart from JILA Keck lab for the SEM and optical characterization, and Ms. B. Cunningham for schematics and illustrations. The involvement of researchers from Norway has been supported by the Research Council of Norway through the SINTEF and NTNU research project 'High-Performance Nano Insulation Materials' (Hi-Per NIM, project no. 250159) within the NANO2021 program. Furthermore, the Research Council of Norway is acknowledged for the support to the 'Norwegian Micro- and Nano-Fabrication Facility' (NorFab, project no. 245963/F50).

References

[1] K. Ismail, J. Henrıquez, Thermally effective windows with moving phase change material curtains, Appl. Therm. Eng. 21 (2001) 1909–1923.
[2] R.C. Temps, K. Coulson, Solar radiation incident upon slopes of different orientations, Sol. Energy 19 (1977) 179–184.
[3] Y. Wang, E.L. Runnerstrom, D.J. Milliron, Switchable materials for smart windows, Annu. Rev. Chem. Biomol. Eng. 7 (2016) 283–304.
[4] H.N. Kim, S. Yang, Responsive smart windows from nanoparticle-polymer composites, Adv. Funct. Mater. (2019) 1902597.
[5] Y. Ke, C. Zhou, Y. Zhou, S. Wang, S.H. Chan, Y. Long, Emerging thermal-responsive materials and integrated techniques targeting the energy-efficient smart window application, Adv. Funct. Mater. 28 (2018): 1800113.
[6] Y. Cui, Y. Ke, C. Liu, Z. Chen, N. Wang, L. Zhang, Y. Zhou, S. Wang, Y. Gao, Y. Long, Thermochromic VO_2 for Energy-Efficient Smart Windows, Joule, 2018.
[7] Z. Chen, Y. Gao, L. Kang, C. Cao, S. Chen, H. Luo, Fine crystalline VO_2 nanoparticles: synthesis, abnormal phase transition temperatures and excellent optical properties of a derived VO_2 nanocomposite foil, J. Mater. Chem. 2 (2014) 2718–2727.
[8] Y. Chen, X. Zeng, J. Zhu, R. Li, H. Yao, X. Cao, S. Ji, P. Jin, High performance and enhanced durability of thermochromic films using VO_2@ ZnO core–shell nanoparticles, ACS Appl. Mater. Interfaces 9 (2017) 27784–27791.
[9] S.-Y. Li, G.A. Niklasson, C.-G. Granqvist, Nanothermochromics: calculations for VO_2 nanoparticles in dielectric hosts show much improved luminous transmittance and solar energy transmittance modulation, J. Appl. Phys. 108 (2010): 063525.
[10] Y. Gao, S. Wang, H. Luo, L. Dai, C. Cao, Y. Liu, Z. Chen, M. Kanehira, Enhanced chemical stability of VO_2 nanoparticles by the formation of SiO_2/VO_2 core/shell structures and the application to transparent and flexible VO_2-based composite foils with excellent thermochromic properties for solar heat control, Energy Environ. Sci. 5 (2012) 6104–6110.
[11] Y. Li, S. Ji, Y. Gao, H. Luo, P. Jin, Modification of Mott phase transition characteristics in VO_2@ TiO_2 core/shell nanostructures by misfit-strained heteroepitaxy, ACS Appl. Mater. Interfaces 5 (2013) 6603–6614.
[12] L. Zhao, L. Miao, C. Liu, C. Li, T. Asaka, Y. Kang, Y. Iwamoto, S. Tanemura, H. Gu, H. Su, Solution-processed VO_2-SiO_2 composite films with simultaneously enhanced luminous transmittance,solar modulation ability and anti-oxidation property, Sci. Rep. 4 (2014) 7000.
[13] R. Lindström, V. Maurice, S. Zanna, L. Klein, H. Groult, L. Perrigaud, C. Cohen, P. Marcus, Thin films of vanadium oxide grown on vanadium metal: oxidation conditions to produce V_2O_5 films for Li-intercalation applications and characterisation by XPS, AFM, RBS/NRA, Surf. Interface Anal. 38 (2006) 6–18.
[14] Y.-X. Ji, S.-Y. Li, G.A. Niklasson, C.G. Granqvist, Durability of thermochromic VO_2 thin films under heating and humidity: effect of Al oxide top coatings, Thin Solid Films 562 (2014) 568–573.
[15] T. Chang, X. Cao, L.R. Dedon, S. Long, A. Huang, Z. Shao, N. Li, H. Luo, P. Jin, Optical design and stability study for ultrahigh-performance and long-lived vanadium dioxide-based thermochromic coatings, Nanomater. Energy 44 (2018) 256–264.
[16] K. Tong, R. Li, J. Zhu, H. Yao, H. Zhou, X. Zeng, S. Ji, P. Jin, Preparation of VO_2/Al-O core-shell structure with enhanced weathering resistance for smart window, Ceram. Int. 43 (2017) 4055–4061.
[17] Y. Li, S. Ji, Y. Gao, H. Luo, M. Kanehira, Core-shell VO_2@TiO_2 nanorods that combine thermochromic and photocatalytic properties for application as energy-saving smart coatings, Sci. Rep. 3 (2013) 1370.
[18] S. Long, X. Cao, N. Li, Y. Xin, G. Sun, T. Chang, S. Bao, P. Jin, Application-oriented VO_2 thermochromic coatings with composite structures: optimized optical performance and robust fatigue properties, Sol. Energy Mater. Sol. Cell. 189 (2019) 138–148.
[19] A. Huang, Y. Zhou, Y. Li, S. Ji, H. Luo, P. Jin, Preparation of $V_xW_{1-x}O_2$(M)@SiO_2 ultrathin nanostructures with high optical performance and optimization for smart windows by etching, J. Mater. Chem. 1 (2013) 12545–12552.
[20] Ö. Pekcan, Ş. Uğur, Molecular weight effect on polymer dissolution: a steady state fluorescence study, Polymer 43 (2002) 1937–1941.
[21] L.H. Sperling, Introduction to Physical Polymer Science, John Wiley & Sons, 2005.
[22] K. Balani, V. Verma, A. Agarwal, R. Narayan, Physical, Thermal, and Mechanical Properties of Polymers, John Wiley & Sons, Inc, Hoboken, NJ, United States, 2014.
[23] L. Tan, F. Yang, M.R. Kim, P. Li, D.T. Gangadharan, J.I. Margot, R. Izquierdo, M. Chaker, D. Ma, Enhanced long-term and thermal stability of polymer solar cells in air at high humidity with the formation of unusual quantum dot networks, ACS Appl. Mater. Interfaces 9 (2017) 26257–26267.
[24] S.C. George, S. Thomas, Transport phenomena through polymeric systems, Prog. Polym. Sci. 26 (2001) 985–1017.
[25] A. Berens, H. Hopfenberg, Diffusion of organic vapors at low concentrations in glassy PVC, polystyrene, and PMMA, J. Membr. Sci. 10 (1982) 283–303.
[26] M. Klinger, L.P. Tolbod, K.V. Gothelf, P.R. Ogilby, Effect of polymer cross-links on oxygen diffusion in glassy PMMA films, ACS Appl. Mater. Interfaces 1 (2009) 661–667.
[27] M. Li, S. Magdassi, Y. Gao, Y. Long, Hydrothermal synthesis of VO_2 polymorphs: advantages, challenges and prospects for the application of energy efficient smart windows, Small 13 (2017): 1701147.
[28] W. Li, S. Ji, Y. Li, A. Huang, H. Luo, P. Jin, Synthesis of VO_2 nanoparticles by a hydrothermal-assisted homogeneous precipitation approach for thermochromic applications, RSC Adv. 4 (2014) 13026–13033.
[29] R. Li, S. Ji, Y. Li, Y. Gao, H. Luo, P. Jin, Synthesis and characterization of plate-like VO_2 (M)@SiO_2 nanoparticles and their application to smart window, Mater. Lett. 110 (2013) 241–244.
[30] U. Ali, K.J.B.A. Karim, N.A. Buang, A review of the properties and applications of poly (methyl methacrylate)(PMMA), Polym. Rev. 55 (2015) 678–705.
[31] D.J. Carbaugh, J.T. Wright, R. Parthiban, F. Rahman, Photolithography with polymethyl methacrylate (PMMA), Semicond. Sci. Technol. 31 (2015): 025010.
[32] C. Wochnowski, M.S. Eldin, S. Metev, UV-laser-assisted degradation of poly (methyl methacrylate), Polym. Degrad. Stabil. 89 (2005) 252–264.
[33] H. Albeladi, A. Al-Romaizan, M. Hussein, Role of cross-linking process on the performance of PMMA, Int. J. Biosens. Bioelectron 3 (2017) 279–284.
[34] S. Eve, J. Mohr, Study of the surface modification of the PMMA by UV-radiation, Proc. Eng. 1 (2009) 237–240.
[35] M.M. Qazilbash, M. Brehm, B.-G. Chae, P.-C. Ho, G.O. Andreev, B.-J. Kim, S.J. Yun, A. Balatsky, M. Maple, F. Keilmann, Mott transition in VO_2 revealed by infrared spectroscopy and nano-imaging, Science 318 (2007) 1750–1753.
[36] Y. Kim, S. Yu, J. Park, D. Yoon, A.M. Dayaghi, K.J. Kim, J.S. Ahn, J. Son, High-throughput roll-to-roll fabrication of flexible thermochromic coatings for smart windows with VO_2 nanoparticles, J. Mater. Chem. C 6 (2018) 3451–3458.
[37] M.A. Hussein, R.M. El-Shishtawy, B.M. Abu-Zied, A.M. Asiri, The impact of cross-linking degree on the thermal and texture behavior of poly (methyl methacrylate), J. Therm. Anal. Calorim. 124 (2016) 709–717.
[38] G. Wyszecki, W.S. Stiles, Color Science, Wiley, New York, 1982.
[39] C. Riordan, R. Hulstron, What is an air mass 1.5 spectrum?(Solar cell performance calculations), in: IEEE Conference on Photovoltaic Specialists, IEEE, 1990, pp. 1085–1088.
[40] ASTM D1003-13-Standard Test Method for Haze and Luminous Transmittance of Transparent, ASTM International West Conshohocken, 2013.
[41] C.F. Bohren, D.R. Huffman, Absorption and Scattering of Light by Small Particles, John Wiley & Sons, 2008.
[42] B.J. Park, M.S. Kim, H.J. Choi, Fabrication and magnetorheological property of core/shell structured magnetic composite particle encapsulated with cross-linked poly (methyl methacrylate), Mater. Lett. 63 (2009) 2178–2180.
[43] B.P. Jelle, Accelerated climate ageing of building materials, components and structures in the laboratory, J. Mater. Sci. 47 (2012) 6475–6496.
[44] B.P. Jelle, E. Sveipe, E. Wegger, A. Gustavsen, S. Grynning, J.V. Thue, B. Time, K.R. Lisø, Robustness classification of materials, assemblies and buildings, J. Build. Phys. 37 (2014) 213–245.
[45] R. Eymard, T. Gallouët, R. Herbin, Finite volume methods, Handb. Numer. Anal. 7 (2000) 713–1018.
[46] B.P. Jelle, Solar radiation glazing factors for window panes, glass structures and electrochromic windows in buildings-Measurement and calculation, Sol. Energy Mater. Sol. Cell. 116 (2013) 291–323.
[47] https://maps.nrel.gov/nsrdb-viewer/.
[48] P. Lyons, D. Arasteh, C. Huizenga, Window performance for human thermal comfort, Trans.-Am. Soc. Heat. Refrig. Air Cond. Eng. 106 (2000) 594–604.

Article XII

Yinmo Xie, Xinpeng Zhao, Sohrab A. Mofid, Jianyu Tan, Bjørn Petter Jelle and Ronggui Yang, **Influence of shell materials on the optical performance of VO_2 core-shell nanoparticle-based thermochromic films**, *Materials Today Nano*, (2020) 100102.

Influence of Shell Materials on the Optical Performance of VO_2 Core-Shell Nanoparticle-Based Thermochromic Films

Yinmo Xie[a,b,c], Xinpeng Zhao[c], Sohrab Alex Mofid[c,d], Jianyu Tan[a,b], Bjørn Petter Jelle[d,e], and Ronggui Yang[f,g,*]

[a]*School of Energy Science and Engineering*, *Harbin Institute of Technology*, *Harbin 150001*, *PR China*

[b]*School of New Energy, Harbin Institute of Technology, Weihai 264209*, *PR China*

[c]*Department of Mechanical Engineering, University of Colorado, Boulder, CO 80309, USA*

[d]*Department of Civil and Environmental Engineering, Norwegian University of Science and Technology (NTNU), NO-7491 Trondheim, Norway*

[e]*Department of Materials and Structures, SINTEF Community, NO-7465 Trondheim, Norway.*

[f]*School of Energy and Power Engineering, Huazhong University of Science and Technology, Wuhan 430074, PR China.*

[g]*State Key Laboratory of Coal Combustion, Huazhong University of Science and Technology, Wuhan 430074, PR China*

ABSTRACT

VO_2 nanoparticle-based thermochromic films have shown great promise for applications in smart windows due to their relatively high luminous transmittance and solar modulation ability. In order to improve the lifetime of VO_2 nanoparticles, environmentally stable oxide materials like TiO_2, SiO_2, and ZnO have been utilized as protecting shells. However, the shell material changes the optical performance of the

Corresponding author.

E–mail: ronggui@hust.edu.cn (R.G. Yang).

thermochromic films due to the variation of the dielectric environment of the VO_2 nanoparticles. In this work, the effective medium theory is coupled with the transfer matrix method to study the influence of the optical constants of the shell materials and the shell thickness on the luminous transmittance and solar modulation ability of the VO_2 core-shell nanoparticle-based thermochromic films. The calculation results showed that it is challenging to simultaneously improve both the luminous transmittance and the solar modulation ability of core-shell structures. With the refractive index of the shell material being between 1.6 to 2.3 (e.g., ZnO and Cr_2O_3), there exists an optimal shell thickness to obtain the maximum solar modulation ability. The results reported in this study can be exploited to guide the design and development of high-performance VO_2 core-shell nanoparticle-based thermochromic smart window films.

Keywords: Thermochromic, Smart window, Vanadium dioxide, VO_2, Nanoparticle, Luminous transmittance, Solar modulation

1. Introduction

Vanadium dioxide (VO_2) based thermochromic smart windows can dynamically regulate the solar heat gain by adapting to the change of ambient temperature. This is due to the reversible metal-insulator transition (MIT) of VO_2 at the critical phase transition temperature T_c, which was discovered in 1959 [1]. In 1966, Barker *et al*. [2] showed that the infrared optical properties of VO_2 above and below the transition temperature are different. When the temperature is lower than the critical phase transition temperature ($T < T_c$), VO_2 is in the semiconducting state and is transparent to near -infrared (NIR) spectra of solar radiation. When the temperature is higher than the critical phase transition temperature ($T > T_c$), VO_2 is in the metallic state and becomes translucent in the NIR region [2-4]. VO_2 film has been discussed for window applications since the early 1980s [5-7]. However, as the critical phase transition temperature of bulk crystalline VO_2 is around 68 °C [1], which is not suitable for practical utilization in buildings, much effort has been devoted to lowering its critical phase transition temperature [8-11]. Previous experiments and the first principle theory calculations [12-15] have proven that the incorporation of doping elements such as tungsten and molybdenum are the most effective way to reduce the phase change temperature of VO_2. These make VO_2 a promising thermochromic material for energy-efficient smart window applications. The performance of thermochromic smart windows could be evaluated by two crucial optical performance parameters: 1) luminous (visible) transmittance (τ_{lum}, for wavelengths ranging between 380-780 nm), which represents the transmission of visible light useful for human vision under normal conditions, and 2) solar modulation ability ($\Delta\tau_{sol}$, the difference of solar radiation transmittance τ_{sol} before and after the phase transition for wavelengths ranging between 300-2500 nm), which represents the modulation of solar radiation energy passing

through the window [16, 17].

VO_2 thin films usually possess relatively low τ_{lum} and $\Delta\tau_{sol}$ [18-24]. For example, the experimental study by Mlyuka *et al*. [19] showed that the τ_{lum} and $\Delta\tau_{sol}$ of a 90-nm-thick VO_2 thin-film are only ~ 38% and ~ 6%, respectively. Another study by Taylor *et al.* [24] reported that the highest $\Delta\tau_{sol}$ for a VO_2 thin film is near 15%, but the corresponding τ_{lum} is only ~ 20%. To increase both the τ_{lum} and $\Delta\tau_{sol}$, VO_2 nanoparticle-based composite films in which the VO_2 nanoparticles were randomly dispersed in a transparent matrix were proposed by Li *et al*. [25] in 2010. Their theoretical calculations demonstrated that dilute composites with VO_2 nanoparticles embedded in dielectric hosts could significantly increase the τ_{lum} and $\Delta\tau_{sol}$. In such a way, the effective refractive index of the VO_2 nanocomposite film can be reduced to a much smaller value by employing a host medium with a low refractive index. The reflectance of the nanocomposite film can dramatically decrease, which in turn increases τ_{lum} of the nanocomposite film. Furthermore, the effective refractive index difference between the metallic state and the semiconducting state of the nanocomposite film can also be significantly lowered, which improves the solar modulation ability $\Delta\tau_{sol}$ of the nanocomposite film.

Although randomly dispersing VO_2 nanoparticles in a transparent host matrix with a low refractive index can effectively improve both τ_{lum} and $\Delta\tau_{sol}$, VO_2 nanoparticles can be easily oxidized to non-switchable V_2O_5, reducing the $\Delta\tau_{sol}$ of the nanoparticle-based thermochromic films [26, 27]. To increase the lifetime of VO_2 nanoparticles, a protective shell layer such as TiO_2, ZnO, and SiO_2 was used to prevent the VO_2 nanoparticle from oxygen and vapor exposure in ambient air [26, 28-31]. However, due to the change of the dielectric environment of VO_2 nanoparticles, the optical

performance of VO_2 core-shell nanoparticle-based thermochromic nanocomposite film also changes. For example, Li *et al*. [29] showed that an addition of 1-nm-thick TiO_2 shell layer reduced the $\Delta\tau_{sol}$ of a VO_2 nanorods-based film from ~ 12% to ~ 10%. In another study, Chen *et al*. [30] reported an ~ 2% increase in the $\Delta\tau_{sol}$ when a 15-nm-thick ZnO shell layer was employed to enhance the durability of VO_2 nanoparticles. However, a systematic study on the influence of the optical constants and the thickness of various shell materials on the optical performance of VO_2 core-shell nanoparticle-based thermochromic films is still lacking.

In this work, the effective medium theory was coupled with the transfer matrix method to evaluate the influence of shell material, including the optical constants and the shell thickness, on the optical performance of the VO_2 core-shell nanoparticle-based thermochromic films. Our results show that it is difficult to simultaneously improve both the luminous transmittance and solar modulation ability with the core-shell nanoparticles. With the refractive index of the shell material being between 1.6 to 2.3 (e.g., ZnO and Cr_2O_3), there exists an optimal shell thickness to obtain the maximum solar modulation ability. The results reported in this study can be exploited to guide the design and development of high-performance VO_2 core-shell nanoparticle-based thermochromic smart window films.

2. Modeling methodology

Figure 1 illustrates a smart window where a glass window is covered with a VO_2 core-shell nanoparticle-based thermochromic film that modulates the spectral transmittance. In the thermochromic nanocomposite film, a low volume fraction (~ 0.01)

of VO_2 core-shell nanoparticles are uniformly distributed in a transparent host medium. Figure 1a illustrates the case when the temperature of VO_2 nanoparticles T is higher than the critical phase transition temperature T_c ($T > T_c$). The VO_2 nanoparticle is in the metallic state and the NIR spectral transmittance is low due to the high NIR reflectance and absorbance of the metallic VO_2, while maintaining a high transmittance in the visible region. When $T < T_c$, the VO_2 nanoparticles are in the semiconducting state, and both the NIR and visible spectral transmittance are high due to the weak NIR absorption of semiconducting VO_2, as depicted in Fig. 1b.

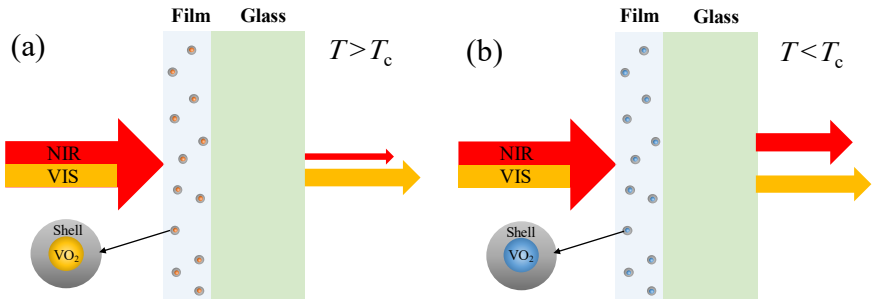

Fig. 1. Schematic illustration of the spectral transmittance modulation of VO_2 core-shell nanoparticle-based thermochromic smart window. (a) When $T > T_c$, VO_2 is in the metallic state and the NIR transmittance is low due to the high NIR reflectance and absorbance of metallic VO_2. (b) When $T < T_c$, VO_2 is in the semiconducting state and the NIR transmittance is high due to the low absorbance of semiconducting VO_2.

The optical performance of the thermochromic smart window films is quantified by the luminous transmittance τ_{lum} and solar modulation ability $\Delta\tau_{sol}$ defined as

$$\tau_{lum}(T) = \frac{\int_{380}^{780} \varphi_{lum}(\lambda)\tau(\lambda,T)d\lambda}{\int_{380}^{780} \varphi_{lum}(\lambda)d\lambda} \quad (1)$$

$$\tau_{\mathrm{sol}}(T)=\frac{\int_{300}^{2500}\varphi_{\mathrm{sol}}(\lambda)\tau(\lambda,T)\,d\lambda}{\int_{300}^{2500}\varphi_{\mathrm{sol}}(\lambda)\,d\lambda} \tag{2}$$

$$\Delta\tau_{\mathrm{sol}}=\tau_{\mathrm{sol}}(T<T_c)-\tau_{\mathrm{sol}}(T>T_c) \tag{3}$$

where $\tau(\lambda)$ represents the transmittance at wavelength λ, $\varphi_{\mathrm{lum}}(\lambda)$ is the standard luminous efficiency function for vision (380–780 nm) [32, 33], and $\varphi_{\mathrm{sol}}(\lambda)$ is the solar irradiance spectrum at air mass 1.5 (AM 1.5) [34].

Since the thickness of glass (several millimeters) is much larger than that of VO_2 core-shell nanoparticle-based thermochromic film (a few microns or less), the glass can be modeled as a semi-infinitely thick layer in our calculations. To calculate the spectral transmittance, the transfer matrix method [35, 36] is used to simulate the light propagation through the VO_2 core-shell nanoparticle-based thermochromic nanocomposite film and the glass window. It should be noted that the effective optical constants (complex refractive index $m = n + ik$, n is refractive index and k is extinction coefficient, or complex dielectric function $\varepsilon=\varepsilon'+i\varepsilon''=m^2$) of the nanocomposite film are required for the transfer matrix method calculation. Here, we assume that the diameter of the nanoparticles and the thickness of the coatings are much smaller than the wavelength of the incident light, thus the Maxwell-Garnett (MG) effective medium approximation theory [37, 38] can be applied to calculate the effective optical constants with a small volumetric fraction of the core-shell nanoparticles [39, 40]. According to Li *et al.* [41] and Bergman [42], the effective optical constants can be calculated from the known optical constants of the core, shell and the host medium materials by using the MG effective medium approximation theory. Because a core-shell nanoparticle can be considered as an inclusion (core with dielectric function ε_{c}) in a host medium (shell with dielectric function ε_{s}), the effective complex dielectric function $\varepsilon_{\mathrm{c\text{-}s}}$ of the core-

shell nanoparticle can be calculated by

$$\frac{\varepsilon_{\text{c-s}}-\varepsilon_s}{\varepsilon_{\text{c-s}}+2\varepsilon_s}=f_{\text{c}}\frac{\varepsilon_{\text{c}}-\varepsilon_s}{\varepsilon_{\text{c}}+2\varepsilon_s} \quad (4),$$

where f_{c} is the filling factor that in the case of a spherical core-shell, which is given by

$$f_{\text{c}}=\left[R_{\text{core}}/\left(R_{\text{core}}+t_{\text{shell}}\right)\right]^3.$$

The effective complex dielectric function of a nanocomposite film which is comprised of core-shell spherical nanoparticles with a host medium is then given by

$$\frac{\varepsilon_{\text{film}}-\varepsilon_{\text{m}}}{\varepsilon_{\text{film}}+2\varepsilon_{\text{m}}}=f_{\text{c-s}}\frac{\varepsilon_{\text{c-s}}-\varepsilon_{\text{m}}}{\varepsilon_{\text{c-s}}+2\varepsilon_{\text{m}}} \quad (5)$$

Here, $f_{\text{c-s}}$ is the filling factor, i.e., the volume fraction of the core-shell nanoparticles. $\varepsilon_{\text{film}}$ and ε_{m} are the effective complex dielectric function of the core-shell nanocomposite film and the complex dielectric function of the host medium, respectively. After the effective optical constants of the VO_2 core-shell nanoparticle-based film being calculated using Eqs. (4) and (5), the transfer matrix method calculations are performed to calculate the optical performance of the VO_2 core-shell nanoparticle-based thermochromic films.

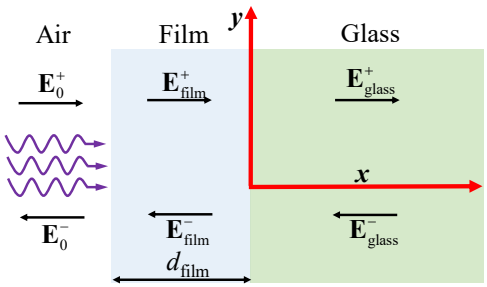

Fig. 2. Schematic of the electromagnetic wave propagation through the thermochromic nanocomposite film covered on a window glass pane. The electric field at any point is represented by two components: one propagating in the positive and one in the negative *x* direction, which are denoted by $\mathbf{E}^+$ and $\mathbf{E}^-$, respectively.

Consider a plane wave incident from left at a nanocomposite film between a semi-infinite transparent ambient and a semi-infinite glass substrate as schematically described in Fig. 2. The optical electric field at any point in the system can be resolved into two components: one component propagating in the positive x direction and one in the negative x direction, which are denoted by $\mathbf{E}^+$ and $\mathbf{E}^-$, respectively. Spectral transmittance of the nanocomposite film can be obtained by $\tau=|t|^2$, where t is the total complex transmission coefficient and can be calculated by [36]

$$t=\frac{\mathbf{E}_{\text{glass}}^{+}}{\mathbf{E}_{0}^{+}}=\frac{1}{S_{11}} \tag{6}$$

In Eq. (6), $\mathbf{E}_{\text{glass}}^{+}$ and $\mathbf{E}_{0}^{+}$ are the electric field propagating in the positive x direction at glass substrate side and ambient side, respectively. S_{11} denotes a matrix element of the system transfer matrix $\mathbf{S}_{\text{film}}$, which relates the electric field at the ambient side and the glass substrate side by

$$\begin{bmatrix}\mathbf{E}_{0}^{+}\\ \mathbf{E}_{0}^{-}\end{bmatrix}=\mathbf{S}_{\text{film}}\begin{bmatrix}\mathbf{E}_{\text{glass}}^{+}\\ \mathbf{E}_{\text{glass}}^{-}\end{bmatrix} \tag{7}$$

The system transfer matrix $\mathbf{S}_{\text{film}}$ of the nanocomposite film can be expressed by using the interface matrix (matrix of refraction) $\mathbf{I}$ and the layer matrix (phase matrix) $\mathbf{L}$ as

$$\mathbf{S}_{\text{film}}=\begin{bmatrix}S_{11} & S_{12}\\ S_{21} & S_{22}\end{bmatrix}=\mathbf{I}_{\text{air-film}}\cdot\mathbf{L}_{\text{film}}\cdot\mathbf{I}_{\text{film-glass}} \tag{8}$$

The interface matrix $\mathbf{I}$ is described by

$$\mathbf{I}_{jk}=\frac{1}{t_{jk}}\begin{bmatrix}1 & r_{jk}\\ r_{jk} & 1\end{bmatrix} \tag{9}$$

where t_{jk} and r_{jk} are the Fresnel complex transmittance and reflectance coefficients at

interface *jk*, and both can be easily calculated by using the optical constants of each layer (ambient air, nanocomposite film, and glass) and the incident angle in the ambient (0° is this work).

The layer matrix which describes the change of phase while the light propagating through the nanocomposite film layer is described by

$$\mathbf{L}_{\text{film}} = \begin{bmatrix} e^{-i\xi_{\text{film}}d_{\text{film}}} & 0 \\ 0 & e^{i\xi_{\text{film}}d_{\text{film}}} \end{bmatrix} \tag{10}$$

where

$$\xi_{\text{film}} = \frac{2\pi}{\lambda}\left[m_{\text{film}}^2 - n_0^2 \sin^2 \phi_0\right]^{1/2} \tag{11}$$

and m_{film} is the effective complex refractive index of the core-shell nanocomposite film, n_0 is the refractive index of the ambient, ϕ_0 is the incident angle in the ambient. Note that the incident angle is 0° in all the simulations in this work.

Furthermore, to study how the shell thickness influences the optical performance of the VO_2 core-shell nanoparticle-based thermochromic film, we defined the relative shell thickness (α) of the core-shell nanoparticle as the thickness of the shell divided by the radius of the core, i.e., $\alpha = t_{\text{shell}}/R_{\text{core}}$. The optical constants of VO_2 in different phase states applied in the calculations were taken from Mlyuka *et al*. [19], as shown in Fig. 3. Since polymers are the most commonly used materials as the transparent embedding host medium of the VO_2 nanoparticle-based film, and many of them have refractive index near 1.5 [e.g., PDMS (~1.43), PMMA (~1.48), and PVP (~1.52)], the optical constants of the transparent embedding host medium in this work is set as $m = 1.5$.

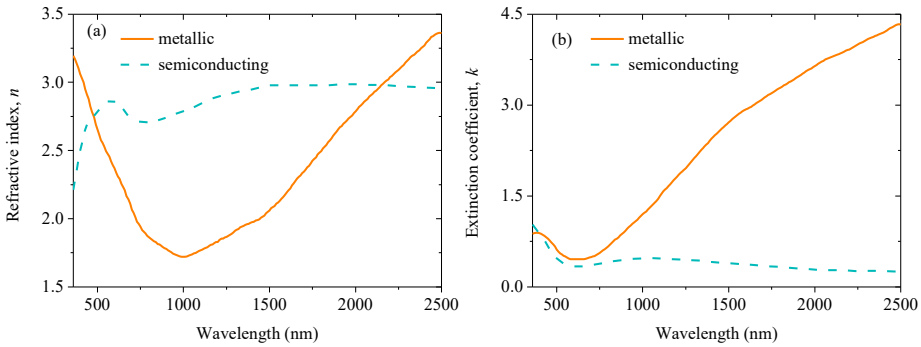

Fig. 3. The optical constants of VO_2 as applied in this work, adapted from Mlyuka *et. al*. [19].

3. Results and discussion

3.1 Model validation

To verify the MG effective medium theory adopted in this work, we compared the transmittances of the metallic state VO_2 nanoparticle-based films from MG effective medium theory with the results from finite-difference time-domain (FDTD) method in Fig. 4, in which the volume fraction of the VO_2 nanoparticles is 0.01, and the film thickness is 5 μm. With regard to the particle diameter, our previous experimental study showed that the average diameters of the VO_2 nanoparticles that we were able to fabricate were in the range of 50 nm to 80 nm [27], where we randomly chose 70 nm which locates in this region as the diameter of VO_2 nanoparticle in the FDTD simulation. Moreover, previous work by Ji *et al.* [43] also shows that VO_2 powder with an average size of less than 20 nm and narrow size distribution has been obtained by pre-reduction and hydrothermal treatment. As Fig. 4 shows, the results from MG effective medium theory agrees well with that of the FDTD simulation. Hence, we are confident that the calculated results from the MG effective medium theory used in this work are reliable.

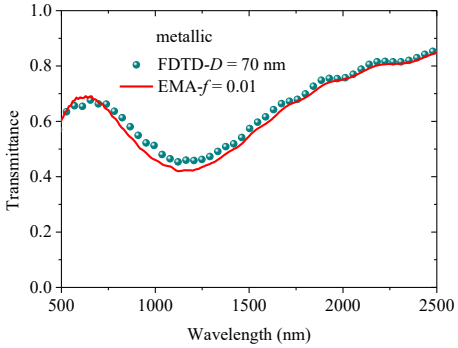

Fig. 4. Transmittances of the metallic state VO_2 nanoparticle-based films from both the MG effective medium theory and the FDTD simulation, in which the volume fraction of VO_2 nanoparticles (diameter 70 nm) and the film thickness are assumed to be 0.01 and 5 μm, respectively.

3.2 Effect of optical constants of the shell

The spectral transmittance of the VO_2 core-shell nanoparticle-based thermochromic film depends on the optical constants of VO_2 and the shell material, nanoparticle volume fraction, relative shell thickness and the thin-film thickness. In this work, we set the volume fraction at 0.01 and thin film thickness at 5 μm for our calculations and then investigated how the refractive index of the shell material affects the optical performance of the nanocomposite film. The effective refractive index and effective extinction coefficient of a VO_2 core-shell nanocomposite film, with a relative shell thickness of 0.2, as a function of wavelength and shell refractive index, are shown in Fig. 5. The complex refractive index of the shell material is changed from 1 to 3 with an interval of 0.5. Figures 5a and 5b show that the effective refractive index increases with the increasing shell complex refractive index in both the metallic phase state and the semiconducting phase state. However, the effective extinction coefficient of the VO_2 core-shell nanocomposite film does not show monotonic change for all wavelengths

with increasing shell complex refractive index. Figure 5c shows that in the metallic VO_2 phase, the effective extinction coefficient increases when the shell complex refractive index increases from 1 to 2 in the wavelength range below approximately 1400 nm, whereas the effective extinction coefficient decreases when the shell complex refractive index increases from 2 to 3 in this wavelength range below approximately 1400 nm (and opposite above 1400 nm, see Fig. 5). Figure 5d shows that the change of effective extinction coefficient in the semiconducting VO_2 phase can be negligible for a shell complex refractive index larger than 1.5 as compared to the change in the metallic VO_2 phase.

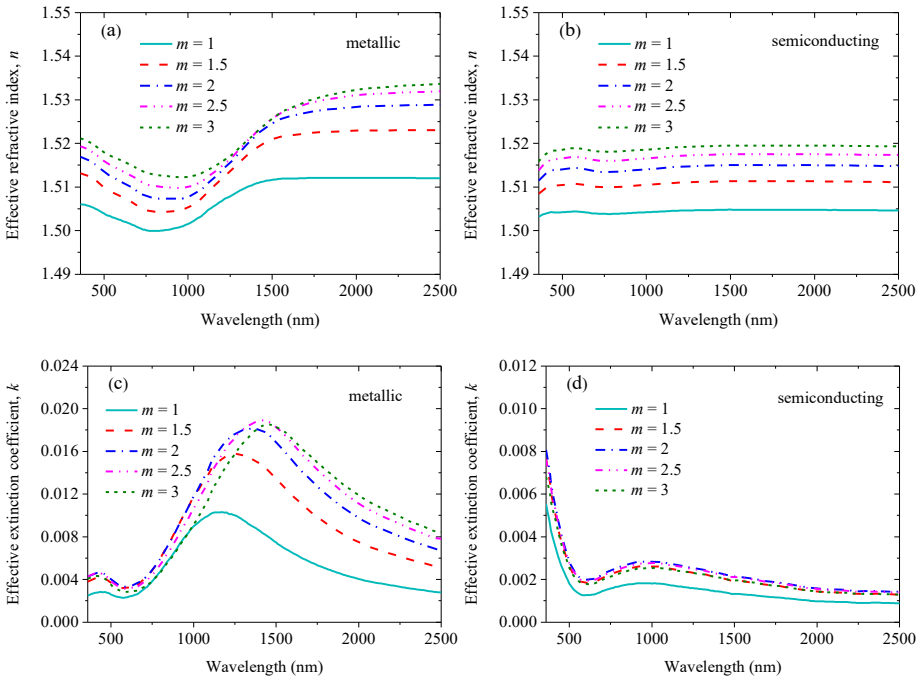

Fig. 5. Effective refractive index of metallic state (a) and semiconducting state (b), and effective extinction coefficient of metallic state (c) and semiconducting state (d), of a VO_2 core-shell nanocomposite film as a function of wavelength and shell complex refractive index *m*. Here the relative shell thickness is assumed to be 0.2.

Figure 6 shows the results for the transmittance of the thermochromic films, with a relative shell thickness of 0.2, as a function of the shell complex refractive index and the wavelength. The spectral transmittance of the thin film with a shell complex refractive index of 1 is much larger than that of 1.5 in the entire wavelength range. Figure 6a shows that in the metallic VO_2 phase, the transmittance dramatically decreases when going from a wavelength of 1000 nm to 1300 nm due to the large absorption induced by the plasmonic resonance of metallic VO_2. When the shell complex refractive index increases from 1.5 to 2, the transmittance of the nanocomposite film decreases in the whole wavelength range from 1100 nm to 2500 nm, but the decrease of the transmittance is very small when the wavelength is below 1100 nm. With the shell complex refractive index increasing from 2 to 3, the transmittance in the wavelength range from 1400 nm to 2500 nm drops further and the transmittance increases in the wavelength below 1400 nm. This may be attributed to the change of the effective extinction coefficient of the VO_2 core-shell nanocomposite, induced by the variation of the shell complex refractive index. The effective extinction coefficient increases as the shell complex refractive index increases from 1 to 2, but decreases as the shell complex refractive index increases from 2 to 3 in the wavelength range below 1400 nm (as shown in Fig. 5c). Figure 6b shows that in the semiconducting state, the change of the spectral transmittance is rather small for a shell complex refractive index larger than 1.5 as the changes of the effective extinction coefficient is relatively small (as shown in Fig. 5).

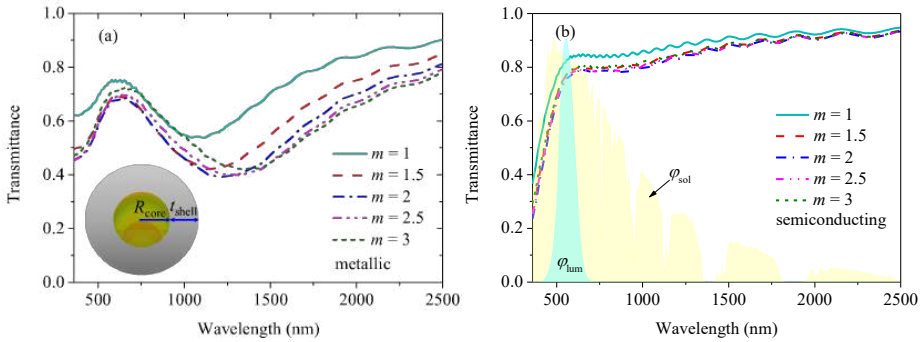

Fig. 6. Spectral transmittance of VO_2 core-shell nanoparticle-based film, in the case of (a): $T > T_c$ (VO_2 is in the metallic state); and (b): $T < T_c$ (VO_2 is in the semiconducting state). The standard luminous efficiency function for vision, φ_{lum}, and the solar irradiance spectrum at air mass 1.5 (AM 1.5), φ_{sol}, are also plotted in Fig. 6b.

Figure 7 shows the luminous transmittance and the solar modulation ability of the VO_2 core-shell nanoparticle-based thermochromic films as a function of the refractive index of the shell material. Figure 7a shows that for both metallic and semiconducting states of VO_2 the τ_{lum} of the nanocomposite films decreases first and then increases when the shell refractive index increases from 1 to 3. This is because of the increased reflectance and absorbance induced by the increased effective refractive index and effective extinction coefficient when the shell complex refractive index increases from 1 to 2. However, when complex refractive index of the shell is above 2, the absorbance in the visible range begins to decrease due to the decrease of the effective extinction coefficient in the visible region (as shown in Fig. 5c).

To guide the reading in Fig. 7, two dashed lines representing the τ_{lum} of the uncoated VO_2 nanoparticle-based film under two different VO_2 phase states are drawn to show the enhanced or weakened trend of the τ_{lum} of the VO_2 core-shell nanoparticle-based film. It is shown that only a low refractive index (less than 1.5) can significantly

enhance the τ_{lum} of the nanocomposite film, and there exists a minimum τ_{lum} when the shell refractive index is near 2.1. Four different oxides materials, SiO_2, TiO_2, Cr_2O_3, and ZnO were analyzed to study the influence of commonly used oxides on the optical performance of VO_2 core-shell nanoparticle-based thermochromatic films. The optical constants of these oxides are obtained from Palik [44], and Kuhaili and Durranni [45]. Figure 7a shows that among the four oxides, SiO_2 can slightly enhance the τ_{lum} of VO_2 core-shell nanoparticle-based film for both metallic and semiconducting phase states of VO_2, due to its relatively low refractive index to the host medium and its near-zero extinction coefficient in the visible range. τ_{lum} of the VO_2@Cr_2O_3 nanoparticle-based film is smaller than that of non-absorbing shell material for both metallic and semiconducting phase states of VO_2, due to the relatively high extinction coefficient of the Cr_2O_3 in the visible range.

Figure 7b shows that the influence of the shell refractive index on $\Delta\tau_{sol}$ is relatively smaller than that on the τ_{lum}. Only when the shell refractive index is in the range of 1.6 to 2.3, is the $\Delta\tau_{sol}$ larger than that of the case without shell. Indeed, the improvement is quite negligible (< 3%). Therefore, it is challenging to simultaneously improve, i.e. increase, the luminous transmittance and the solar modulation ability using the VO_2@shell nanoparticle structure. Similar conclusions were also made by previous research studies. For example, Li *et al.* [41] found that moderately thin-walled hollow spherical VO_2 nanoshells could enable a higher solar modulation ability than solid nanoparticles, however, the luminous transmittance becomes lower. Among the four oxides studied, ZnO and Cr_2O_3 enhance $\Delta\tau_{sol}$ due to their suitable refractive indices, while SiO_2 and TiO_2 have a slightly lower $\Delta\tau_{sol}$ compared to the uncoated case. We should note that Fig. 7 only gives the tendency of the influence of the shell refractive index on τ_{lum} and $\Delta\tau_{sol}$ of VO_2 core-shell nanoparticle-based film, at a volume fraction

of VO_2 nanoparticles of 0.01, relative shell thickness of 0.2, and the film thickness of 5μm. However, the specific enhanced or weakened value can also be adjusted by changing the volume fraction of the VO_2 core-shell nanoparticles, the shell thickness, and the thickness of the nanocomposite film.

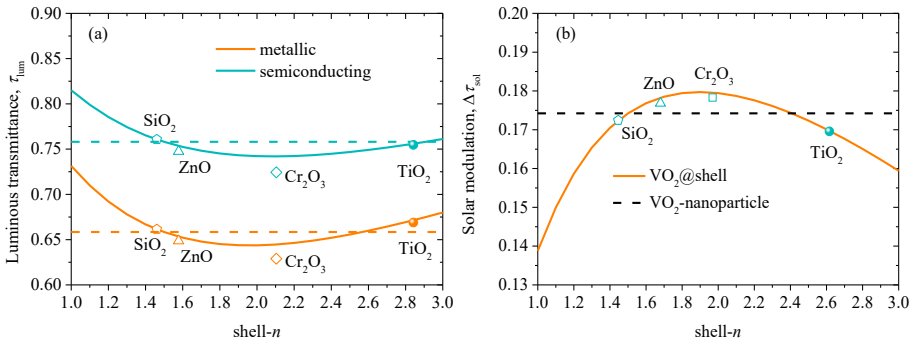

Fig. 7. Luminous transmittance (a) and solar modulation ability (b) of a VO_2 core-shell nanoparticle-based film, as a function of shell refractive index. The performance of the VO_2 nanoparticle film without shell is depicted by the dashed lines. The performance of the VO_2 core-shell nanoparticle-based film with non-absorbing shell materials are shown by the solid lines.

3.3 Effect of shell thickness

Figures 8a and 8b show the relation between the optical performance parameters and the relative shell thickness. The τ_{lum} of the VO_2@SiO_2 nanoparticle-based thermochromic film can be slightly increased for both metallic and semiconducting phase states of VO_2 when the relative shell thickness increases because SiO_2 is non-absorbing. However, both the τ_{lum} of the VO_2@ZnO and VO_2@Cr_2O_3, nanoparticle-based films monotonically decrease as the relative shell thickness increases, with τ_{lum} of the VO_2@Cr_2O_3 nanoparticle-based film decreasing the fastest. This is mainly because Cr_2O_3 does not only have a high extinction coefficient in the visible range but

also has a refractive index close to 2.1. The τ_{lum} of the VO_2@TiO_2 nanoparticle-based film can be slightly increased for metallic phase state of VO_2 and slightly decreased for semiconducting state of VO_2 when the relative shell thickness increases.

Fig. 8c shows that using ZnO and Cr_2O_3 as shell material can increase the $\Delta\tau_{sol}$ of VO_2 core-shell nanoparticle-based film as a result of their suitable refractive indices. However, this advantage is gradually lost with the increase of a relative shell thickness due to the increase of the dissipation associated with their extinction coefficients. Therefore, there exists an optimal relative shell thickness to obtain the largest $\Delta\tau_{sol}$. In a recent experimental study, Chen *et al*. [30] showed that for the VO_2@ZnO nanoparticle-based film, there exists a maximum $\Delta\tau_{sol}$ as the relative shell thickness changes, which is consistent with our calculation results. However, Chen *et al*. [30] also showed that τ_{lum} of the VO_2@ZnO nanoparticle-based film is also increased compared to the uncoated case. The $\Delta\tau_{sol}$ of the VO_2@SiO_2 nanoparticle-based film is close to the $\Delta\tau_{sol}$ for the uncoated VO_2 nanoparticle-based film and the change with the shell thickness is negligible. The $\Delta\tau_{sol}$ of the VO_2@TiO_2 nanoparticle-based film is smaller than $\Delta\tau_{sol}$ for the uncoated case and decreases with increasing shell thickness. In short, to increase the $\Delta\tau_{sol}$, a low absorption material with a refractive index in the range between 1.6 to 2.3, such as ZnO should be selected, whereas the relative shell thickness should be controlled in the range between 0.1 to 0.3 to maintain a high τ_{lum}.

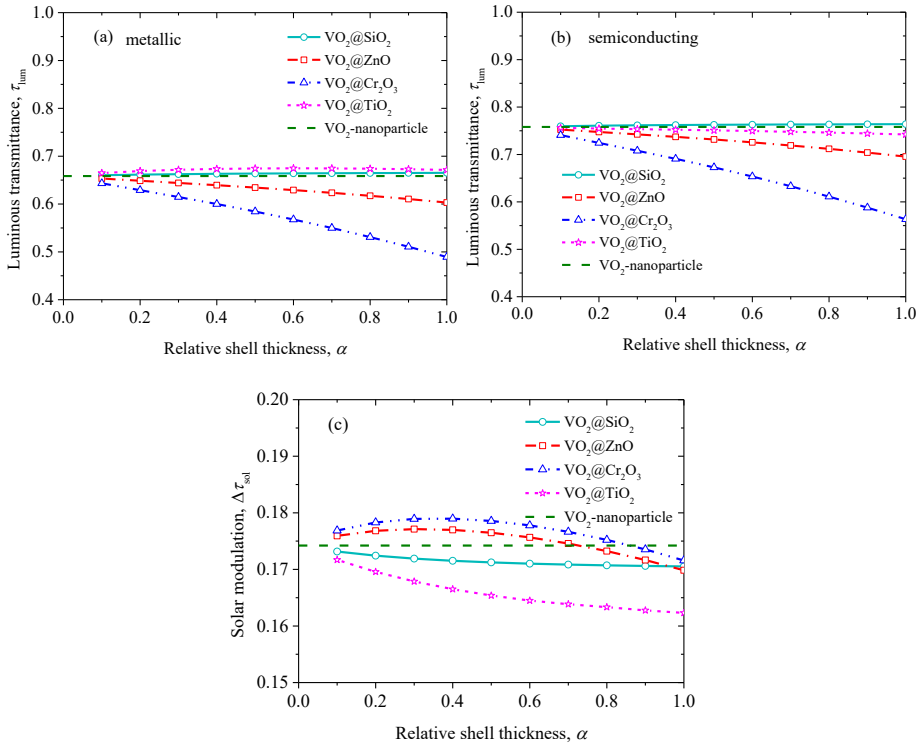

Fig. 8. Luminous transmittance of the metallic state (a) and the semiconducting state (b), and solar modulation ability (c) for different VO_2 core-shell nanoparticle-based films. The performance of the uncoated case is shown by the dashed line.

3.4 Effects of volume fraction of nanoparticle and film thickness

To illustrate the effect of volume fraction of VO_2 core-shell nanoparticles on the optical performance of a nanocomposite film, we take a VO_2@ZnO nanoparticle as an example for calculation, where the relative shell thickness is 0.2 and the film thickness is fixed at 5 μm. Figures 9a and 9b present the variation of the luminous transmittance and the solar modulation ability of the VO_2 core-shell nanoparticle-based thermochromic films as a function of the volume fraction of VO_2 nanoparticles. As Figure 9a shows, the luminous transmittance of the nanocomposite films decreases with

the increasing volume fraction of the nanoparticles for both the metallic and semiconducting phase states of VO_2. Due to the shadow effect between the nanoparticles in the film, we notice that the decrease rate of the τ_{lum} becomes smaller when the volume fraction of the VO_2 nanoparticles is larger than 0.03. From Fig. 9b, it can be seen that the solar modulation ability of the nanoparticle composite film first increases before the volume fraction of the VO_2 nanoparticles reaches 0.03, and then decreases as the volume fraction of the VO_2 nanoparticles continue to increase. Therefore, when the volume fraction of the VO_2 nanoparticles is too large (above 0.03 in this case), increasing the volume fraction of the VO_2 nanoparticles reduces both the luminous transmittance and the solar modulation ability of VO_2 core-shell nanoparticle-based thermochromic films.

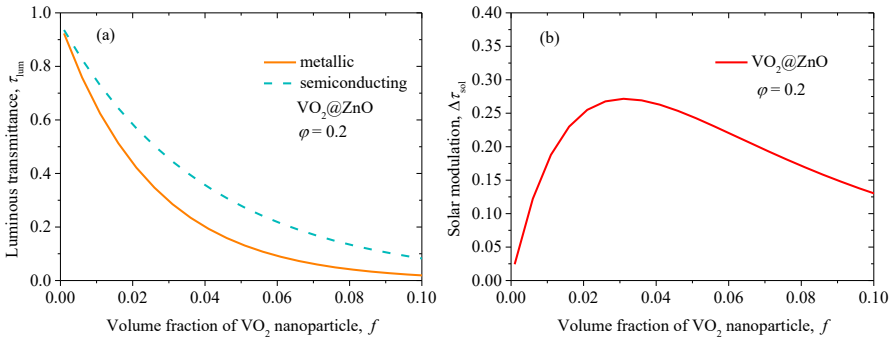

Fig. 9. Luminous transmittance (a) and solar modulation ability (b) of a VO_2 core-shell nanoparticle-based film, as a function of volume fraction of the VO_2 nanoparticles, in which the film thickness is 5 μm.

Figure 10 shows the variation of the luminous transmittance and the solar modulation ability of the VO_2@ZnO nanoparticle-based thermochromic films as a

function of the film thickness, in which the relative shell thickness is 0.2, and the volume fraction of the VO_2 nanoparticles is 0.01. From Fig. 10a and 10b, we can see that the influence of the film thickness on the luminous transmittance and the solar modulation ability of the nanocomposite film is similar to that of the volume fraction of the VO_2 nanoparticles. The luminous transmittance of the nanocomposite film decreases with increasing film thickness for the VO_2 in both the metallic and the semiconducting phase states. The solar modulation ability of the nanocomposite film increases with increasing film thickness when the film thickness is below 12 μm. However, a further increase of the film thickness (above 12 μm) cannot improve the solar modulation ability.

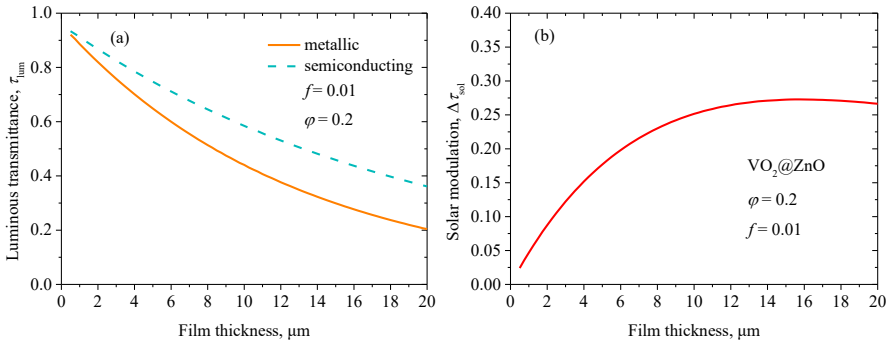

Fig. 10. Luminous transmittance (a) and solar modulation ability (b) of a VO_2 core-shell nanoparticle-based film, as a function of film thickness, in which the volume fraction of the VO_2 nanoparticle is 0.01.

4. Conclusions

In summary, the effective medium theory coupled with the transfer matrix method is used to study the influence of the optical constants of shell materials, shell thickness, volume fraction of VO_2 nanoparticles, and film thickness, on the luminous

transmittance and the solar modulation ability of VO_2 core-shell nanoparticle-based thermochromic films. It is shown that the shell refractive index can significantly affect the luminous transmittance, while its influence on the solar modulation ability is negligible. The luminous transmittance could be enhanced by applying a shell refractive index less than that of the host medium, such as e.g. SiO_2. With the refractive index of the shell material being between 1.6 to 2.3 (e.g., ZnO and Cr_2O_3), there exists an optimal relative shell thickness of 0.3 to obtain the maximum solar modulation ability. The luminous transmittance of the film decreases with the increase of the volume fraction of VO_2 nanoparticles or the film thickness. However, the solar modulation ability of the nanocomposite film only increases when the volume fraction of the VO_2 nanoparticles or the film thickness is below a certain value, above which a further increase of the volume fraction of the VO_2 nanoparticles or the film thickness cannot improve/increase the solar modulation ability. The results reported in this work may be used to guide the design and development of high-performance VO_2 core-shell nanoparticle-based thermochromic smart window films.

Acknowledgements

Yinmo Xie acknowledges the financial support from the program of the China Scholarships Council (No. 201806120168) for him to study as a visiting student at University of Colorado, Boulder, USA. The involvement of research scientists from Norway is supported by the Research Council of Norway within the Nano2021 program through the SINTEF and NTNU research project “High-Performance Nano Insulation Materials” (Hi-Per NIM, project no. 250159).

REFERENCES

[1] F. Morin, Oxides which show a metal-to-insulator transition at the Neel temperature, Physical review letters, 3 (1959) 34.

[2] A. Barker Jr, H. Verleur, H. Guggenheim, Infrared optical properties of vanadium dioxide above and below the transition temperature, Physical Review Letters, 17 (1966) 1286.

[3] Q. Hao, W. Li, H. Xu, J. Wang, Y. Yin, H. Wang, L. Ma, F. Ma, X. Jiang, O.G. Schmidt, VO_2/TiN Plasmonic Thermochromic Smart Coatings for Room-Temperature Applications, Advanced materials, 30 (2018) 1705421.

[4] Y. Ke, X. Wen, D. Zhao, R. Che, Q. Xiong, Y. Long, Controllable fabrication of two-dimensional patterned VO_2 nanoparticle, nanodome, and nanonet arrays with tunable temperature-dependent localized surface plasmon resonance, ACS nano, 11 (2017) 7542-7551.

[5] C.B. Greenberg, Undoped and doped VO_2 films grown from $VO(OC_3H_7)_3$, Thin solid films, 110 (1983) 73-82.

[6] G. Jorgenson, J. Lee, Doped vanadium oxide for optical switching films, Solar Energy Materials, 14 (1986) 205-214.

[7] S. Babulanam, T. Eriksson, G. Niklasson, C. Granqvist, Thermochromic VO_2 films for energy-efficient windows, Solar energy materials, 16 (1987) 347-363.

[8] S. Hu, S.-Y. Li, R. Ahuja, C.-G. Granqvist, K. Hermansson, G.A. Niklasson, R.H. Scheicher, Optical properties of Mg-doped VO_2: Absorption measurements and hybrid functional calculations, Applied Physics Letters, 101 (2012) 201902.

[9] W. Burkhardt, T. Christmann, S. Franke, W. Kriegseis, D. Meister, B. Meyer, W. Niessner, D. Schalch, A. Scharmann, Tungsten and fluorine co-doping of VO_2 films, Thin Solid Films, 402 (2002) 226-231.

[10] S. Chen, Z. Wang, L. Fan, Y. Chen, H. Ren, H. Ji, D. Natelson, Y. Huang, J. Jiang, C. Zou, Sequential insulator-metal-insulator phase transitions of VO_2 triggered by hydrogen doping, Physical Review B, 96 (2017) 125130.

[11] G. Khan, K. Asokan, B. Ahmad, Room temperature tunability of Mo-doped VO_2 nanofilms across semiconductor to metal phase transition, Thin Solid Films, 625 (2017) 155-162.

[12] J. Zhang, H. He, Y. Xie, B. Pan, Theoretical study on the tungsten-induced reduction of transition temperature and the degradation of optical properties for VO_2, The Journal of chemical physics, 138 (2013) 114705.

[13] L. Hu, H. Tao, G. Chen, R. Pan, M. Wan, D. Xiong, X. Zhao, Porous W-doped VO_2 films with

simultaneously enhanced visible transparency and thermochromic properties, Journal of Sol-Gel Science and Technology, 77 (2016) 85-93.

[14] L. Mai, B. Hu, T. Hu, W. Chen, E. Gu, Electrical property of Mo-doped VO_2 nanowire array film by melting− quenching sol− gel method, The Journal of Physical Chemistry B, 110 (2006) 19083-19086.

[15] D. Li, M. Li, J. Pan, Y. Luo, H. Wu, Y. Zhang, G. Li, Hydrothermal synthesis of Mo-doped VO_2/TiO_2 composite nanocrystals with enhanced thermochromic performance, ACS applied materials & interfaces, 6 (2014) 6555-6561.

[16] Y. Cui, Y. Ke, C. Liu, Z. Chen, N. Wang, L. Zhang, Y. Zhou, S. Wang, Y. Gao, Y. Long, Thermochromic VO_2 for energy-efficient smart windows, Joule, 2 (2018) 1707-1746.

[17] I. Balin, V. Garmider, Y. Long, I. Abdulhalim, Training artificial neural network for optimization of nanostructured VO_2-based smart window performance, Optics express, 27 (2019) A1030-A1040.

[18] S.-Y. Li, G.A. Niklasson, C.-G. Granqvist, Thermochromic fenestration with VO_2-based materials: Three challenges and how they can be met, Thin Solid Films, 520 (2012) 3823-3828.

[19] N.R. Mlyuka, G.A. Niklasson, C.G. Granqvist, Thermochromic VO_2- based multilayer films with enhanced luminous transmittance and solar modulation, physica status solidi (a), 206 (2009) 2155-2160.

[20] F. Xu, X. Cao, H. Luo, P. Jin, Recent advances in VO_2-based thermochromic composites for smart windows, Journal of Materials Chemistry C, 6 (2018) 1903-1919.

[21] C.G. Granqvist, Oxide-based chromogenic coatings and devices for energy efficient fenestration: brief survey and update on thermochromics and electrochromics, Journal of Vacuum Science & Technology B, Nanotechnology and Microelectronics: Materials, Processing, Measurement, and Phenomena, 32 (2014) 060801.

[22] Y. Ji, A. Mattsson, G.A. Niklasson, C.G. Granqvist, L. Österlund, Synergistic TiO_2/VO_2 Window Coating with Thermochromism, Enhanced Luminous Transmittance, and Photocatalytic Activity, Joule, (2019).

[23] Y. Gao, H. Luo, Z. Zhang, L. Kang, Z. Chen, J. Du, M. Kanehira, C. Cao, Nanoceramic VO_2 thermochromic smart glass: A review on progress in solution processing, Nano Energy, 1 (2012) 221-246.

[24] A. Taylor, I. Parkin, N. Noor, C. Tummeltshammer, M.S. Brown, I. Papakonstantinou, A bioinspired solution for spectrally selective thermochromic VO_2 coated intelligent glazing, Optics express, 21 (2013) A750-A764.

[25] S.-Y. Li, G.A. Niklasson, C.-G. Granqvist, Nanothermochromics: calculations for VO_2 nanoparticles in dielectric hosts show much improved luminous transmittance and solar energy transmittance modulation, Journal of Applied Physics, 108 (2010) 063525.

[26] Y. Gao, S. Wang, H. Luo, L. Dai, C. Cao, Y. Liu, Z. Chen, M. Kanehira, Enhanced chemical stability of VO_2 nanoparticles by the formation of SiO_2/VO_2 core/shell structures and the application to transparent and flexible VO_2-based composite foils with excellent thermochromic properties for solar heat control, Energy & Environmental Science, 5 (2012) 6104-6110.

[27] X. Zhao, S. Mofid, T. Gao, G. Tan, B.P. Jelle, X. Yin, R. Yang, Durability-enhanced vanadium dioxide thermochromic film for smart windows, Materials Today Physics, 13 (2020) 100205.

[28] K.P. Velikov, A. van Blaaderen, Synthesis and characterization of monodisperse core- shell colloidal spheres of zinc sulfide and silica, Langmuir, 17 (2001) 4779-4786.

[29] Y. Li, S. Ji, Y. Gao, H. Luo, M. Kanehira, Core-shell $VO_2@TiO_2$ nanorods that combine thermochromic and photocatalytic properties for application as energy-saving smart coatings, Scientific reports, 3 (2013) 1370.

[30] Y. Chen, X. Zeng, J. Zhu, R. Li, H. Yao, X. Cao, S. Ji, P. Jin, High performance and enhanced durability of thermochromic films using VO_2@ZnO core-shell nanoparticles, ACS applied materials & interfaces, 9 (2017) 27784-27791.

[31] X. Zhao, S.A. Mofid, B.P. Jelle, G. Tan, X. Yin, R. Yang, Optically-switchable thermally-insulating VO_2-aerogel hybrid film for window retrofits, Applied Energy, 278 (2020) 115663.

[32] G. Wyszecki, W.S. Stiles, Color science, Wiley New York, 1982.

[33] B.P. Jelle, Solar radiation glazing factors for window panes, glass structures and electrochromic windows in buildings-Measurement and calculation, Solar Energy Materials and Solar Cells, 116 (2013) 291-323.

[34] A. International, ASTM G173-03 (reapproved 2008), Standard Tables for Reference Solar Spectral Irradiances: Direct Normal and Hemispherical on 37° Tilted Surface, ASTM Internacional, 2008.

[35] G.F. Burkhard, E.T. Hoke, M.D. McGehee, Accounting for interference, scattering, and electrode absorption to make accurate internal quantum efficiency measurements in organic and other thin solar cells, Advanced Materials, 22 (2010) 3293-3297.

[36] L.A. Pettersson, L.S. Roman, O. Inganäs, Modeling photocurrent action spectra of photovoltaic devices based on organic thin films, Journal of Applied Physics, 86 (1999) 487-496.

[37] J.M. Garnett, XII. Colours in metal glasses and in metallic films, Philosophical Transactions of the Royal Society of London. Series A, Containing Papers of a Mathematical or Physical Character, 203 (1904) 385-420.

[38] J. Maxwell Garnett, Colours in metal glasses, in metallic films, and in metallic solutions. II, Philosophical Transactions of the Royal Society of London Series A, 205 (1906) 237-288.

[39] M. Born, E. Wolf, Principles of Optics, 7th (expanded) edition, United Kingdom: Press Syndicate

of the University of Cambridge, 461 (1999).

[40] K. Laaksonen, S.-Y. Li, S. Puisto, N. Rostedt, T. Ala-Nissila, C.-G. Granqvist, R. Nieminen, G.A. Niklasson, Nanoparticles of TiO_2 and VO_2 in dielectric media: Conditions for low optical scattering, and comparison between effective medium and four-flux theories, Solar Energy Materials and Solar Cells, 130 (2014) 132-137.

[41] S.-Y. Li, G.A. Niklasson, C.-G. Granqvist, Nanothermochromics with VO_2-based core-shell structures: Calculated luminous and solar optical properties, Journal of Applied Physics, 109 (2011) 113515.

[42] D.J. Bergman, The dielectric constant of a composite material-a problem in classical physics, Physics Reports, 43 (1978) 377-407.

[43] S. Ji, F. Zhang, P. Jin, Preparation of high performance pure single phase VO_2 nanopowder by hydrothermally reducing the V_2O_5 gel, Solar energy materials and solar cells, 95 (2011) 3520-3526.

[44] E.D. Palik, Handbook of optical constants of solids, Academic press, 1998.

[45] M. Al-Kuhaili, S. Durrani, Optical properties of chromium oxide thin films deposited by electron-beam evaporation, Optical Materials, 29 (2007) 709-713.